TECHNISCHE UNIVERSITÄT WIEN

DISSERTATION

Energy transport and symmetry breaking in open quantum systems

ausgeführt zum Zwecke der Erlangung des akademischen Grades eines Doktors der technischen Wissenschaften unter der Leitung von

Associate Prof. Dr.rer.nat Peter Rabl
E141
Atominstitut

eingereicht an der Technischen Universität Wien
Fakultät für Physik

von

Julian Huber
Matrikelnummer: 1027246
[redacted]

Wien, am

Julian Huber

Diese Dissertation haben begutachtet:

Prof. Dr. Christoph Bruder

Prof. Dr. Helmut Ritsch

Abstract

In this thesis, we study the effect of dissipation on quantum systems. Because of the unavoidable interaction with its environment, every quantum system is subject to dissipation. This usually limits the performance of quantum devices and washes out interesting physics. However, in this thesis we are interested in a limit where the dissipation strengths are comparable to the intrinsic coupling strengths of the system. We find that this competition between coherent dynamics and dissipation leads to many interesting phenomena.

The effect of PT-symmetry breaking in coupled classical systems with balanced gain and loss can be understood as a competition of coherent and incoherent processes. While it has been demonstrated in various classical systems, it is still unclear how this definition can be extended to open quantum system. In this thesis, we provide a definition of PT-symmetry for Liouville operators and show the analogy to the classical case.

Furthermore, we extend this analysis to large spin systems with gain and loss. In order to investigate such extended systems it requires new numerical techniques. In this thesis, we introduce the truncated Wigner method for open quantum spins (TWOQS) to simulate the dynamics and steady states of collective spin systems in the presence of gain, loss and dephasing.

We use the TWOQS to explore the non-equilibrium properties of a spin lattice where coherent interactions between neighboring lattice sites compete with alternating gain and loss processes. In this very simple model we find rather unconventional phase transitions such as a discontinuous phase transition without phase coexistence between two distinct phases at the critical point and a discontinuous mixed-order phase transition with long-range correlations but without any symmetry breaking.

In systems with sources of gain and loss, there is naturally a flow of energy. This motivates the study of energy transport through a network of harmonic oscillators, where a microscopic generator injects energy on one site of the network and a microscopic engine extracts energy from the other site. We investigate the chain in the macroscopic, thermal and in the quantum regime, and describe how the transport is affected by the competition between coherent and incoherent processes and nonlinear saturation effects. We find a coherent and a noise dominated transport regime, which is associated with the breaking of the spatial symmetries.

Finally, we extend the discrete truncated Wigner approximation (DTWA) to dissipative systems (DDTWA). The DDTWA enables an accurate simulation of realistic experiments with hundred-thousand spins while taking account of all different types of dephasing, decay and inhomogeneities.

Kurzfassung

In dieser Arbeit anlysieren wir den Einfluss von Dissipation auf Quantensysteme. Da man ein reales Quantensystem nie perfekt vor äußeren Einflüssen schützen kann, unterliegt jedes System der Dekohärenz. Diese kleine Kopplung mit der Umgebung kann das Vorkommen interessanter Quanteneffekte verhindern. In dieser Arbeit erforschen wir das Gegenspiel zwischen der kohärenten Dynamik und der Dissipation und zeigen das dies zu sehr interessanten Effekten führen kann.

In klassischen PT-symmetrischen Systemen kann dieses Gegenspiel zur Brechung der Symmetrie führen. Während dieser Effekt schon in einer Reihe von klassichen Systemen experimentell nachgewiesen wurde, ist die Definition von PT-symmetrischen offen Quantensystemen noch ungeklärt. In dieser Doktorarbeit liefern wir eine Definition für PT-symmetrische offene Quantensysteme und zeigen die Analogie zu klassischen Systemen anhand mehrerer Beispiele.

Des Weiteren untersuchen wir die Wechselwirkung zwischen kohärenter Dynamik und Dissipation in großen Spingittern. Dieses System besitzt außergewöhnliche Phasenübergänge, wie einen diskontinuierlichen Übergang ohne Phasenkoexistenz am kritischen Punkt und einen diskontinuierlichen Übergang mit langreichweitigen Korrelationen, jedoch ohne Brechung einer Symmetrie.

Da eine exakte Berechnung nur für sehr kleine Systeme möglich ist, benötigt es neue numerische Methoden um so eine Analyse zu ermöglichen. Wir führen deshalb eine neue Methode TWOQS (Truncated Wigner method for Open Quantum Spins) ein, welche die Simulation der Dynamik und des stationären Zustandes von offenen kollektiven Spinsystemen ermöglicht.

Außerdem erweitern wir die Discrete Truncated Wigner Approximation (DTWA) für geschlossene Quantensysteme zu offenen Quantenystemen (DDTWA). Dadurch können wir realistische Experimente mit $N = 10^5$ Spinteilchen unter der Berücksichtigung diverser inkohärenter Prozesse wie Zerfall oder Dephasierung und diverser Imperfektionen wie Inhomogenitäten mit sehr hoher Genauigkeit numerisch berechnen.

Darüber hinaus analysieren wir in dieser Dissertation den Energietransport in offenen Quantensystemen. Wir betrachten dazu ein Netzwerk von harmonischen Oszillatoren an dem an einer Seite Energie hineingepumpt und an der anderen Seiten Energie entfernt wird. Wir analysieren dieses System sowohl im makroskopischen, thermischen als auch quantenmechanischen Bereich und finden einen Übergang zwischen einem kohärenten und einem stark verrauschten Transportbereich. Diese unterschiedlichen Transporteigenschaften hängen von der Topologie und der Symmetrie des Systems ab.

Contents

1 Introduction

"Ich wollte kein 0850 Produkt."

- Marko Arnautovic

1.1 Open quantum systems

The performance of quantum devices such as quantum computer [1, 2], quantum simulators [3–5] or quantum cryptography systems [6] are usually limited by the coupling of the system to a noisy environment. This unavoidable interaction of the quantum system with its surroundings generates system-environment correlations and leads to an irretrievable loss of quantum coherence [7]. All real quantum system are thus open quantum systems that must be described by a non-unitary dynamics which takes the dissipation of energy and the decay of quantum coherences and correlations into account [8]. This decoherence tends to destroy and wash out the interesting quantum effects that give rise to the power of quantum computation, simulation and communication. While for most quantum technologies reducing the dissipation is one of the biggest challenges, dissipation can be also used to prepare systems in certain quantum states [9, 10] and even to perform quantum computation, by designing environments that drive the system into a steady state that encodes the outcome of the computation [11]. Moreover, dissipation can be used, for example, to cool trapped ions to the motional ground state [12, 13], which is essential for implementing high-fidelity quantum gates [14].

Non-equilibrium phase transitions. The study of open quantum systems is also of interest from a different point of view. Recently, there has been a growing interest in non-equilibrium properties of many-body quantum systems, in particular, in the presence of external driving and dissipation. While the equilibrium states and phases of closed systems can be understood by energetic considerations or by the minimization of a thermodynamic potential, such a general theoretical framework is not available for describing the steady states of open quantum systems. As a consequence, there is still little known about the nature of non-equilibrium phase transitions of driven-dissipative quantum systems.

Recently there has been extensive work on this topic. In the context of spin systems, a lot of previous work extended the analysis of the transverse field Ising and related XYZ models to open systems [15–22]. For 1D systems matrix product states (MPS) methods can be used to numerical investigate

such spin models, however typically there are no sharp phase transitions in 1D [18, 22]. In 2D and higher dimensions numerical simulations are very challenging and reliable results can be mostly obtained by exact numerical simulations, which are restricted to rather small lattices [18–20, 22]. Therefore, most of our more reliable insights about dissipative phase transitions are currently based on studies of zero-dimensional models such as collective spin systems [23–28], weakly nonlinear bosonic modes [29–31] or combinations of both [32–34]. In these systems the steady states can be calculated numerically for sufficiently large system sizes or even solved analytically [29, 31, 35].

From the analysis of many such systems a common picture of dissipative phase transitions emerged [24, 36], where the energy gaps are replaced by asymptotic decay rates, but the actual phenomenology is still very similar to the equilibrium case: There are discontinuous first-order phase transitions where two distinct stationary states can coexist at the critical point and continuous second-order phase transitions associated with the breaking of a symmetry. Naturally, this motivates the search for non-equilibrium critical phenomena that lie outside of this conventional framework and for the basic mechanisms that may cause such behavior.

In Chapter 4, we study a spin lattices with alternating gain and loss. We show that this simple model already exhibits several phase transitions, which do not follow the usual phenomenology of first and second-order phase transitions [36]. We study these unconventional phase transitions in detail and compare them with previously known dissipative phase transitions.

Phase space methods. In order to search for such unconventional non-equilibrium phase transitions, the development of new numerical techniques is of imminent relevance. For spin-1/2 systems in 1D there exist reliable tensor network methods to simulate dissipative many-body spin systems [37–39]. As simulations are already challenging for spin-1/2 systems, simulations in the limit of large collective spins $S \gg 1$ can not be performed with these methods. In this limit of $S \gg 1$, mean field theory, the classical description of the system, might give a proper description of the first order mean values for certain models, however it does not give any insight about the correlations of the system. It therefore requires new numerical techniques which accurately predict correlations and can be applied to study large system sizes. In Chapter 6, we introduce the truncated Wigner method for open quantum spins (TWOQS). The TWOQS is based on the truncated Wigner approximation (TWA), where different initial states are time evolved classically. As the initial states are randomly drawn from a Wigner distribution, the correct amount of quantum mechanical uncertainties are included at all times. This usually gives substantially more accurate results and access to correlations. In order to simulate open quantum systems, the classical evolution by the mean-field equations has to be replaced by stochastic equations, which ensures that the initial quantum fluctuations are preserved. This allows us to simulate large spin systems in any dimension and for arbitrary interaction pattern in the prescence of dephasing and decay. We provide a detailed derivation of this

simulation technique and discuss and benchmark its performance in terms of several explicit examples.

The Wigner function can not represent a Fock state with a positive distribution [40], which is necessary to do a TWA simulation. A Fock state therefore must be approximated by a coherent state. The discrete TWA (DTWA) [41] overcomes this problem by introducing a discrete phase space where even higher spin correlations of a spin-1/2 particles are reproduced correctly. In Chapter 7, we use a similar approach as for TWOQS to extend the DTWA to open quantum systems. The dissipative discrete truncated Wigner approximation (DDTWA) can be used to study systems in the presence of local and collective dephasing and decay. Moreover, this extension of the DTWA is not only restricted to white noise processes but also systems in the prescence of colored noise can be simulated very efficiently. Since the number of equations scales linearly with the number of spins, spin systems consisting up to hundred-thousands of spins can be simulated very efficiently. We benchmark this method on the transverse long-range Ising model as well as the driven Dicke model.

PT-symmetry. A prototypical example of a classical dissipative phase transition is the phenomenon of PT (parity and time reversal) symmetry breaking, where the eigenvalues of the dynamical matrix of system change from purely real to purely imaginary. Over the past years, this effect has attracted considerable attention and has been demonstrated in various optical [42–44], electrical [45] and mechanical [46] settings. These works were motivated by a work of Bender and Boettcher, who found a new class of non-Hermitian Hamiltonians with a purely real energy spectrum and attributed this fact to the underlying combined PT symmetry [47]. This opened a whole new field of PT-symmetric quantum theory, where the condition that the Hamiltonian is Hermitian is replaced by the weaker condition that it possesses invariance under space-time inversion [48]. While these are primarily mathematical considerations, there exist many classical systems with balanced gain and loss, whose dynamics can be mapped onto such PT-symmetric Hamiltonians [47, 49–52]. For a recent review of non-Hermitian physics and PT-symmetry see Refs. [51, 52]. However, in a full master equation formulation of open quantum system [7], there is no such transition between purely real and purely imaginary eigenvalues of the corresponding Liouville operator. Also, at a microscopic level, the time-reversal equivalence between loss and gain is broken by quantum fluctuations [53–56]. Therefore, it is still an unresolved question how to formally define PT-symmetry for dissipative quantum systems [57] and if the breaking of this symmetry can exist at all on a microscopic level [56].

In Chapter 5, we introduce for the first time a symmetry transformation for Liouville operators which extends the conventional definition of PT symmetry to arbitrary open quantum systems. This definition is chosen to reproduce the conventional PT-symmetry definition in the classical limit for bosonic systems, but can be used for arbitrary open quantum systems. We show that under very generic conditions there exists a fully symmetric phase and

that this symmetry can be broken. As the dimension of the Hilbert space increases we find a sharp PT-symmetry breaking transition. We illustrate our findings on several examples in order to show the universality of this symmetry breaking transition.

Microscopic energy transport. PT-symmetric systems contain regions with gain and loss and naturally there will be a flow of energy between these different regions. Therefore, a more general question to ask is, how energy is distributed in networks with gain and loss and how this symmetry breaking transition will affect energy transport properties at the micro-scale. The conventional energy transfer in electric systems has been investigated since hundreds of years [58] and is used in our every day lives, as electric energy is transfered from an electric generator of a power plant to our homes, so we can use all kinds of electric devices. These kind of electric transfer can be describes by Ohm's law [58], which states that the current depends on the potential gradient.

However, there is still little known about the energy transport in the microscopic regime, where the electric generators and devices are replaced a microscopic generators and microscopic engines. Recently there has been a growing interest in the performance of microscopic generators, engines or refrigerators, which may even be realized with single quantum systems [59–63]. However, while many theoretical [64–79] and first experimental [80–87] studies of individual quantum machines have already been performed, there is still little known about interfacing multiple such devices. For example, how is energy transfered at the microscopic scale, where quantum and thermal fluctuations become important?

In Chapter 3, we analyze the energy transfer between two quantum machines, which are connected through a chain of coupled harmonic oscillators. Such quantum devices can be operated in different regimes and we therefore investigate the resulting transport phenomena in the macroscopic, in the thermal and in the quantum regime.

1.2 Outline of this thesis

This thesis is organized as follows: In Chapter 2, we first introduce the most common description of open quantum systems and give an overview of different numerical methods to simulate such open quantum systems. In Chapter 3, we then discuss energy transport and symmetry breaking effects in a microscopic power grid, where on one side energy is injected by a microscopic generator while on the other side of the chain energy is absorbed by a microscopic engine. In Chapter 4, we analyze dissipative phase transitions of large spin systems with alternating gain and loss. In Chapter 5, we extend the conventional PT-symmetry breaking in classical systems to open quantum system with gain and loss and demonstrate our finding in terms of a few simple models. In Chapter 6, we introduce the truncated Wigner method

for open quantum spins (TWOQS) to study large dissipative spin systems. Finally, in Chapter 7, we extend the discrete truncated Wigner approximation (DTWA) to study large many-body spin-1/2 systems in the prescence of dephasing and decay and benchmark the method with exact simulations.

1.3 List of publications

The content of this thesis is primarily based on the results contained in the following five publications:

PHYSICAL REVIEW A **100**, 012129 (2019) [88]
Active energy transport and the role of symmetry breaking in microscopic power grids
J. Huber and P. Rabl

In this article, we study the energy flow through a chain of harmonic oscillators, where on one side energy is injected by a microscopic generator while on the other side of the chain energy is absorbed by a microscopic engine. We investigate the flow of energy through this system for different injection and extraction rates of the microscopic generator and the microscopic engine. Moreover, we investigate the energy transport phenomena in the macroscopic, in the thermal and in the quantum regime. Finally, we extend the analysis to networks of harmonic oscillators. For this work, I performed all the analytical and numerical calculations under the supervision of Prof. P. Rabl.

PHYSICAL REVIEW A **102**, 012219 (2020) [89]
Non-equilibrium magnetic phases in spin lattices with gain and loss
J. Huber, P. Kirton and P. Rabl

In this article, we study a chain of coupled spins with alternating gain and loss. We especially focus on the phase transitions of this model and compare these rather unconventional phase transitions to well studied models. We demonstrate that dissipative phase transitions can be very different from the ones in equilibrium systems. For this work, I performed all analytical and numerical calculations except the iMPS simulation, which was performed by P. Kirton. All work was done under the supervision of P. Kirton and Prof. P. Rabl.

SCIPOST PHYSICS **9**, 052 (2020) [90]
Emergence of PT-symmetry breaking in open quantum systems
J. Huber, P. Kirton, S. Rotter and P. Rabl

In this article, we introduce a symmetry transformation for Liouville operators, which extends the conventional definition of PT symmetry for classical systems to arbitrary open quantum systems. We proof that under very generic conditions, the existence of this symmetry implies that the steady state of the system can be tuned between a fully symmetric and a symmetry-broken phase. We demonstrate this for simple models such as coupled spin systems as well as for randomly generated systems and systems with multiple gain and loss processes. Furthermore, we investigate the spectrum and dynamics of such PT-symmetric Liovillian system. For this work, I performed all of the numerical calculations and most of the analytical calculation under the supervision of Prof. P. Rabl. P. Kirton provided the proof of the existence of the symmetric phase.

SCIPOST PHYSICS **10**, 045 (2021) [91]
Phase-Space Methods for Simulating the Dissipative Many-Body Dynamics of Collective Spin Systems
J. Huber, P. Kirton, and P. Rabl

In this article, we use phase-space methods to simulate open quantum spin systems. This extension of the well-known truncated Wigner approximation to open spin systems can be used to study large spin systems very efficiently. By benchmarking the method with exact solutions and exact simulations, we show that this method gives accurate results and can even predict higher correlations correctly, especially in the limit of large spin quantum numbers. For this work, I performed all numerical and analytical calculation under the supervision of P. Kirton and Prof. P. Rabl.

arXiv:2105.00004 (2021) [92]
Realistic simulations of spin squeezing and cooperative coupling effects in large ensembles of interacting two-level systems
J. Huber, A. M. Rey, and P. Rabl

In this article, we extend the discrete truncated Wigner approximation to study open quantum systems. We benchmark this method by comparing it to exact simulations of the long-range transverse Ising model in the presence of local and collective dephasing and decay, where we find excellent agreement even for higher correlations. Additionally, we benchmark the system by simulating the open driven Dicke model, where we find excellent agreement in the dynamic as well as in the steady state of the system when comparing to exact simulations. In this work, I performed all analytical and numerical calculations under the supervision of Prof. P. Rabl.

Further Publications during my PhD

Circulating tissue-resident memory T cells are poised for a systemic Th2-driven host-versus-graft reaction
J. Strobl, L. Gail, L. Kleissl, R. Pandey, V. Puxkandl, R. Dingelmaier-Hovorka, D. Atzmüller, V. Smejkal, J. Huber, T. Krausgruber, C. Bock, P. Wohlfarth, W. Rabitsch, G. Stary

Physical Review B **97** (11), 115205
Zero-field optical magnetic resonance study of phosphorus donors in 28-silicon
K. J. Morse, P. Dluhy, J. Huber, J. Z. Salvail, K. Saeedi, H. Riemann, N. V. Abrosimov, P. Becker, H.-J. Pohl, S. Simmons, M. L. W. Thewalt

2 Open quantum systems

"Früher hab dich immer das gemacht, was in meinem Kopf war, das war natürlich der Fehler."

- Marko Arnautovic

In this chapter, we introduce the most common description of open quantum systems, the Lindblad master equation. Based on the explicit example of a damped harmonic oscillator, we then give a short overview of the most common numerical methods to simulate such open quantum systems.

2.1 Master equation

The Lindblad master equation [8] describes the time evolution of a system's density operator interacting with a bath. It is assumed that the system-bath interaction is weak and that this interaction does not considerably change the state of the bath (Born approximation). Another assumption is that the bath has very short memory time (Markov approximation) and that the timescales of the system dynamics are faster than the loss and gain rates (secular approximation). The master equation preserves the trace and the positivity of the density operator for all times. The master equation has the following form

$$\dot{\rho} = -\frac{i}{\hbar}[H, \rho] + \sum_j \Gamma_j \mathcal{D}[c_j]\rho, \tag{2.1}$$

with the Lindblad superoperator

$$\mathcal{D}[c]\rho = 2c\rho c^\dagger - c^\dagger c\rho - \rho c^\dagger c. \tag{2.2}$$

The first part of Eq. (2.1) is the von Neumann equation and describes the unitary Hamiltonian dynamics, while the last part describes the non-unitary dynamics due to the coupling to external degrees of freedom, which are represented by a set of jump operators c_j and the corresponding rates Γ_j

Alternatively, we can express the master equation Eq. (2.1) as an evolution of a non-hermitian effective Hamiltonian and additional recycling terms:

$$\dot{\rho} = -\frac{i}{\hbar}\left(H_{\text{eff}}\rho - \rho H_{\text{eff}}^\dagger\right) + 2\sum_j \Gamma_j c_j \rho c_j^\dagger, \tag{2.3}$$

with the effective Hamiltonian

$$H_{\text{eff}} = H - i\sum_j \Gamma_j c_j^\dagger c_j. \tag{2.4}$$

The effective Hamiltonian has only negative real eigenvalues and therefore the evolution with the effective Hamiltonian decreases the populations of the density matrix. The last part in Eq. (2.3) recycles the populations that are lost from certain states and transfers them to other states.

Example

The master equation for a bosonic system coupled to thermal bath reads [7]

$$\dot{\rho} = -i\omega[a^\dagger a, \rho] + \gamma(N_{\text{th}} + 1)\mathcal{D}[a] + \gamma N_{\text{th}}\mathcal{D}[a^\dagger], \tag{2.5}$$

where a is the bosonic annihilation operator. The first term describes the unitary dynamics of the Hamiltonian $H = \hbar\omega a^\dagger a$ while the last two terms describe the non-unitary loss and gain processes due to the coupling to a thermal bath with a mean occupation number $N_{\text{th}} = (e^{\hbar\omega/k_B T} - 1)^{-1}$ at frequency ω.

Note that especially for composite systems the validity of all approximations mentioned above must be carefully checked as a wrong description can lead to unphysical results [93]. Throughout this thesis we will consider systems and parameter regimes, where such a master equation description can be applied.

A master equation can consist of many subsystems and due to the exponential growth of the Hilbert space it usually a very hard task to solve the master equation of large systems. In the following we describe the most common approaches to do so numerically.

2.2 Exact simulation

We can simulate a master equation exactly by vectorizing the density matrix. This can be done by reshaping the density matrix into a vector $\rho \to |\rho\rangle$. As a consequence, we also have to transform the master equation. We use the following transformation rules for an arbitrary operator A:

$$A\rho \to (A \otimes \mathbb{1})|\rho\rangle \tag{2.6}$$

and

$$\rho A \to (\mathbb{1} \otimes A^T)|\rho\rangle. \tag{2.7}$$

Example

A master equation for a simple dissipative system as given by Eq. (2.5) with the loss rate γ and $N_{\text{th}} = 0$ can be rewritten into the following vectorized form

$$\frac{d}{dt}|\rho\rangle = \gamma\left[2a \otimes (a^\dagger)^T - a^\dagger a \otimes \mathbb{1} - \mathbb{1} \otimes (a^\dagger a)^T\right]|\rho\rangle. \tag{2.8}$$

This equation can be written in short as $\frac{d}{dt}|\rho\rangle = \mathcal{L}|\rho\rangle$, where $\mathcal{L}$ is the Liouville operator. By vectorizing the density matrix and transforming the

master equation, we can simulate open quantum systems the same way as in the non-dissipative case, but the dimension of the system changes from d to d^2. We can therefore simply time evolve an open quantum system by using standard numerical routines such as the Runge-Kutta algorithm. If we are only interested in the steady state of a system, we can directly calculate the steady state by finding the eigenvector of the Liouvillian operator $\mathcal{L}$ with the zero eigenvalue, or simply evolve the system for a sufficiently long time.

2.3 Quantum trajectories

Quantum trajectories can be used much like the master equation to simulate small quantum systems coupled to a large reservoir. However, in contrast to the master equation, one simulates the system's wave function and not the full density operator [94, 95]. The idea is to let the system evolve with an effective Hamiltonian, where at each time step a quantum jump (discontinuity) may take place with some probability. A quantum jump would correspond, for example, to an optical cavity losing one photon to the bath. The big advantage of quantum trajectories is that for a state vector with n elements, only n elements must be computed, while by using the master equation one must evolve a density matrix with n^2 elements.

There are mainly two ways to implement quantum trajectories in a computer program. One is to calculate the probability of a jump for every time step and then choose a random number to determine if a jump occurs or not. Another way is to let the state evolve until the norm of the state equals the chosen random number and then a jump happens for sure. This is in general more effective and will be discussed in more detail in the following.

2.3.1 Algorithm for one trajectory

1. Choose the inital state $|\psi(0)\rangle$.

2. Choose the random number $r \in [0, 1]$.

3. Time-evolve with the non-Hermitian effective Hamiltonian H_{eff} until $r > \langle\psi(t)|\psi(t)\rangle$. For the simple dissipative system of Eq. (2.5) with $N_{\text{th}} = 0$ we arrive at

$$\dot{\rho} = -\frac{i}{\hbar}[H, \rho] + \gamma\mathcal{D}[a] = -\frac{i}{\hbar}H_{\text{eff}}\rho + \frac{i}{\hbar}\rho H_{\text{eff}}^{\dagger} + 2\gamma a\rho a^{\dagger}, \tag{2.9}$$

   where $H_{\text{eff}} = H - i\gamma a^{\dagger}a$.

4. Apply the quantum jump and normalize the wavefunction $|\psi\rangle = \frac{c|\psi\rangle}{\langle\psi|c^{\dagger}c|\psi\rangle}$. Note: If the system has N jump operators c_i, the probability which quantum jump happens is computed by $p_i = \frac{\langle\psi|c_i^{\dagger}c_i|\psi\rangle}{\sum_{i=0}^{N}\langle\psi|c_i^{\dagger}c_i|\psi\rangle}$.

5. Go to step 2. until $t = t_{end}$.

To obtain the same evolution as by solving the master equation, hundreds of trajectories must be calculated and averaged. The relative error goes with $\frac{1}{\sqrt{n_{\text{traj}}}}$ where n_{traj} is the number of trajectories. In general the time evolution can be done in many different ways such as the Runge-Kutta method, calculating the time evolution operator, Lanczos algorithm, just to name a few. Note that as an alternative to simulating the dissipative dynamics in terms of discrete quantum jumps, an equivalent stochastic equation for the wave function can be applied, where random updates occur at every timestep [96]. Again, this has to be done several times to reproduce the wave function.

2.4 Phase space methods

One way to solve the master equation for a bosonic system, Eq. (2.5), is to map the master equation onto an equivalent partial differential equation for a class of phase-space distributions, which contain the same information as the density operator [97].

We parameterize the set of distributions by the variable k and define

$$F_k(\alpha,t) = \frac{1}{\pi^2}\int d^2\lambda\, e^{(\alpha\lambda^*-\alpha^*\lambda)}\,\mathrm{Tr}\left\{e^{\lambda a^\dagger}\rho e^{-\lambda^* a}\right\} e^{\frac{(1+k)}{2}|\lambda|^2}, \tag{2.10}$$

where a is the bosonic annihilation operator and α is a complex number. When $k=0$ this phase space distribution corresponds to the Wigner function [98], for $k=1$ it is the Glauber-Sudarshan P-representation [99] and when $k=-1$ we obtain the Husimi Q-function [100].

Eq. (2.10) defines all three distributions in a very compact way, however it's hard to obtain any insights from this. In the following we will provide alternative definitions of these distributions [101].

P-distribution

The P-distribution can also be introduced in the following way [99]

$$\rho = \int d^2\alpha P(\alpha)|\alpha\rangle\langle\alpha|, \tag{2.11}$$

where $|\alpha\rangle = e^{-|\alpha|^2/2}\sum_{n=0}^{\infty}\frac{\alpha^n}{\sqrt{n!}}|n\rangle$ is the bosonic coherent state. The P-function therefore expresses a density matrix as an integral over coherent states. The P-function is convenient to calculate normally-ordered expectation values

$$\langle a^{\dagger n}a^m\rangle = \int d^2\alpha\ \alpha^n\alpha^{*m}P(\alpha). \tag{2.12}$$

From the definition of Eq. (2.11) it directly follows that a coherent state $|\alpha_0\rangle$ is represented as a delta peak

$$P(\alpha) = \delta(\alpha-\alpha_0). \tag{2.13}$$

However any state with smaller width than a coherent state such as a Fock state $|n\rangle$ can not be represented by a positive non-singular P-distribution. For Fock state $|n\rangle$ the P-distribution reads [102]

$$P(\alpha) = \frac{1}{n!}\left(\frac{\partial^2}{\partial\alpha\partial\alpha^*}\right)\delta^2(\alpha). \tag{2.14}$$

In order to represent a Fock state by a non-singular positive probability we can introduce the positive P-function [103, 104]

$$\rho = \int d^2\alpha d^2\beta P(\alpha,\beta)\frac{|\alpha\rangle\langle\beta^*|}{\langle\beta^*|\alpha\rangle}, \tag{2.15}$$

which doubles the degrees of freedom. The positive P-function is a probability distribution which can represent all states.

Q-distribution

The Q-distribution [100] can be defined as

$$Q(\alpha) = \frac{1}{\pi}\langle\alpha|\rho|\alpha\rangle. \tag{2.16}$$

Since the density operator is a positive operator, the Q-function is non-negative and bounded, $Q(\alpha) < \frac{1}{\pi}$. Moreover, the Q-distriubtion can represent a Fock state $|n\rangle$ with

$$Q(\alpha) = \frac{1}{\pi}e^{-|\alpha|^2}\frac{|\alpha|^{2n}}{n!}, \tag{2.17}$$

while coherent states can be represented by a normal distribution

$$Q(\alpha) = \frac{1}{\pi}e^{-|\alpha-\alpha_0|^2}. \tag{2.18}$$

Furthermore, the Q-distribution is an overcomplete map and therefore contains unphysical states such as $Q(\alpha) = \delta(\alpha)$. The fact that this Q-function is unphysical can be easily shown by calculating anti-normally ordered moments

$$\langle a^n a^{\dagger m}\rangle = \int d^2\alpha\ \alpha^n\alpha^{*m}Q(\alpha). \tag{2.19}$$

Wigner-distribution

The Wigner function [98] is a quasi-probability function and defined the following way

$$W(x,p) = \frac{1}{h}\int e^{-ipy}\langle x+y/2|\hat{\rho}|x-y/2\rangle dy. \tag{2.20}$$

Although the marginal distributions of the Wigner function are proper probability distributions of position, $W(x) = \int dpW(x,p) \geq 0$, and momentum $W(p) = \int dxW(x,p) \geq 0$, the full distribution $W(x,p)$ can become negative

and is therefore not a probability density. The Wigner function of a Fock state $|n\rangle$ is

$$W(\alpha) = \frac{2}{\pi}(-1)^n L_n(4|\alpha|^2)e^{-2|\alpha|^2}, \tag{2.21}$$

where $L_n(x)$ is the Laguerre polynomial. This Wigner function is clearly negative for $n > 0$ while the Wigner function of a coherent state is everywhere positive with

$$W(\alpha) = \frac{2}{\pi}e^{-2|\alpha-\alpha_0|^2}. \tag{2.22}$$

The Wigner function can be used to evaluate symmetrically ordered operators

$$\langle\{a^{\dagger n}a^m\}_{sym}\rangle = \int d^2\alpha\ \alpha^n\alpha^{*m}W(\alpha), \tag{2.23}$$

where, for example, $\{a^\dagger a\}_{sym} = \frac{1}{2}(a^\dagger a + aa^\dagger)$. Because the ordering is different in all three distributions, not only the distribution but also the mean values of the complex amplitude α are completely different. For the vacuum state $|0\rangle$ we arrive at $\langle|\alpha|^2\rangle = 0, 1/2, 1$ for the P-,W-,Q-function.

2.4.1 Master equation mapping

We can use the general definition of Eq. (2.10) or, equivalently, Eqs. (2.11), (2.16) and (2.20) to calculate what form each term in the master equation takes in the equation for F_k [97, 102]. For example, for a single mode one finds the mapping

$$a\rho \rightarrow \left[\alpha + \frac{(1-k)}{2}\frac{\partial}{\partial\alpha^*}\right]F_k(\alpha,t), \tag{2.24}$$

$$a^\dagger\rho \rightarrow \left[\alpha^* - \frac{(1+k)}{2}\frac{\partial}{\partial\alpha}\right]F_k(\alpha,t), \tag{2.25}$$

$$\rho a^\dagger \rightarrow \left[\alpha^* + \frac{(1-k)}{2}\frac{\partial}{\partial\alpha}\right]F_k(\alpha,t), \tag{2.26}$$

$$\rho a \rightarrow \left[\alpha - \frac{(1+k)}{2}\frac{\partial}{\partial\alpha^*}\right]F_k(\alpha,t). \tag{2.27}$$

Again for $k = 0$ this corresponds to the Wigner function, for $k = 1$ to the Glauber-Sudarshan P-representation and $k = -1$ to the Husimi Q-function. This translation lets us recast the master equation for ρ of N bosonic modes in the form of a partial differential equation for the phase space distribution,

$$\frac{\partial}{\partial t}F_k(\vec{\alpha},t) = LF_k(\vec{\alpha},t), \tag{2.28}$$

with L some linear differential operator, which depends on the specific problem under consideration, and $\vec{\alpha} = (\alpha_1, \alpha_2, \ldots, \alpha_N)$.

2.4.2 Truncated Wigner approximation

The result in Eq. (2.28) is still exact but in general not very useful. In particular, the differential operator L may contain third- or higher-order derivatives, which prevent an efficient stochastic sampling of F_k. We can therefore perform the truncated Wigner approximation [105–107] by neglecting all third- and higher order terms and obtain a Fokker-Planck equation of the form

$$\frac{\partial}{\partial t}F_k(\vec{x},t) = \left[-\frac{\partial}{\partial x_j}A_j(\vec{x}) + \frac{1}{2}\frac{\partial}{\partial x_i}\frac{\partial}{\partial x_j^*}D_{ij}(\vec{x})\right]F_k(\vec{x},t), \tag{2.29}$$

with a drift matrix A and a diffusion matrix D. Here we have assumed Einstein's sum convention, where the indices i and j run over the $2N$ components of the vector $\vec{x} = (\alpha_1, \alpha_1^*, \alpha_2, \alpha_2^*, \dots)$.

Example

The master equation of a bosonic system coupled to a thermal bath, Eq. (2.5), can be transformed into the following Fokker-Planck equation

$$\begin{aligned}\frac{\partial}{\partial t}F_k(\alpha,t) = \Bigg[&(i\omega+\gamma)\frac{\partial}{\partial\alpha}\alpha + (-i\omega+\gamma)\frac{\partial}{\partial\alpha^*}\alpha^* \\ &+ \gamma\left(N_{\text{th}} + \frac{(1-k)}{2}\right)\frac{\partial^2}{\partial\alpha\partial\alpha^*}\Bigg]F_k(\alpha,t).\end{aligned} \tag{2.30}$$

Note that in this example no third- and higher-order terms had to be neglected.

2.4.3 Stochastic simulations

If the diffusion matrix of the Fokker-Planck equation Eq. (2.29) is positive definite, the Fokker-Planck equation can be mapped onto an equivalent set of stochastic (Ito) differential equations [108],

$$dx_i = A_i(\vec{x})dt + B_{ij}(\vec{x})dW_j(t), \tag{2.31}$$

where dW_i are real-valued independent Wiener processes with $\langle dW_i dW_j\rangle = \delta_{ij}dt$ and $B(\vec{x})$ is the factorized diffusion matrix with $B(\vec{x})B(\vec{x})^\dagger = D(\vec{x})$. This set of equations can be efficiently simulated with the Euler-Maruyama method [108]. This means that we do not calculate the full probability distribution, but instead obtain the required expectation values by averaging over n_{traj} trajectories of these stochastic equations. For sufficiently many trajectories and with initial values sampled according to the distribution $F_k(\vec{\alpha}, t=0)$, these stochastic averages provide accurate approximations of the corresponding quantum mechanical expectation values

$$\langle (a_i^\dagger)^n a_j^m\rangle_{P|Q|W} = \int d^{4N}\alpha\,(\alpha_i^*)^n\alpha_j^m F_k(\vec{\alpha},t) \approx \langle(\alpha_i^*)^n\alpha_j^m\rangle_{\text{stoch}}(t), \tag{2.32}$$

where, depending on the chosen distribution function, $\langle \dots \rangle_{P|Q|W}$ denotes the normally-ordered, anti-normally-ordered or symmetrically-ordered expectation value.

To sum up, by using phase space methods we can map a master equation exactly or with approximation (TWA) to a set of stochastic equations which can be solved numerically very efficiently.

Example

In case of master equation Eq. (2.5), a bosonic mode coupled to a thermal bath, we arrive at following stochastic equation

$$d\alpha = -i(\omega + \gamma)\alpha dt + \sqrt{\gamma\left(N_{\text{th}} + \frac{1-k}{2}\right)}(dW_1 + i dW_2). \tag{2.33}$$

2.5 Cumulant expansion

In general the equation of motion of an expectation value depends on higher order expectation values. This usually leads to an infinite hierarchy of equations. The cumulant expansion keeps all correlations until a certain order and approximates all higher correlations with a combination of lower correlations. The approximation to the lowest order is equivalent to mean-field theory, where correlations are approximated in the following way

$$\langle AB \rangle \approx \langle A \rangle \langle B \rangle. \tag{2.34}$$

This expression becomes exact if there are no correlations between the two subsystems A and B and the system behaves classical. All third and fourth order correlations are approximated the following way [109]

$$\langle ABC \rangle \approx \langle AB \rangle\langle C \rangle + \langle AC \rangle\langle D \rangle + \langle BD \rangle\langle A \rangle - 2\langle A \rangle\langle B \rangle\langle C \rangle, \tag{2.35}$$

$$\begin{aligned}\langle ABCD \rangle \approx\ & \langle ABC \rangle\langle D \rangle + \langle ABD \rangle\langle C \rangle + \langle ACD \rangle\langle B \rangle + \langle ACD \rangle\langle B \rangle \\ & + \langle AB \rangle\langle CD \rangle + \langle AC \rangle\langle BD \rangle + \langle AD \rangle\langle BC \rangle - 2\langle AB \rangle\langle C \rangle\langle D \rangle \\ & + \langle AC \rangle\langle B \rangle\langle D \rangle + \langle AD \rangle\langle B \rangle\langle C \rangle + \langle BC \rangle\langle A \rangle\langle D \rangle \\ & + \langle BD \rangle\langle A \rangle\langle C \rangle + \langle CD \rangle\langle A \rangle\langle B \rangle + 6\langle A \rangle\langle B \rangle\langle C \rangle\langle D \rangle.\end{aligned} \tag{2.36}$$

In order to solve a system containing N subsystems, the number of equations scales with $\mathcal{O}(N^k)$, where k is the order of the cumulant expansion. While the number of mean-field equations scales only linearly with the system size N, simulations including higher orders are again restricted to rather small system sizes. By increasing the order of the approximation, the results becomes more and more exact. However, when simulating these non-linear equations instabilities can occur that lead to unphysical results. Nevertheless, this approach has been successfully used in several works [110–114] and even numerical packages are available [115].

2.6 Tensor network methods

Tensor network methods are very efficient methods for simulating quantum systems as they restrict the Hilbert space to a smaller subspace by expressing states by a sum of the most important product states [116].

2.6.1 Matrix Product States (MPS)

The most prominent example of a tensor network are MPS, which can be used to efficiently study 1D systems [117–120]. The success of MPS relies on the fact that the entanglement entropy of the ground state of 1D gapped Hamiltonians [121] follows an area law of entanglement entropy. However, it still remains unclear whether transient or steady states in open quantum systems can be represented efficiently. Nevertheless, most algorithms for closed system can be straightfowardly extended to open quantum systems. By vectorizing the master equation, as done in Section 2.2, the time evolution can be performed by the typical methods such as time-evolving block decimation (TEBD), Runge-Kutta, Krylov methods and time-dependent variational principle (TDVP) [122, 123]. The density matrix can be represented as a Matrix Product Operator (MPO) to ensure the positivity of the density matrix [37]. Moreover, quantum trajectories as explained in Section 2.3 can be simulated with MPS [95, 124].

Instead of implementing the time evolution, the steady state can be determined directly by finding the eigenvector of the zero eigenvalue. This can be done by finding the ground state of $\mathcal{L}^\dagger\mathcal{L}$ [38]. The other possibility is to use the same algorithm as for ground state search on $\mathcal{L}$, but always look for the eigenstate closest to the zero eigenvalue instead of the eigenstate of the lowest eigenvalue. In certain cases this can converge faster, but it is very often less numerical stable [125].

Moreover, the MPS concept can be extended to infinite 1D spin chain (iMPS). The time evolution can be done by the iTEBD algorithm, which is the extension of the TEBD algorithm to infinte systems [126]. To calculate observables the network is contracted using a termination tensor, which corresponds to the eigenvector with the largest eigenvalue of the transfer matrix. This is not restricted to unitary dynamics and can be applied to simulate Lindblad master equations [39].

2.6.2 Projected Entangled Pair Source (PEPS)

PEPS is the extension of MPS to two-dimensional systems [127, 128] which also allows to simulate infinite lattices (iPEPS) [129]. Simulation of 2D tensor networks is particularly challenging as a 2D network of tensors needs to be contracted and several numerical parameters have to be chosen carefully. Nevertheless, iPEPS can be adapted to simulate 2D open quantum systems [130]. This is of particular interest as there are usually no symmetry breaking phase transition in 1D open quantum system, but they can exist in

2D systems. However, simulation of 2D open quantum systems with tensor network system is very challenging and often the solution are not converging or numerical instabilities can appear [131, 132].

2.6.3 Neural networks

Neural networks can be seen a special kind of tensor network system [133] and can be used to store many-body states also for states of higher dimensional systems [134]. This was first demonstrated by Carleo et al. [135] by doing a variational Monte-Carlo simulation of the Ising model where the wave function is represented as a restricted Boltzmann machine. Moreover, this can be extended to open quantum systems [136–139]. However, the simulations so far are restricted to small system sizes and some results showed rather large errors. At the moment these works should be therefore seen more as a proof of principle.

3 Energy transport and the role of symmetry breaking in microscopic power grids*

"And all this science I don't understand, It's just my job five days a week."

- Elton John (Rocket Man)

Energy transport takes place in many parts of our lives. One prominent example is the transport of electric energy. In order to use all kinds of electronic devices, electric energy is typically transferred from an electric generator of a power plant to our homes. This kind of electric energy transfer can be described by Ohm's law [58], which states that the current depends on the potential gradient.

While this macroscopic energy transport has been investigated for hundreds of years, there is still little known about the energy transport in the microscopic regime. In this regime, the electric generators and devices are replaced by microscopic generators and microscopic engines. Recently there has been extensive theoretical works on microscopic quantum machines [64–79] and there has been several experiments investigating such quantum machines [80–87]. The aim of most of these works is to compare the efficiency of these quantum machines with the one of the classical Carnot process. However, here we are interested in a different scenario.

In this chapter, we investigate the energy transport by connecting such quantum machines through an oscillator network. We mainly focus on the situation, where a microscopic generator injects energy on one site of a harmonic oscillator chain and a microscopic engine extracts energy from the other site. Such quantum devices can be operated in different regimes and we therefore investigate the resulting transport phenomena in the macroscopic, thermal and quantum regime. Furthermore, we show that these findings don't depend on the specific type of the microscopic generators and engines and that these effects are robust to any imperfections of the system. At the end of this chapter we extend our analysis to more complex networks of harmonic oscillators.

* This chapter is based on the article: J. Huber and P. Rabl, Active energy transport and the role of symmetry breaking in microscopic power grids, Phys. Rev. A **100**, 012129 (2019).

3.1 Model

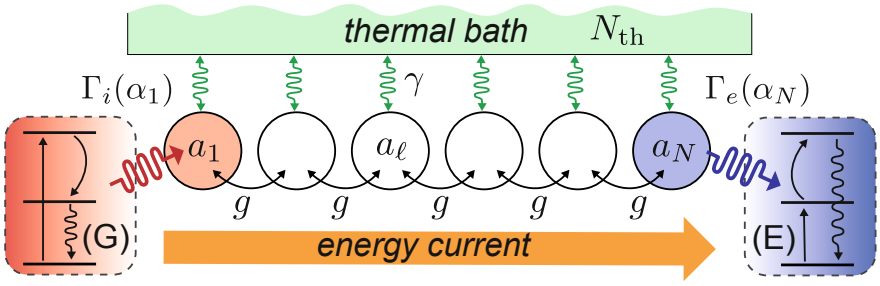

Figure 3.1: Sketch of a microscopic power grid realized by an array of coupled harmonic oscillators. Energy is injected at one end by a microscopic generator (G) with rate Γ_i and extracted at the other end by a microscopic engine (E) with rate Γ_e. Both processes are energy-dependent and saturate above a characteristic amplitude $\sqrt{n_0}$. All oscillators are coupled weakly to a thermal environment. See text for more details.

We consider a chain of $N \geq 2$ coupled harmonic oscillators, as schematically shown in Fig. 3.1. The oscillators have a frequency ω_0 and they are coupled to their neighbors with strength g. Energy is injected at the first site with a rate Γ_i and extracted at the other end with rate Γ_e. In addition, all oscillators are weakly coupled to a thermal environment at temperature T. In the frame rotating with $\omega_0 \gg g, \Gamma_{i,e}$, the whole network is described by a master equation for the density operator ρ,

$$\begin{aligned}\dot{\rho} = &-\frac{i}{\hbar}[H_g,\rho] + \Gamma_i \mathcal{D}[A_1^\dagger]\rho + \Gamma_e \mathcal{D}[A_N]\rho \\ &+ \sum_{\ell=1}^{N} \gamma(N_{\rm th}+1)\mathcal{D}[a_\ell]\rho + \gamma N_{\rm th}\mathcal{D}[a_\ell^\dagger]\rho,\end{aligned} \tag{3.1}$$

where a_ℓ ($a_\ell^\dagger$) are the annihilation (creation) operators for each oscillator and $\mathcal{D}[a]\rho \equiv a\rho a^\dagger - (a^\dagger a\rho - \rho a^\dagger a)/2$. The first term of Eq. (3.1) describes the coherent exchange of energy along the chain with the Hamiltonian

$$H_g = -\frac{\hbar g}{2}\sum_{\ell=1}^{N-1}(a_\ell^\dagger a_{\ell+1} + a_\ell a_{\ell+1}^\dagger)\ , \tag{3.2}$$

while the second and the third term model the incoherent pump and dissipation processes, respectively.

In this chapter, we are interested in energy transport, where source and drain are represented by driven few-level quantum systems. However, to keep our analysis on a general level and to avoid details of specific implementations, we simply mimic the main characteristics of such microscopic generators and engines (providing gain, being saturable) by introducing in Eq. (3.1) the nonlinear jump operators $A_{\ell=1,N} = f(a_\ell^\dagger a_\ell)a_\ell$. Here the cutoff function $f(x)$,

where $f(0) = 1$ and $f(x \gg n_0) \to 0$, accounts for the fact that both the injection as well as the extraction of energy saturate above a characteristic occupation number n_0. By changing this saturation parameter, we can tune the degree of microscopicity of the network without changing any other properties of the system. For concreteness, we will mainly focus here on the cutoff function

$$f(a^\dagger a) = \frac{1}{(1 + a^\dagger a/n_0)}, \tag{3.3}$$

which reproduces the saturation dependence of driven three-level generators and engines [140], as depicted in Fig. 3.1. In Section 3.6, we simulate the system for different shapes of the cutoff function $f(x)$ and we show that none of our central conclusions depend on the specific from of $f(x)$. Note by using a different shape of $f(x)$ other realizations of quantum machines [64–79] can be simulated.

Finally, the second line of Eq. (3.1) describes the coupling of each oscillator to a local thermal bath, where $N_{\text{th}} = (e^{\hbar\omega_0/k_BT} - 1)^{-1}$ is the equilibrium occupation number and γ the damping rate, which we assume to be much smaller than Γ_i and Γ_e. Note that the use of local jump operators in Eq. (3.1) is justified by the assumption that ω_0 is large compared to both the coherent intra-system coupling g and the dissipation rates [141, 142].

Typical systems which can be used to implement this model include coupled nanomechanical resonators [143–146], linear chains of trapped ions [147–149] or arrays of coupled LC oscillators [150–152]. For all those platforms various techniques for engineering local gain and loss processes at the quantum level are already experimentally available [14, 153, 154].

3.1.1 Fokker-Planck equation

For most parts of the following discussion we will be interested in the regime $n_0 \gg 1$, where the cutoff function $f(x)$ in Eq. (3.3) varies slowly on the scale of individual excitations and the master equation can be mapped onto a Fokker-Planck equation for the Glauber-Sudarshan P-representation [97, 99, 102] and expressed as a set of stochastic differential equations as explained in Chapter 2.4).

In the limit of $n_0 \gg 1$, we can therefore rewrite the master equation Eq. (3.1) as following set of stochastic Ito-equations (a detailed derivation can be found in Appendix A.1)

$$\dot{\alpha_1} = \frac{\Gamma_i(\alpha_1) - \gamma}{2}\alpha_1 + i\frac{g}{2}\alpha_2 + \sqrt{D_{\text{th}} + \Gamma_i(\alpha_1)}\xi_1(t), \tag{3.4}$$

$$\dot{\alpha_\ell} = -\frac{\gamma}{2}\alpha_\ell + i\frac{g}{2}(\alpha_{\ell-1} + \alpha_{\ell+1}) + \sqrt{D_{\text{th}}}\xi_\ell(t), \tag{3.5}$$

$$\dot{\alpha_N} = -\frac{\Gamma_e(\alpha_N) + \gamma}{2}\alpha_N + i\frac{g}{2}\alpha_{N-1} + \sqrt{D_{\text{th}}}\xi_N(t). \tag{3.6}$$

Here $\Gamma_{i,e}(\alpha) = \Gamma_{i,e} f^2(|\alpha|^2)$ and $D_{\text{th}} = \gamma N_{\text{th}}$ is the thermal diffusion rate. The $\xi_\ell(t)$ are white noise processes, which satisfy $\langle \xi_\ell^*(t)\xi_{\ell'}(t')\rangle = \delta_{\ell\ell'}\delta(t - t')$. We

are primarily interested in the steady-state energy current

$$\langle J_\ell \rangle = i\frac{g}{2}\langle a_\ell^\dagger a_{\ell-1} - a_{\ell-1}^\dagger a_\ell \rangle = g\mathrm{Im}\langle\langle \alpha_{\ell-1}^* \alpha_\ell \rangle\rangle, \tag{3.7}$$

which can be obtained from the longtime average over many trajectories, denoted by $\langle\langle\cdot\rangle\rangle$. In the regime of interest, $\gamma \to 0$, the average current is approximately constant throughout the chain and we can drop the index ℓ. In the following, we will analyze the system in the following three parameter regimes:

- macroscopic regime: $n_0 \gg 1$ and $N_{\mathrm{th}} \ll n_0$,
- thermal regime: $n_0 \gg 1$ and $N_{\mathrm{th}} \sim n_0$,
- quantum regime: $n_0 \sim 1$ and $N_{\mathrm{th}} \ll n_0$.

3.2 Anomalous energy transport

We first consider the macroscopic regime $n_0 \gg 1$ and $N_{\mathrm{th}} \ll n_0$, where both thermal and quantum noise effects in Eqs. (3.4)-(3.6) can be neglected. The steady state is then described by a set of amplitudes α_ℓ^0 and in Fig. 3.2(a) we plot the corresponding current $\langle J \rangle$ for $N = 10$ sites. We see that transport in this system is very different from Ohm's law, but also from the ballistic flow of heat through a coupled chain of harmonic oscillators [147, 148, 155]. Overall, we find regimes of normal transport, where for fixed injection rate Γ_i the current increases with increasing extraction rate Γ_e, but also regimes of anomalous transport, where the opposite dependence is observed.

For $\Gamma_i < g$ there is a range of rates Γ_e where the current is completely stalled and only re-establishes at higher extraction rates. This counterintuitive behavior [156, 157] can be traced back to the fact that within this parameter range all eigenvalues of the linear chain, i.e., when saturation effects are neglected, have a negative real part and the whole network is damped to zero. This is shown in Fig. 3.3(a) where we plot the largest real part of all the eigenvalues obtained from the dynamical matrix of a linear chain where $\Gamma_{i,e}(\alpha) = \Gamma_{i,e}$. As long as all eigenvalues have a negative real part, the chain is damped to zero. This only occurs in the 'stalled' phase where $\Gamma_i < g$ and $\Gamma_i \leq \Gamma_e < g^2/\Gamma_i$. Otherwise, we see that the structure of the current plotted in Fig. 2(a) is not at all reflected in the eigenvalue structure of the linear chain. In all other parameter regimes the analysis of the linear chain predicts amplified solutions with a maximal gain rate that simply increases with increasing Γ_i.

This behavior of the linear chain is not at all reflected in the stationary current shown in Fig. 3.2(a), which instead has a sharp maximum around $\Gamma_e \simeq \Gamma_i$. For balanced injection and extraction rates $\Gamma_e = \Gamma_i$ the current then saturates at $\langle J \rangle \simeq g n_0$ above $\Gamma_i = \Gamma_e = 4g$ as shown in Fig. 3.2(b). Note that for $\gamma \to 0$ the current can exhibit sharp discontinuities near this symmetry

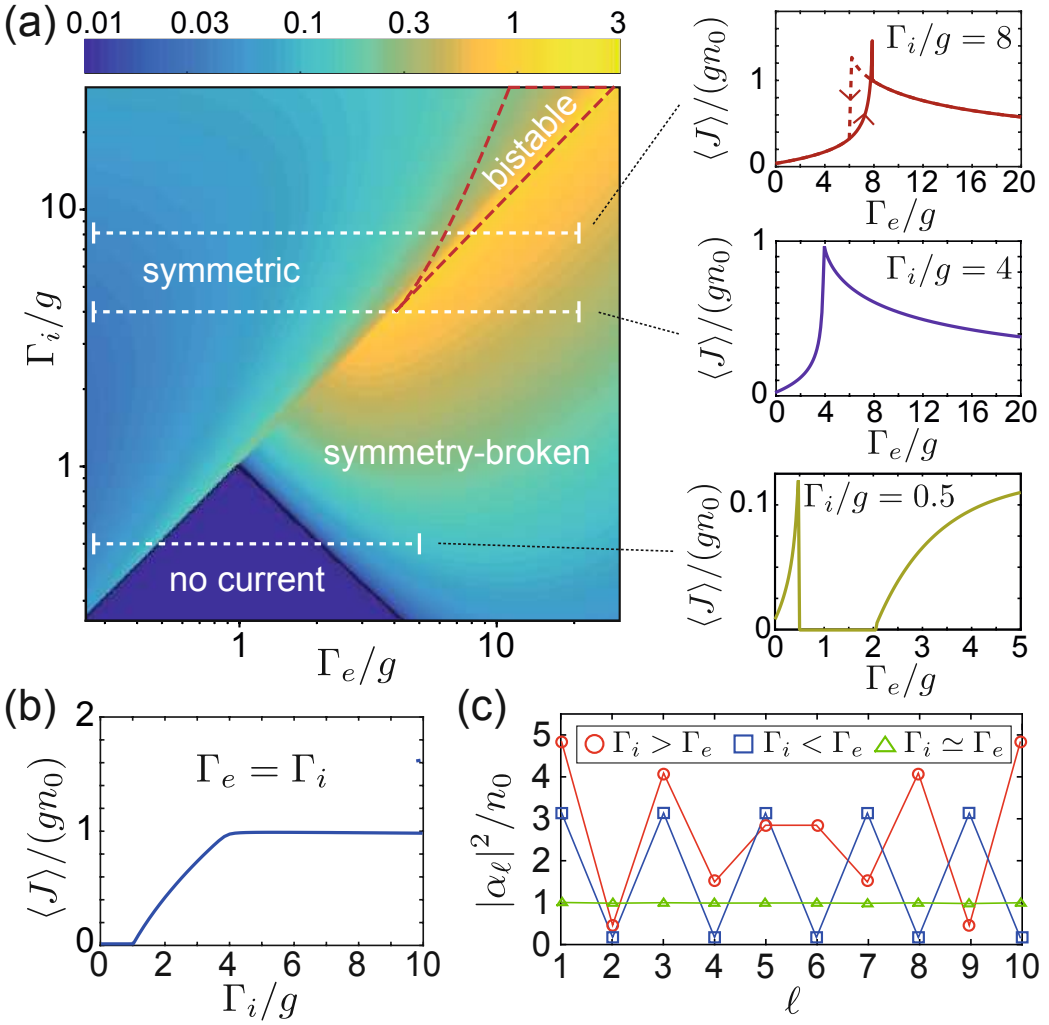

Figure 3.2: (a) Dependence of the normalized steady-state energy current $\langle J\rangle/(gn_0)$ on the energy injection and extraction rates, Γ_i and Γ_e, for a chain of $N = 10$ oscillators. (b) Plot of the average current $\langle J\rangle$ under fully symmetric conditions, $\Gamma_e = \Gamma_i$. (c) The steady-state occupation numbers $|\alpha_\ell^0|^2$ of the whole chain are plotted in the symmetric ($\Gamma_i/\Gamma_e = 1.05$) and the symmetry-broken ($\Gamma_i/\Gamma_e = 2/3$) regime, as well as at the transition point, $\Gamma_e \simeq \Gamma_i$. For all plots $\gamma/g = 10^{-3}$ and $N_{\rm th} = 0$ have been assumed.

line, where it jumps abruptly within a range $\delta\Gamma_e \sim \mathcal{O}(\gamma)$. At high rates, $\Gamma_i/g > 4$, there also exists a bistable regime, where the current depends on the order in which the rates are switched on. However, in our analysis below we find that these fine-tuned features are washed out in the presence of noise and therefore they are less relevant for understanding transport in the microscopic regime.

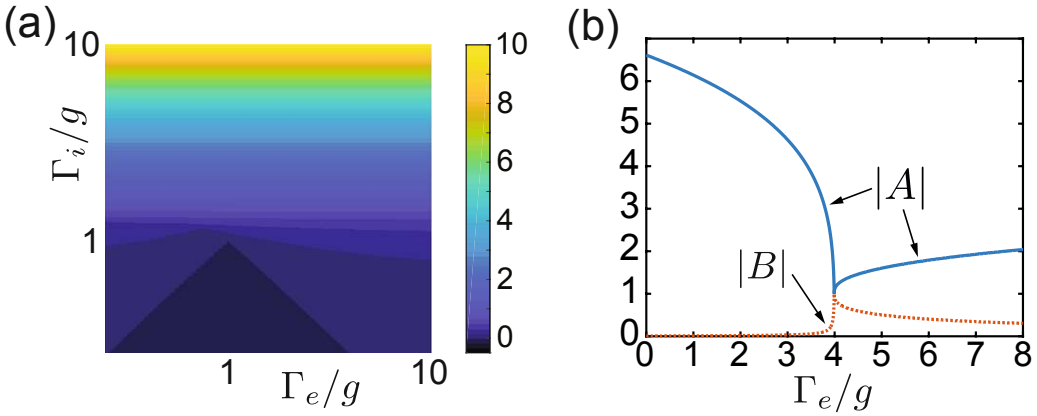

Figure 3.3: (a) Plot of the largest real part of all the eigenvalues of a linear chain of $N = 10$ oscillators. (b) The coefficients $|A|$ (solid line) and $|B|$ (dotted line) used in the ansatz in Eq. (3.8) are plotted for a fixed injection rate $\Gamma_i = 4g$ and as a function of Γ_e. In both plots a damping rate of $\gamma = 10^{-3}g$ has been assumed.

3.3 Symmetry-breaking

In Fig. 3.2(c) we also plot the occupation numbers $|\alpha_\ell^0|^2$, i.e., the stationary distribution of the energy along the channel. In contrast to conventional transport scenarios, where the energy distribution is flat or monotonically decreasing [147, 148, 155], here the chain exhibits an alternating zig-zag structure. To obtain analytic insights about the steady state of the chain in this regime, we consider in the following the slightly simplified scenario, where only sites $\ell = 1$ and $\ell = N$ are affected by the bare decay $\gamma \ll g$, while all the other oscillators evolve coherently.

We are interested in the long-time dynamics of the chain and make the following ansatz for the amplitudes

$$\alpha_\ell^0(t) = \sqrt{n_0} e^{-i\omega t} \left[A \sin(k_0 \ell) + B \cos(k_0 \ell)\right], \tag{3.8}$$

where $A, B \in \mathbb{C}$ and $\omega = g\cos(k_0)$. With this ansatz the current between two sites is

$$\langle J_\ell \rangle = g\mathrm{Im}\{(\alpha_{\ell-1}^0)^* \alpha_\ell^0\} = g n_0 \mathrm{Im}\{AB^*\} \sin(k_0). \tag{3.9}$$

To obtain a steady state configuration that maximizes the energy transfer, we look for solutions with k_0 equal or close to $\pi/2$. By writing $k_0 = \pi/2 + \delta$ we obtain the equation

$$\left[\frac{\Gamma_i/2}{(1 + |A\cos(\delta) - B\sin(\delta)|^2)^2} - \frac{\gamma}{2}\right](A\cos(\delta) - B\sin(\delta)) - i\frac{g}{2}B = 0, \tag{3.10}$$

from the equation of motion for α_1. Similarly, from the equation of motion for α_N we obtain

$$\begin{aligned}\left[-\frac{\Gamma_e/2}{(1 + |A\sin(\delta N) + B\cos(\delta N)|^2)^2} - \frac{\gamma}{2}\right](A\sin(\delta N) + B\cos(\delta N)) \\ -i\frac{g}{2}(A\cos(\delta(N+1)) - B\sin(\delta(N+1)) = 0,\end{aligned} \tag{3.11}$$

for the case where N is even. To proceed with our analysis we must distinguish between the symmetric ($\Gamma_i > \Gamma_e$) and the symmetry-broken regime ($\Gamma_e > \Gamma_i$) and between an even and an odd number of oscillators. In the following we will only carry out the analysis for an even number of oscillators, however the analysis for N odd can be done in an equivalent manner.

3.3.1 Symmetry-broken phase

We first consider the regime $\Gamma_e > \Gamma_i$ and N even. In this case the choice $k_0 = \pi/2$ results in $\omega = 0$ and a symmetry-broken solution for the amplitudes, $|\alpha_1^0| \gg |\alpha_N^0|$. The remaining parameters A and B are determined by the two coupled equations

$$\left(\frac{\Gamma_i}{(1+|A|^2)^2} - \gamma\right) A - igB = 0, \tag{3.12}$$

$$\left(\frac{-\Gamma_e}{(1+|B|^2)^2} - \gamma\right) B - igA = 0. \tag{3.13}$$

These equations have a solution for $\Gamma_e \geq \Gamma_i$, but not for $\Gamma_i > \Gamma_e$. Although these equations can still be solved analytically, the results are already quite involved. However, sufficiently deep in the symmetry-broken phase we can neglect the bare decay γ and approximate $\Gamma_e(B) \approx \Gamma_e$. We then obtain

$$|A|^2 \simeq \sqrt{\frac{\Gamma_i \Gamma_e}{g^2}} - 1, \qquad B \simeq -i\frac{g}{\Gamma_e} A, \tag{3.14}$$

and the current

$$\langle J \rangle \simeq \frac{g^2 n_0}{\Gamma_e} \left(\sqrt{\frac{\Gamma_i \Gamma_e}{g^2}} - 1\right). \tag{3.15}$$

3.3.2 Symmetric phase

For N even and $\Gamma_i > \Gamma_e$, the choice $k_0 = \pi/2$ would results in an asymmetric steady state and also the resulting equations for A and B do not have a solution for $\Gamma_i > \Gamma_e$. To recover a symmetric solution with a maximal current we choose $\delta = \pi/(2(N+1))$. In this case the chain undergoes persistent oscillations with frequency $\omega = g\sin(\delta)$. By defining $\tilde{A} = A\cos(\delta)$ and using the approximation $B\sin(\delta) \approx 0$, the resulting equations simplify to

$$\left(\frac{\Gamma_i}{(1+|\tilde{A}|^2)^2} - \gamma\right) \tilde{A} - igB = 0, \tag{3.16}$$

$$\left(-\frac{\Gamma_e}{(1+|\tilde{A}|^2)^2} - \gamma\right) \tilde{A} + igB = 0. \tag{3.17}$$

Therefore, we obtain the amplitudes

$$|\tilde{A}|^2 = \sqrt{\frac{\Gamma_i - \Gamma_e}{2\gamma}} - 1, \qquad B = -i\frac{\gamma}{g}\frac{\Gamma_i + \Gamma_e}{\Gamma_i - \Gamma_e}\tilde{A}, \tag{3.18}$$

and, since $\sin(k_0) = \cos(\delta)$, the current

$$\langle J \rangle = n_0 \gamma \frac{\Gamma_i + \Gamma_e}{\Gamma_i - \Gamma_e} \left(\sqrt{\frac{\Gamma_i - \Gamma_e}{2\gamma}} - 1 \right). \tag{3.19}$$

Note that the current depends on γ and is therefore small for small damping rates $\gamma \ll g$ as opposed to the symmetry-broken regime which is more or less independent of γ.

3.3.3 Symmetry breaking transition

Near the transition point we find $|A| \simeq |B|$. More precisely, from the solution in the symmetric regime we see that $B = -iA$, at a value of

$$\Gamma_e^* = \Gamma_i \frac{g - \gamma}{g + \gamma} \approx \Gamma_i - \frac{2\Gamma_i}{g}\gamma. \tag{3.20}$$

Near this parameter the standing wave turns into a running wave $\alpha_\ell^0 \sim e^{ik_0\ell}$ and the current is close to maximum and scales as $\langle J \rangle_{\max} \propto \sqrt{\Gamma_i}$. Although the symmetric solution exists up to $\Gamma_e^{**} = \Gamma_i - 2\gamma$, the stability analysis reveals that for $\Gamma_i > g$ the symmetric solution becomes unstable before, at around $\Gamma \simeq \Gamma_e^*$. In the regime of interest, $\gamma/g \to 0$, these differences become negligible and the transition is simply given by $\Gamma_e = \Gamma_i$. The dependence of the coefficients A and B around the transition point is shown in Fig. 3.3(b).

3.3.4 Damping of all oscillators

The results derived so far for a chain without damping of the oscillators in the middle agree in essence with the results obtained for two coupled oscillators (see also Ref. [158]). However, while in the symmetry-broken phase the bare damping γ has a negligible effect, it determines the value of the current in the symmetric phase. In this regime it is thus important to analyze the steady state also for the full system, where all oscillators are weakly damped. In this case the equation

$$\dot{\alpha}_\ell = -\frac{\gamma}{2}\alpha_\ell + i\frac{g}{2}(\alpha_{\ell-1} + \alpha_{\ell+1}), \tag{3.21}$$

cannot be fulfilled by the ansatz (3.8). However, for $\gamma/g \ll 1$ the correction are small and we can still use this ansatz with the same k_0 as above as a first approximation. For simplicity we focus on N odd where $k_0 = \frac{\pi}{2}$. Then, summing the equations of motion for every other site we obtain

$$\sum_{\ell=1}^{(N-1)/2} (-1)^{\ell+1} \dot{\alpha}_{2\ell-1} = \sqrt{n_0} \left(\Gamma_i(A)A - \gamma \sum_{\ell=1}^{(N-1)/2} A - igB \right) = 0 \tag{3.22}$$

and for the last site,

$$\dot{\alpha}_N = \sqrt{n_0}\,[(-\Gamma_e(A) - \gamma)A + igB] = 0. \tag{3.23}$$

From this set of equations we obtain the amplitudes

$$|A|^2 = \sqrt{\frac{2(\Gamma_i - \Gamma_e)}{\gamma(N+1)}} - 1, \quad B = -i\frac{\gamma}{2g}\frac{\Gamma_e(N-1) + 2\Gamma_i}{\Gamma_i - \Gamma_e}A, \tag{3.24}$$

and the current

$$\langle J \rangle = n_0 \frac{\gamma}{2}\frac{\Gamma_e(N-1) + 2\Gamma_i}{\Gamma_i - \Gamma_e}\left(\sqrt{\frac{2(\Gamma_i - \Gamma_e)}{\gamma(N+1)}} - 1\right). \tag{3.25}$$

Although this result was derived for N odd, it is also a good approximation for N even when $N > 2$.

Note that near Γ_e^* we obtain a single traveling wave. To account first order corrections due to a finite decay $\gamma/g \ll 1$, we can generalize the ansatz to $\alpha_\ell^0 \sim e^{ik_0\ell}e^{-\kappa\ell}$. From Eq. (3.21) we then obtain $\kappa = \gamma/(2g)$. Therefore, all our analytic estimates will remain valid as long as $N\gamma \ll 1$, although numerical simulations show that most of the qualitative features survive at much larger decay rates.

From the analytical results above follows that the stationary current is carried by a single mode with wavevector $k_0 = \pi(N+2)/(2N+2)$ for $\Gamma_i > \Gamma_e$ and $k_0 = \pi/2$ for $\Gamma_i < \Gamma_e$ for N even, which is the mode supporting the highest current. However, since the saturable absorber can only extract a finite amount of energy per unit of time, most of the energy current is reflected at the extraction site and forms a standing wave. While a standing-wave pattern is observed in all parameter regimes, the boundary conditions depend on the relation between Γ_i and Γ_e. For $\Gamma_i > \Gamma_e$ the two ends of the chain have exactly the same amplitude, $|\alpha_1^0|^2 \simeq |\alpha_N^0|^2 \simeq |A|^2$ and $|B/A| \ll 1$. In contrast, for $\Gamma_i < \Gamma_e$ the amplitude of the gain mode is much higher than the amplitude of the loss mode, $|\alpha_1^0|^2 \gg |\alpha_N^0|^2$. Therefore, for $\Gamma_i > \Gamma_e$ the steady-state energy distribution of this network exhibits a left-right (parity) symmetry, which is broken above the transition point $\Gamma_e \simeq \Gamma_i$. Exactly at this point we obtain $B \simeq -iA$ and the transport becomes unidirectional, $\alpha_\ell^0 \sim e^{ik_0\ell}$. Note that also this behavior of the steady-state amplitudes cannot be derived by looking at the mode function of the most unstable mode of the linear chain. This mode always has the highest amplitude on site $\ell = 1$, such that gain is maximized.

The breaking of a spatial symmetry in systems with gain and loss is reminiscent of the effect of PT-symmetry breaking in systems with equal gain and loss rates (see Chapter 5). Interestingly, in the current system such a symmetry is not present in the underlying equations of motions, since for $\Gamma_i \neq \Gamma_e$ the oscillators at the injection and extraction sites evolve with very different rates.

3.4 Current fluctuations

To understand the consequences of this symmetry-breaking transition for microscopic transport, we consider now the thermal regime, $n_0 \gg 1$ and

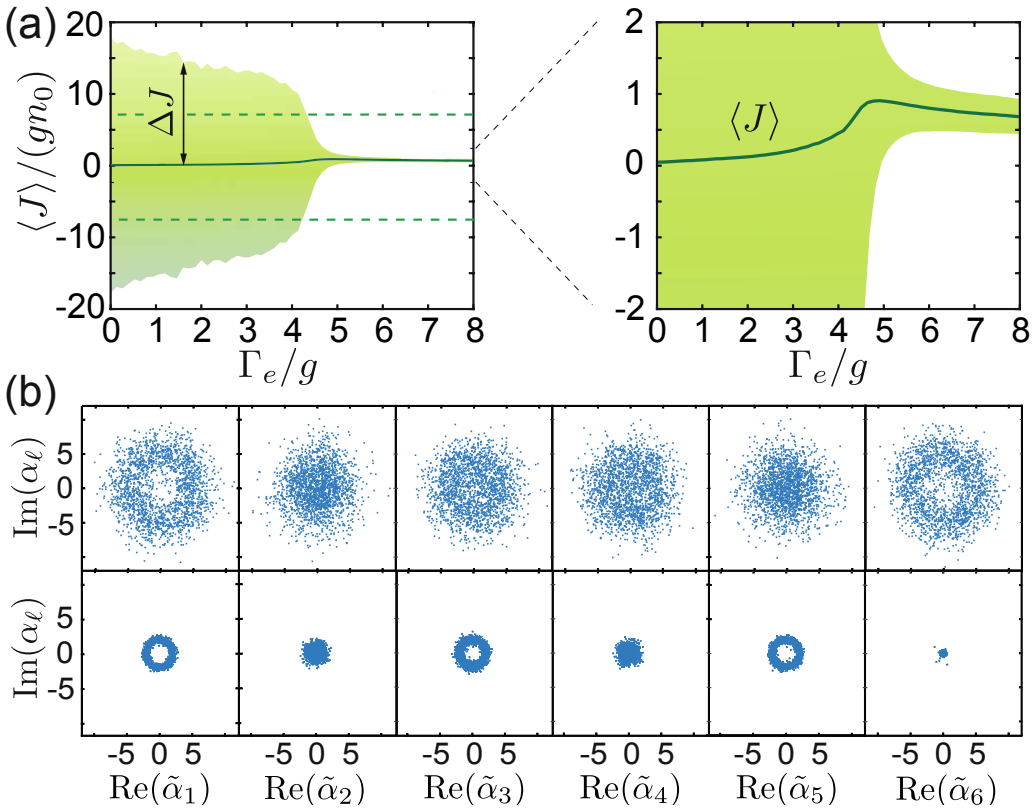

Figure 3.4: (a) The average current $\langle J\rangle$ (solid line) and the current fluctuations ΔJ (shaded area) are plotted for a chain of $N = 6$ oscillators coupled to a thermal environment with $N_{\mathrm{th}}/n_0 = 10$. The dashed lines indicate the range of current fluctuations in thermal equilibrium. The marginal phase space distributions $P_\ell(\alpha_\ell)$ are shown in (b) in the symmetric ($\Gamma_e = 2g$) and in the symmetry-broken ($\Gamma_e = 8g$) regime. Here $\tilde{\alpha}_\ell = \alpha_\ell/\sqrt{n_0}$.

$N_{\mathrm{th}} \sim n_0$. In this case, quantum effects are still small, but noise from the environment can no longer be neglected and induces strong fluctuations of the current, $\Delta J = \sqrt{\langle J^2\rangle - \langle J\rangle^2}$.

For better understanding we first look at the equilibrium case. We consider two coupled oscillators in thermal equilibrium, where $\Gamma_i = \Gamma_e = 0$. In this case we get a closed set of equations for the variances of the linear chain, which can be evaluated assuming a thermal state $\rho_{\mathrm{th}} = \rho^1_{\mathrm{th}} \otimes \rho^2_{\mathrm{th}}$. We obtain

$$\begin{aligned}\frac{(\Delta J)^2}{n_0^2} &= \frac{g^2}{4n_0^2}\left[\langle a_\ell^\dagger a_\ell\rangle\langle a_{\ell+1}a_{\ell+1}^\dagger\rangle + \langle a_\ell a_\ell^\dagger\rangle\langle a_{\ell+1}^\dagger a_{\ell+1}\rangle\right] \\ &= \frac{g^2}{4n_0^2}2(N_{\mathrm{th}}^2 + N_{\mathrm{th}}) \approx \frac{g^2}{2}\left(\frac{N_{\mathrm{th}}}{n_0}\right)^2\end{aligned} \tag{3.26}$$

and we therefore find the current fluctuations are proportional to the bath occupation number with $\Delta J = gN_{\mathrm{th}}/\sqrt{2}$.

In Fig. 3.4(a) we consider this high-noise regime and plot $\langle J\rangle$ and ΔJ for $N_{\mathrm{th}}/n_0 = 10$, $\Gamma_i/g = 4$ and for varying Γ_e. We see that in the symmetric phase

transport is indeed dominated by fluctuations, which even exceed the thermal level. This behavior changes abruptly after the transition point $\Gamma_e \simeq \Gamma_i$, beyond which a well-defined current below the thermal noise level is established. This transition is also clearly visible in the steady-state distributions of the individual oscillators, $P_\ell(\alpha_\ell)$, shown in Fig. 3.4(b). For $\Gamma_i > \Gamma_e$ we observe strong fluctuations, but the distributions are still symmetric with respect to the center of the chain, i.e., $P_\ell \simeq P_{N-\ell+1}$. For $\Gamma_e > \Gamma_i$ this symmetry is broken and fluctuations are strongly suppressed.

For better understanding, we derive analytic solutions for both the symmetric regime and the symmetry-broken regime.

3.4.1 Symmetric regime

For $\Gamma_e < \Gamma_i$ the system is strongly influenced by thermal fluctuations. By calculating the expectation values of higher order moments we can find approximate solutions for the mean occupation and their fluctuations. For $\gamma/g \ll 1$, we can approximate $\Gamma(\alpha) = \frac{\Gamma}{(1+|\alpha|^2/n_0)^2} \approx \frac{\Gamma n_0^2}{|\alpha|^4}$ and arrive at following equation of motion

$$\langle \dot{|\alpha_1|^2} + \dot{|\alpha_2|^2} \rangle = \left\langle \frac{\Gamma_i n_0^2}{|\alpha_1|^2} - \frac{\Gamma_e n_0^2}{|\alpha_2|^2} \right\rangle - \gamma(\langle |\alpha_1|^2 \rangle + \langle |\alpha_2|^2 \rangle) + 2\gamma N_{\mathrm{th}} = 0. \tag{3.27}$$

In the symmetric regime $\langle |\alpha_1|^2 \rangle = \langle |\alpha_N|^2 \rangle$ and by approximating $\langle \frac{1}{|\alpha|^2} \rangle \approx \frac{1}{\langle |\alpha|^2 \rangle}$, we obtain

$$\begin{aligned} \frac{\langle |\alpha_1|^2 \rangle}{n_0} = \frac{\langle |\alpha_2|^2 \rangle}{n_0} &\approx \sqrt{\frac{\Gamma_i - \Gamma_e}{2\gamma} + \left(\frac{N_{\mathrm{th}}}{2n_0}\right)^2} + \frac{N_{\mathrm{th}}}{2n_0} \\ &\approx \frac{N_{\mathrm{th}}}{n_0} + \sqrt{\frac{\Gamma_i - \Gamma_e}{2\gamma}}. \end{aligned} \tag{3.28}$$

By assuming that the noise doesn't considerable change the mean value of the relative phase and just broadens the phase distribution, we can approximate the mean current by

$$\langle J \rangle \approx n_0 \gamma \frac{\Gamma_i + \Gamma_e}{\Gamma_i - \Gamma_e} \left(\sqrt{\frac{\Gamma_i - \Gamma_e}{2\gamma}} + \frac{N_{\mathrm{th}}}{n_0} \right). \tag{3.29}$$

Therefore, for $\gamma/g \ll 1$ and not too large thermal noise the mean current is hardly affected by thermal fluctuations, which agrees very well with numerical simulations.

The variances of $|\alpha_\ell|^2$ can be calculated from the equations of motion for higher moments. For the occupation fluctuations we obtain

$$\begin{aligned} \langle \dot{|\alpha_1|^4} + \dot{|\alpha_2|^4} \rangle = 2(\Gamma_i - \Gamma_e) n_0^2 - 2\gamma(\langle |\alpha_1|^4 \rangle + \langle |\alpha_2|^4 \rangle) \\ + 4\gamma N_{\mathrm{th}}(\langle |\alpha_1|^2 \rangle + \langle |\alpha_2|^2 \rangle) = 0. \end{aligned} \tag{3.30}$$

In the symmetric regime $\langle|\alpha_1|^n\rangle = \langle|\alpha_2|^n\rangle$ and using Eq. (3.28), we find

$$\begin{aligned}\langle|\alpha_1|^4\rangle &\approx \frac{(\Gamma_i-\Gamma_e)n_0^2}{2\gamma} + 2N_{\text{th}}\langle|\alpha_1|^2\rangle = \frac{(\Gamma_i-\Gamma_e)n_0^2}{2\gamma} + 2N_{\text{th}}\langle|\alpha_1|^2\rangle \\ &= \frac{(\Gamma_i-\Gamma_e)n_0^2}{2\gamma} + 2N_{\text{th}}\left(\sqrt{\frac{(\Gamma_i-\Gamma_e)n_0^2}{2\gamma} + \left(\frac{N_{\text{th}}}{2}\right)^2} + \frac{N_{\text{th}}}{2}\right),\end{aligned} \tag{3.31}$$

and for the variance

$$\frac{\text{Var}(|\alpha_\ell|^2)}{n_0^2} \approx \frac{N_{\text{th}}}{n_0}\left(\sqrt{\frac{\Gamma_i-\Gamma_e}{2\gamma} + \left(\frac{N_{\text{th}}}{2n_0}\right)^2} + \frac{N_{\text{th}}}{2n_0}\right) = \frac{N_{\text{th}}}{n_0}\frac{\langle|\alpha_\ell|^2\rangle}{n_0}. \tag{3.32}$$

In the regime $\gamma/g \ll 1$, the occupation $\langle|\alpha_i|^2\rangle$ is hardly affected by the thermal noise, but the variance depends linearly on N_{th}. Furthermore, we can approximate the variance of the current by

$$\begin{aligned}\frac{\text{Var}(\langle J\rangle)}{g^2n_0^2} \approx& \langle|\alpha_1|^2\rangle\text{Var}(|\alpha_N|^2) + \langle|\alpha_N|^2\rangle\text{Var}(|\alpha_1|^2) + \text{Var}(|\alpha_1|^2)\text{Var}(|\alpha_N|^2) \\ \approx& \frac{2N_{\text{th}}\langle|\alpha_1|^2\rangle + N_{\text{th}}^2}{n_0^2},\end{aligned} \tag{3.33}$$

where we again observe linear dependence on N_{th} in the limit of $\gamma/g \ll 1$ and $\langle|\alpha_1|^2\rangle \gg N_{\text{th}}$. Again, this approximate result reproduces well all our numerical findings.

3.4.2 Symmetry-broken regime

For $\Gamma_e > \Gamma_i$ we find that in steady state $\Gamma_e(\alpha_2^0) \approx \Gamma_e$. By making this approximation we can linearize around the steady state amplitude and obtain the following expression for the variance of the current in the limit of $\gamma \to 0$,

$$\frac{\text{Var}(\langle J\rangle)}{n_0^2} = \gamma N_{\text{th}} g^2 \frac{\left(\tilde{\Gamma}-g\right)\left[g^2\left(4g-5\tilde{\Gamma}\right) + \Gamma_e\left(\Gamma_e\tilde{\Gamma}+2\Gamma_i g\right)\right]}{\Gamma_e\left(\tilde{\Gamma}-2g\right)\left[\Gamma_e^2\tilde{\Gamma} + g^2\left(4g-3\tilde{\Gamma}\right]\right)}, \tag{3.34}$$

where $\tilde{\Gamma} = \sqrt{\Gamma_i\Gamma_e}$. We see that for small damping rate γ, the fluctuations of the current are small. In particular, deep in the symmetry-broken phase, this can be simplified to

$$\frac{\text{Var}(\langle J\rangle)}{n_0^2} \approx \frac{\gamma N_{\text{th}} g^2}{\Gamma_e}, \qquad \frac{\Delta J}{J} \approx \sqrt{\frac{\gamma N_{\text{th}}(\gamma\Gamma_e + g^2)}{g^2\Gamma_i}}. \tag{3.35}$$

We therefore find that in the symmetric regime the variance of the current scales with $\text{Var}(\langle \text{J}\rangle) \propto \text{N}_{\text{th}}$, while in the symmetry-broken regime with $\text{Var}(\langle \text{J}\rangle) \propto \gamma\text{N}_{\text{th}}$ and we therefore find a significant difference in the limit of $\gamma \ll g, N_{th}$.

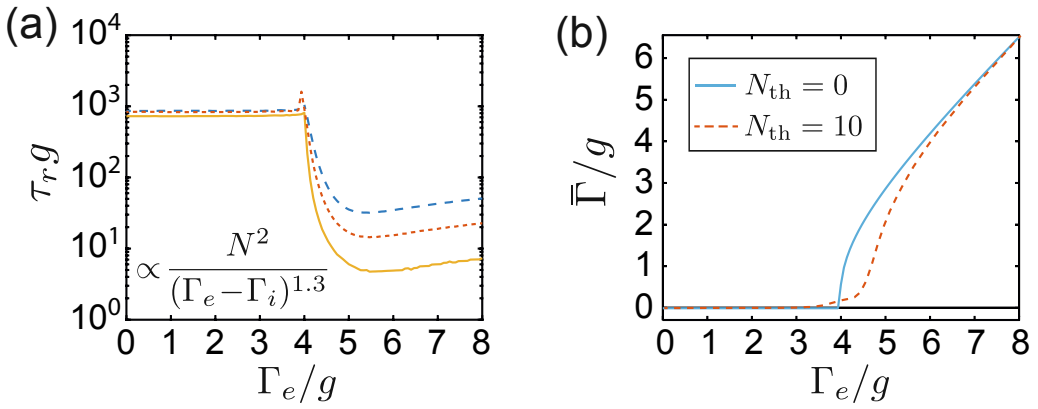

Figure 3.5: (a) Plot of the relaxation time τ_r as a function of Γ_e for $N = 4, 6, 8$ oscillators and $N_{\rm th} = 0$. (b) The average dissipation rate $\bar{\Gamma} = \langle\langle \Gamma_e(\alpha_N) - \Gamma_i(\alpha_1)\rangle\rangle$ in the absence and presence of thermal noise. In all plots fixed values of $\Gamma_i/g = 4$ and $\gamma/g = 10^{-3}$ have been assumed.

3.4.3 Relaxation time - mean damping rate

The striking difference in the current noise can be also related to an equivalent change in the response of the network. In Fig. 3.5(a) we plot the relaxation time τ_r, i.e., the time it takes for the amplitude α_1 to relax back to its steady-state value after a small perturbation has been applied to site $\ell = 1$. This was done the following way. We first determined the steady state amplitudes with high accuracy and then changed the amplitude of the gain oscillator by $\delta\alpha_1 = 1/10$ and performed time evolution until the system relaxed. From the time difference Δt_r between the pint where the occupation is just $\delta|\alpha_1|^2 = 10^{-5}$ and $\delta|\alpha_1|^2 = 10^{-8}$ away from the real steady state, we obtain the relaxation rate as $\tau_r = \Delta t_r/\ln(10^3)$. Note that in Fig. 3.5(a) the relaxation rate exhibits a peak in a very small region around the transition point $\Gamma_e = \Gamma_i$, where we find almost no relaxation.

In the symmetric phase this time constant is approximately independent of Γ_i, Γ_e and N. It is essentially determined by the bare damping rate, $\tau_r \sim \gamma^{-1}$, and diverges in the limit $\gamma \to 0$. In the symmetry-broken phase a much faster response, $\tau_r \sim \mathcal{O}(\Gamma_e^{-1}) \sim N^2$ is observed. At the transition point the relaxation time diverges as $\tau_r \sim (\Gamma_e - \Gamma_i)^{-\xi}$, where we find $\xi \simeq 1.3$ from numerical simulations. This behavior is very different from a laser or from other non-equilibrium phase transitions, where the relaxation time diverges only at the transition point, but is finite and of similar magnitude in both phases [24, 159–163]. As shown in Fig. 3.5(a), in the current system the relaxation time diverges (in the limit $\gamma \to 0$) within the whole symmetric phase.

To provide a connection between the symmetry of $P(\{\alpha_\ell\})$ and the current noise, it is useful to consider the mean damping rate [55]

$$\bar{\Gamma} = \langle \Gamma_e(\alpha_N) - \Gamma_i(\alpha_1)\rangle, \tag{3.36}$$

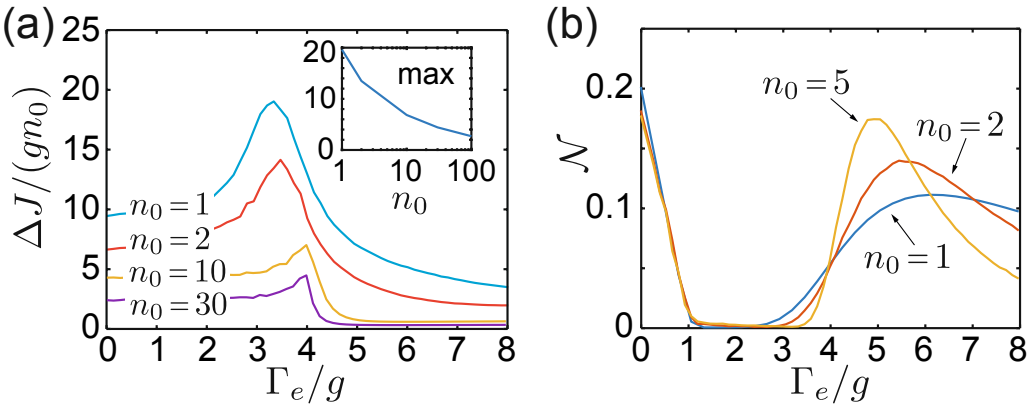

Figure 3.6: (a) Plot of the current fluctuations ΔJ for $N = 2$ oscillators in the quantum noise limit, $N_{\rm th} = 0$, and for different saturation numbers $n_0 = 1, 2, 10, 30$. The inset shows the scaling of the maximum of the fluctuation peak as a function of n_0. (b) Entanglement negativity $\mathcal{N}$ [164, 165] of the steady-state density operator for $n_0 = 1, 2, 5$. For these plots a fixed injection rate $\Gamma_i/g = 4$ and a bare damping rate of (a) $\gamma/g = 10^{-3}$ and (b) $\gamma/g = 10^{-2}$ have been assumed. The results in this figure have been obtained from the semiclassical stochastic differential equations (3.4)-(3.6) for $n_0 \geq 10$ and from stochastic wavefunction simulations of the full density operator for $n_0 = 1, 2, 5$.

i.e., the average difference between energy injection and extraction rates. Due to the symmetry of the marginal distributions, this rate is vanishing small in the symmetric phase, $\bar{\Gamma} \sim \mathcal{O}(\gamma)$ [see Fig. 3.5(b)]. By breaking this symmetry, a finite value $\bar{\Gamma} \gg \gamma$ is established for $\Gamma_e > \Gamma_i$. This then leads on average to an efficient cooling of fluctuations and the possibility for subthermal energy transport. Again this behavior shows a close analogy to conventional PT-symmetric systems [51]. In such systems the breaking of the parity symmetry of the eigenstates of a non-Hermitain matrix is accompanied by a transition from real to imaginary eigenvalues, i.e. a transition from a purely oscillatory to an exponentially damped or amplified dynamic (see Chapter 5 for more details). The order parameter $\bar{\Gamma}$ generalizes this effect to steady-state distributions of nonlinear gain-loss systems [55], where the conventional definition of PT-symmetry breaking is no longer meaningful.

3.5 Quantum noise limit

From Eq. (3.4) we see that even for $N_{\rm th} \approx 0$, the network is still affected by quantum noise $\sim \sqrt{\Gamma_i(\alpha_1)}\xi_1(t)$. In the regime $N_q = \Gamma_i/\gamma > N_{\rm th}$, this noise dominates over thermal fluctuations and represents a fundamental limitation for energy transport deep in the quantum regime, $n_0 \sim \mathcal{O}(1)$. Fig. 3.6(a) shows that for $n_0 \gg 1$ the sharp transition between a noisy and a coherent transport regime still prevails, even for $N_{\rm th} = 0$. As the saturation number n_0 is lowered, the relative level of fluctuations increases, develops a peak at the

transition point and becomes much more pronounced also in the symmetry-broken phase. Note that for small $n_0 \lesssim 10$ the mapping of the master equation onto a Fokker-Planck equation is no longer valid and a full simulation of Eq. (3.1) must be performed. Therefore, due to the large Hilbert space and large separation of time scales involved in such simulations, the results in Fig. 3.6 are restricted to $N = 2$ oscillators.

Access to the full density operator also allows us to investigate true non-classical quantities, such as the entanglement established between the injection and extraction sites. As shown in Fig. 3.6(b) for different $n_0 = 1, 2, 5$, a significant amount of entanglement exists for $\Gamma_e < g$, it then vanishes in the rest of the symmetric phase, and peaks again right after the transition point. Therefore, this plot reveals an additional substructure, which is not reflected in the mean current or its fluctuations. This entanglement between source and drain can be relevant for thermodynamical considerations, where not only the flow of energy, but also changes in entropy through mutual (quantum) correlations must be taken into account. Note, however, that for a more detailed study of entanglement it is necessary to go beyond our simply model and explicitly include specific implementations of quantum generators and engines in the dynamics.

3.6 Universality of the symmetry-breaking transition

So far, we have assumed a specific cutoff function and the same saturation occupation number n_0 for the gain and the loss mechanism. While the precise quantitative findings will of course depend on these assumptions, we will now demonstrate with several other examples that the essential qualitative features of the symmetry-breaking transition do not depend on these details.

3.6.1 Different gain/loss mechanisms

As there are many ways to engineer gain and loss, we will therefore first show that our findings do not depend on the precise form of the saturation function $f(x)$. In Fig. 3.7 we consider the example of a cutoff function $f(a^\dagger a) = 1/(1 + a^\dagger a/n_0)^{\nu/2}$, where we have assumed $\nu = 1$ to model a system with a weaker saturation dependence. This case corresponds, for example, to the saturation of a regular laser. Again we see the characteristic structure of the current with a maximum at $\Gamma_e \simeq \Gamma_i$ and that this maximum is associated with a transition between a symmetric and a symmetry-broken energy distribution. For $\Gamma_i \gtrsim 3.4g$ we obtain a region, where the current does not have a precise value and the whole chain settles into a limit cycle. Such a behavior has previously been predicted for a PT-symmetric system, $\Gamma_i = \Gamma_e$, where $\nu = 1$ has been identified as a special case, where no real symmetry-breaking occurs [55]. However, in the presence of thermal noise [see Fig. 3.7(d)] these limit cycles are no longer visible and qualitatively we obtain the same transition between

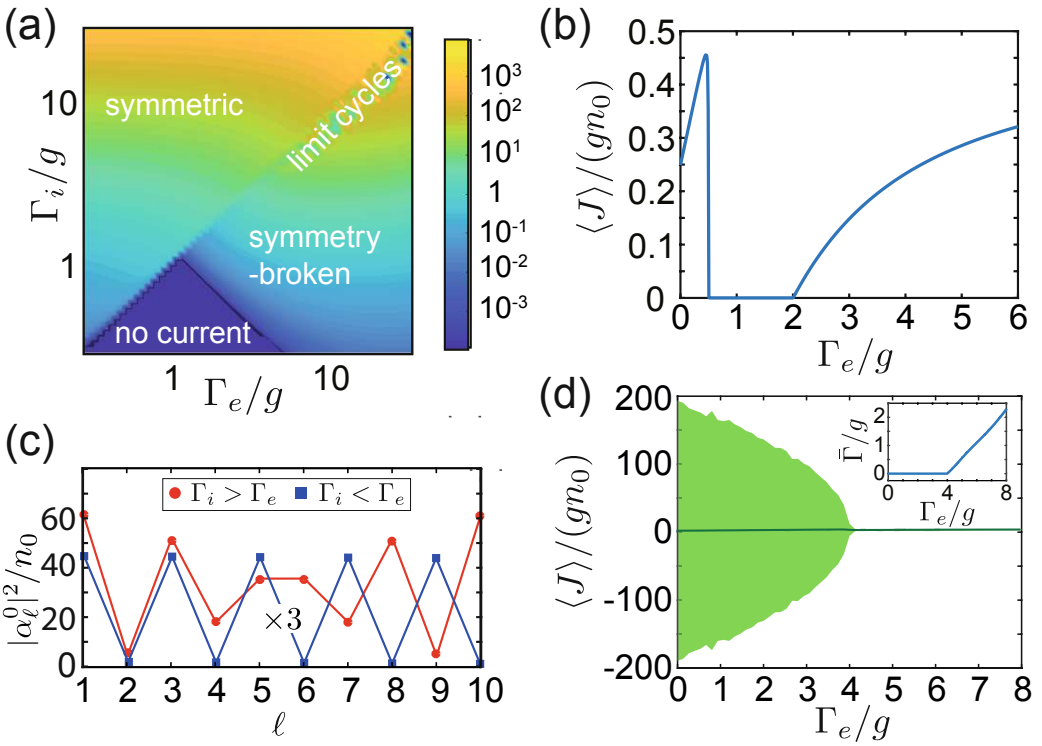

Figure 3.7: Energy current and symmetry-breaking for a chain of $N = 10$ oscillators and for the case where the saturation function is of the form $f(a^\dagger a) = 1/(1 + a^\dagger a/n_0)^{1/2}$. (a) Plot of the normalized steady-state energy current $\langle J\rangle/(gn_0)$ as a function of Γ_i and Γ_e and for a damping rate $\gamma = 10^{-2}g$. (b) Variation of the current as a function of Γ_e for fixed injection rate $\Gamma_i/g = 0.5$ and $\gamma = 10^{-3}g$. (c) Steady-state amplitudes of the chain for $\Gamma_i = 4g$ and $\Gamma_e = 0.5g$ (red) and $\Gamma_e = 8g$ (blue). For better visibility the blue line is scaled by a factor of three. (d) Mean current (solid line) and range of current fluctuations (shaded area) for a network coupled to a thermal bath with $N_{\rm th}/n_0 = 10$. The inset shows the value of the average damping rate $\bar{\Gamma}$, as defined in Section 3.4. For this plot $\Gamma_i = 4g$ and $\gamma/g = 10^{-3}$ have been assumed.

a noise-dominated and a coherent transport regime as shown in Section 3.4 for $\nu = 2$. Moreover, simulations reveal that the same behavior is also found for stronger nonlinearities, $\nu = 3$, and other saturation functions with different functional dependencies.

3.6.2 Different saturation numbers

To further illustrate that the physical effects discussed in this work are very generic, we now return to the cutoff function given in Eq. (3.3), but consider the case where the gain and the loss oscillator saturate at different amplitudes, i.e., $n_0^{(1)} \neq n_0^{(N)}$. The resulting mean currents and fluctuations are shown in Fig. 3.8. We see that also in this case all the qualitative features of the symmetry-breaking phase transition remain unaffected, except that the

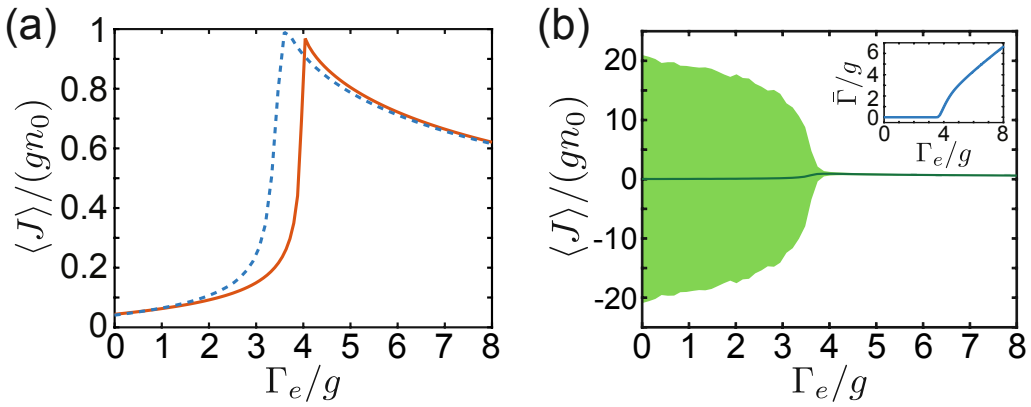

Figure 3.8: (a) Plot of the current for fixed injection rate $\Gamma_i = 4g$ and varying extraction rate Γ_e for a network of $N = 10$ oscillators and $N_{\rm th} = 0$. The plot compares the case where the saturation numbers for gain and loss are equal, $n_0^{(1)} = n_0^{(N)}$, (red solid line) with the case where they differ by 10%, $n_0^{(1)} = 1.1 n_0^{(N)}$, (blue dashed line). (b) Mean current (solid line) and range of current fluctuations (shaded area) for the case $n_0^{(1)} = 1.1 n_0^{(N)}$, but coupled to a thermal bath with $N_{\rm th}/n_0 = 10$. For both plots $\gamma/g = 10^{-3}$ and a cutoff function as given in Eq. (3.3) have been assumed.

transition point is now shifted from $\Gamma_i = \Gamma_e$ to $\Gamma_i \simeq \Gamma_e \left(n_0^{(N)}/n_0^{(1)}\right)^2$. Importantly, this example shows that even when different saturation mechanisms for energy injection and extraction are considered, there is still an emergent symmetric phase, which is characterized by an almost complete cancellation of the average dissipation rate $\bar{\Gamma} = \langle\langle \Gamma_e(\alpha_N) - \Gamma_i(\alpha_1)\rangle\rangle$.

3.6.3 Conditions for a symmetric phase

To obtain a more general result for the symmetry-breaking point, we derive a minimal condition under which a symmetric phase can exist. This condition follows from the fact that in the steady state the total energy of the system must be conserved. This means that the absorbed and dissipated energy must be the same, or

$$\Gamma_i(\alpha_1^0)|\alpha_1|^2 = \Gamma_e(\alpha_N^0)|\alpha_N^0|^2 + \gamma \sum_{\ell=1}^{N} |\alpha_\ell^0|^2. \tag{3.37}$$

For a symmetric state, where $|\alpha_1^0| = |\alpha_N^0| = \alpha^0$ and $|\alpha_\ell^0|^2 = \eta_\ell |\alpha^0|^2$, we obtain

$$\Gamma_i(\alpha^0) - \Gamma_e(\alpha^0) = \gamma\mathcal{N}, \qquad \mathcal{N} = \sum_{\ell=1}^{N} \eta_\ell. \tag{3.38}$$

Here $\mathcal{N} = 2$ for $N = 2$, $\mathcal{N} \simeq (N+1)/2$ for N odd and in general $\mathcal{N} \approx N/2$ for $N \gg 1$. For identical cutoff functions this condition can always be satisfied by increasing the value of α^0, as long as $\Gamma_e < \Gamma_i - \gamma\mathcal{N}$. For non-identical

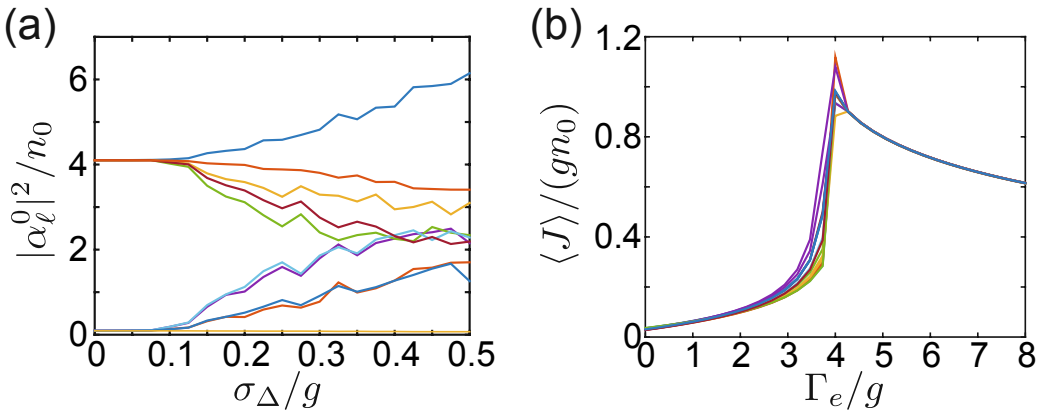

Figure 3.9: (a) Plot of the occupation numbers $|\alpha_\ell^0|^2$ of a chain of $N = 10$ oscillators averaged over 100 realizations of random site detunings $\Delta_\ell \in [-\sigma_\Delta, \sigma_\Delta]$. (b) Current for 15 different random detuning realizations with $\sigma_\Delta = 0.05g$. For both plots the values $\Gamma_i = 4g$, $\Gamma_e = 8g$ and $\gamma/g = 10^{-3}$ have been assumed.

saturation parameters, $n_0^{(1)} \neq n_0^{(N)}$, and by approximating $f(\alpha^0) \simeq n_0^2/|\alpha^0|^4$, this argument also explains the shift of the transition point discussed above. Thus, Eq. (3.38) provides a simple minimal condition for the existence of a symmetric phase. Note, however, that for larger systems one find that for $\Gamma_i > g$ symmetry breaking already occurs closer to the point where $|A| = |B|$. For example, for $n_0^{(1)} = n_0^{(N)}$ we find the transition point approximately at

$$\Gamma_e^* = \frac{2\Gamma_i(g-\gamma)}{2g+\gamma(N-1)}. \tag{3.39}$$

As long as $\gamma N \ll g$, this result does not considerable change by changing the system size and for all results presented in this chapter the transition point derived from Eq. (3.38) is a sufficient approximation.

3.6.4 Disorder

So far we have considered chains of oscillators with identical frequencies $\omega_\ell = \omega_0$. To understand the robustness of the observed effects with respect to small frequency variations, which will be unavoidable in any real system, we numerically simulate the steady state of a chain of $N = 10$ oscillators with frequencies $\omega_\ell = \omega_0 + \Delta_\ell$. Here the random frequency offsets for each site are chosen from a uniform distribution $\Delta_\ell \in [-\sigma_\Delta, \sigma_\Delta]$.

In Fig. 3.9 (a) and (b) we plot the disorder-averaged steady-state occupation numbers $|\alpha_\ell^0|^2$ for each of the oscillators and the current for a few disorder realizations. We find that for $\sigma_\Delta < 0.1g$, the steady-state amplitudes reproduce almost perfectly the alternating structure predicted for the ideal case, $\Delta_\ell = 0$. In this regime also the current exhibits the characteristic peak structure for each individual disorder realization and is hardly affected for parameters away from the transition point. This shows that all the effects discussed in this work are insensitive to a small amount of disorder. For

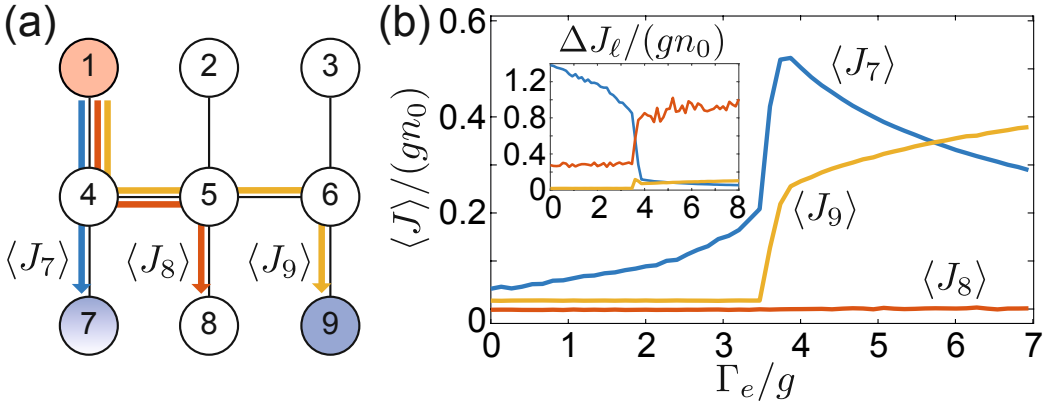

Figure 3.10: (a) Sketch of a 2D power grid with multiple multiple quantum machines. (b) Plot of the average currents $\langle J_\ell \rangle$ flowing from site 1 to sites $\ell = 7, 8, 9$ for fixed $\Gamma_i^{(1)}/g = \Gamma_e^{(9)}/g = 4$ and varying rate $\Gamma_e^{(7)}$. For this plot it is assumed that all oscillators are coupled to a thermal bath with a moderate occupation number $N_{\rm th}/n_0 = 3$ and $\gamma/g = 10^{-3}$. The inset shows the resulting current fluctuations.

$0.1 < \sigma_\Delta/g < 0.3$, the amplitudes still follow more or less a zig-zag structure, while for $\sigma_\Delta/g > 0.3$ the energy distribution is completely different from the non-detuned case and most of the energy gets localized around the gain mode.

3.7 Microscopic networks

The transport effects analyzed here in detail for a single channel will be highly relevant for understanding the flow of energy through more complex networks with multiple quantum machines. To illustrate this point, we consider in Fig. 3.10(a) a small multi-port network where energy injected at site 1 with the rate $\Gamma_i^{(1)}$ and extracted at the two sites 7 and 9 with rates $\Gamma_e^{(7)}$ and $\Gamma_e^{(9)}$, respectively. Fig. 3.10(b) shows that although $\Gamma_e^{(9)} \gg \Gamma_e^{(7)}$, only a residual thermal current is initially flowing from site 1 to site 9. This counterintuitive behavior can be explained by the fact that a symmetric standing wave is formed between sites 1 and 7, which results in a vanishing amplitude $\alpha_4 \approx 0$ at the crossing site. Once $\Gamma_e^{(7)}$ is increased above the value of about $\Gamma_i^{(1)}$, the symmetry breaks and $\alpha_4 \neq 0$ now supports a large current flowing to site 9. As a result, we obtain a transistor-like behavior, where a small increase of losses in one site leads to a sudden increase of the energy current through another part of the network. Simultaneously, there are sharp jumps in the level of current fluctuations, in analogy to what we have found above for the 1D chain. This shows that the combination of interference, nonlinear (symmetry-breaking) effects and the prominent role of noise makes the operation of microscopic power grids a very rich and complex problem, which is still little understood. The current analysis reveals the important part in this problem that is played by quantum fluctuations as a fundamental source

of noise as well as by the topology of the network, which determines whether these fluctuations are enhanced or suppressed.

3.8 Conclusion

In this chapter, we studied the energy transport between a microscopic generator and a microscopic user. We showed that the flow of energy at microscopic scale can be very different what one would intuitively expects from Ohm's law. Moreover, we found that under the influence of thermal or quantum fluctuations there is abrupt change between a noise dominated and a coherent transport regime. This sudden change is accompanied by the breaking of the spatial symmetries. By extending the analysis to complex networks, we found that the properties of the systems strongly depend on the topology of the system and in a 2D grid transistors can be engineered. While there are many ways to realize such quantum machines, we showed that none of our findings depend on the specific realization of the quantum machines or any other imperfections.

4 Non-equilibrium magnetic phases in spin lattices with gain and loss[†]

"Wenn man einem Physiker den Computer wegnimmt, ist das wie ein Tod."

- Frei nach Marko Arnautovic

In the last chapter, we studied the energy transport through a chain of harmonic oscillators and found a phase transition between two different spatial steady state structures depending on the gain and loss rates at the ends of the chain. Moreover, we found that the transport properties crucially differ between these two different phases. While the analysis focused on transport through a chain of harmonic oscillator, there naturally arise the question: Are there are any phase transitions in spin systems with gain and loss?

In classical systems, phase transitions can be investigated by calculating the free energy of the system, where the non-analyticity of the free energy characterizes a classical phase transition and the minimization of the free energy defines the state of the system. In quantum systems, the ground state can be found by finding the lowest eigenstate of the Hamiltonian and the phase transition usually occurs when the gap, the energy difference between the two lowest energies, vanishes. Furthermore, one can distinguish between discontinuous first-order phase transitions and continuous second-order phase transition. While first-order transitions are usually accompanied by phase coexistence between two distinct phases at the critical point, second-order transitions are typically characterized by an infinite correlation length. Moreover, the second-order transitions are usually associated with a breaking of a symmetry.

This classification can successfully describe most phase transitions in equilibrium very well and it is therefore assumed that this classification can be extended to open quantum systems [24, 36]. In such systems the steady state is defined by the zero eigenvalue eigenstate of the Liouvillian and the gap is replaced by the asymptotic decay rate, the real part of the eigenvalue closest to the zero eigenvalue.

However, there is still little known about dissipative phase transitions in spin systems as in 1D systems typically no phase transitions occur [18, 22]

[†] This chapter is based on the article: J. Huber, P. Kirton, and P. Rabl, Non-equilibrium magnetic phases in spin lattices with gain and loss, Phys. Rev. A **102**, 012219 (2020).

and for higher dimensional systems the most reliable results come from exact simulations which are restricted to small system sizes [18–20, 22]. It is therefore of great relevance to find models which lie outside this framework of phase transitions.

In this chapter, we consider a spin lattice with alternating gain and loss where spins are coupled via excitation conserving interactions. The steady state phases are therefore solely induced by dissipation. While many previous works on open spin lattices focused on spin models which exhibit phase transitions in equilibrium [15–22], our model doesn't show any phase transition in equilibrium. We study the non-equilibrium properties of this system when the dissipation strengths are comparable to the coherent interaction strengths and investigate the different phase transitions appearing in this simple model. Furthermore, we compare these phase transitions with well studied models to show that these transitions lies outside of the usual considered framework. At the end of the chapter, we discuss a possible implementation of the system with cold atoms.

4.1 Model

We consider a one dimensional (1D) chain of $2N$ spin-S systems, which is divided into two sublattices A and B as shown in Fig. 4.1(a). The spins precess around a static field along the z-direction with Larmor frequency ω_0 and are coupled to their neighbors via spin-flip interactions with alternating strengths g and h. The coherent dynamics of this system is described by the Heisenberg model $H = \hbar\omega_0 M_z + H_{XX}$, where $M_z = \sum_{n=1}^{N}(S^z_{a,n} + S^z_{b,n})$ is the total magnetization and

$$H_{XX} = \frac{\hbar}{2S}\sum_{n=1}^{N}\left(gS^+_{a,n}S^-_{b,n} + hS^+_{b,n}S^-_{a,n+1} + \text{H.c.}\right). \tag{4.1}$$

The $S^k_{a,n}$ and $S^k_{b,n}$, with $k \in \{x, y, z, \pm\}$, denote the usual spin operators for sublattices A and B. Within the parameter regime of interest, $\omega_0 \gg g, h$, this model only has a trivial, fully polarized ground state, which would be stabilized by adding decay for all spins. To obtain non-trivial dissipation effects, we thus consider alternately pumping the spins along opposite directions. By changing into a frame rotating with ω_0, the resulting evolution of the system density operator ρ is then described by the master equation,

$$\dot{\rho} = \frac{i}{\hbar}[\rho, H_{XX}] + \frac{1}{2S}\sum_{n=1}^{N}\left(\Gamma_g\mathcal{D}[S^+_{a,n}] + \Gamma_l\mathcal{D}[S^-_{b,n}]\right)\rho, \tag{4.2}$$

where $\mathcal{D}[S^\pm]\rho = (2S^\pm\rho S^\mp - S^\mp S^\pm\rho - \rho S^\mp S^\pm)$ and Γ_g and Γ_l are the gain and loss rates, respectively. In Eqs. (4.1) and (4.2) the couplings and pumping rates are scaled by the spin quantum number S to ensure that the relevant timescales of the system dynamics remain the same for different total spins.

Note that Eq. (4.2) preserves the $U(1)$ symmetry associated with a common rotation of all the spins in the x–y plane. In Section 4.5 below we discuss possible experimental implementations of this model using, for example, ensembles of cold atoms or solid-state defects in coupled cavity arrays. As depicted in Fig. 4.1(b), the dissipative terms in Eq. (4.2) drive the sys-

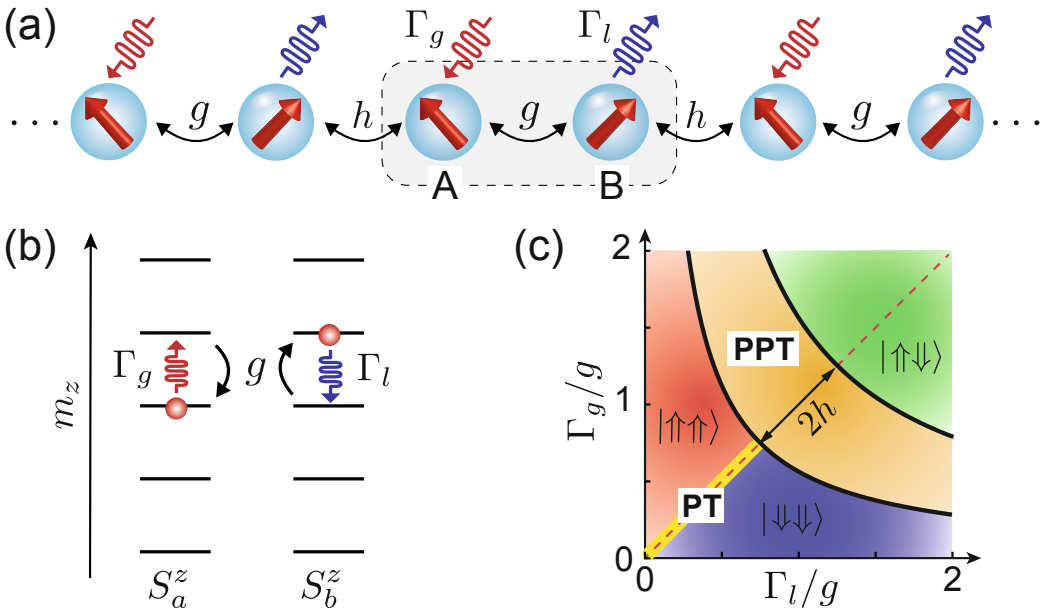

Figure 4.1: (a) Sketch of a 1D spin chain, where the individual spins are coherently coupled to their neighbors and alternately pumped with rate Γ_g or cooled with rate Γ_l. (b) Illustration of the coherent and dissipative processes within a single unit cell. (c) Plot of the steady-state phase diagram of the dissipative spin chain as a function of the gain and loss rates. The solid lines indicate the phase boundaries for $S \to \infty$.

tem into a state with a staggered magnetization, while the coherent coupling tends to counteract this imbalance. This competition leads to several distinct phases for the steady state of the spin chain, $\rho_0 = \rho(t \to \infty)$, which are summarized in Fig. 4.1(c). We identify two types of ordered phases, which exhibit either anti-ferromagnetic (AM) or ferromagnetic (FM) alignment of the spins. In addition, there are two strongly disordered phases, which are labeled as PT-symmetric (PT) and pseudo-PT-symmetric (PPT) for reasons that will be discussed in more detail below. In the limit $S \to \infty$ the five different phases are separated by sharp boundaries defined by the lines

$$\Gamma_g \Gamma_l = (g \pm h)^2 \tag{4.3}$$

and $\Gamma_g = \Gamma_l$ for $\Gamma_g \Gamma_l < (g - h)^2$, which can be derived from a Holstein-Primakoff approximation (HPA) (see Appendix B.1).

4.2 Dissipative spin dimer

To understand some basic properties of the model, it is instructive to first consider the limit $h \to 0$, where the chain separates into decoupled spin dimers. In this case the intermediate mixed phase disappears and for the remaining phases the order parameter $\mathcal{M}_z = \langle M_z \rangle/(2S)$ is shown in Fig. 4.2(a). For $\Gamma_{g,l} \gg g$ dissipation always dominates and the spins are simply pumped into an anti-aligned AM configuration, where $\mathcal{M}_z \approx 0$, but $\langle S^z_a \rangle = -\langle S^z_b \rangle \approx S$. For $\sqrt{\Gamma_g \Gamma_l} < g$, this arrangement is destabilized by the coherent coupling, which, in this regime, efficiently redistributes energy between the two sites. As a result, the stationary state is only determined by the sign of the net damping rate, $\delta\Gamma = (\Gamma_g - \Gamma_l)$, and exhibits FM alignment, $\mathcal{M}_z \simeq \pm 1$. This ordered phase extends into the regime $\Gamma_{g,l} \ll g$, where the coherent interaction dominates and where one would thus expect a highly mixed, depolarized phase. At the same time the spin alignment opposes the applied dissipation in one of the sublattices, which shows that this type of order still depends on a non-trivial interplay between coherent and incoherent processes. Interestingly, even for $S \gg 1$ this stationary ferromagnetic alignment is not captured by the mean-field equations of motion (see Appendix B.2), which instead predict a limit cycle for one of the spins with a vanishing average magnetization.

4.2.1 PT-symmetry

Of specific interest is the behavior of this system along the diagonal $\Gamma_l = \Gamma_g$, which for $\bar{\Gamma} = (\Gamma_g + \Gamma_l)/2 < g$ marks the boundary between the two FM phases. Along this line the model becomes PT symmetric as explained in more detail in Chapter 5. This means that the master equation, Eq. (4.2), is invariant under the combined exchange of sublattices A and B (parity) and the conjugation of the jump operators $S^+ \leftrightarrow S^-$ (exchanging loss and gain, i.e., reversing time).

The steady state for $\bar{\Gamma} \ll g$ is close to the (symmetric) fully mixed state as (for a proof see Chapter 5.3),

$$\rho_0 \simeq \frac{1}{(2S+1)^2}\left[\mathbb{1} + O\left(\frac{\bar{\Gamma}}{g}\right)\right], \tag{4.4}$$

with $\langle M_z \rangle \simeq \langle S^z_{a,b} \rangle \simeq 0$, and that this phase is separated from the (symmetry-broken) AM phase by a sharp transition in the limit $S \to \infty$. This behavior is clearly visible in Fig. 4.2(b), where we plot the individual magnetizations along the line $\Gamma_l = \Gamma_g$ for increasing S.

In Fig. 4.2(c) and (d) we also plot the real part of the smallest magnitude non-zero eigenvalues, λ_n, of the Liouville superoperator $\mathcal{L}$, which is defined by $\dot{\rho} = \mathcal{L}\rho$. As we approach the transition point $\bar{\Gamma} = g$ from the AM phase, we observe a closing of the Liouvillian gap, $\varepsilon_L \sim 1/S$, where $\varepsilon_L = \min\{-\mathrm{Re}(\lambda_n)\}$. While the closing of the Liouvillian gap is expected for any dissipative phase transition point [24, 36], we also find that many of the larger magnitude

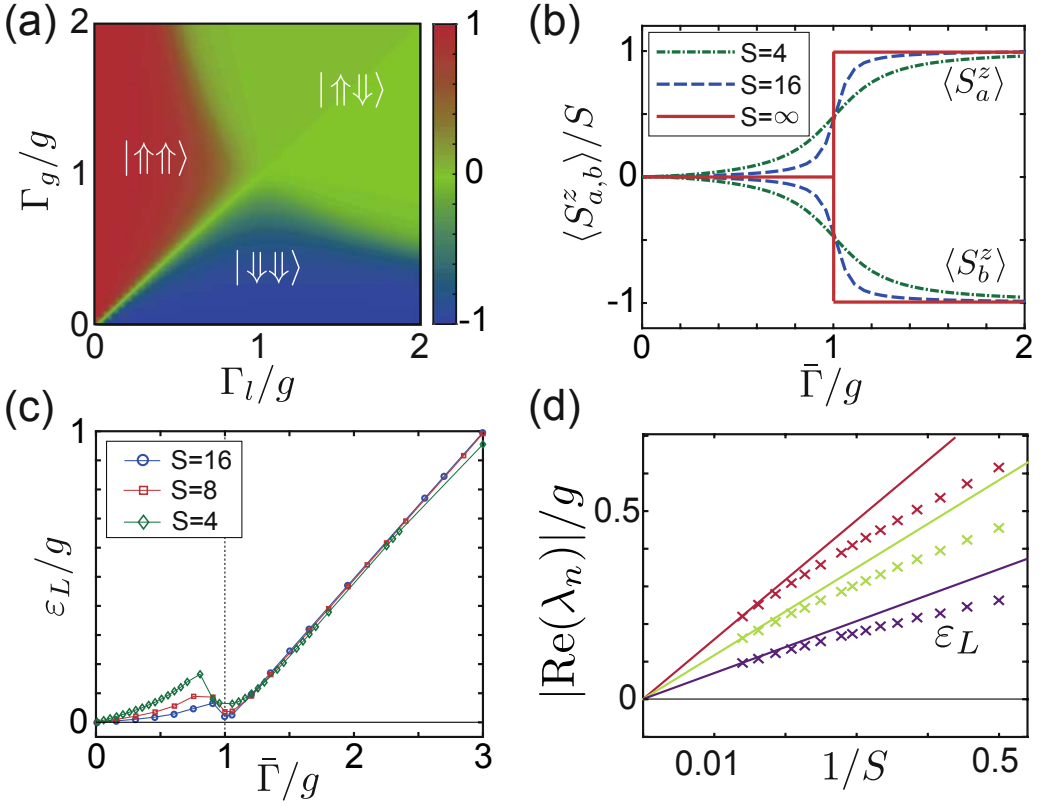

Figure 4.2: (a) Plot of the order parameter $\mathcal{M}_z = \langle M_z\rangle/(2S)$ for a spin dimer with $S = 12$. (b) Magnetization of the individual spins along the symmetry line, $\Gamma_l = \Gamma_g = \bar{\Gamma}$, for different spin quantum numbers. For the same parameters, (c) shows the dependence of the Liouvillian gap, ε_L, on the ratio $\bar{\Gamma}/g$. (d) Scaling of ε_L and of two additional eigenvalues at the transition point, $\bar{\Gamma} = g$. The crosses are the exact numerical results for up to $S = 18$ and the solid lines are linear extrapolations to zero, i.e., $\varepsilon_L \sim 1/S$.

eigenvalues of $\mathcal{L}$ vanish and remain vanishingly small (in the limit of large S) within the whole PT phase. This indicates that for $\bar{\Gamma} < g$ the gain and loss processes cancel out on average. In contrast, fluctuations, which still occur with rates $\Gamma_{g,l}$, are not reduced correspondingly and drive the system into a highly mixed state. Since the energy levels of the system do not change at the transition point, this sudden increase of entropy translates into a jump of the systems' effective temperature [24, 28, 166]. This is a crucial difference to equilibrium systems, where the level of fluctuations is determined by a fixed temperature in all phases.

More specifically, as already pointed out in Eq. (4.4) above, the steady state in this PT symmetric phase is close to the fully mixed, i.e., infinite temperature state. This must be contrasted to states with a high, but finite temperature as observed in other models [24, 166], since the impurity of the

system, $\mathcal{I} = 1/\mathcal{P}$, becomes extensive,

$$\lim_{S\to\infty} \frac{\mathcal{I}(\delta\Gamma = 0)}{(2S+1)^2} > 0. \tag{4.5}$$

This implies that such a state cannot be accurately described by a mean-field ansatz, since for any observable fluctuations dominate over its mean value. As we will discuss in the following, many of the unusual features of the current model can be traced back to this specific property of the PT symmetric phase. Note that a similar transition between low and infinite temperature phases can also occur in various other models [26, 28]. It is thus important to develop a more general understanding of this type of transition, in particular in extended lattice systems, where the fate of such infinite temperatures phases is still unknown.

4.2.2 Absence of phase co-existence

For the dimer model, Fig. 4.2(a) shows that all transitions are of first order, meaning that at the respective transition lines the magnetization in the limit $S \to \infty$ jumps abruptly between two different values. For concreteness, we will focus in the following on the transition between the two FM phases for $\bar{\Gamma} < g$. This situation is reminiscent of a regular Ising ferromagnet in the presence of an external bias field B, a role which is here taken by the rate imbalance $\delta\Gamma$. In an equilibrium magnetic system and for $B = 0$, there is no externally imposed direction and the magnetic moments then spontaneously align themselves along one of the two possible directions. When averaged over these two equally probable configurations, the resulting density operator corresponds to an equal mixture between the two FM states.

It has been previously conjectured [36] that such a picture should also apply, very generically, to discontinuous transitions in driven-dissipative systems. This conclusion is primarily based on the analysis of the dissipative Kerr-oscillator (see discussion below), where this analogy between equilibrium and non-equilibrium phase transitions is indeed very accurate. However, the current model demonstrates that there are other types of first-order phase transitions, where this analogy does not apply. To illustrate this point we study in Fig. 4.3 in more detail the behavior of the system as we tune it across the transition line for a fixed $\bar{\Gamma}/g = 0.5$ and varying $\delta\Gamma$. First of all, Fig. 4.3(a) shows the expected closing of the Liouvillian gap at $\delta\Gamma = 0$ confirming the existence of a sharp phase transition in the limit $S \to \infty$ [see also Fig. 4.2(c)]. In Fig. 4.3(b) we plot the purity of the steady state, which vanishes as $\mathcal{P} \sim 1/(2S+1)^2$ at the transition point. More explicitly, Fig. 4.3(c) shows the probability distribution $P(m_z^A, m_z^B)$ for the magnetization values of each spin just below, at and just above the transition point. This comparison demonstrates that the state at $\delta\Gamma = 0$ is clearly different from a naively expected mixture between the two neighboring phases. Although in the middle plot we still see some small variations in $P(m_z^A, m_z^B)$, the scaled impurity in

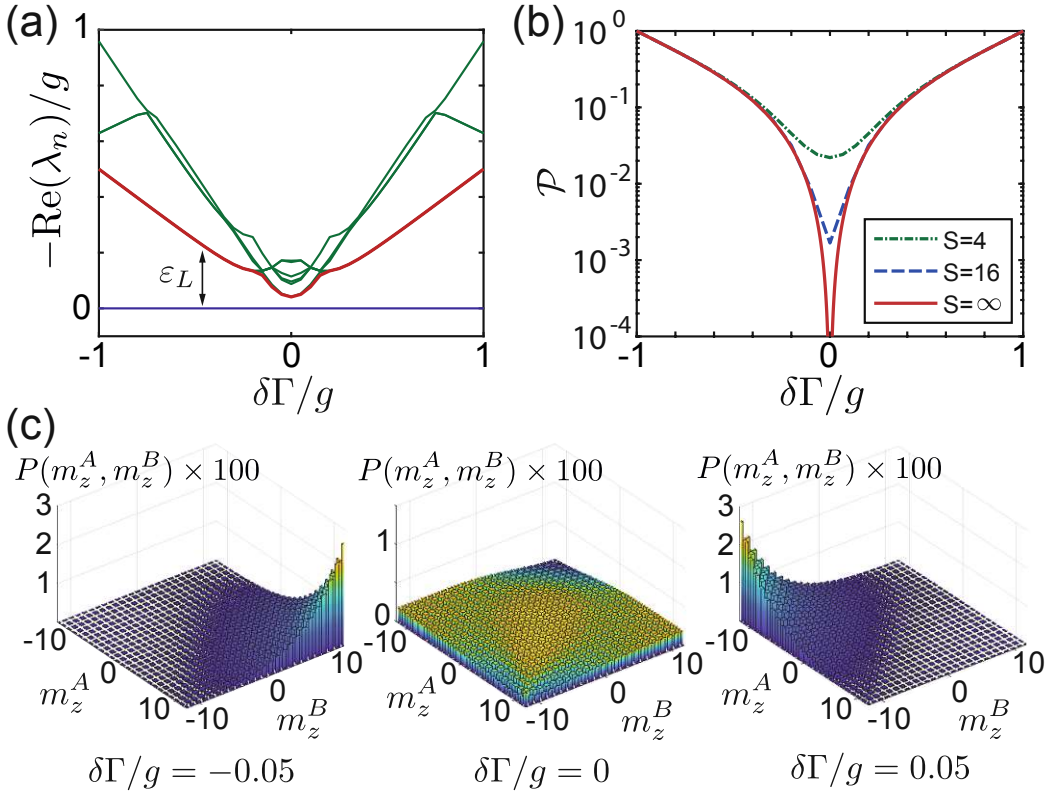

Figure 4.3: (a) The real part of the first 8 eigenvalues λ_n of the Liouvillian $\mathcal{L}$ for a fixed value $\bar{\Gamma} = 0.5g$ and $S = 16$. In the limit $S \to \infty$, the point $\delta\Gamma = 0$ marks the phase transition line between the two FM states. (b) Purity of the steady-state, $\mathcal{P} = \mathrm{Tr}\{\rho_0^2\}$, for the same parameters but different values of S. The line labelled $S = \infty$ shows the analytic prediction obtained from a HPA (see Appendix B.1). (c) The probability distribution $P(m_z^A, m_z^B)$ for the magnetization values of each spin is shown for three different values of $\delta\Gamma$ representing the steady state just below, at, and just above the transition point for $S = 12$.

this (finite S) example reaches a value of $\mathcal{I}/(2S+1)^2 \simeq 0.957$. This confirms that for $S \gg 1$ the system transitions between the two opposite FM configurations via an intermediate, fully mixed phase.

It is instructive to contrast the behavior in Fig. 4.3 with the regular first-order phase transition in the dissipative Kerr oscillator mentioned above. The Kerr oscillator is a single nonlinear bosonic mode with annihilation operator c, which is described by the Hamiltonian [29–31]

$$H_{\mathrm{K}} = -\hbar\Delta c^\dagger c + \hbar\frac{U}{D} c^\dagger c^\dagger c c + \hbar\sqrt{D}F(c^\dagger + c). \tag{4.6}$$

Here U is the strength of the nonlinearity and F the strength of an external driving field, which is detuned from resonance by Δ. The parameter D plays the role of an effective Hilbert space dimension such that $D \to \infty$ represents the thermodynamic limit of this model. The dynamics of the dissipative Kerr

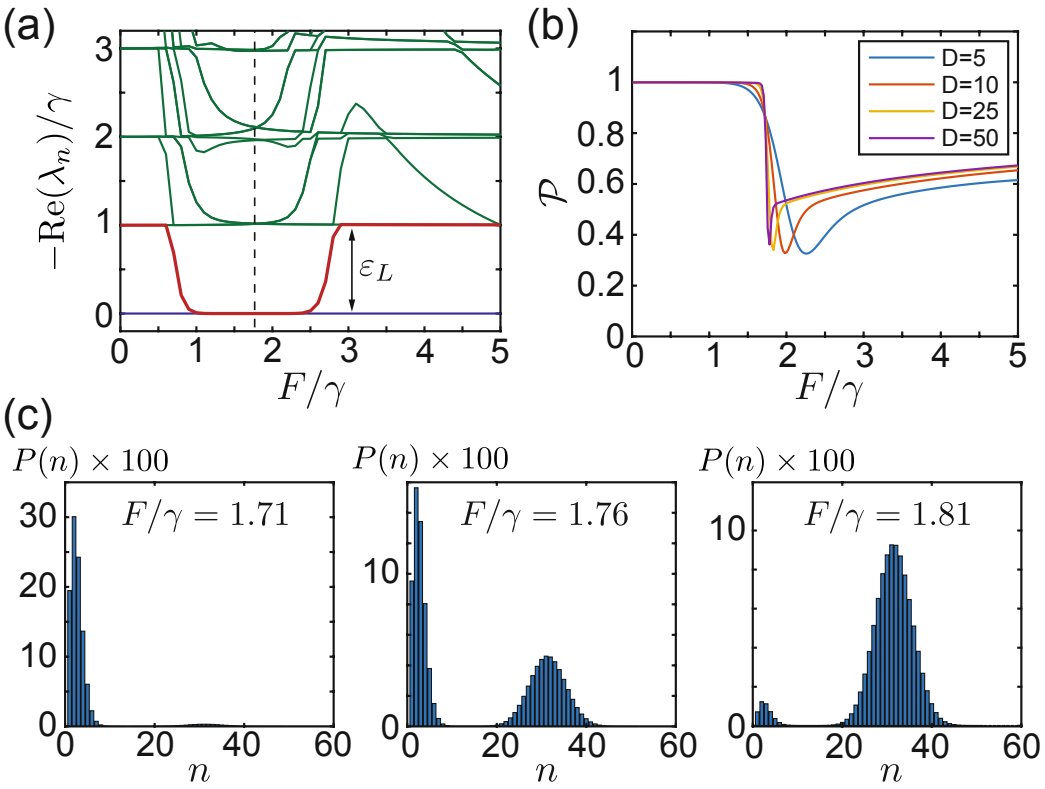

Figure 4.4: First-order phase transition in the disspative Kerr oscillator as defined in Eq. (4.7). (a) The real part of smallest eigenvalues, λ_n, of the Liouvillian $\mathcal{L}_\mathrm{K}$ as a function of F/γ and for $U/\gamma = 10$, $\Delta/\gamma = 10$ and $D = 50$. The dashed vertical line marks the phase transition point at $F/\gamma \simeq 1.76$. (b) Purity of the steady-state ρ_0, where $\mathcal{L}_\mathrm{K}\rho_0 = 0$, for the same parameters but different values of D. (c) Probability distribution $P(n)$ for the oscillator number states $|n\rangle$ just below, at, and just above the transition point and for $D = 50$.

oscillator is then described by the master equation

$$\dot{\rho} = -\frac{i}{\hbar}[H_\mathrm{K}, \rho] + \gamma\mathcal{D}[c] \equiv \mathcal{L}_\mathrm{K}\rho, \tag{4.7}$$

where γ is the decay rate. The steady state of this master equation exhibits a first-order phase transition at $F/\gamma \simeq 1.76$, where the system switches between states with a low and high photon number expectation value.

Figure 4.4 summarizes the behavior of the Kerr oscillator when it is tuned across this transition point, which we can contrast with the observations in Fig. 4.3. We first notice that the Liouvillian gap is vanishingly small over a larger parameter range and it vanishes as $\varepsilon_L \sim e^{-D}$ at the transition point [30]. In contrast to the spin model, only two eigenvalues vanish, which already indicates that at the transition point the system is well described by a mixture of two distinct metastable states. This picture is also confirmed by a non-vanishing purity in Fig. 4.4(b) and the distribution of the occupation numbers of the oscillator states, $p(n)$, in Fig. 4.4(c). This last result clearly shows that

the state at the transition point is a mixture of the two neighboring phases, which can also be verified explicitly [36].

The observation that such a co-existence between the two FM states does not occur for the spin dimer can be attributed to the fact that in this model a large number of Liouvillian eigenvalues vanish at the same time near $\delta\Gamma = 0$. This provides, roughly speaking, more flexibility to construct the actual steady state out of many nearly-degenerate eigenvectors of $\mathcal{L}$. Since in the spin model the closing of the Liouvillian gap only scales inversely with the system size and not exponentially also means that other properties, such as the divergence of the relaxation rate, etc., will be very different in these two types of first-order transition.

4.3 Dissipative spin chain

We now return to the fully coupled chain with $0 < h \leq g$ to see how the basic effects discussed above affect the non-equilibrium states of the extended spin lattice. As already mentioned in the introduction, for small spins, $S \sim \mathcal{O}(1)$, there are typically no sharp phase transitions in dissipative spin systems in 1D, even for an infinite number of lattice sites $N \to \infty$. This can be understood from the fact that the fluctuations introduced by the dissipation processes act as a finite effective temperature, which typically prevents long-range order in 1D [167]. Therefore, in the following analysis we retain our focus on the regime $S \gg 1$, as above. While in this limit sharp transitions already occur for a single cell, the resulting phases and the nature of the phase transitions can be very different in the lattice system. In fact, the exact nature of a phase transition can only be determined in extended systems, where, apart from the order parameter, also information about spatial correlations and their critical scaling is available.

4.3.1 Simulation of dissipative spin lattices

While in 1D the dynamics and steady states of dissipative systems with a small local Hilbert space dimension can still be simulated efficiently using matrix product operator techniques [39, 126], this is not possible for the current system when $S \gg 1$. At the same time, we have seen that, even in the limit of a large spin quantum number, fluctuations are dominant, which makes a mean-field approximation unreliable. To overcome these limitations we developed the truncated Wigner method for open quantum system (TWOQS) which is based on the truncated Wigner approximation (TWA) [107, 168–170]. It works the following way: An initial state distribution, which is sampled from a Wigner function of the initial state, is time evolved by the stochastic equations. As quantum fluctuations are included at all times, this gives usually substantially more accurate results and access to correlations. A detailed derivation of TWOQS and its applicability for the simulation of collective spin models is presented in Chapter 6. In addition to TWOQS, we use infi-

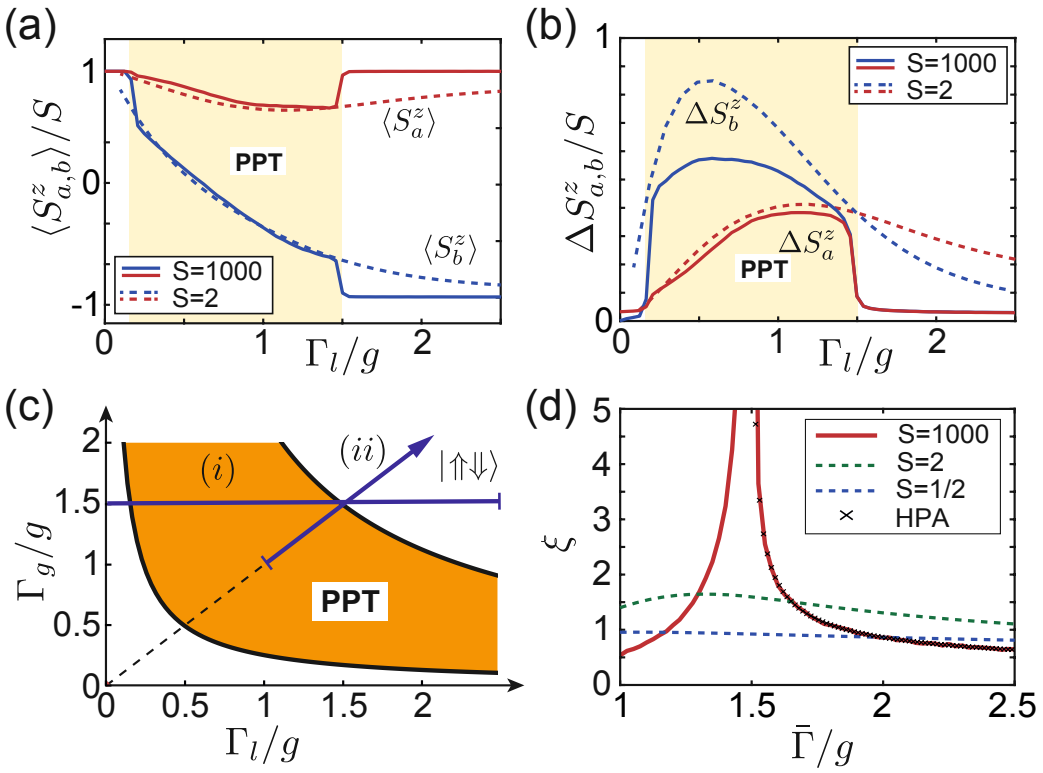

Figure 4.5: Plot of (a) the average magnetization $\langle S^z_{a,b}\rangle$ and (b) the magnetization fluctuations, $(\Delta S^z_{a,b})^2 = \langle (S^z_{a,b})^2\rangle - \langle S^z_{a,b}\rangle^2$. The two quantities are shown along the path (i) indicated in the sketch of the phase diagram in (c), which shows the extent of the PPT phase for a value of $h/g = 0.5$. (d) Plot of the correlation length ξ along the symmetry line $\Gamma_l = \Gamma_g = \bar{\Gamma}$, i.e. the path (ii) in (c). In (a), (b) and (d) the solid lines represent the results from the TWOQS simulation for $N = 50$ units cells, while the dashed lines have been obtained using iMPO techniques [39, 126].

nite matrix product operator (iMPO) [39, 126] and cluster-mean field (CMF) simulations to verify that the main characteristics of the different phases are still present in the limit of small and moderate spin quantum numbers.

4.3.2 The PPT phase

In Fig. 4.5(a) and (b) we apply the numerical techniques discussed above to evaluate the dependence of the average magnetization of each spin and its variance for a fixed $\Gamma_g = 1.5g$ and varying Γ_l. In the limits $\Gamma_l/g \to 0$ and $\Gamma_l/g \gg 1$ we recover the FM and AM phases, respectively, which are again characterized by a well-defined magnetization pattern and almost no fluctuations. However, in the extended system, these phases are no longer directly connected. Instead a new intermediate PPT phase appears between the boundaries $\Gamma_g\Gamma_l = (g \pm h)^2$. Although this PPT phase exhibits an imbalanced average magnetization, i.e., $\langle S^z_a\rangle \neq \langle S^z_b\rangle$, it is dominated by large fluctuations similar to the PT phase discussed above. Importantly, this char-

acteristic behavior is no longer restricted to a single line in parameter space and appears at intermediate values where all dissipation and coherent coupling rates are approximately the same. In the limit $h = g$ the PPT phase completely replaces both FM phases. This shows that the behavior of the lattice systems is considerably different to that of the dimer. For smaller S the boundaries between the phases are much less pronounced, but even in this limit, the three different phases can be clearly distinguished, as can be seen in the results of the iMPO calculations in Fig. 4.5.

4.3.3 Mixed-order transitions

In Fig. 4.5(d) we now take a closer look at the transition between the AM and the PPT phase and evaluate the correlation length ξ for $\delta\Gamma = 0$ as we vary the damping $\bar{\Gamma}$ across the critical point, $\bar{\Gamma}_c = g + h$. The correlation length is extracted from an exponential fit of the spin correlation function $\langle S^+_{a,n} S^-_{a,m}\rangle \sim e^{-|n-m|/\xi}$. Again we find excellent agreement in the ordered phases between the HPA (see Appendix B.1) and the TWOQS. From our numerical simulations we find that $\xi \sim |\bar{\Gamma} - \bar{\Gamma}_c|^{-\nu}$, where $\nu \simeq 0.5$ in both phases. This behavior would be characteristic for a continuous second-order phase transition associated with the breaking of the $U(1)$ symmetry of our model. However, as shown in Fig. 4.5(a) the magnetizations $\langle S^z_{a,b}\rangle$ exhibit a rather sharp jump and, as we will argue below, there is no symmetry breaking.

To asses the order of this phase transition we compare in, Figs. 4.6(a)+(b), the results from the full numerical simulation with the predictions from mean-field theory (see Appendix B.2). Mean-field theory shows that while for small spins the transition is indeed continuous, it becomes steeper and steeper with increasing S. In the limit $S \to \infty$ we then obtain a discrete jump in the order parameter $\Delta = \langle S^-_a\rangle$, where for $\delta\Gamma = 0$ we obtain the explicit result

$$\Delta(\bar{\Gamma}) \simeq \theta(\bar{\Gamma}_c - \bar{\Gamma}) S \sqrt{\frac{\bar{\Gamma}}{g+h}} e^{i\phi}. \tag{4.8}$$

Here $\theta(x)$ is the Heaviside step function and ϕ is an arbitrary phase which breaks the $U(1)$ symmetry [171].

In Fig. 4.6(c) we compare this behavior with two scenarios within the usual Landau free-energy picture of equilibrium phase transitions. The first case illustrates a first-order transition, where the order parameter jumps from one minimum at $\Delta = 0$ to a finite value. If the minima at finite $|\Delta|$ are degenerate, this type of transition can spontaneously break the symmetry, but it will not be associated with a diverging correlation length. The second case depicts a mixed-order transition, where at the transition point the free energy landscape becomes essentially flat. This leads to diverging fluctuations as one approaches the transition point, but also to a jump of the order parameter from $\Delta = 0$ to $|\Delta| \sim S$. For small S this picture smoothly connects to the phenomenology of a continuous second-order phase transition.

Based on this mean-field analogy with conventional Landau theory, we conclude that in the limit of large S the transition from the AM to the PPT phase

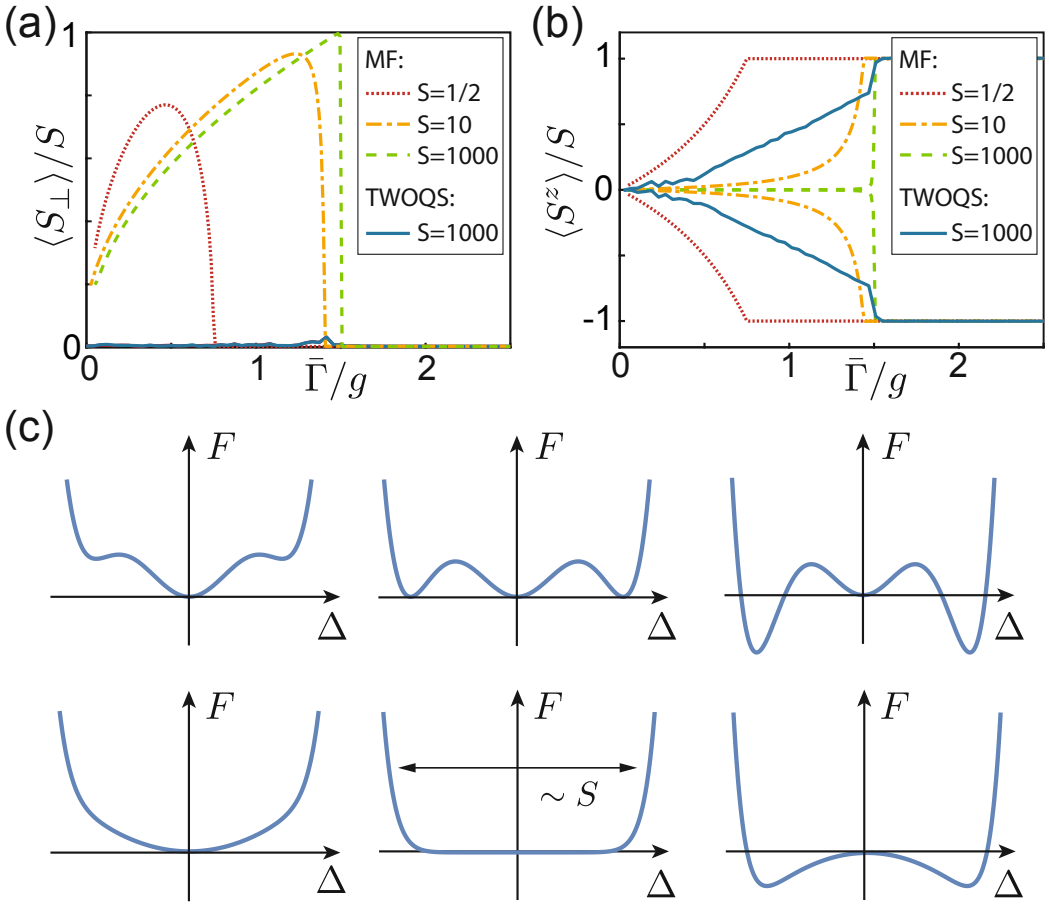

Figure 4.6: Plot of the steady-state expectation values of (a) the transverse polarization $\langle S_\perp \rangle = \sqrt{\langle S_a^x \rangle^2 + \langle S_a^y \rangle^2}$ and (b) the average magnetization $\langle S_z \rangle$ along the symmetry line $\Gamma_g = \Gamma_l = \bar{\Gamma}$. In both plots the results obtained by a TWOQS simulation (solid lines) for $S = 1000$ and $N = 50$ unit cells are compared with the predictions from mean-field (MF) theory (dashed lines) for different spin quantum numbers. (c) Illustration of the difference between a first-order (top row), and a mixed-order (bottom row) phase transition in terms of the usual Landau free energy $F(\Delta)$. The three columns show the variation of the free energy with the order parameter Δ before (left), at (middle) and after (right) the transition point.

is most accurately described by a mixed-order phase transition [21, 172]. In the exact simulations, the same behavior, namely a jump in the order parameter and a diverging correlation length, is also found for the transition between the FM and the PPT phase, although in this case neither the FM nor the PPT phase are captured by the mean-field equations of motion. For the transition between the two FM phases, the HPA does not predict a diverging correlation length, consistent with a first-order transition as discussed in Section 4.2. Of course, this intuitive picture of minimizing an effective potential is very limited and does not take into account the non-equilibrium fluctuations, which, for example, prevent phase-coexistence at the transition

point.

4.3.4 Absence of symmetry-breaking

The mean-field result given in Eq. (4.8) predicts a breaking of the $U(1)$ symmetry of the master equation (4.2), which is associated with a common rotation of all the spins in the x–y plane. However, this symmetry-breaking effect is not observed in our numerical simulations where in all stationary phases $\Delta \simeq 0$. As a consequence other expectation values, which are not sensitive to this phase, differ considerably from the mean-field predictions [see Figs. 4.6(a)+(b)]. While expected for small spins, this observation is very surprising in the limit $S \to \infty$, where mean-field theory usually becomes exact.

The question of whether or not there is symmetry breaking in the steady state of driven-dissipative systems is actually very subtle, since in the exact steady state all the phases ϕ would appear with equal probability and average to zero. Therefore, in the following we use two different numerical approaches to argue that the transition between the AM and PPT phases is inconsistent with our conventional understanding of symmetry-breaking.

Cluster mean field

First, we use the cluster mean field theory to systematically go beyond the results of the mean-field equations from above, we generalize to the case where all quantum correlations between neighboring sites are included, but a mean-field decoupling is made between these clusters [18]. To achieve this we treat a cluster of N_C unit cells exactly, but factorize the interactions between spins in neighboring clusters. Within this approximation the density operator of the whole chain is replaced by a tensor product of N/N_C smaller density matrices,

$$\rho \approx \bigotimes_{\ell=1}^{(N/N_C)} \rho_C^{(\ell)}. \tag{4.9}$$

Taking the limit $N \to \infty$ allows us to assume translational invariance and hence we set $\rho_C^{(\ell)} = \rho_C$. The resulting mean-field master equation for ρ_C is given by

$$\dot{\rho}_C = -\frac{i}{\hbar}[H, \rho_C] + \frac{1}{2S}\sum_{n=1}^{N_C}\left(\Gamma_g \mathcal{D}[S_{a,n}^+] + \Gamma_l \mathcal{D}[S_{b,n}^-]\right)\rho_C, \tag{4.10}$$

where

$$\begin{aligned} H = &\frac{\hbar}{S}\sum_{n=1}^{N_C-1}\left[g\left(S_{a,n}^x S_{b,n}^x + S_{a,n}^y S_{b,n}^y\right) + h\left(S_{b,n}^x S_{a,n+1}^x + S_{b,n}^y S_{a,n+1}^y\right)\right] \\ &+ \frac{\hbar h}{S}\left(\langle S_{b,N_C}^x\rangle S_{a,1}^x + \langle S_{b,N_C}^y\rangle S_{a,1}^y\right) + \frac{\hbar g}{S}\left(\langle S_{b,1}^x\rangle S_{a,N_C}^x + \langle S_{b,1}^y\rangle S_{a,N_C}^y\right). \end{aligned} \tag{4.11}$$

Here, the last two lines of the Hamiltonian account for the mean-field interaction between neighboring clusters. Note that this equation is no longer linear in ρ_C and the evolution of the state and the expectation values must be found self-consistently.

In our model each unit cell consists of two spin-S systems. This limits the applicability of this method to clusters of size $N_C = 1, 2$ for even moderate values of S. To observe the behavior of the system as the cluster size is increased we thus focus on the symmetric case where $\Gamma_g = \Gamma_l = \bar{\Gamma}$ and $h = g$. This then allows us to make a unitary transformation which results in a fully translationally model in which the unit cell is a single site. By redefining the spin on every A lattice site as $S^z_{a,n} \to -S^z_{a,n}$, $S^x_{a,n} \to S^x_{a,n}$, $S^y_{a,n} \to -S^y_{a,n}$, we obtain a model described by the cluster mean-field master equation

$$\dot{\rho}_C = -\frac{i}{\hbar}[H, \rho_C] + \frac{\bar{\Gamma}}{2S}\sum_{n=1}^{n_C} \mathcal{D}[S^-_n]\rho_C, \tag{4.12}$$

with Hamiltonian

$$\begin{aligned} H = &\frac{\hbar g}{S}\sum_{n=1}^{n_C-1}\left(S^x_n S^x_{n+1} - S^y_n S^y_{n+1}\right) \\ &+ \frac{\hbar g}{S}\left(\langle S^x_{n_C}\rangle S^x_1 - \langle S^y_{n_C}\rangle S^y_1 + \langle S^x_{b,1}\rangle S^x_{N_C} - \langle S^y_{n_C}\rangle S^y_1\right). \end{aligned} \tag{4.13}$$

This allows us to simulate cluster sizes of $n_C = 1, 2, 3, 4$ lattice sites for spin $S \leq 4$ systems.

First, in Fig. 4.7(a) and (b) we show the results of a CMF simulation, where the $U(1)$ symmetry is explicitly broken by initializing the spins along a specific direction in the x–y plane. Independent of the phase ϕ, such a state is characterized by a finite value of the transverse spin component

$$\langle S_\perp\rangle = \sqrt{\langle S^x\rangle^2 + \langle S^y\rangle^2}, \tag{4.14}$$

since it indicates a preferred average direction in the x–y plane and hence breaking of the $U(1)$ symmetry. For a cluster size $n_C = 1$ of one lattice site, which corresponds to the regular mean-field approximation, the broken symmetry is retained in the steady states of the PPT and PT phases. However, as one increases the cluster size, the region with broken symmetry rapidly shrinks and does not considerably grow again when the spin S at each lattice site is increased. This shows that even if the symmetry is explicitly broken by a mean-field ansatz, the system restores the symmetry when the accuracy of the approximation is increased. This behavior must be contrasted to the findings in Refs. [18, 20]. In these references the same scaling analysis correctly predicts the absence of symmetry breaking in 1D, where there is also no phase transition, but supports the existence of a phase with broken symmetry in 2D. Here we find a sharp phase transition but no corresponding symmetry-breaking.

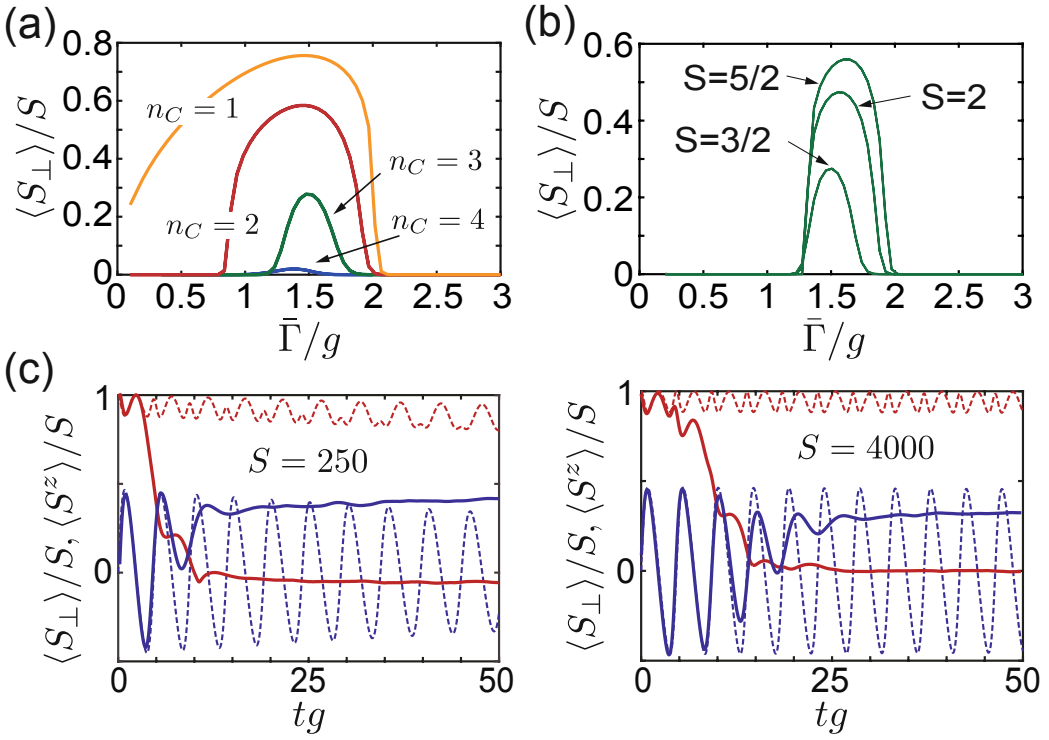

Figure 4.7: (a) Steady-state expectation value of the transverse polarization $\langle S_\perp\rangle = \sqrt{\langle S_a^x\rangle^2 + \langle S_a^y\rangle^2}$ obtained from a CMF simulation with varying cluster size, n_C, and $S = 3/2$. In (b) the same expectation value is plotted for $n_C = 3$ and varying S. In both plots $\Gamma_l = \Gamma_g = \bar{\Gamma}$ and an inter-cell coupling of $h = g$ has been assumed. (c) Dynamics of the spin lattice, which is initially prepared in a symmetry-broken state where all the spins are oriented along the x axis. The solid lines show the TWOQS results for while the dashed lines are obtained from the mean-field equations of motion (see Appendix B.2). In blue we show $\langle S_z\rangle$ and in red the perpendicular magnetization $\langle S_\perp\rangle$. For both plots in (c) the parameters are $\Gamma_g = \Gamma_l = g$, $h = 0.5g$ and $N = 50$.

TWOQS simulations

To obtain further evidence for the absence of symmetry breaking in the limit $S \to \infty$, we perform additional dynamical simulations, where the system is initialized in a symmetry-broken state close to the mean-field prediction. We then study the evolution toward the steady state. If the symmetry is broken in the thermodynamic limit we expect that, as we move towards $S \to \infty$, the timescale, $\tau_{\rm sb}$, over which the symmetry is restored should diverge. A prototypical example for such a symmetry-breaking effect is a conventional laser, where the phase diffusion rate decreases inversely with the mean photon number [97].

In Fig. 4.7(c) we perform such a numerical experiment on our model in the PPT phase, with $\Gamma_l = \Gamma_g = g$, $h = 0.5g$ and $N = 50$ unit cells. According to mean-field theory this expectation value stays close to its initial value for the whole duration of the simulation. However, the stochastic simulation, which

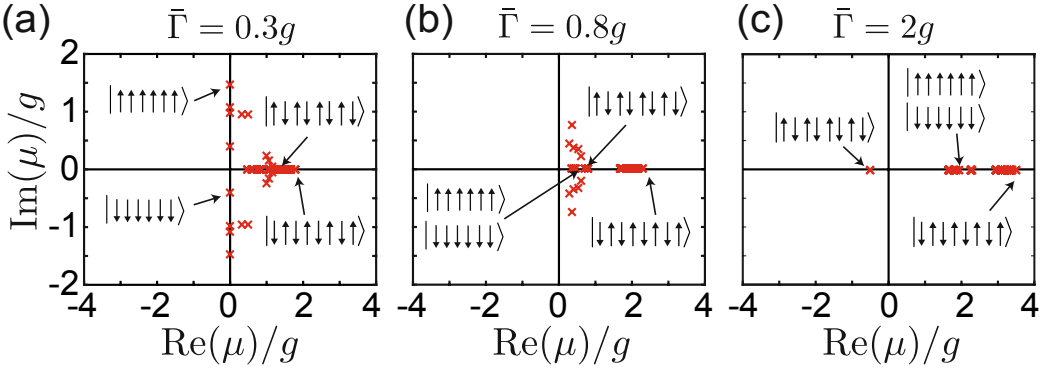

Figure 4.8: Plot of the eigenvalues μ of the least stable fluctuation modes for a chain of $N = 4$ unit cells and $h = 0.5g$, which is initialized in all spin configurations with $\langle S^z_{a,b}\rangle = \pm S$. A few configurations and the corresponding eigenvalues are shown as examples.

includes quantum fluctuations from the dissipative processes, shows that this average rapidly approaches zero after a time $\tau_{\mathrm{sb}} \sim 10g^{-1}$, which is also on the order of $\Gamma^{-1}_{g,l}$. Importantly, this time does not considerably increase (by less than a factor of 2), when the spin quantum number is increased by a factor of 16. This gives further evidence to the lack of symmetry breaking in the PPT phase.

We note at this point that the presence of a continuous phase transition without the breaking of the corresponding Z_2 symmetry has been previously pointed out for a single-site collective spin model [28], but interpreted as a limiting case of a first-order transition. Since this model also exhibits an infinite-temperature phase, our current analysis suggests an alternative interpretation, namely a purely fluctuation-induced suppression of symmetry breaking.

4.4 PT-symmetry breaking in quantum many-body systems

In the case of the dimer we have already pointed out that the master equation Eq. (4.2) posses an additional PT-symmetry when $\Gamma_l = \Gamma_g$ (for detailed discussion of PT-symmetry in open quantum system see Chapter 5) and that the PT and AM phases represent the corresponding symmetric and symmetry-broken phases, respectively.

Compared to the dimer, an important observation is the appearance of the intermediate PPT phase in the lattice model, which exists over a large parameter range away from the symmetry line. For these parameters the analogue non-Hermitian oscillator model [173] has both real and imaginary eigenvalues. Therefore, in this phase the system shares many characteristics of the PT phase, but the symmetry is not fully established.

To further illustrate this behavior, in Fig. 4.8 we show the results of a

numerical quench experiment. Here, a chain with $N = 4$ unit cells and $h = 0.5g$ is initialized in all 2^8 possible spin configurations with $\langle S^z_{a,b}\rangle = \pm S$. The successive transient dynamics is characterized by the set of 2^8 complex eigenvalues $\{\mu_{\sigma,i}\}$ of the linearized fluctuation matrix. For each configuration labeled by σ, the eigenvalue with the largest real part, representing the least stable fluctuation mode, is shown. For example, in the ordered AM phase, in Fig. 4.8(c), there is only a single point with $\mathrm{Re}(\mu) < 0$. This implies that there is only one configuration where all the fluctuations are damped. All other configurations are rapidly destabilized due to fluctuations that are amplified with rates $\mathrm{Re}(\mu) \sim \Gamma_{g,l}$. In the PPT phase, Fig. 4.8(b), all configurations are unstable, but for a considerable fraction of possible spin orientations the maximal growth rate is very slow, $\mathrm{Re}(\mu) \ll \Gamma_{g,l}$. Thus, the system transitions slowly between many metastable orientations, which is reflected in the significant fluctuations observed in this phase. Another qualitative change is then found in the PT phase, $\Gamma_l = \Gamma_g < (g - h)$, shown in Fig. 4.8(a). Here there are several configurations, where the fluctuations exhibit a purely oscillatory behavior, i.e., $\mathrm{Re}(\mu) = 0$, $\mathrm{Im}(\mu) \sim g$, even in the presence of strong local dissipation. These configurations are neither stable nor unstable, which explains the peculiar properties of this phase. Overall, we see that the pattern of growth rates of spin fluctuations provides a characteristic fingerprint for the different non-equilibrium phases, which can also be used to classify stationary phases of larger lattices, where the exact Liouvillian spectrum is no longer accessible.

Note, that by redefining the orientation of all spins on sublattice A, i.e., $S^z_a \to -S^z_a$, $S^+_a \to S^-_a$, our model can be mapped onto an XY model with only decay. This model has been studied, for example, in Ref. [16] using mean-field theory, where a so-called staggered XY phase with broken $U(1)$ symmetry has been predicted. Our current analysis shows that this phase is more accurately described by a PPT phase without symmetry breaking. This basic example already shows that the effects predicted here are relevant for a much broader class of non-equilibrium models, where such PT-symmetry breaking effects and phase transitions outside the usual framework must be taken into account.

4.5 Implementation

While the above analysis is primarily targeted at a conceptual understanding of non-equilibrium phase transition phenomena, we emphasize that the model in Eq. (4.2) can be implemented using existing experimental techniques. The basic idea is illustrated in Fig. 4.9(a) for a system of cold atoms coupled to multiple optical cavity modes. In this setting, each ensemble contains N_S atoms and is used to encode a collective spin $S = N_S/2$ degree of freedom using two stable atomic ground states $|0\rangle$ and $|1\rangle$, i.e., $S^+ = \sum_{i=1}^{N_S} |1\rangle_i\langle 0|$ and $S^z = \sum_{i=1}^{N_S}(|1\rangle_i\langle 1| - |0\rangle_i\langle 0|)/2$. These ground states are coupled via Raman processes involving the excited states $|e\rangle$ and $|f\rangle$ to three different cavity

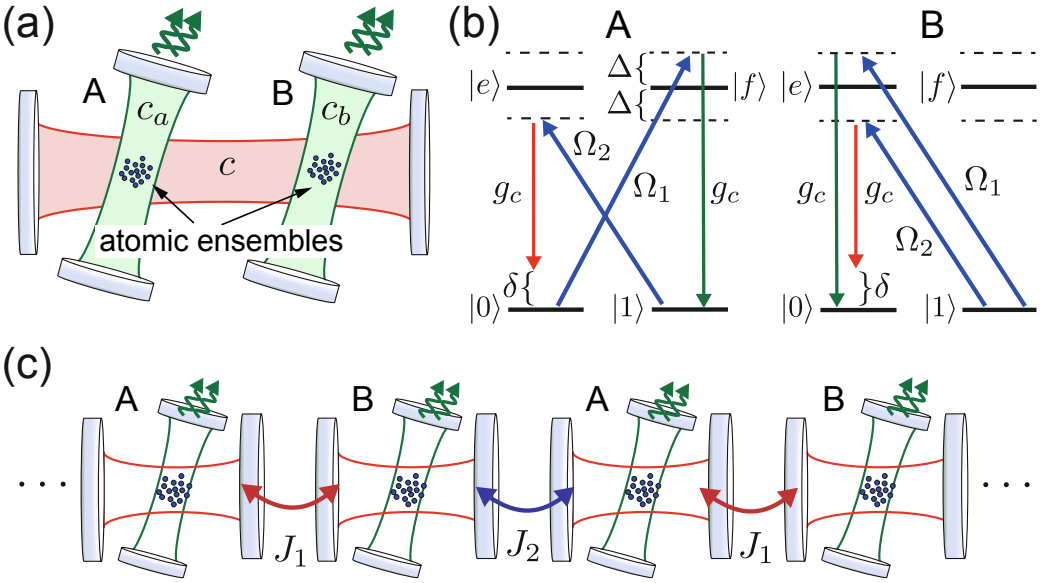

Figure 4.9: (a) Sketch of a setup for implementing a dissipative spin dimer with gain and loss. The collective cavity mode c is used to mediate coherent interactions between two spin ensembles. The other two cavity modes, c_a and c_b, are used to implement collective dissipation channels. (b) Energy level diagram and illustration of the relevant Raman-coupling schemes for realizing effective couplings between the cavity modes and collective spin excitations in the atomic ground states. (c) Generalization to a lattice of tunnel-coupled cavities for implementing the full 1D model considered in this work. See text for more details.

modes with annihilation operators c, c_a and c_b. The appropriate Raman processes are selected by the choice of detuning and polarization of classical driving fields and are proportional to the atom-cavity coupling strength g_c. For simplicity, we assume this coupling to be the same for all modes. For the transitions and detunings indicated in Fig. 4.9(b), the resulting effective Hamiltonian for the ground-state spins and the cavity mode is given by [32]

$$\begin{aligned} H_{\text{eff}} \simeq \hbar\delta c^\dagger c - \hbar G_c \left[\left(S_a^- + S_b^- \right) c^\dagger + c \left(S_a^+ + S_b^+ \right) \right] \\ + \hbar G \left(S_a^+ c_a^\dagger + c_a S_a^- \right) + \hbar G \left(S_b^- c_b^\dagger + c_b S_b^+ \right), \end{aligned} \tag{4.15}$$

where we have defined the Raman couplings $G = g_c\Omega_1/\Delta$ and $G_c = g_c\Omega_2/\Delta$ and $\Omega_{1,2}$ are the Rabi frequencies of the classical driving fields.

By also including the decay of the cavity modes with rates γ_c (for mode c) and γ (for modes c_a and c_b), the dynamics of the full system density operator ρ_{tot} is described by the master equation

$$\dot{\rho}_{\text{tot}} = -\frac{i}{\hbar}[H_{\text{eff}}, \rho_{\text{tot}}] + \frac{1}{2} \left(\gamma_c \mathcal{D}[c] + \gamma \mathcal{D}[c_a] + \gamma_L \mathcal{D}[c_b] \right) \rho_{\text{tot}}. \tag{4.16}$$

To proceed we now assume that (i) $|\delta| \gg \gamma_c, G_c$ and (ii) $\gamma \gg G$. Under these conditions, the coupling to the collective mode c mediates coherent spin-flip

interactions, while the resonant coupling to the lossy local modes generates a collective dissipation mechanism. Therefore, after adiabatically eliminating the fast dynamics of the cavity modes we obtain a reduced master equation for the state of the spins, $\rho = \mathrm{Tr}_{c,c_a,c_b}[\rho_{\mathrm{tot}}]$. By neglecting common Stark-shift terms for both ensembles, we obtain

$$\dot{\rho} \simeq -i[g\left(S_a^+ S_b^- + S_a^- S_b^+\right), \rho] + \Gamma_g \mathcal{D}[S_a^+] + \Gamma_l \mathcal{D}[S_b^-], \tag{4.17}$$

where $g = -G_c^2/\delta$ and $\Gamma_{g,l} = 2G^2/\gamma$. This is equivalent to the master equation (4.2) restricted to a single unit cell. To obtain the full 1D chain, the same schemes can be implemented in an array of coupled cavities, as depicted in Fig. 4.9(c), where the 'coherent' mode c from above is replaced by a whole band of the extended modes c_k of the coupled cavity array. As long as the photon-tunneling rates J_1 and J_2 are small compared to the detuning δ, we obtain approximately nearest-neighbor couplings with $g \simeq -J_1 G_c^2/\delta^2$, $h = -J_2 G_c^2/\delta^2$.

The described setting can be implemented, for example, using cold atoms in multi-mode optical cavities, similar to the experimental setups in Refs. [174–176]. To realize the full lattice model, one can extend the same techniques to arrays of photonic crystal cavities, as suggested for example in Refs. [177, 178]. The coupling of atoms to such nanophotonic structures is currently pursued in several experiments [179, 180]. In addition, equivalent Raman coupling schemes can be realized with ensembles of solid-state spin qubits, which are coupled magnetically to arrays of microwave resonators [181]. This also provides a promising approach for scalable implementations of large-S dissipative spin chains.

4.6 Conclusion

In this chapter, we studied the non-equilibrium properties of a spin chain in the presence of alternating gain and loss. We found that this system experiences phase transitions which are different from what we expected from equilibrium phase transitions. We identified a discontinuous phase transition without phase coexistence of the two distinct phases. Moreover, when simulating large lattices of spins we found long-range correlations at the critical point, however this phase transition was not accompanied by any symmetry breaking in the system. This shows that dissipative phase transitions can be very different from the usual framework of equilibrium systems and it still requires more investigations of critical dissipative systems to get a more complete framework of dissipative phase transitions.

5 PT-symmetry breaking in open quantum systems [‡].

"Ich verdiene soviel, ich kann mir deine Dissertation kaufen."

- Frei nach Marko Arnautovic

One of the fundamental axioms in quantum mechanics is that the Hamiltonian operators corresponding to the total energy of a system are Hermitian $H = H^\dagger$. This conventional Hermiticity condition is sufficient to ensure that the Hamiltonian H has a real spectrum. However, Bender and Boettcher found a new class of non-Hermitian Hamiltonians with a purely real energy spectrum and attributed this fact to the underlying combined PT (parity and time reversal) symmetry [47]. This opened a whole new field of PT-symmetric quantum theory, where the condition that the Hamiltonian is Hermitian is replaced by the weaker condition that it possesses invariance under space-time inversion (PT-symmetry) [48]. Although these are primarily mathematical considerations, there exist many classical systems with balanced gain and loss, whose dynamics can be mapped onto such PT-symmetric Hamiltonians [47, 49–52].

A classical PT-symmetric system in the simplest configuration consists of two coupled harmonic oscillators, where one experiences gain while the other one experiences an equal amount of loss. For such a gain-loss system the classical dynamics in rotating frame with respect to the oscillators frequency ω can be described by

$$\begin{pmatrix} \dot{\alpha} \\ \dot{\beta} \end{pmatrix} = \begin{pmatrix} \Gamma & -ig \\ -ig & -\Gamma \end{pmatrix} \begin{pmatrix} \alpha \\ \beta \end{pmatrix}, \tag{5.1}$$

where α and β are the classical amplitudes of the two systems, g the coupling strength between the two systems and Γ determines the strength of gain and loss. By comparing this equation with the Schrödinger equation $\dot{\psi} = -iH\psi$ for $\psi = (\alpha, \beta)^T$ one arrives at

$$H = \begin{pmatrix} i\Gamma & g \\ g & -i\Gamma \end{pmatrix}. \tag{5.2}$$

This non-Hermitian Hamiltonian is PT-symmetric. By applying time-reversal

[‡] This chapter is based on the article: J. Huber, P. Kirton, S. Rotter, and P. Rabl, Emergence of PT-symmetry breaking in open quantum systems, SciPost Phys. **9**, 052 (2020)

$\mathcal{T}(i \to -i)$ and parity transformation $\mathcal{P}$ $(\alpha \Leftrightarrow \beta)$, the equations do not change.

The eigenvalues and (unnormalized) eigenvectors of the Hamiltonian are

$$\lambda_{1,2} = \pm\sqrt{g^2 - \Gamma^2}, \tag{5.3}$$

and

$$\psi_1 = \begin{pmatrix} e^{i\frac{\theta}{2}} \\ e^{-i\frac{\theta}{2}} \end{pmatrix}, \qquad \psi_2 = \begin{pmatrix} ie^{-i\frac{\theta}{2}} \\ -ie^{i\frac{\theta}{2}} \end{pmatrix}, \tag{5.4}$$

respectively, where $\sin(\theta) = \Gamma/g$.

For $\Gamma < g$ both eigenvalues $\lambda_{1,2}$ are real. In this regime, the eigenvectors are eigenstates of the symmetry operator $\mathcal{PT}\psi_{1,2} = \psi_{1,2}$. For $\Gamma > g$, both eigenvalues become imaginary and correspond to a gain and a loss eigenmode. In this regime $\mathcal{PT}\psi_{1,2} \neq \psi_{1,2}$, i.e. the eigenvectors no longer have the same symmetry as the Hamiltonian. The PT-symmetry breaks at $\Gamma = g$.

Over the past years, this effect has attracted considerable attention and has been demonstrated in various optical [42–44], electrical [45] and mechanical [46] settings. In all these experimental works demonstrating PT-symmetry breaking the two modes are in a highly classical state and the dynamics can be described by classical physics. In this chapter, we will go beyond the classical picture and address an interesting and still open question: how is PT-symmetry defined in an open quantum systems and is there PT-symmetry breaking in the quantum regime?

Preliminary work in this direction was already done by Kepesidis et al. [55] by studying PT-symmetry breaking in the steady state of two coupled mechanical resonators with balanced gain and loss in the presence of thermal noise. Surprisingly, the breaking of the PT-symmetry can still be observed in this noisy environment and there is an unconventional transition from a high-noise symmetric thermal state to a low-amplitude lasing state with broken symmetry and strongly reduced fluctuations. However, this result was still based on a semi-classical approach and many important questions are still left open. For example, what happens in a full quantum description of this problem and are there any non-classical signatures or correlations associated with this symmetry-breaking transition?

In the last two chapters we have already studied open quantum systems with gain and loss. We found that in the limit of balanced gain and loss these models show different phases depending of the ratio between the dissipation strength and the coupling strength. However, it remains still unclear under which conditions can an open quantum system be considered as PT-symmetric and is there an analogues breaking of the symmetry associated by a change from a purely oscillatory behavior to a damped regime as in the classical case? Moreover, are there any quantum features such as entanglement seen in such systems?

In this chapter, we introduce for the first time a symmetry transformation for Liouville operators, which extends the conventional definition of PT

symmetry to arbitrary open quantum systems. We illustrate this on several examples and show the universality of this transition. Moreover, we investigate the dynamics as well as the spectrum of such Liouvillians.

5.1 PT-symmetric quantum systems

In order to find a definition of PT-symmetry for open quantum system, we consider a generic bipartite quantum system with a total Hamiltonian H. The two subsystems, A and B, have the same Hilbert space dimension, d, and they are subject to dissipation described by the local jump operators c_A and c_B, respectively. The master equation for the system density operator ρ can then be written as ($\hbar = 1$) [7]

$$\begin{aligned}\dot{\rho} &= -i[H,\rho] + \mathcal{D}[c_A]\rho + \mathcal{D}[c_B]\rho \\ &= -i\left(H_{\text{eff}}\rho - \rho H_{\text{eff}}^\dagger\right) + 2c_A\rho c_A^\dagger + 2c_B\rho c_B^\dagger \equiv \mathcal{L}\rho.\end{aligned} \tag{5.5}$$

Here $\mathcal{D}[c]\rho = 2c\rho c^\dagger - c^\dagger c\rho - \rho c^\dagger c$ and $\mathcal{L} \equiv \mathcal{L}[H; c_A, c_B]$ is the Liouvillian superoperator, which is specified, according to the first line in Eq. (5.5), in terms of the Hermitian Hamiltonian H and the two local jump operators c_A and c_B. As already shown in Chapter 2.1 the master equation can be rewritten in an evolution of a quantum state under the action of the effective non-Hermitian Hamiltonian

$$H_{\text{eff}} = H - ic_A^\dagger c_A - ic_B^\dagger c_B. \tag{5.6}$$

This term does not conserve the norm of the state and thus the recycling terms $\sim 2c\rho c^\dagger$ must be added to obtain a trace-preserving dynamics.

Given the decomposition of a master equation in Eq. (5.5), it is tempting to define PT-symmetric quantum systems in analogy to the classical case as explained at the beginning of this chapter, namely as open quantum systems where $(\mathcal{PT})H_{\text{eff}}(\mathcal{PT})^{-1} = H_{\text{eff}}$. Here $\mathcal{P}$ is the parity operator with $\mathcal{P}(A \otimes B)\mathcal{P}^{-1} = B \otimes A$ and $\mathcal{T}i\mathcal{T}^{-1} = -i$. However, H_{eff} has only negative imaginary parts because the norm of a state evolving under H_{eff} always decreases and this symmetry relation can only be satisfied in closed systems. The same is also true for the eigenvalues of the full Liouville operator $\mathcal{L}$ whose real part must always be negative or zero. Therefore, while according to Eq. (5.6) there is a natural way to introduce non-Hermitian Hamiltonians in open quantum systems and even probe them via conditional measurements [182–186], there are no PT-symmetric (super-)operators in the conventional sense. To overcome this problem, one could be less strict and only demand that the PT symmetry criterion applies to the resulting equations of motion for the expectation values of system operators. However, this identification is restricted to linear bosonic systems, where the quantum and classical dynamics of mean values are the same. For fermions, spins or other finite-dimensional quantum systems the same method is not applicable, as illustrated by a simple example in Appendix C.1. We conclude that none of

approaches used in the literature so far offers meaningful way to define PT symmetry for generic quantum systems.

To provide such a definition, it is important to keep in mind that the relevant physical effect of the $\mathcal{T}$-operator is to exchange loss and gain and not to implement a time-reversal transformation. While for classical systems both operations are equivalent and usually no distinction is made, this is no longer true for quantum systems. In the simplest example of a quantum harmonic oscillator the effect of loss with rate Γ is modeled by a jump operator $c = \sqrt{\Gamma}a$, where a is the annihilation operator. In turn, the effect of gain with the same rate can be described by modifying the jump operator to be $c = \sqrt{\Gamma}a^\dagger$. Therefore, in this case we find that the transformation between loss and gain is implemented in the master equation formalism by replacing the jump operator by its adjoint, $c \to c^\dagger$, and not by replacing i with $-i$ in any part of the master equation.

Guided by this explicit example, we introduce the following anti-unitary transformation for operators O,

$$\mathbb{PT}(O) = \mathcal{P}O^\dagger\mathcal{P}^{-1}, \tag{5.7}$$

and define an open quantum system to be PT-symmetric, if the corresponding Liouvillian satisfies

$$\mathcal{L}[\mathbb{PT}(H); \mathbb{PT}(c_A), \mathbb{PT}(c_B)] = \mathcal{L}[H; c_A, c_B]. \tag{5.8}$$

This condition implies that the Hamiltonian H is parity-symmetric and that the local jump operators are of the form

$$c_A = \sqrt{\Gamma}O \otimes \mathbb{1}, \qquad c_B = \sqrt{\Gamma}\mathbb{1} \otimes O^\dagger, \tag{5.9}$$

where O can be an arbitrary dimensionless operator.

Relation to other symmetries

Before we proceed with a discussion of the physical implications of Eq. (5.8), let us briefly comment on some related symmetries and classifications of open quantum systems. First of all, we remark that the definition given in Eq. (5.8) differs from the PT-symmetric Liouville operators introduced originally in Ref. [57] and analyzed for different spin models in Refs. [187–189]. In those systems, the eigenvalues of the Liouvillian exhibit a particular symmetry in terms of a cross-shaped pattern in the complex plane, which is broken at larger values of Γ. However, this property is rather specific and while the systems studied in Refs. [57, 187–189] satisfy Eq. (5.8) with a redefinition of $\mathcal{P}$, none of the examples discussed below exhibits the symmetry considered in these references when $d > 2$.

Moreover, there has been considerable interest in the classifications of the symmetries of non-Hermitian Hamiltonians [190–193] and Liouvillian [194, 195] lattice models for dissipative fermions. Connected to the classifications of non-Hermitian Hamiltonians, we emphasize that according to Eq. (5.7) the

$\mathbb{PT}$ map is applied to the Hermitian Hamiltonian H and the jump operators separately, i.e., the transformed Liouvillian is constructed as

$$\begin{aligned}\mathcal{L}[\mathbb{PT}(H);\mathbb{PT}(c_A),\mathbb{PT}(c_B)] = &-i[\mathbb{PT}(H),\rho] \\ &+\mathcal{D}[\mathbb{PT}(c_A)]\rho+\mathcal{D}[\mathbb{PT}(c_B)]\rho,\end{aligned} \tag{5.10}$$

which ensures that the whole transformation remains physically meaningful. This would not be the case when applying the same map to the non-Hermitian Hamiltonian H_{eff}, as defined in Eq. (5.6). As a result, the Hermitian adjoint operation $O \to O^\dagger$ in Eq. (5.7) is not related to a state transformation [194–196]. As the transformation is applied to the full operators H, c_A and c_B, rather than to individual operators, the symmetry introduced here is in general different from the well-known particle-hole symmetry. For example, consider a jump operator $c = a^\dagger a$, where a is a fermionic annihilation operator. Then, leaving parity aside, $\mathbb{PT}(a^\dagger a) = a^\dagger a \neq aa^\dagger$. While basic $\mathbb{PT}$-symmetric systems with linear jump operators, i.e., $c_A = a^\dagger$ and $c_B = a$, may exhibit a particle-hole symmetry as well (see, e.g., the example in Appendix C.1) this symmetry is not, per se, relevant for the physics discussed below.

5.2 Phenomenology

As a first step, let us illustrate the physical implications of Eq. (5.8) in terms of two simple examples as illustrated in Fig. 5.1: (i) Two coupled spin $S = (d-1)/2$ systems with $O = S^+$, where $S^+ = S^x + iS^y$ is the spin raising operator, and (ii) two coupled harmonic oscillators with $O = a^\dagger$. In the second example we introduce a finite cutoff occupation number, i.e., $a^\dagger|n = d-1\rangle = 0$. This cutoff mimics the effect of saturation in realistic systems [88] and allows us to vary the Hilbert space dimension. In both examples we consider a Hamiltonian of the form

$$H = g(O_A O_B^\dagger + O_A^\dagger O_B), \tag{5.11}$$

where $O_A = O \otimes \mathbb{1}$ and $O_B = \mathbb{1} \otimes O$. This Hamiltonian describes the coherent exchange of energy between the two subsystems with a strength g. The resulting Liouvillian, $\mathcal{L}[H; \sqrt{\Gamma}O_A, \sqrt{\Gamma}O_B^\dagger]$, then satisfies Eq. (5.8).

We calculate the steady state, ρ_0, satisfying $\mathcal{L}\rho_0 = 0$, for different ratios Γ/g and show in Fig. 5.1 the symmetry parameter [55]

$$\Delta = \frac{|\langle O_A^\dagger O_A - O_B^\dagger O_B\rangle|}{\langle O_A^\dagger O_A + O_B^\dagger O_B\rangle} \leq 1. \tag{5.12}$$

This is an experimentally observable quantity, which only requires the measurement of local operators, and provides a measure for the symmetry of the system, i.e., $\Delta = 0$ for a parity-symmetric density operator, $\mathcal{P}\rho\mathcal{P}^{-1} = \rho$. For the current examples, Δ represents the normalized population imbalance between the two subsystems. For small dimensions d, this parameter changes gradually from 0 to 1 with increasing Γ. This smooth variation is expected

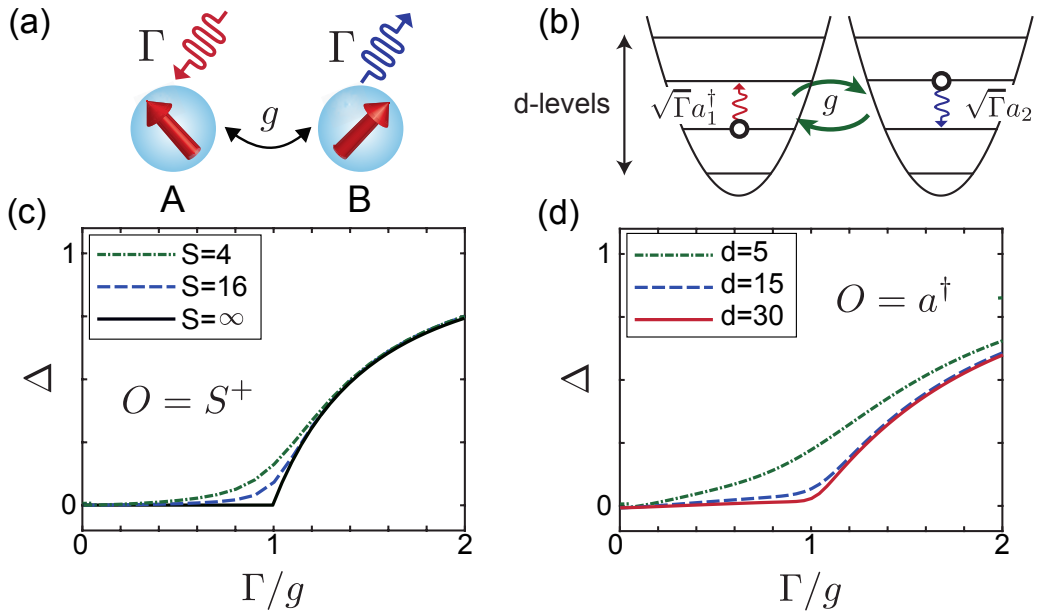

Figure 5.1: Two basic examples of PT-symmetric quantum systems with a finite Hilbert space dimension d: (a) two coupled spin $S = (d-1)/2$ systems and (b) two coupled harmonic oscillators with a finite number of energy levels. In (c) and (d) we plot the corresponding dependence of the symmetry parameter Δ defined in Eq. (5.12) on the ratio Γ/g. In (c) the line for $S = \infty$ is obtained from a Holstein-Primakoff approximation [see discussion of Eq. (5.24)].

since observables of finite dimensional quantum systems cannot exhibit any non-analytic behavior. However, as the system size increases, Δ vanishes for $\Gamma/g < 1$ in the limit $d \to \infty$, while it retains a finite value for $\Gamma/g > 1$. In both examples, the critical ratio is $\Gamma/g = 1$, which corresponds to the dynamical PT-symmetry breaking point of an equivalent linear oscillator system with gain and loss [51, 52]. We thus conclude that PT-symmetry breaking, i.e., a non-analytic transition between two steady states with different symmetries, exists even for non-harmonic and finite dimensional quantum systems, but only as an emergent phenomenon in the semiclassical limit.

To obtain better insights into the nature of the two phases, we plot in Fig. 5.2(a) the purity, $P = \mathrm{Tr}\{\rho_0^2\}$, for the steady state of the spin system. This quantity again exhibits a sharp transition around $\Gamma = g$ and shows that the symmetric and symmetry-broken phases are characterized by a highly mixed and an almost pure steady state, respectively. More precisely, the scaling $P(\Gamma \to 0) \simeq d^{-2}$ implies that in the symmetric phase the steady state is close to the maximally mixed state, $\rho_0(\Gamma \ll g) \simeq \mathbb{1}/d^2$. This indicates that for $\Gamma < g$ the gain and loss processes cancel out on average while quantum fluctuations still occur with rate Γ and completely randomize the system's long-time dynamics [55, 88]. In contrast, for $\Gamma > g$, the incoherent processes dominate and pump the spins into the polarised pure state, $\rho_0(\Gamma \gg g) \simeq |\psi_0\rangle\langle\psi_0|$, which satisfies $O_A|\psi_0\rangle = O_B^\dagger|\psi_0\rangle = 0$. Closer to the

transition point, the coherent coupling creates excitations $\sim O_A^\dagger O_B|\psi_0\rangle$ on top of this state, which are strongly correlated. As shown in Fig. 5.2(b), this results in a characteristic peak in the entanglement negativity $\mathcal{N}$ around the transition point, which is a measure of non-classical correlations between the two subsystems [164, 165]. These correlations vanish again in the symmetric phase due to fluctuations. Consistent with similar features observed in saturable oscillator systems [88], this peak in the entanglement shows that even for $d \gg 1$ the PT-symmetry breaking transition retains genuine quantum mechanical properties.

5.3 Existence of a fully symmetric steady state

We will now show that the properties discussed above for specific examples are indeed a general consequence of the symmetry relation in Eq. (5.8). Firstly, we demonstrate that, for any Liouvillian that satisfies this condition and where the spectrum of H is non-degenerate, the fully mixed state,

$$\rho_0(\Gamma \to 0^+) = \frac{\mathbb{1}}{d^2}, \tag{5.13}$$

is a stationary state of $\mathcal{L}$ in the limit of a vanishingly small, but finite Γ. To do so we decompose $\mathcal{L} = \mathcal{L}_H + \mathcal{L}_\Gamma$, where $\mathcal{L}_H\rho = -i[H,\rho]$ describes the coherent evolution and $\mathcal{L}_\Gamma\rho = \sum_{\eta=A,B}(2c_\eta\rho c_\eta^\dagger - c_\eta^\dagger c_\eta\rho - \rho c_\eta^\dagger c_\eta)$. As a starting point we write the density operator as

$$\rho = \sum_{n,m}\rho_{n,m}|E_n\rangle\langle E_m|, \tag{5.14}$$

where $|E_n\rangle$ are the energy eigenstates of H, i.e. $H|E_n\rangle = E_n|E_n\rangle$. From the PT-criterion in Eq. (5.8), we know that $[H,\mathcal{P}] = 0$, and hence we may simultaneously diagonalise the parity operator $\mathcal{P}|E_n\rangle = \zeta_n|E_n\rangle$, where $|\zeta_n|^2 = 1$ without loss of generality.

For $\Gamma = 0$ the fully mixed state, $\rho = \mathbb{1}/d^2$, is a stationary solution of the master equation $\dot\rho = \mathcal{L}_H\rho = -i[H,\rho]$, but this is also true for any other diagonal state. Therefore, we make the ansatz $\rho_{n,m} = \delta_{n,m}/d^2 + \delta\rho_{n,m}$ and evaluate the evolution of $\delta\rho_{n,m}$ up to first order in Γ [noting that $c_{A,B} \sim O(\sqrt{\Gamma})$],

$$\delta\dot\rho_{n,m} = -\frac{i}{\hbar}(E_n - E_m)\rho_{n,m} + \frac{2}{d^2}\langle E_n|[c_A, c_A^\dagger] + [c_B, c_B^\dagger]|E_m\rangle. \tag{5.15}$$

We first assume that $E_n \neq E_m$. In this case the elements $\rho_{n,m}$ represent coherences between non-degenerate eigenstates and we obtain

$$\delta\rho_{n,m}(t) \simeq -i\frac{2\hbar}{d^2(E_n - E_m)}\langle E_n|[c_A, c_A^\dagger] + [c_B, c_B^\dagger]|E_m\rangle \times \left(1 - e^{-i(E_n - E_m)t/\hbar}\right). \tag{5.16}$$

Therefore, to lowest order in Γ all these off-diagonal elements of the density matrix remain bounded and $|\delta\rho_{n,m}| \to 0$ for $\Gamma \to 0$.

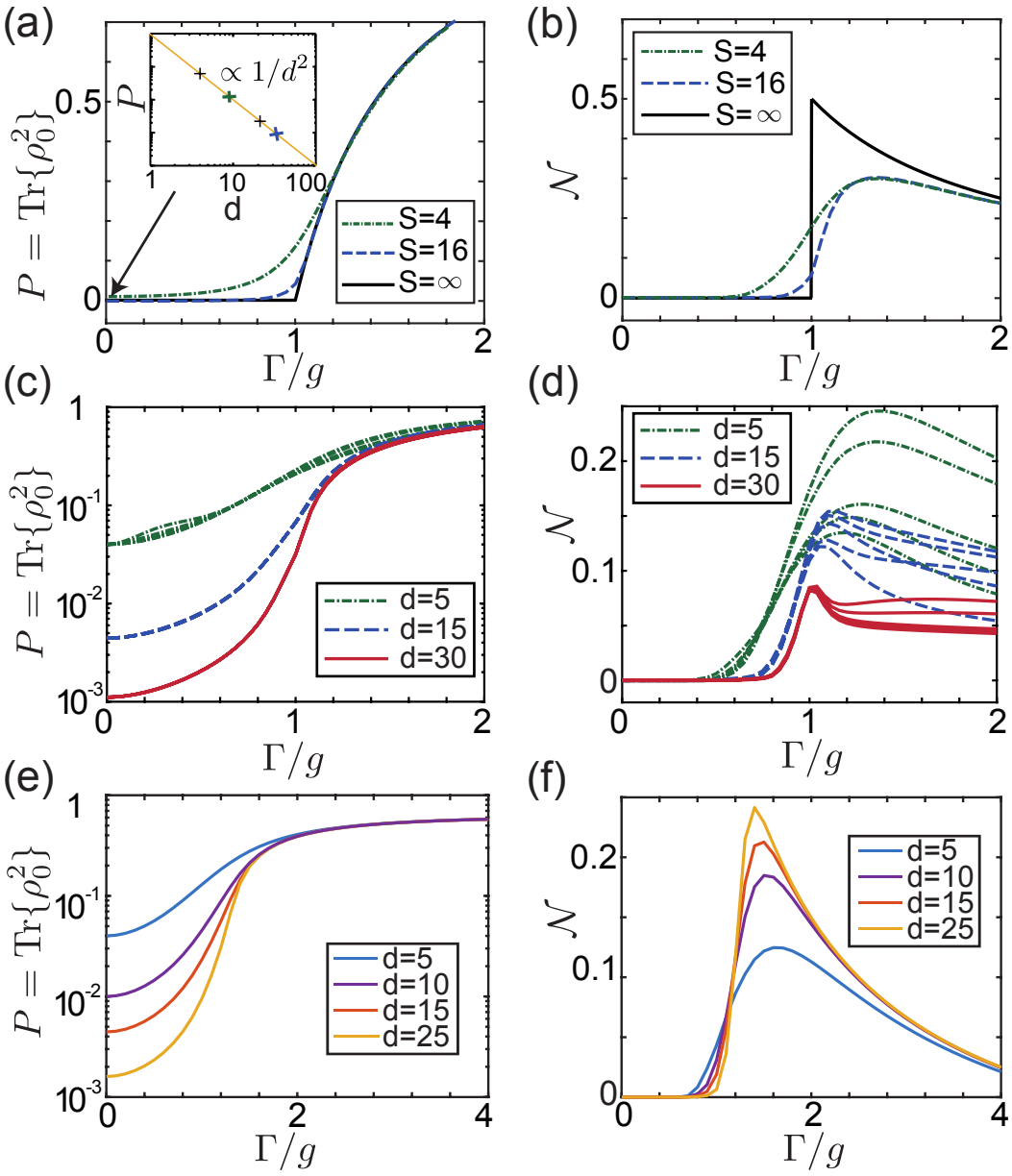

Figure 5.2: (a) Plot of the purity P of the steady state of a PT-symmetric spin dimer [see Fig. 5.1(a)] as a function of the dissipation rate and for different values of S. The inset shows that the purity satisfies $P \simeq 1/d^2$ for $\Gamma \ll g$. (b) Plot of the entanglement negativity $\mathcal{N}$ [164, 165] for the same model. In (c) and (d) the same quantities are plotted for PT-symmetric systems with random jump operators, as described in Section 5.4.1, and in (e) and (f) for the generalized spin model defined in Section 5.5.

For all other matrix elements with $E_n = E_m$ the coherent evolution vanishes and

$$\delta\dot{\rho}_{n,m} = \frac{2}{d^2}\langle E_n|[c_A, c_A^\dagger] + [c_B, c_B^\dagger]|E_m\rangle. \tag{5.17}$$

This results in a linear growth in time, unless the matrix element on the right-hand side is zero. We now make use of the relation

$$\mathcal{P}c_B\mathcal{P}^{-1} = c_A^\dagger, \tag{5.18}$$

which follows from the PT-symmetry relation for the Liouville operator. Based on this transformation we obtain

$$\begin{aligned}\langle E_n|[c_B, c_B^\dagger]|E_m\rangle &= \langle E_n|\mathcal{P}^{-1}\mathcal{P}[c_B, c_B^\dagger]\mathcal{P}^{-1}\mathcal{P}|E_m\rangle \\ &= \langle E_n|\mathcal{P}^{-1}[c_A^\dagger, c_A]\mathcal{P}|E_m\rangle \\ &= -\zeta_n^*\zeta_m\langle E_n|[c_A, c_A^\dagger]|E_m\rangle,\end{aligned} \tag{5.19}$$

and the evolution equation from above can be written as

$$\delta\dot{\rho}_{n,m} = \frac{2}{d^2}\langle E_n|[c_A, c_A^\dagger]|E_m\rangle\left(1 - \zeta_n^*\zeta_m\right). \tag{5.20}$$

In the case of a Hamiltonian H with a non-degenerate spectrum, Eq. (5.20) only applies to the populations $p_n = \rho_{n,n}$, in which case $|\zeta_n|^2 = 1$ and the right hand side vanishes.

This result shows that for PT-symmetric quantum systems the fully mixed state is stationary in the presence of a small amount of dissipation, even when each individual jump operator $c_{A,B}$ would drive the system into a polarized state.

A bit more care must be taken for Hamiltonians with degeneracies imposed by extra symmetries beyond that generated by $\mathcal{P}$. Even though the populations in a given basis still remain fixed, the build-up of coherences between degenerate levels leads to a deviation from the fully mixed state. If the Hamiltonian has a symmetry, $\mathcal{S}$, such that $[H, \mathcal{S}] = 0$, then the states generated by applying $\mathcal{S}$ to $|E_n\rangle$ are degenerate. From Eq. (5.20) we see that this leads to a non-identity steady state when two states $|E_n\rangle$ and $|E_m\rangle$ with the same energy have a different parity, $\zeta_n \neq \zeta_m$. However, if $[\mathcal{P}, \mathcal{S}] = 0$ then it is straightforward to see that $\zeta_n = \zeta_m$. Therefore, for the existence of a fully mixed symmetric phase it is in general not enough that $[H, \mathcal{P}] = 0$. In addition, we require that all other non-trivial symmetries of the Hamiltonian also commute with the parity operator, at least within each degenerate subspace. A simple example where such non-trivial symmetries play a role is the spin model described by the Hamiltonian

$$H = g(S_A^+ S_B^+ + S_A^- S_B^-) \tag{5.21}$$

and the PT-symmetric master equation

$$\dot{\rho} = -i[H, \rho] + \Gamma\mathcal{D}[S_A^-]\rho + \Gamma\mathcal{D}[S_B^+]\rho. \tag{5.22}$$

This model has a symmetry generated by $\mathcal{S} = S_A^z - S_B^z$ which does not commute with $\mathcal{P}$ and indeed one can show that the steady state for this model has spin-A pointing down and spin-B pointing up independent of the value of Γ/g.

5.4 Symmetry-breaking transition

While the existence of a fully symmetric steady state follows directly from Eq. (5.8), there are many trivial cases where this is also the only stationary state, for example, when O is Hermitian. Therefore, we are interested in systems where there is a competing asymmetric phase in the limit $\Gamma \to \infty$. To ensure that such a phase exists we now restrict ourselves to a Hamiltonian as given in Eq. (5.11) and a non-Hermitian jump operator of rank $d-1$ with $\mathrm{Tr}\{O\} = 0$. This implies that there are dark states $|D\rangle$ and $|D^*\rangle$, which satisfy $O|D\rangle = 0$ and $O^\dagger|D^*\rangle = 0$. Under these assumptions we obtain the symmetry-broken phase

$$\rho_0(\Gamma \to \infty) = |D\rangle\langle D| \otimes |D^*\rangle\langle D^*|, \tag{5.23}$$

which is fully asymmetric, $\Delta = 1$, and has maximal purity, $P = 1$. Note, however, that for observing symmetry-breaking effects it is not essential that $\rho_0(\Gamma \to \infty)$ is a pure state and, later in this manuscript, we discuss examples where the symmetry-broken state is mixed.

Given the two distinct limiting phases, the remaining question is, if there is a sharp phase transition between them at a critical intermediate value Γ_c. For the spin system discussed above this question can be rigorously answered in the limit $S \gg 1$ by examining the stability of linear fluctuations on top of the fully polarized state. This can be done using a Holstein-Primakoff approximation [197], where the spin operators are replaced by a pair of bosonic operators, $S_A^- \simeq \sqrt{2S}\, a^\dagger$, $S_A^+ \simeq \sqrt{2S}\, a$, $S_B^- \simeq \sqrt{2S}\, b$ and $S_B^+ \simeq \sqrt{2S}\, b^\dagger$, where $[a, a^\dagger] = [b, b^\dagger] = 1$. This approximate transformation brings the master equation into a quadratic form,

$$\dot{\rho} = -i[H_{\mathrm{lin}}, \rho] + \Gamma\mathcal{D}[a]\rho + \Gamma\mathcal{D}[b]\rho, \tag{5.24}$$

with Hamiltonian $H_{\mathrm{lin}} = g(ab + a^\dagger b^\dagger)$. From the analytic solution of this linearized model we find that the fluctuations $\langle a^\dagger a\rangle$ and $\langle b^\dagger b\rangle$ diverge at the point $\Gamma_c = g$. Explicitly, in terms of the original spin expectation values we obtain

$$\langle S^z_{A/B}\rangle_0 = \pm S \mp \frac{g^2}{2(\Gamma^2 - g^2)}. \tag{5.25}$$

Similarly, we can use well-known results for Gaussian states [198] and derive analytic expressions for the purity and the entanglement negativity,

$$P = 1 - \frac{g^2}{\Gamma^2}, \qquad \mathcal{N} = \frac{g}{2\Gamma}. \tag{5.26}$$

Detailed calculations can be found in Appendix B.1.s These predictions are shown as the curves labeled by $S \to \infty$ in Fig. 5.2(a)–(b). Within this Holstein-Primakoff approximation, the substantial amount of entanglement with a maximum of $\mathcal{N}(\Gamma = \Gamma_c) = 1/2$ at the transition point can be directly understood from the form of H_{lin}, which represents a two-mode squeezing interaction.

5.4.1 Random jump operators

In general, such an analytic treatment is not possible and, in many situations, PT-symmetry breaking can occur as a smooth crossover, rather than a sharp phase transition. Nevertheless, it turns out that the appearance of a sharp transition in the limit of large d does not require any specific fine tuning of the dissipation mechanism. This point is illustrated in Fig. 5.2(c)–(d), where we consider a set of PT-symmetric quantum systems with randomly generated jump operators O. For each individual line in this plot a random jump operator O has been constructed.

We use following procedure to construct the random jump operators: We first create a random matrix R from the Gaussian orthogonal ensemble (GOE), i.e., a symmetric matrix with real entries which follow a Gaussian distribution [199]. This matrix is then shifted by its lowest eigenvalue such that $R' = R - \lambda_0 \mathbb{1}$ is positive semidefinite with a guaranteed zero eigenvalue. This assures that dissipator has a single dark state, such that in the limit $\Gamma \to \infty$ the purity $P \to 1$. To obtain the jump operator O we then perform a Cholesky decomposition on the resulting matrix,

$$R' = OO^\dagger, \tag{5.27}$$

such that O is a lower triangular matrix. Since the Cholesky decomposition for positive semi-definite matrices is not unique, we implement this step by first diagonalizing the random matrix R',

$$R' = UDU^\dagger, \tag{5.28}$$

with U a unitary matrix and $D = \mathrm{diag}(0, \lambda_1, \ldots, \lambda_{d-1})$, a diagonal matrix where λ_n are non-zero eigenvalues. The diagonal matrix D can be decomposed as $D = LL^\dagger$, where only the first superdiagonal of $L^\dagger$ is non-zero with $(\sqrt{\lambda_1}, \sqrt{\lambda_2}, \ldots, \sqrt{\lambda_{d-1}})$. As a result the jump operator is

$$O = ULU^\dagger. \tag{5.29}$$

This procedure of constructing a random jump operator ensures that most of the resulting decay rates are $\mathcal{O}(1)$, due to the fact that the spacing between the eigenvalues of R will follow a Wigner surmise distribution $P(\Delta E) \sim \Delta E \exp(-A\Delta E^2)$ [199], meaning that there are very few almost degenerate states. This operator O is then used to obtain both the dissipative and coherent terms as in Eqs. (5.9) and (5.11).

By using this procedure to obtain the random jump operators we observe the characteristic transition between the fully mixed and pure states. Moreover, we find an asymmetric entanglement peak for each individual instance. These features sharpen as the Hilbert space dimension is increased. Therefore, this study demonstrates that sharp PT-symmetry breaking transitions are not restricted to systems with a direct classical counterpart and are expected to occur in a wide range of systems that obey Eq. (5.8).

Note that by enforcing $L^\dagger$ to only have non-vanishing elements in the first upper diagonal ensures that it is possible to observe the PT-symmetry breaking transition. This is not guaranteed in general. For example, by decomposing the diagonal matrix D in Eq. (5.28) in terms of two diagonal matrices $D = \sqrt{D}\sqrt{D}$, the resulting jump operator would be Hermitian and there would be no phase transition since the trivial identity state is always a steady state of such a model.

5.5 Generalizations

The symmetry defined in Eq. (5.8) and the proof of the fully mixed symmetric phase presented in Section 5.3 can be generalized in a straightforward manner to systems with multiple jump operators.

5.5.1 Phase transition between a positive and negative temperature reservoir

For example, we see the same symmetry-breaking effect in a spin system, with Hamiltonian as above, but considering two competing jump operators for each site,

$$c_A^{1,2} = \sqrt{\frac{1 \pm p}{2}} S_A^{\pm}, \qquad c_B^{1,2} = \sqrt{\frac{1 \mp p}{2}} S_B^{\pm}. \tag{5.30}$$

This model, $\mathcal{L}[H; \{\sqrt{\Gamma} c_A^{1,2}\}, \{\sqrt{\Gamma} c_B^{1,2}\}]$, represents two coupled spins, where one is coupled to a positive temperature reservoir with $N_{\text{th}} = \frac{1-p}{2p}$ and $\kappa = \Gamma p$ while the other is coupled to an equivalent negative temperature reservoir. While negative temperatures don't exist in our every day life, the effective temperature of an inverted spin system such as a laser medium can be negative. Crucially, this model still obeys the symmetry relation defined in Eq. (5.8). In Fig. 5.2(e)–(f) we plot the purity and entanglement negativity for this model with $p = 0.8$. Although in this case the symmetry-broken phase in the limit $\Gamma \to \infty$ is mixed and the transition is shifted to $\Gamma/g = 1/p$, all the signatures of PT-symmetry breaking described above are still clearly visible. This is very surprising as there wouldn't be any phase transition nor entanglement between two coupled spins connected to different thermal reservoirs with positive temperature. However, in the case where one of the two spins is coupled to a bath with negative temperature we can identify a phase transition as well as entanglement. By extending the Holstein-Primakoff approximation calculation of Section 5.4, we find entanglement for $p > 1/3$ or equivalently $N_{\text{th}} < 1$.

5.5.2 Unitary symmetries

Even more relevant is the fact that all the arguments presented above still apply to systems where parity is complemented by another unitary symmetry, $\mathcal{P} \to \mathcal{P}U$. For example, by choosing $U = e^{i\pi(S_A^x + S_B^x)}$ and a Hamilto-

nian $H = g(S_A^+ S_B^+ + S_A^- S_B^-)$, we obtain a PT-symmetric quantum system $\mathcal{L}[H; \sqrt{\Gamma} S_A^-, \sqrt{\Gamma} S_B^-]$. While this model contains only loss processes and the occupation numbers $\langle S_A^+ S_A^- \rangle = \langle S_B^+ S_B^- \rangle$ remain symmetric for all ratios of Γ/g, the Liouvillian respects the symmetry of Eq. (5.8) with a generalized anti-unitary map

$$\mathbb{PT}(O) = \mathcal{P} U O^\dagger (U\mathcal{P})^{-1}. \tag{5.31}$$

As a consequence one observes the same transition from a fully mixed to a low-entropy state, as in the spin model discussed above. The symmetry relation in Eq. (5.8) is thus a powerful tool to identify PT-symmetry breaking effects, even in systems where our naive intuition fails.

We have introduced the symmetry relation, Eq. (5.8), for Liouville operators, which extends the notion of PT symmetry to bipartite open quantum systems. This definition is consistent with previous examples of linear PT-symmetric quantum systems for which the conventional definition of PT symmetry is recovered in the limit of large oscillation amplitudes. At the same time the map, $\mathbb{PT}$, in Eq. (5.7) is completely general and can be used to define PT symmetry in highly nonlinear systems or for dissipation processes that have no direct classical counterpart.

5.6 Dynamics and exceptional points

In this chapter we have mainly focused on the steady state ρ_0 of PT symmetric quantum systems, which is determined for all parameters by the zero eigenvector of $\mathcal{L}$, i.e.$\mathcal{L}\rho_0 = 0$. In classical systems, PT-symmetry breaking is usually discussed in terms of a transition from purely oscillatory to exponentially damped or amplified dynamics, which is associated with the appearance of exceptional points in the eigenspectrum of the dynamical matrix. This has motivated similar studies of the appearance of exceptional points in the spectra of Liouville operators [200, 201]. While symmetries as introduced in Ref. [57] lead to remarkable patterns in the complex eigenvalues, which can be broken above a certain dissipation strength, such transitions are not necessarily associated with a qualitative change in the dynamics of physical observables. However, the symmetry relations we introduce here, such dynamical changes can be well observed. This can be see in Fig. 5.3, where we consider the example of two spin $S = 4$ systems, as shown in Fig. 5.1(a). The two plots show the full Liouville spectrum below and above the transition point in Fig. 5.3(a)–(b) and the associated dynamics in panels (c)–(d). For the two cases we don't observe any significant differences in the overall eigenvalue structure. Still the evolution of the observables $\langle S_{A,B}^z \rangle$ undergoes the classically expected change from an oscillatory to an overdamped behavior.

This final example confirms our previous conclusion, namely that PT-symmetry breaking is an emergent phenomenon in the dynamics and stationary expectation values of macroscopic observables, which, in general, depend little on individual eigenvalues of H_{eff} or $\mathcal{L}$. Based on the symmetry in Eq. (5.8), this effect can now be studied more systematically and used

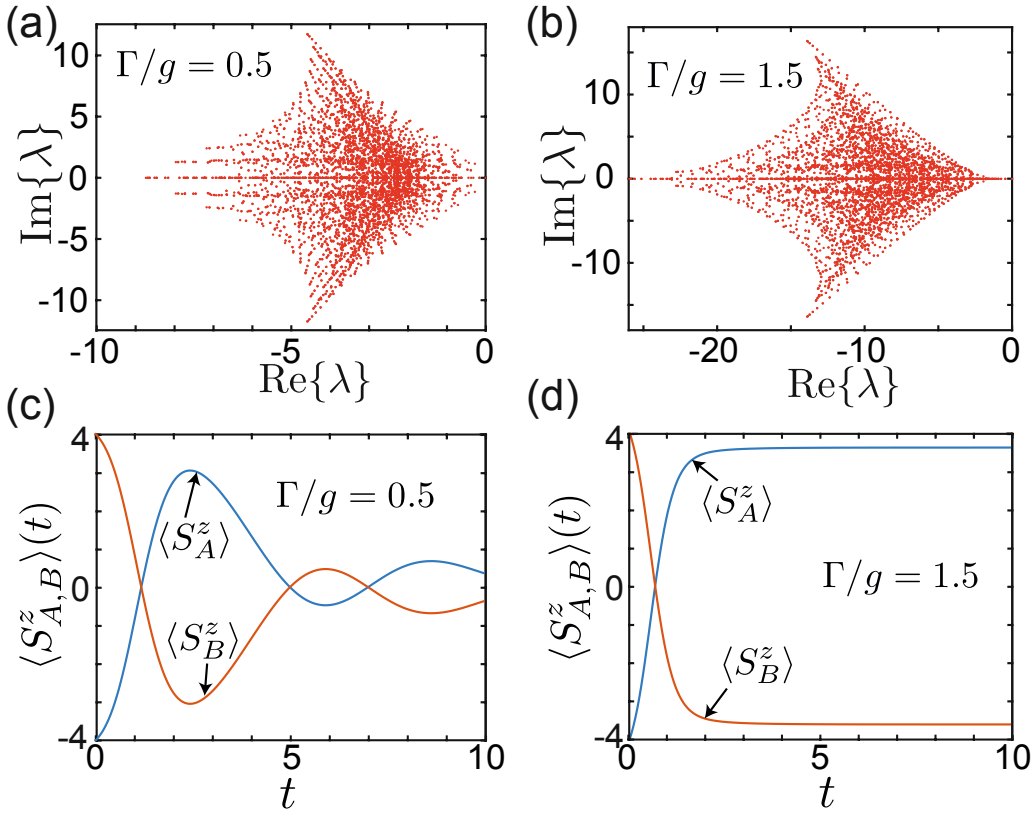

Figure 5.3: Plot of all complex eigenvalues λ_i of the Liouvillian $\mathcal{L}$ for the PT-symmetric spin system introduced in Fig. 5.1(a) with $S = 4$. In (a) the spectrum is shown below ($\Gamma/g = 0.5$) and in (b) above ($\Gamma/g = 1.5$) the transition point. For the same parameters, (c) and (d) show the corresponding time evolution of the observables $\langle S^z_{A,B} \rangle(t)$, starting from the initial state $\rho(t = 0) = |-S\rangle\langle -S| \otimes |S\rangle\langle S|$.

to make physically consistent predictions for real experiments. This will be important, for example, for trapped atoms [14], optomechanics [153] or circuit QED systems [154], where gain and loss but also much more complex dissipation processes can be engineered [10, 202]. A detailed description of an implementation with cold atoms can be found in Chapter 4.5.

5.7 Conclusion

In this chapter, we have introduced for the first time a symmetry relation for Liouville operators, which extends the PT-symmetry definition for classical systems to open quantum systems. Moreover, we proved that systems fulfilling this symmetry relation possess a symmetric phase and by increasing the dissipation strength this symmetry can be broken. In the thermodynamic limit, the competition between coherent dynamics and dissipation leads to a sharp phase transition between a symmetric and a symmetry broken regime in analogy to the classical transition. We illustrated these findings on sev-

eral examples such as two coupled collective spins and even for randomly generated systems. Moreover, we find that in this examples, the quantum phase transition features a highly entangled state at the symmetry breaking point. While the dynamics is crucially different in both regimes, we find that the overall eigenvalue structure of the Liouvillian hardly depends on the symmetry of the system.

6 Truncated Wigner method for open quantum spins §

Studying open quantum systems is particularly challenging as the Hilbert space scales with $(d^2)^N$, where d is the dimension of the subsystem and N the number of lattice sites (see Chapter 2.2). Exact simulations are therefore limited to very small system sizes and as a result there is still little know about dissipative phase transitions. In order to search for such unconventional non-equilibrium phase transitions, the development of new numerical techniques is of imminent relevance. For spin-1/2 systems there exist reliable tensor network methods to simulate dissipative many-body spin systems [37–39]. As simulations are already challenging for spin-1/2 systems, simulations in the limit of large collective spins $S \gg 1$ can not be performed by any of these methods. In this limit of $S \gg 1$, mean field theory, the classical description of the system, might give a proper description of the first order mean values for certain models, however it does not give any insight about the correlations of the system.

For bosonic systems there exist phase space methods such as the truncated Wigner approximation (TWA) [107], where an initial state distribution, which is sampled from a Wigner function of the initial state, is time evolved by the classical equations. As quantum fluctuations are included at all times, this usually gives substantially more accurate results and access to correlations. This has been sucessfully used to simulate dissipative weakly interacting bosonic lattice systems [203, 204] and non-equilibrium condensation phenomena [105, 106].

Another phase space representation for bosonic systems is the positive P-function (see Chapter 2.4). By mapping the spin systems to bosons via the Schwinger representation and using the positive P-function, the coherent dynamics of lattices of spin-1/2 systems [169, 170] and of collective spins [107] can be simulated. Moreover, this approach can be used to simulate the collective decay of an atomic ensemble [168]. However, these simulations were limited to short times as the corresponding stochastic trajectories tend to diverge after rather short times [97, 168–170].

In this chapter, we show how this problem can be overcome for systems with $S \gg 1$ by working with the Wigner function, but performing an additional positive diffusion approximation (PDA). As a result of this approximation, the stochastic equations in phase space are well-behaved for arbitrary times,

§ This chapter is based on the article: J. Huber, P. Kirton, and P. Rabl, Phase-Space Methods for Simulating the Dissipative Many-Body Dynamics of Collective Spin Systems, SciPost Phys. **10**, 045 (2021).

which allows us to evaluate the long-time dynamics and the steady states of dissipative spin systems that have been inaccessible so far. In Chapter 4 we have already used TWOQS to study unconventional phase transitions of large spin systems. In this chapter, we first give an outline of this method and explain how the original master equation can be mapped, under certain approximations, onto a set of stochastic differential equations. Furthermore, we benchmark this method by comparison to exact simulations of single spin systems as well as large spin lattices in the presence of dephasing and decay.

6.1 Outline of the method

We are interested in the open system dynamics of N coupled spin-S systems, which can be modeled by a master equation for the system density operator ρ,

$$\dot{\rho} = -i[H,\rho] + \sum_j \Gamma_j \mathcal{D}[c_j]\rho. \tag{6.1}$$

Here H is the many-body Hamiltonian describing the coherent evolution and the Lindblad superoperators, where $\mathcal{D}[c]\rho = 2c\rho c^\dagger - c^\dagger c\rho - \rho c^\dagger c$, account for incoherent processes with jump operators c_j and rates Γ_j. In the following we assume that H and all c_j can be written in terms of products of the collective spin operators S_i^z and $S_i^\pm = (S_i^x \pm iS_i^y)$, which obey the usual spin commutation relations, $[S_i^z, S_j^+] = \delta_{ij}S_i^+$ and $[S_i^+, S_j^-] = 2\delta_{ij}S_i^z$.

Equation (6.1) conserves the length of each individual spin, $\partial_t\langle\vec{S}_i^2\rangle = 0$, and therefore the dynamics of each subsystem can be restricted to a $d_S = (2S+1)$ dimensional subspace. However, the dimension of the full density operator, $d_\rho = (d_S)^{2N}$, still scales exponentially with the number of subsystems or lattices sites N. This scaling makes an exact numerical integration of Eq. (6.1) impossible when S or N are large. Here we introduce an approximate method to simulate such systems in the limit $S \gg 1$, which only scales linearly with the system size N. The derivation of this method consists of four main steps:

1. The N spins are mapped onto a set of $2N$ bosonic modes using the Schwinger boson representation.

2. The master equation for the bosons is mapped onto an equivalent partial differential equation for the Wigner phase-space distribution.

3. We use the TWA and the PDA to obtain a Fokker-Planck equation (FPE) for the Wigner function with an almost positive diffusion matrix.

4. This FPE is mapped onto an equivalent set of stochastic Ito equations, which can be efficiently simulated numerically.

In the following, we first give a brief general outline of the individual steps in this derivation, while the application of this method for concrete examples is discussed in more detail in Section 6.2.

6.1.1 Bosonization

In a first step, we use the Schwinger boson representation to map each of the spins, $\vec{S}_i$, onto two independent bosonic modes, a_i and b_i, by identifying

$$S_i^+ = a_i^\dagger b_i, \qquad S_i^- = a_i b_i^\dagger, \qquad S_i^z = \frac{1}{2}(a_i^\dagger a_i - b_i^\dagger b_i). \tag{6.2}$$

One can easily show that this transformation preserves all the spin commutation relations given above. For all models constructed from collective spin operators only, the total number of excitations at each site, $a_i^\dagger a_i + b_i^\dagger b_i$, is conserved. The initial condition can then be chosen such that

$$\frac{1}{2}(a_i^\dagger a_i + b_i^\dagger b_i) = S \tag{6.3}$$

to simulate spins of different lengths. This is more useful than mapping each site to a single Holstein-Primakoff boson [197], since the transformation above does not involve any operator square roots, which can be numerically difficult to work with.

6.1.2 Phase space distributions

The main advantage of switching to a representation expressed in terms of bosonic modes is that the master equation, Eq. (6.1), can be mapped onto an equivalent partial differential equation for a class of phase-space distributions, which contain the same information as the density operator (see Chapter 2.4 for details). We parameterize the set of distributions by the variable k and define

$$F_k(\vec{\alpha}, t) = \frac{1}{\pi^{4N}} \int d^{4N}\lambda \, e^{(\vec{\alpha}\vec{\lambda}^* - \vec{\alpha}^*\vec{\lambda})} \operatorname{Tr}\left\{ e^{\vec{\lambda}\vec{v}^\dagger} \rho e^{-\vec{\lambda}^*\vec{v}} \right\} e^{\frac{(1+k)}{2}|\vec{\lambda}|^2}, \tag{6.4}$$

where $\vec{v} = (a_1, b_1, a_2, b_2, \ldots, a_N, b_N)$ is a vector of all $2N$ bosonic operators and $\vec{\alpha}$ and $\vec{\lambda}$ are vectors containing the same amount of complex numbers. When $k = 0$ this phase space distribution corresponds to the Wigner function, for $k = 1$ it is the Glauber-Sudarshan P-representation and when $k = -1$ we obtain the Husimi Q-function. As explained in Chapter 2.4 in more detail, the master equation Eq. (6.1) can be mapped to a partial differential equation for the phase space distribution,

$$\frac{\partial}{\partial t} F_k(\vec{\alpha}, t) = L F_k(\vec{\alpha}, t), \tag{6.5}$$

with L some linear differential operator, which depends on the specific problem under consideration.

6.1.3 Truncated Wigner approximation

The result in Eq. (6.5) is still exact and therefore in general not very useful. In particular, the differential operator L may contain third- or higher-order

derivatives, which prevent an efficient stochastic sampling of F_k. For example, for the coherent dynamics generated by the master equation $\dot{\rho} = -i\Omega[S_x^2, \rho]$, the corresponding partial differential equation for $F_k \equiv F_k(\alpha, \beta, t)$ reads

$$\begin{aligned}\frac{\partial F_k}{\partial t} = \frac{i\Omega}{4}\Bigg[&\frac{\partial}{\partial\alpha}\left(2\alpha^*\beta^2 + 2\alpha|\beta|^2\right) + \frac{\partial}{\partial\beta}\left(2\beta^*\alpha^2 + 2|\alpha|^2\beta\right)\\ &\underline{- k\frac{\partial^2}{\partial\alpha^2}\beta^2} - \underline{k\frac{\partial^2}{\partial\beta^2}\alpha^2} - \underline{k\frac{\partial^2}{\partial\alpha\beta}\alpha\beta}\\ &+ \frac{1-k^2}{2}\left(\frac{\partial^3}{\partial\alpha\partial\alpha^*\partial\beta}\beta - \frac{\partial^3}{\partial\beta\partial\beta^*\partial\alpha}\alpha + \frac{\partial^3}{\partial\alpha^2\partial\beta}\beta^* - \frac{\partial^3}{\partial\alpha^*\partial\beta^2}\alpha\right)\\ &-c.c.\Bigg] F_k.\end{aligned} \tag{6.6}$$

To proceed we neglect all third- and higher-order derivatives, which in this example corresponds to omitting all terms in the second line of Eq. (6.6). This approximation is just the usual TWA [107] applied to arbitrary distribution functions. For spin systems we expect this approximation to become accurate in the limit of large S, since terms proportional to αF_k or βF_k scale as $\sim\sqrt{S}$ compared to derivatives such as $\partial F_k/\partial\alpha \sim \mathcal{O}(1)$. After performing the TWA we obtain a FPE of the form

$$\frac{\partial}{\partial t}F_k(\vec{x},t) = \left[-\frac{\partial}{\partial x_j}A_j(\vec{x}) + \frac{1}{2}\frac{\partial}{\partial x_i}\frac{\partial}{\partial x_j^*}D_{ij}(\vec{x})\right]F_k(\vec{x},t), \tag{6.7}$$

with a drift matrix A and a diffusion matrix D. Here we have assumed Einstein's sum convention, where the indices i and j run over the $4N$ components of the vector $\vec{x} = (\alpha_1, \alpha_1^*, \beta_1, \beta_1^*, \alpha_2, \alpha_2^*, \beta_2, \beta_2^*, \dots)$.

6.1.4 Positive diffusion approximation

For stochastic simulations, performing the TWA is not enough since in general the diffusion matrix D obtained in this way is not positive semi-definite. This can already be seen from the underlined terms in Eq. (6.6). Similarly, we find that an incoherent decay process, $\dot{\rho} = \Gamma\mathcal{D}[S^-]\rho$, is mapped under the TWA onto the FPE

$$\begin{aligned}\frac{\partial}{\partial t}F_k = \Gamma\Bigg[&\frac{\partial}{\partial\alpha}\left(|\beta|^2 + \frac{(1+k)}{2}\right)\alpha - \frac{\partial}{\partial\beta}\left(|\alpha|^2 - \frac{(1-k)}{2}\right)\beta - \underline{\frac{\partial^2}{\partial\alpha\partial\beta}\alpha\beta}\\ &+ \frac{(1-k)}{2}\frac{\partial^2}{\partial\alpha\partial\alpha^*}\left(|\beta|^2 + \frac{(1+k)}{2}\right)\\ &+ \frac{(1+k)}{2}\frac{\partial^2}{\partial\beta\partial\beta^*}\left(|\alpha|^2 - \frac{(1-k)}{2}\right) + c.c.\Bigg]F_k,\end{aligned} \tag{6.8}$$

and there are again second-order derivatives that can lead to negative diffusion rates. Thus, in a second step we perform a PDA by neglecting some of

these diffusion terms. In the two examples above this approximation amounts to omitting all the underlined terms in Eq. (6.6) and Eq. (6.8), while keeping the diffusion terms in the second and third line of Eq. (6.8). This choice cannot be justified by simple scaling arguments and in Section (6.2) we discuss and verify the applicability of this approximation in terms of several explicit examples. In general, the PDA can be motivated by the fact that it eliminates the dominating negative contributions to D, while conserving the total spin S and leaving the equations of motion for the mean values $\langle S_i^k \rangle$ unaffected. The price we pay for this last requirement is that for $k = 0$ the resulting diffusion matrix can become negative for certain values of α. However, the corrections scale as $\sim 1/S$ compared to other terms and for $S \gg 1$ the residual negative contributions do not affect considerably the stochastic sampling of trajectories in actual simulations.

Before we proceed let us remark that the problem of non-positivity can also be overcome by working with a positive-P representation, where α_i and α_i^* are replaced by a pair of independent complex variables [97, 168, 204]. In this case, a positive semi-definite diffusion matrix can be obtained for this larger set of variables without neglecting any terms. However, it is known that the resulting stochastic equations are often not well-behaved [97]. In particular, the appearance of "spikes", where individual trajectories diverge at a finite time [97, 169, 170], often prevents the simulation of the long-time behavior of a system or its steady state.

6.1.5 Stochastic simulations

After applying the TWA and the PDA, we end up with a FPE with an (almost) positive semi-definite diffusion matrix D. This FPE can be mapped onto an equivalent set of stochastic (Ito) differential equations (for details see Chapter 2.4),

$$dx_i = A_i(\vec{x})dt + B_{ij}(\vec{x})dW_j(t), \tag{6.9}$$

where dW_i are real-valued independent Wiener processes with $\langle dW_i dW_j \rangle = \delta_{ij} dt$ and $B(\vec{x})$ is the factorized diffusion matrix with $B(\vec{x})B(\vec{x})^\dagger = D(\vec{x})$. This set of equations can be efficiently simulated with the Euler-Maruyama method [108].

Initial conditions

In many situations of interest the initial state can be chosen as a fully polarized state with $\langle S_i^z \rangle = -S$ at each site. This corresponds to a state where one of the two Schwinger bosons is prepared in the vacuum state $|0\rangle$, the other one in the Fock state $|2S\rangle$. For $k = -1$ this state is described by the Q-function

$$Q_0(\alpha, \beta) = \frac{1}{\pi^2} e^{-(|\alpha|^2+|\beta|^2)} \frac{|\beta|^{4S}}{(2S)!}, \tag{6.10}$$

which is positive everywhere and can be used as an initial probability distribution for the trajectories. As already shown in Chapter 2.4 for $k = 1$ and

$k = 0$ the corresponding P- and Wigner distributions for Fock states are singular or have negative values. It is thus necessary to approximate the initial state by replacing the Fock state $|2S\rangle$ by a coherent state with the same mean amplitude. The corresponding initial conditions are then given by

$$P_0(\alpha, \beta) = \delta(\alpha)\delta(\beta - \sqrt{2S}), \tag{6.11}$$

and

$$W_0(\alpha, \beta) = \frac{4}{\pi^2} e^{-2(|\alpha|^2 + |\beta - \sqrt{2S}|^2)}, \tag{6.12}$$

respectively. This approximation introduces an uncertainty in the spin quantum number S, which, however, scales only with $\sqrt{S}$ and becomes negligible in the limit of interest, $S \gg 1$.

In order to initialize the system in an arbitrary spin coherent state $|\theta, \phi\rangle$ on the Bloch sphere we can simply rotate this state by the angle θ around the y-axis and ϕ around the z-axis. This amounts to replacing α and β by the rotated amplitudes

$$\tilde{\alpha} = e^{i\phi}(\cos(\theta/2)\alpha - \sin(\theta/2)\beta), \tag{6.13}$$
$$\tilde{\beta} = \sin(\theta/2)\alpha + \cos(\theta/2)\beta, \tag{6.14}$$

i.e., $W_{\theta,\phi}(\alpha, \beta) = W_0(\tilde{\alpha}, \tilde{\beta})$, etc.

6.1.6 P-, Q-, or Wigner distribution?

Up to now we have kept our analysis completely general and derived all the results for arbitrary distribution functions $F_k(\vec{\alpha})$. But which distribution works best in an actual simulation? It is well-known that the P-distribution ($k = 1$) cannot represent states with an uncertainty smaller than that of a coherent state. This includes, for example, squeezed states that appear commonly in interacting spin systems. The Q-distribution ($k = 1$) has the obvious advantage that it can represent spin states with a well-defined spin quantum number, i.e., there is no need to approximate the initial state. Further, as can be seen from Eq. (6.8), after the PDA the diffusion matrix for the Q-distribution is strictly positive semi-definite. However, it turns out that for models that include $(S^x)^2$ or similar interaction terms in the Hamiltonian, performing the PDA eliminates relevant contributions to the coherent dynamics. As can be seen from Eq. (6.6), this is not the case for the Wigner distribution ($k = 0$), since there are no second-order derivatives in the Hamiltonian dynamics and the PDA only affects incoherent processes. This is true for all quadratic coupling terms in the Hamiltonian $\sim S_i^\nu S_j^\mu$ ($\nu, \mu = z, \pm$), which already includes the most common types of spin-spin interactions. Therefore, while below we will also discuss several basic examples where the P- or the Q-distribution yield equally accurate results, we find that for generic interacting systems it is necessary to work with the Wigner function, which reproduces most accurately the Hamiltonian part of the dynamics.

6.2 Examples and applications

In this section we will present several explicit examples, to show how our method can be applied to simulate some of the most frequently encountered interactions and decoherence processes. To do so we will mainly focus on systems with a single collective spin, where all the results can still be compared with exact numerical results. This will allow us to test the validity of the approximations described above and make a comparison of how the different phase space representations perform under different circumstances. In Section 6.2.5 we will then extend these results and discuss the simulation of a whole chain of collective spins, for which exact numerical methods are no longer available.

6.2.1 Spontaneous emission

As a first example we consider the collective decay of a large ensemble of two-level systems, which can be described by the master equation

$$\dot{\rho} = \frac{\Gamma}{2S}\mathcal{D}[S^-]\rho. \tag{6.15}$$

Note that here we rescale the emission rate by a factor $2S$ in order to obtain the same time scale for the dynamics for different values of S. After performing the TWA the resulting FPE for this model is already given in Eq. (6.8) above. The PDA then corresponds to neglecting the underlined term in this equation, after which we can map the FPE onto the following set of stochastic Ito equations

$$d\alpha = \tfrac{-\Gamma}{2S}\left(|\beta|^2 + \tfrac{(1+k)}{2}\right)\alpha dt + \sqrt{\tfrac{\Gamma(1-k)}{4S}\left(|\beta|^2 + \tfrac{(1+k)}{2}\right)}dW_1, \tag{6.16}$$

$$d\beta = \tfrac{\Gamma}{2S}\left(|\alpha|^2 - \tfrac{(1-k)}{2}\right)\beta dt + \sqrt{\tfrac{\Gamma(1+k)}{4S}\left(|\alpha|^2 - \tfrac{(1-k)}{2}\right)}dW_2. \tag{6.17}$$

Here the $dW_n = dW_n^R + i dW_n^I$ are complex noise increment, where the dW_n^R and dW_n^I are real-valued and independent Wiener processes with $\langle dW_n^R dW_m^R\rangle = \langle dW_n^I dW_m^I\rangle = \delta_{nm}dt$.

In Fig. 6.1 we plot the outcome of a stochastic simulation of this coupled set of equations for $k = 0, \pm 1$ and for two different spin quantum numbers, $S = 10$ and $S = 100$. In these examples it is assumed that the spin is initially prepared in the maximally excited state with $S^z|S\rangle = S|S\rangle$, which we represent by initial distributions as given in Section 6.1.5. For the considered values of S we can also solve the full master equation exactly and use these results to benchmark our approximate approach. We find that for about $n_{\mathrm{traj}} = 1000$ trajectories the TWOQS reproduces very accurately the superradiant decay of a large ensemble, with higher accuracy for larger values of S. For this example we find almost no visible differences between the three different distribution functions. However, a closer inspection shows that in

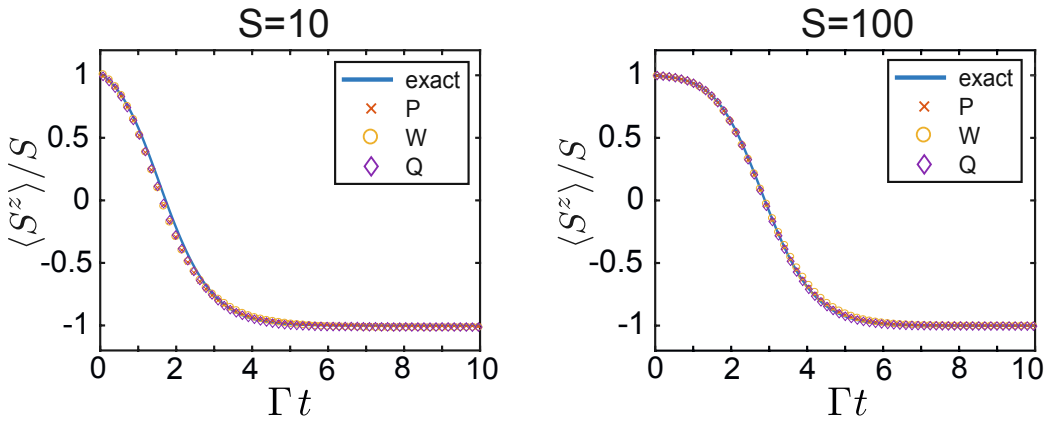

Figure 6.1: Simulation of the superradiant decay of a single collective spin with spin quantum number $S = 10$ and $S = 100$. The system is initially prepared in the highest excited state, $|S^z = S\rangle$. The stochastic simulations for the P-, Q- and Wigner-distribution are compared to the exact integration of the master equation, Eq. (6.15). In both plots $n_{\mathrm{traj}} = 1000$ trajectories have been simulated to compute the stochastic averages.

the case of the Wigner function ($k = 0$), the square root in Eq. (6.17) can become negative for some trajectories. This becomes a crucial problem for very small values of S and restricts stimulations to short integration times, since at longer times these unphysical trajectories can dominate the dynamics. For larger spins, this error is suppressed by $1/S$ and becomes a negligible effect for $S \gtrsim 100$, as shown in Fig. 6.1. In a simulation, possible errors arising from the negative diffusion term can be easily tracked by monitoring the change of the total spin, i.e., $\langle |\alpha|^2 + |\beta^2| \rangle$, over time.

This example illustrates that even for the Wigner function, residual negative diffusion terms are not a practical limitation for simulating dissipative processes in collective spin systems when S is large. Instead, when using the exact positive P-representation [168], the same simulation would be limited to times of about $t \lesssim \Gamma^{-1}$, before the appearance of spikes prevents any converging results. Note that the same conclusions also apply to master equations with a gain term, $\mathcal{D}[S^+]$, which can be described by simply exchanging the two bosonic modes, i.e., $\alpha \leftrightarrow \beta$ in Eqs. (6.16) and (6.17).

6.2.2 Dephasing

We now proceed with the derivation of the stochastic equations of motion for a collective spin which is subject to dephasing. In the absence of any other interactions, dephasing can be described by the master equation

$$\dot{\rho} = \Gamma_\phi \mathcal{D}[S^z]\rho. \tag{6.18}$$

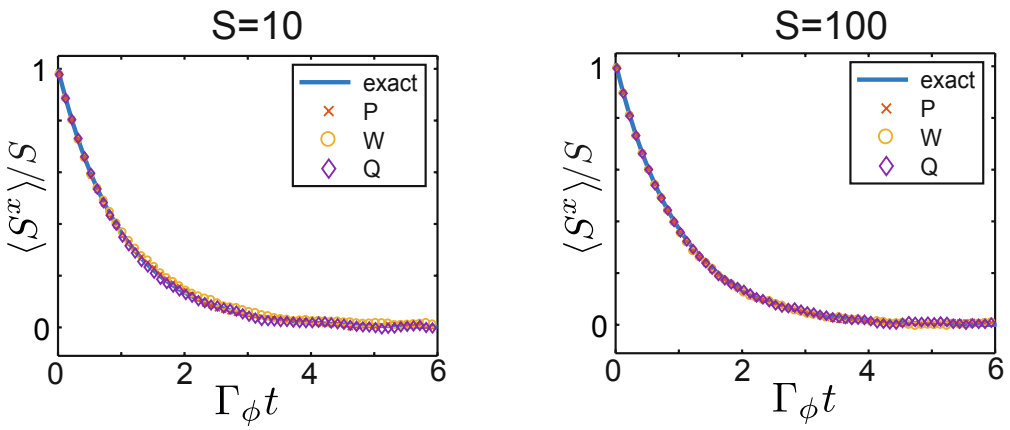

Figure 6.2: Dephasing of a collective spin as described by Eq. (6.18). For this plot, it is assumed that the system is initially prepared in a spin coherent state pointing along the x-direction, $|S^x = S\rangle$, and the successive evolution of $\langle S^x \rangle(t)$ is shown as a function of time. For this example the other two spin components vanish up to statistical errors. The exact results obtained from the full master equation are compared with stochastic simulations of Eq. (6.21) and Eq. (6.22) for $k = 0, \pm 1$. To obtain this data $n_{\mathrm{traj}} = 1000$ trajectories were simulated.

The bosonized form of this equation is obtained by substituting $S^z \to (a^\dagger a - b^\dagger b)/2$ and under the TWA the resulting FPE reads

$$\frac{\partial}{\partial t} F_k(\vec{\alpha}, t) = \frac{\Gamma_\phi}{4} \left\{ \frac{\partial}{\partial \alpha}\alpha + \frac{\partial}{\partial \beta}\beta - \frac{\partial^2}{\partial \alpha^2}\alpha^2 - \frac{\partial^2}{\partial \beta^2}\beta^2 + \frac{\partial^2}{\partial \alpha \partial \alpha^*}|\alpha|^2 \right. \\ \left. - \frac{\partial^2}{\partial \alpha \partial \beta}\alpha\beta + \frac{\partial^2}{\partial \alpha \partial \beta^*}\alpha\beta^* - \frac{\partial^2}{\partial \beta \partial \beta^*}|\beta|^2 + c.c. \right\} F_k(\vec{\alpha}, t). \quad (6.19)$$

Although also in this case there are second-order derivatives with negative prefactors, a straight-forward diagonalization of the diffusion matrix shows that $D(\alpha, \beta)$ is already positive semi-definite for all α and β. In this case the PDA is obsolete and we can factorize the diffusion matrix as $D(\alpha, \beta) = B(\alpha, \beta) B(\alpha, \beta)^\dagger$, where

$$B(\alpha, \beta) = \sqrt{\frac{\Gamma_\phi}{2}} \frac{i}{4} \begin{pmatrix} \alpha & -\alpha & \alpha & -\alpha \\ -\alpha^* & \alpha^* & -\alpha^* & \alpha^* \\ -\beta & \beta & -\beta & \beta \\ \beta^* & -\beta^* & \beta^* & -\beta^* \end{pmatrix}. \quad (6.20)$$

Note that this factorization is not unique, but with the current choice we obtain a very simple and symmetric form for the stochastic equations,

$$d\alpha = -\frac{\Gamma_\phi}{4}\alpha dt + i\sqrt{\frac{\Gamma_\phi}{2}}\alpha dW, \quad (6.21)$$

$$d\beta = -\frac{\Gamma_\phi}{4}\beta dt - i\sqrt{\frac{\Gamma_\phi}{2}}\beta dW, \quad (6.22)$$

where dW is a single real-valued Wiener processes. These equations are independent of k and there is no preferred phase space distribution to simulate dephasing. In the example plotted in Fig. 6.2, which shows the dephasing of a spin that is initially polarized along the x direction, the stochastic averages for all distributions agree within the statistical errors with the exact dynamics, keeping in mind that for $k = 1$ and $k = 0$ the initial distributions are only approximate.

6.2.3 Dynamics and steady states of driven spin systems

We now consider slightly more complicated models in which there is an interplay between coherent driving and incoherent decay. The simplest model in this class is that of a collective spin driven by a transverse field of strength Ω and including a collective decay with rate Γ. The corresponding master equations reads

$$\dot{\rho} = -i[H_D, \rho] + \frac{\Gamma}{2S}\mathcal{D}[S^-]\rho, \tag{6.23}$$

with a Hamiltonian $H_D = \Omega S_x$.

Transient dynamics

In Fig. 6.3 we show again a comparison between the TWOQS and the exact numerical simulations of this master equation for all three distribution functions and for the spin quantum numbers $S = 10$ and $S = 100$. For $S = 10$, we find clearly visible deviations from the exact oscillations, which can in part be traced back to the approximation we made in the initial condition (see Section 6.1.5). For this reason, sampling of the Q-function is most accurate in this situation. However, these deviations become negligible when we consider higher spins and already for $S = 100$ all distribution functions reproduce very precisely the exact spin dynamics over many oscillation periods.

Steady states

A specific interest in the model given in Eq. (6.23) arises from the fact that it exhibits a non-equilibrium phase transition at a driving strength of $\Omega = \Gamma$ [28, 29, 205]. At this point the steady state of this system changes from a spin coherent state on the lower half of the Bloch sphere to a highly mixed state with $\langle S_z \rangle = 0$.

From the analysis of coherent bosonic or spin systems it is known that the TWA often leads to inaccurate results for long simulation times [107]. The same problem is encountered when the TWOQS is used to simulate, for example, the oscillations shown in Fig. 6.3 for much longer times. However, the timescale beyond which significant errors occur increases with S and for many practical applications the system reaches a steady state before problems arise. This is demonstrated in Fig. 6.4, where we use our stochastic approach to simulate the master equation for a driven spin with $S = 1000$ up to a time $t = 50\Gamma^{-1}$. Note that for Eq. (6.23) there still exists an analytic solution for

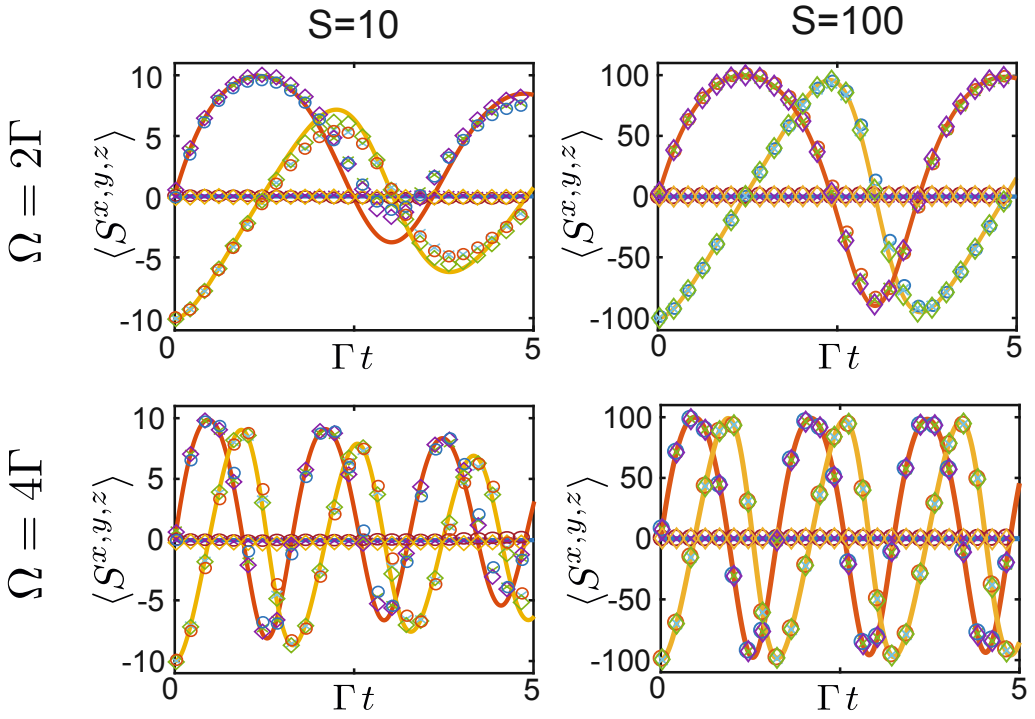

Figure 6.3: Time evolution of a driven collective spin in the presence of dissipation, as described by Eq. (6.23). The solid lines represent the exact dynamics of the spin expectation values $\langle S^z \rangle$ (yellow line), $\langle S^y \rangle$ (red line) and $\langle S^x \rangle$ (blue line), while the crosses, diamonds and circles are obtained from the stochastic sampling of the P-, the Q- and the Wigner-distribution, respectively. For this simulation, the system is initialized in the fully polarized state $|S^z = -S\rangle$.

the steady state [28, 29, 205], which allows us to compare these simulations with the exact results for the mean values and the fluctuations of the spin components.

In the polarized phase, $\Omega < \Gamma$, we find that both the mean values as well as the fluctuations of all spin components agree almost perfectly with the exact results. For the considered example of $S = 1000$ there are still some visible differences for the predicted spin fluctuations at and above the transition point, $\Omega/\Gamma = 1$. However, as shown in the inset of Fig. 6.4(a) the non-analyticity at the phase transition point becomes more pronounced and closer to the exact result by increasing the spin quantum number S. We emphasize that in the whole mixed phase, $\Omega/\Gamma \geq 1$, the Liouvillian gap of the considered model, i.e., the smallest decay rate in the problem, scales as $\sim 1/S$. This means that in the mixed phase this system is particularly challenging to simulate and oscillations around the steady state can persist for very long times. Nevertheless, we see that by simply approximating the steady state at a fixed time $t = 40\Gamma^{-1}$ by an average over a time span of $\Delta t = 10\Gamma^{-1}$, all the essential features of the model are already rather accurately reproduced. In particular, for $\Omega \gg \Gamma$, all the fluctuations are around $\langle (S^k)^2 \rangle \sim S^2/3$, indicating that the system is close to a fully mixed state. This and other

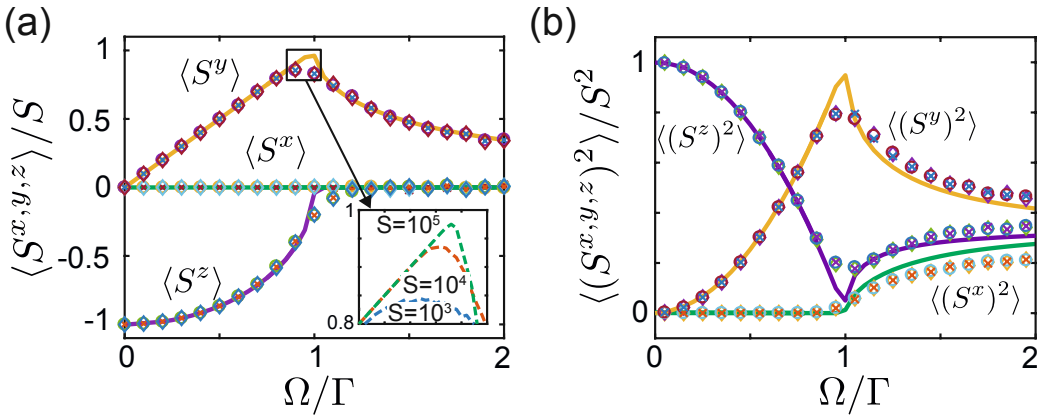

Figure 6.4: Simulation of the steady state of a driven spin system described by Eq. (6.23). The two plots show (a) the mean values and (b) the fluctuations of the three components of a spin with $S = 1000$. The solid lines are obtained from the exact solution for the steady state of this system [28, 29, 205], while the crosses, diamonds and circles are obtained from a stochastic sampling of the P-, the Q- and the Wigner-distribution. The inset in (a) shows the simulations of the Wigner distribution for even larger spin numbers S around the transition point $\Omega/\Gamma = 1$. The steady state was obtained by time averaging after $t = 40\Gamma^{-1}$ for another period of $\Delta t = 10\Gamma^{-1}$ and for $n_{\mathrm{traj}} = 2500$.

examples show that by using the TWOQS it is possible to access the steady states of driven-dissipative collective spin models.

6.2.4 Spin squeezing

Spin squeezing is an important non-classical effect in quantum metrology, which reduces the variance of one spin component below the value of $S/2$ obtained for $\mathcal{N}_{\mathrm{TLS}}$ independent two-level systems. In the presence of collective decay and dephasing, the effect of spin squeezing can be described by the master equation

$$\dot{\rho} = -i\frac{g}{2S}[S_x^2, \rho] + \frac{\Gamma}{2S}\mathcal{D}[S^-]\rho + \Gamma_\phi \mathcal{D}[S^z]\rho, \tag{6.24}$$

where the Hamiltonian term $\sim S_x^2$ has already been discussed as an example in Section 6.1. Therefore, under the TWA and the PDA we obtain the stochastic equations,

$$d\alpha = -i\frac{g}{4S}\left(\alpha^*\beta^2 + \alpha|\beta|^2\right)dt + d\alpha|_{\mathrm{decay}} + d\alpha|_{\mathrm{deph}}, \tag{6.25}$$

$$d\beta = -i\frac{g}{4S}\left(\beta^*\alpha^2 + |\alpha|^2\beta\right)dt + d\beta|_{\mathrm{decay}} + d\beta|_{\mathrm{deph}}, \tag{6.26}$$

where the last two terms in each line account for the decay and dephasing processes described by Eqs. (6.16)-(6.17) and Eqs. (6.21)-(6.22), respectively.

In Fig. 6.5, we use the approximate stochastic equations to simulate the spin squeezing parameter ξ as a function of time. For a state pointing in the

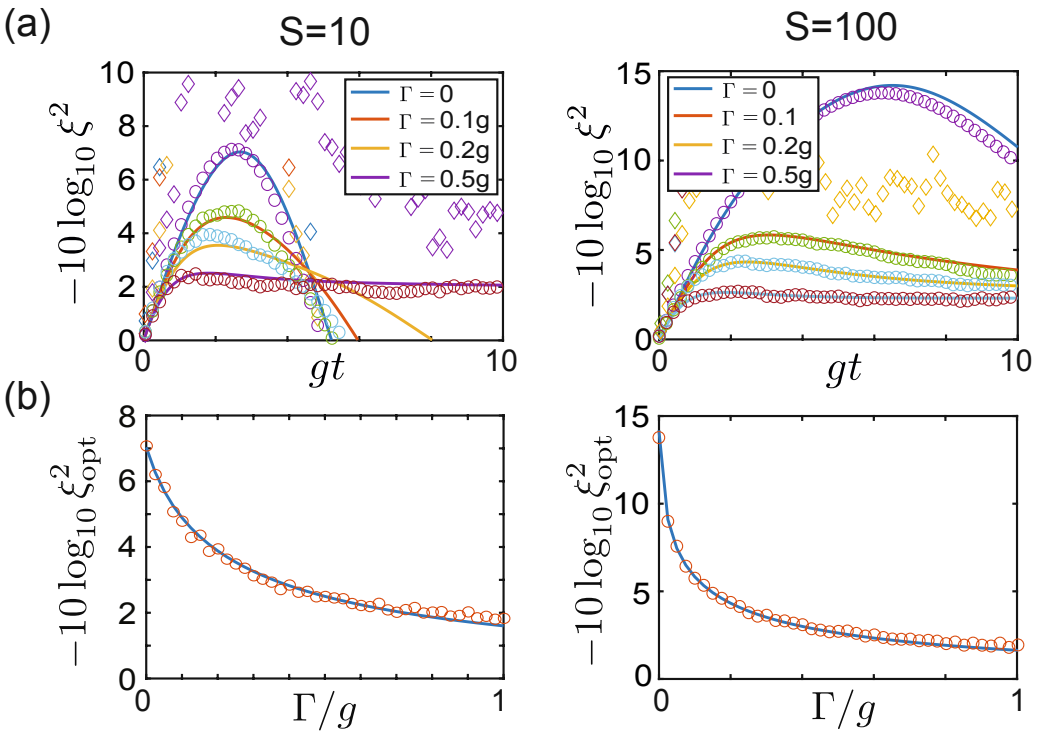

Figure 6.5: (a) Time evolution of the squeezing parameter ξ for different decay rates $\Gamma/g = 0, 0.125, 0.25, 0.5$ and for $S = 10$ and $S = 100$. (b) Maximum of the squeezing parameter $\xi_{\rm opt}$ as a function of the decay rate Γ. In all plots the solid lines represent the exact results, while the diamonds and circles have been obtained from a stochastic sampling of the Q- and Wigner distribution. The system is initialized in the state with all spins pointing down, $|S^z = -S\rangle$.

z-direction this parameter is defined as [206]

$$\xi^2 = \min_{\phi} \frac{2S(\Delta S^{\phi})^2}{|\langle S^z\rangle|^2}, \tag{6.27}$$

where $(\Delta S^{\phi})^2 = \langle (S^{\phi})^2\rangle - \langle S^{\phi}\rangle^2$ and $S^{\phi} = \cos(\phi)S^x + \sin(\phi)S^y$. Note that a squeezing parameter below unity, $\xi < 1$, requires a finite amount of entanglement between the two-level systems [207].

Compared to all the previous examples, we now see a clear difference between the results obtained for different distributions. For $k = 1$ the value of the squeezing parameter is $\xi \geq 1$ for all times, since squeezed states can only be represented by a non-positive P-distribution. Therefore, these results have not been included in Fig. 6.5. For the Q-distribution we obtain a finite amount of squeezing, but the predicted values for ξ do not match at all the exact results. This discrepancy can be traced back to the fact that in the PDA we neglect essential contributions to the coherent dynamics, which appear whenever there are spin-spin interactions. Therefore, in such cases neither the P- nor the Q-distribution give reliable predictions.

For simulations based on the Wigner function, we find very accurate results for ξ at short times, but considerable deviations from the exact behavior

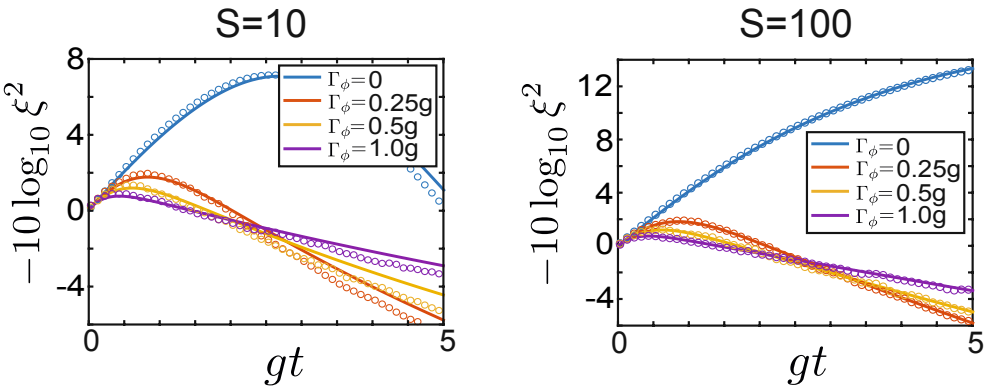

Figure 6.6: Time evolution of the squeezing parameter ξ for different dephasing rates $\Gamma_\phi/g = 0, 0.25, 0.5, 1.0$ and for $S = 10$ and $S = 100$. The solid lines represent the exact results, while circles have been obtained from a stochastic sampling of the Wigner distribution. The system is initialized in the state with all spins pointing down, $|S^z = -S\rangle$.

for longer simulations when Γ is small. This is consistent with the general observation that the TWA is not well suited to simulate coherent dynamics over longer times. However, these discrepancies are significantly reduced for larger dissipation rates and for larger spin quantum numbers. Importantly, Fig. 6.5 shows that already for $S = 100$ the dissipative evolution into an entangled quantum state with $\xi^2 \approx 0.05 - 0.5$ can be accurately simulated with our method. As further demonstrated in the lower two panels of Fig. 6.5, this level of accuracy is sufficient to predict optimal squeezing parameters in open quantum systems, as relevant for metrological applications. Very similar conclusions can be obtained from the investigation of squeezing in the presence of dephasing, as summarized in Fig. 6.6. In general we find that dephasing processes are more accurately captured by our method than decay.

6.2.5 Spin chains

In all the examples so far we have considered the dynamics of a single spin, where for $S \approx 100$ the full master equation can still be solved exactly. This is no longer possible for systems involving $N \gtrsim 2$ collective spins, while the TWOQS scales only linearly with N. This feature becomes highly relevant, for example, for the study of non-equilibrium magnetic phases in driven-dissipative spin chains. In this context, one typically considers generic Heisenberg models of the form [16, 18]

$$H = \sum_{i=1}^{N} \left(\tilde{J}_x S_i^x S_{i+1}^x + \tilde{J}_y S_i^y S_{i+1}^y + \tilde{J}_z S_i^z S_{i+1}^z \right), \tag{6.28}$$

where in addition each spin is subject to decay. Thus, the master equation for this system reads

$$\dot{\rho} = -i[H,\rho] + \sum_{i=1}^{N} \tilde{\Gamma}\mathcal{D}[S_i^-]\rho, \tag{6.29}$$

where $\tilde{J}_k = J_k/(2S)$ and $\tilde{\Gamma} = \Gamma/(2S)$ are the rescaled coupling strengths and the rescaled dissipation rate for general spin-S systems.

For $S = 1/2$, Eq. (6.29) can still be simulated for large 1D chains using numerical techniques based on matrix-product operators [18]. However, in this case one does not observe any sharp phase transitions for finite Γ, while the reliability and applicability of related techniques for 2D systems are still under investigation [130–132]. Both in 1D and 2D, such tensor network methods have very unfavorable scaling for larger S. The current method allows us to address the limit $S \gg 1$, where already in 1D distinct non-equilibrium phases and sharp transitions between them are expected. In Chapter 4, we have already applied this approach to study PT-symmetry breaking transitions in spin chains with both gain and loss, which can be mapped back onto a loss-only model with $\tilde{J}_x = -\tilde{J}_y$ and $\tilde{J}_z = 0$. Here we outline the implementation of this method for the general Heisenberg model in Eq. (6.28). Since we are dealing with in interacting spin system we must use the Wigner function, i.e., $k = 0$. After carrying out the general procedure described in Section 6.1 we obtain the stochastic equations

$$\begin{aligned} d\alpha_n = -\frac{i}{4}\Big[&(\tilde{J}_x+\tilde{J}_y)(\alpha_{n+1}\beta^*_{n+1}+\alpha_{n-1}\beta^*_{n-1})\beta_n \\ &+(\tilde{J}_x-\tilde{J}_y)(\alpha^*_{n+1}\beta_{n+1}+\alpha^*_{n-1}\beta_{n-1})\beta_n \\ &+\tilde{J}_z(|\alpha_{n+1}|^2-|\beta_{n+1}|^2+|\alpha_{n-1}|^2-|\beta_{n-1}|^2)\alpha_n\Big]\,dt + d\alpha|_{\text{decay}}, \end{aligned} \tag{6.30}$$

and

$$\begin{aligned} d\beta_n = -\frac{i}{4}\Big[&(\tilde{J}_x+\tilde{J}_y)(\alpha^*_{n+1}\beta_{n+1}+\alpha^*_{n-1}\beta_{n-1})\alpha_n \\ &+(\tilde{J}_x-\tilde{J}_y)(\alpha_{n+1}\beta^*_{n+1}+\alpha_{n-1}\beta^*_{n-1})\alpha_n \\ &+\tilde{J}_z(|\beta_{n+1}|^2-|\alpha_{n+1}|^2+|\beta_{n-1}|^2-|\alpha_{n-1}|^2)\alpha_n\Big]\,dt + d\beta|_{\text{decay}}. \end{aligned} \tag{6.31}$$

Depending on the relations between all the coupling parameters and the dissipation rate, the model in Eq. (6.28) exhibits many different stationary phases, which have been analyzed in Ref. [16] using mean-field theory. As a proof-of-concept demonstration of the TWOQS we consider here the case $J_z = 0$. Then for $J_x J_y > -\Gamma^2$ the steady state of the system is the fully polarized state along the z-direction and we can use a Holstein-Primakoff approximation to study the fluctuations around this state, similar to the analysis in [16, 90]. Beyond the transition point, e.g. for $J_x > 0$ and $J_y < -\Gamma^2/J_x$, we expect

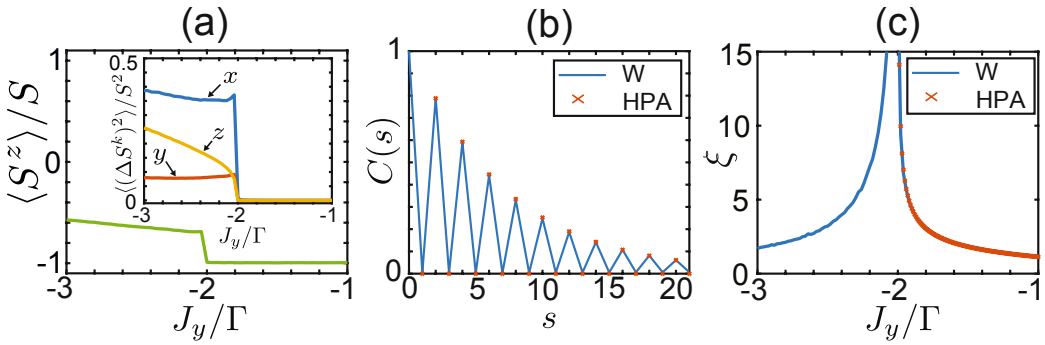

Figure 6.7: Stochastic simulation of the steady state of a dissipative Heisenberg chain as described by Eq. 6.29. (a) Magnetization $\langle S^z\rangle$ and variances $\langle(\Delta S^{x,y,z})^2\rangle$ as a function of J_y/Γ for a fixed value of $J_x = \Gamma/2$. (b) Plot of the spin-spin correlations $C(s) = \langle S_n^+ S_{n+s}^-\rangle/\langle S_n^+ S_n^-\rangle$ for a value of $J_y/\Gamma = -1.96$ near the phase transition point. (c) Plot of the correlation length ξ extracted from a fit of $C(s) = e^{-|s|/\xi}$ (for s even) as a function of J_y. In all plots the solid line represent the results obtained using the TWOQS and the crosses show the analytic predictions obtain from the Holstein-Primakoff approximation in the polarized phase. For the stochastic simulations we have assumed a chain of $N = 100$ sites with periodic boundary conditions and $S = 5000$.

a strongly mixed phase, but in this regime mean-field theory and linearization techniques are no longer applicable. In Fig. 6.7 we show the results of a stochastic simulation of a spin chain with $N = 100$ sites and $S = 5000$. This simulation confirms that in the limit of large S there is a non-equilibrium phase transition between a polarized and a highly mixed phase, even in 1D. At the transition point the mean value of $\langle S^z\rangle$ and the fluctuations of all spin components exhibit a sharp jump and spin-spin correlations along the chain diverge. In the polarized phase we can still use the Holstein-Primakoff approximation to benchmark the simulations also in this extended chain and we find almost perfect agreement. Importantly, the TWOQS also allows us to explore the non-polarized phase, where the strong fluctuations cannot be captured by a Holstein-Primakoff or mean-field approximation. While a detailed analysis of this phase is outside the scope of this work, we find many similarities with the pseudo PT-symmetric phase described in Chapter 4, where further discussions about its physical properties can be found.

6.3 Conclusion

In this chapter, we introduced a new method, the truncated Wigner approximation for open quantum spin (TWOQS). This method is based on the Schwinger boson representation and uses the truncated Wigner approximation and the positive diffusion approximation (PDA) to map a master equation to a set of stochastic differential equations. The PDA has to be performed to ensure the positivity of the diffusion terms. Although this seems

a very crude approximation, it does not affect the accuracy of actual simulations for large S and allows us to access the long-time dynamics of open spins systems. This was not possible using previous approaches based on the otherwise more accurate positive P-distribution. We have benchmarked this method on various spin models with dephasing and decay and showed that TWOQS is able to reproduce spin squeezing very accurately. We showed that even steady states can be reproduced very accurately and TWOQS is therefore very well suited to study dissipative phase transitions of large system as done in Chapter 4. Moreover, the method scales only linearly with the number of spins and there are no restriction on the dimensionality of the system. It will be therefore very interesting to extend the analysis of Chapter 4 to higher dimensional systems in the near future. Moreover, this method can be combined with existing TWA simulation techniques for bosonic systems to simulate Dicke-type models.

7 Dissipative discrete truncated Wigner approximation ¶

Recent advances in experiments with cold atoms [208–216], trapped ions [217–223], Rydberg atoms [224–230] or hybrid quantum systems [231–237] made it possible to engineer large spin systems. However, exact theoretical modeling is very challenging and while exact diagonalization is limited to very small spin numbers, time-dependent density matrix renormalization group (t-DMRG) methods become inefficient in higher dimensional systems (see Chapter 2.6). Due to imperfections of the system, all quantum systems are always subject to decoherence mechanisms, making a theoretical modeling even more difficult. It therefore requires new approximate methods to simulate large interacting spin systems in the presence of dephasing and decay.

In the previous chapter, we have already introduced the truncated Wigner method for open quantum spins (TWOQS), which gives very accurate results, however only in the limit of large spins $S \gg 1$. For spin-1/2 systems, one of the reason for the inaccuracies is that a Fock state has to be approximated by a coherent state in order to sample from a positive distribution (see Chapter 6.1.5). One way to overcome this problem is by the discrete truncated Wigner approximation (DTWA) [41], where the initial states are sampled from a discrete phase distribution. In this chapter, we take a similar approach as for TWOQS (see Chapter 6) and replace the classical equations of motion by stochastic equations in order to extend the DTWA to dissipative quantum systems (DDTWA). While existing numerical techniques often rely on certain symmetries and other idealizations, which do not represent the actual experimental situation, the DDTWA fully accounts for all types of inhomogeneities, dephasing and decay. In the following, we summarize the DTWA technique for simulating the coherent dynamics of interacting spin ensembles which we then extend to take dephasing and decay processes into account. Furthermore, we benchmark the method in terms of a few basic examples, for which exact solutions still exist.

¶ This chapter is based on the article: J. Huber, A. M. Rey, and P. Rabl, Realistic simulations of spin squeezing and cooperative coupling effects in large ensembles of interacting two-level systems, arXiv:2105.00004 (2021).

7.1 Discrete truncated Wigner approximation

We are interested in the time evolution of interacting spin ensembles and cavity QED setups with $N \gg 1$ effective spin-1/2 systems. For concreteness we will first focus on pure spin systems described by a Hamiltonian of the form ($\hbar = 1$)

$$H = \frac{1}{2}\sum_{i=1}^{N} \vec{\Omega} \cdot \vec{\sigma}_i + \frac{1}{2}\sum_{i \neq j}^{N} \vec{\sigma}_i^T \mathbf{J}_{ij} \vec{\sigma}_j. \tag{7.1}$$

Here $\vec{\sigma} = (\sigma^x, \sigma^y, \sigma^z)^T$, where the σ^k are the usual Pauli operators, and $\vec{\Omega}$ and $\mathbf{J}_{ij}$ are the local field and the spin-spin interaction matrix, respectively. Later below we will also consider additional couplings of the spin ensemble to a common bosonic mode, as encountered in cavity QED. Even without the bosonic mode, the spins evolving under the action of H will in general get entangled over time and exact numerical simulations of the full quantum state of the system is only possible for a few tens of spins.

In Ref. [41] the DTWA was introduced as an approximate numerical method to simulate the coherent dynamics of interacting spin systems. In the following, we will first discuss the truncated Wigner approximation for continuous degrees of freedom and then discuss the discrete truncated Wigner approximation. As already discussed in Chapter 2.4, the regular Wigner function for a continuous degree of freedom is defined the following way

$$W(x,p) = \frac{1}{h}\int e^{-ipy} \langle x + y/2 | \hat{\rho} | x - y/2 \rangle dy. \tag{7.2}$$

To calculate the time evolution of the expectation value of an operator $\hat{O}$, it's Weyl transformed operator $\tilde{O}(x,p)$ is integrated over the whole phase space,

$$\langle \hat{O}(t) \rangle = \int\int dx dp \tilde{O}(x,p) W(x,p,t). \tag{7.3}$$

Here

$$\tilde{O}(x,p) = \int e^{-ipy} \langle x + y/2 | \hat{O} | x - y/2 \rangle dy, \tag{7.4}$$

through which an operator $\hat{O}$ is mapped to a function $\tilde{O}(x,p)$ of x and p. For larger systems, it is in general not possible to calculate Eq. (7.3) exactly, since the time-evolved Wigner function is not known. However, the TWA approximates the dynamics by only taking the first-order quantum fluctuations into account. In the Heisenberg picture the Wigner distribution is fixed to its initial state $W(x,p) \to W(x_0,p_0)$, and the Weyl operator evolves in time. The TWA makes the approximation that the Weyl operator follows a classical evolution $\tilde{O}(x,p)(t) \to \tilde{O}(x_{cl}(t), p_{cl}(t))$, where $x_{cl}(t)$ and $p_{cl}(t)$ are the classical equations of motion. Thus, we find,

$$\langle O(t) \rangle \approx \int\int dx_0 dp_0 \tilde{O}(x_{cl}(t), p_{cl}(t)) W(x_0, p_0). \tag{7.5}$$

In the case of the discrete truncated Wigner approximation integrals are replaced by sums. A density matrix $\hat{\rho}$ can be expressed as a discrete distribution w_α with

$$\hat{\rho} = \sum_\alpha w_\alpha \hat{A}_\alpha \tag{7.6}$$

where

$$w_\alpha = \frac{1}{2}\mathrm{tr}(\hat{\rho} A_\alpha). \tag{7.7}$$

While there are many basis choices for A_α, we choose the following parametrization for a spin-1/2 particle

$$\hat{A}_\alpha = \frac{(1 + \vec{r}_\alpha \cdot \vec{\sigma})}{2}, \tag{7.8}$$

with

$$\begin{aligned} &\vec{r}_1 = (1,1,1)^T, \quad &&\vec{r}_2 = (-1,-1,1)^T, \quad &&\vec{r}_3 = (1,-1,-1)^T, \\ &\vec{r}_4 = (-1,1,-1)^T, \quad &&\vec{r}_{5-8} = -\vec{r}_{1-4}, \end{aligned} \tag{7.9}$$

where the phase space of each spin consists of eight points. By using this discrete basis of operators, any operator can be Weyl transformed back and forth the following way

$$O^W_\alpha = \mathrm{tr}(\hat{O}\hat{A}_\alpha)/2, \quad \text{and} \quad \hat{O} = \sum_\alpha \hat{A}_\alpha O^W_\alpha. \tag{7.10}$$

Equivalently to the continuous case we can make the approximation that the Weyl operator follows a classical evolution as done in Eq. (7.5). Thus, we find,

$$\langle \hat{O(t)} \rangle = \sum_\alpha w_\alpha(0) O^W_\alpha(t) \approx \sum_\alpha w_\alpha(0) O^{W,cl}_\alpha(t), \tag{7.11}$$

where $w_\alpha(0)$ is the initial Wigner function on the discrete phase space and $O^{W,cl}_\alpha$ is the classically evolved Weyl symbol.

The basic principle of the TWA and the DTWA can be explained in the following way. By time evolving different initial states with the mean-field equations, quantum uncertainties are included as the initial states are randomly drawn from a probability distribution that accounts for the correct quantum mechanical uncertainties. A DTWA simulation can be therefore summarized as follows [see Fig. 7.1(a)]:

1. Draw n_t random initial states from the discrete Wigner distribution $W_D(\{\vec{s}_i\})$ [238]. A single spin pointing down $|\downarrow\rangle$ is represented by following discrete Wigner function

$$\begin{aligned} W_D(\vec{s}_i) = \frac{1}{4}\delta(s_i^z + 1)\left(\delta(s_i^x + 1) + \delta(s_i^x - 1)\right) \\ \times\left(\delta(s_i^y + 1) + \delta(s_i^y - 1)\right) \end{aligned} \tag{7.12}$$

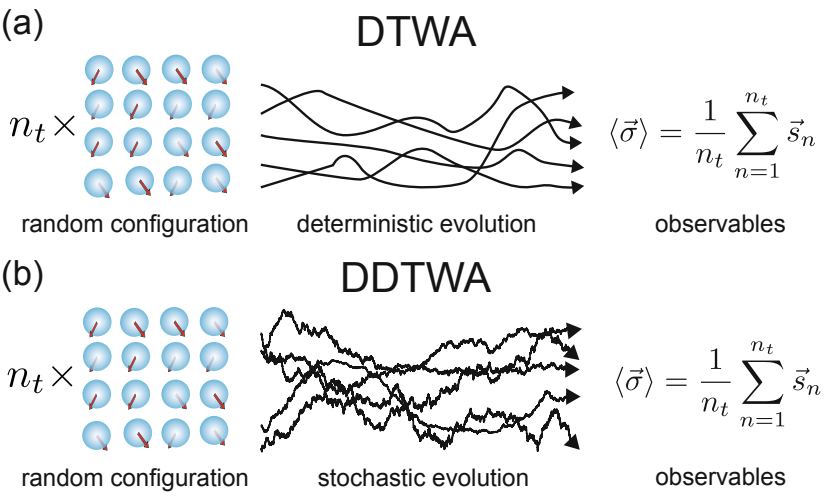

Figure 7.1: Illustration of (a) the DTWA algorithm [41] for coherent spin systems and (b) the DDTWA algorithm introduced in this work for open quantum spin systems. See text for more details.

where we find four discrete spin configurations

$$(s_i^x, s_i^y, s_i^z) = (\pm 1, \pm 1, -1) \tag{7.13}$$

which occur with the same probability of $W_D = 1/4$. By rotating the state, all states of the Bloch sphere can be represented and by an additional statistical mixture of different states, all density matrices can be represented.

2. The time evolve all n_t configurations with the mean-field equations. For the Hamiltonian Eq. (7.1) we arrive at following mean-field equations

$$\frac{d\vec{s}_i}{dt} = \vec{\Omega}_{\text{eff}}^i \times \vec{s}_i, \qquad \vec{\Omega}_{\text{eff}}^i = \vec{\Omega} + 2 \sum_{j=1}^{N} \mathbf{J}_{ij} \vec{s}_j. \tag{7.14}$$

3. Calculate expectation values of spin observables from the average over all trajectories as

$$\langle \sigma_i^k \rangle (t) \simeq \frac{1}{n_t} \sum_{n=1}^{n_t} s_{i,n}^k(t), \tag{7.15}$$

and

$$\langle \{\sigma_i^k, \sigma_j^l\}_{\text{sym}} \rangle (t) \simeq \frac{1}{n_t} \sum_{n=1}^{n_t} s_{i,n}^k(t) s_{j,n}^l(t). \tag{7.16}$$

We immediately see that by averaging over the four configurations of Eq. (7.13) all expectation values of the state of a spin pointing down $|\downarrow\rangle$ are reproduced correctly.

The number of stochastic equations scales only linearly with N and therefore allows one to simulate the time evolution of thousands of spins. At the

same time, the quantum mechanical uncertainties of the initial state are fully included by averaging over a distribution of initial spin vectors and in general $\langle \sigma_i^k \sigma_j^\ell \rangle \neq \langle \sigma_i^k \rangle \langle \sigma_j^\ell \rangle$. In particular, since the mean-field equations, Eq. (7.14), preserve the length of each individual spin, $\vec{s}_i^2(t) = 3$, its magnitude is equal to the exact quantum mechanical value along each individual trajectory. This means that compared to mean-field theory, the effect of spin-spin interactions, which scale as $\sim |\vec{s}_i(t)||\vec{s}_j(t)|$, are more accurately taken into account leading to very precise results in many situations of interest, for example, in spin-squeezing experiments with trapped ions or cold atoms. A more detailed discussion of the DTWA and many explicit examples can found in Refs. [41, 239–242].

Note by sampling from the Wigner distribution of a coherent state

$$W(\vec{s}_i) = \frac{2}{\pi} e^{-2((s_i^x)^2+(s_i^y)^2)} \delta(s_i^z + 1), \tag{7.17}$$

instead of the discrete distribution of Eq. (7.12), we perform a TWA simulation [107]. While we focus here on the DTWA, all the results below can be also applied to do a TWA simulation.

7.2 Dissipative discrete truncated Wigner approximation

In real experiments the spins or atoms are never completely isolated and will spontaneously decay or undergo dephasing due to residual interactions with the environment. Such an open system scenario can be modeled by a master equation for the system density operator ρ,

$$\dot{\rho} = -i[H, \rho] + \mathcal{L}_{\text{deph}}(\rho) + \mathcal{L}_{\text{decay}}(\rho). \tag{7.18}$$

Here, the first correction to the Hamiltonian evolution accounts for pure dephasing, where for the case of uncorrelated dephasing of each spin with rate Γ_ϕ we obtain

$$\mathcal{L}_{\text{deph}}(\rho) = \frac{\Gamma_\phi}{2} \sum_{i=1}^{N} \left(\sigma_i^z \rho \sigma_i^z - \rho \right). \tag{7.19}$$

In the other limit of interest, where the noise is fully correlated across the ensemble, we can use instead

$$\mathcal{L}_{\text{deph}}(\rho) = \Gamma_\phi^{\text{C}} \left[2 S_z \rho S_z - (S_z)^2 \rho - \rho (S_z)^2 \right], \tag{7.20}$$

where $S_z = \frac{1}{2} \sum_i \sigma_z^i$. The last term in Eq. (7.18) is given by

$$\mathcal{L}_{\text{decay}}(\rho) = \frac{\Gamma}{2} \sum_{i=1}^{N} \left(2\sigma_i^- \rho \sigma_i^+ - \sigma_i^+ \sigma_i^- \rho - \rho \sigma_i^+ \sigma_i^- \right), \tag{7.21}$$

and describes the uncorrelated decay of each two-level system with rate Γ.

Naively, one could simply account for these decoherence processes by evaluating the mean-field dynamics for $\langle \sigma^k \rangle$ using the master equation in Eq. (7.18) and by including the additional terms in the mean-field equations of motion in Eq. (7.14). This approach is still exact for noninteracting spins and would also in general correctly capture the decay of coherences of the transverse spin components, $\langle \sigma_i^x \rangle$ and $\langle \sigma_i^y \rangle$. However, in this case the spin length $|\vec{s}_i(t)|$ is no longer conserved along a trajectory. As a consequence, the effect of spin-spin interactions is also reduced and the accuracy of the DTWA simulation degrades considerably. Therefore, in order to avoid this degradation, not only damping terms, but also an appropriate amount of fluctuations must be included in the dynamics.

7.2.1 Dephasing

Let us first focus on pure dephasing. In this situation we can make use of the fact that the incoherent dynamics generated by $\mathcal{L}_{\text{deph}}$ in Eq. (7.18) is simply the limiting case of a coherent evolution of the spins under the rapidly fluctuating Hamiltonian

$$H_{\text{fluc}}(t) = \frac{1}{2} \sum_{i=1}^{N} \xi_i(t) \sigma_i^z. \tag{7.22}$$

Here the $\xi_i(t)$ are classical noise processes with zero mean and we can set $\langle \xi_i(t) \xi_j(t') \rangle \sim \delta_{ij}$ to model individual dephasing or $\xi_i(t) = \xi(t)$ for collective noise. The evolution under this Hamiltonian introduces an additional term in the mean-field dynamics,

$$\left. \frac{d\vec{s}_i}{dt} \right|_{\text{deph}} = \xi_i(t) \vec{e}_z \times \vec{s}_i, \tag{7.23}$$

i.e., a rotation around the z-axis with a fluctuating frequency.

White noise limit

If the noise is uncorrelated over the typical timescales of the spin dynamics, which is also assumed in the derivation of the master equation in Eq. (7.18), we can take the white-noise limit $\langle \xi_i(t) \xi_i(t') \rangle \simeq 2\Gamma_\phi \, \delta(t - t')$ and interpret Eq. (7.23) as a Stratonovich stochastic differential equation. For numerical simulations it is more convenient to convert Eq. (7.23) into an Ito differential equation, where the added noise in each time step is independent of $\vec{s}_i(t)$. Using the usual rules of stochastic calculus [108] we then obtain the following stochastic increments for the spin variables

$$ds_i^x|_{\text{deph}} = -\Gamma_\phi s_i^x dt - \sqrt{2\Gamma_\phi} s_i^y dW_i, \tag{7.24}$$

$$ds_i^y|_{\text{deph}} = -\Gamma_\phi s_i^y dt + \sqrt{2\Gamma_\phi} s_i^x dW_i, \tag{7.25}$$

$$ds_i^z|_{\text{deph}} = 0, \tag{7.26}$$

where the $dW_i \equiv dW_i(t)$ are real-valued and independent Wiener increments for the time step $[t, t+dt]$. These increments satisfy $\langle dW_i \rangle = 0$ and $\langle dW_i dW_j \rangle = \delta_{ij} dt$ for individual dephasing and again we can simply set $dW_i = dW$ to describe spatially correlated noise.

In summary, we end up with a DDTWA algorithm as illustrated in Fig. 7.1(b). In this algorithm the sampling of the initial spin values, $\vec{s}_i(t=0)$, is implemented as before, but the deterministic mean-field equations of motion for the dynamics are replaced by the following set of stochastic differential equations

$$d\vec{s}_i = \vec{\Omega}^i_{\text{eff}} \times \vec{s}_i dt + d\vec{s}_i|_{\text{deph}}\,, \tag{7.27}$$

where the dephasing-induced contribution is defined in Eqs. (7.24)-(7.26). This set of equations can be efficiently simulated numerically with the Euler-Maruyama method [108].

We see that Eq. (7.27) still describes the same coherent dynamics for $\langle \vec{s}_i \rangle(t)$, but also accounts for the loss of coherences. Importantly, this loss is accompanied by an appropriate amount of noise, which ensures that

$$\langle d\vec{s}_i^{\,2} \rangle = \langle d\vec{(}(s_i^x)^2 + (s_i^y)^2 + (s_i^z)^2) \rangle = 0. \tag{7.28}$$

Therefore, although coherences decay over time, the length of each spin and, as a consequence, also the magnitude of the spin-spin interactions are preserved on average. In the examples discussed in Section 7.3 below we find that this property results in an excellent agreement between these approximate stochastic simulations and the exact results obtained for a large variety of models and parameter regimes. Note that the Eqs. (7.24)-(7.26) are equivalent to Eqs. (6.21)-(6.22) for a spin-1/2, but written in the Schwinger-boson basis. In both cases the derivation was done without performing any approximation.

Colored noise

Compared to the original master equation, an important benefit of the derivation presented above is that it can be readily generalized, without any approximation, to colored noise with a finite correlation time. For example, let us consider the evolution of the spins in the presence of noisy fields with a correlation function of the form

$$\langle \xi_i(t) \xi_j(t') \rangle \simeq \delta_{ij} \sigma^2 e^{-|t-t'|/\tau_c}. \tag{7.29}$$

We see that in the limit $\tau_c \to 0$ we recover the δ-correlated noise from above with $\Gamma_\phi = \sigma^2 \tau_c$, while for $\tau_c \to \infty$ we obtain the case of static noise with $\langle \xi_i(t) \xi_j(t') \rangle \simeq \delta_{ij} \sigma^2$. In general, the random noises ξ_i can be obtained by simulating an Ornstein-Uhlenbeck process [108, 243]

$$d\xi_i = -\frac{1}{\tau_c} \xi_i dt + \sqrt{\frac{2}{\tau_c}} \sigma d\eta_i, \tag{7.30}$$

where $d\eta_i$ are Wiener increments with $\langle d\eta_i \rangle = 0$ and $\langle d\eta_i d\eta_j \rangle = \delta_{ij} dt$. In our numerical simulations we can then account for the effect of colored noise by simulating the coherent dynamics in Eq. (7.23), but assuming noisy fields $\xi_i(t)$ that are calculated according to Eq. (7.30). Note that compared to the Markovian case, this only increases the number of simulated equations by N or even just by one in the case of collective noise. However, for very short correlation times τ_c, also the integration time steps must be reduced and it becomes much more efficient to use the Markovian dephasing dynamics described by Eqs. (7.24)-(7.26).

7.2.2 Decay

In the previous derivation we made use of the fact that dephasing can be described by classical noise. This is not the case for decay processes, where the system couples to a quantum environment represented by noise operators with non-vanishing commutation relations. We have already seen this difference between dephasing and decay processes in Chapter 6, where the Fokker-Planck equation of the collective decay required an additional approximation, the positive diffusion approximation (PDA). In stochastic simulations of the full quantum mechanical wavefunction, decay is usually modelled by introducing random quantum jumps [97], after which the system is projected into the state of the spin pointing down $|\downarrow\rangle$. Within the truncated Wigner function formalism, this would corresponds to a random projection into one of the four configurations listed in Eq. (7.13). However, in this approach the system evolution between the jumps is described by a non-Hermitian Hamiltonian, which again reduces the spin length $|\vec{s}_i|$ and degrades the accuracy of the DTWA.

To circumvent these problems, we propose here to simulate the decay dynamics of dissipative spin systems by a continuous stochastic process with the following increments for the classical spin trajectories

$$d\vec{s}_i = \vec{\Omega}^i_{\text{eff}} \times \vec{s}_i dt + d\vec{s}_i|_{\text{decay}}\,, \tag{7.31}$$

where

$$ds_i^x|_{\text{decay}} = -\frac{\Gamma}{2} s_i^x dt - \sqrt{\Gamma} s_i^y dW_i, \tag{7.32}$$

$$ds_i^y|_{\text{decay}} = -\frac{\Gamma}{2} s_i^y dt + \sqrt{\Gamma} s_i^x dW_i, \tag{7.33}$$

$$ds_i^z|_{\text{decay}} = -\Gamma(s_i^z + 1) dt + \sqrt{\Gamma}(s_i^z + 1) dW_i. \tag{7.34}$$

Let us emphasize that these equations are not derived from an underlying system-bath Hamiltonian, but rather constructed in order to satisfy two crucial properties. First, the deterministic terms in these equations reproduce

the correct decay dynamics for the average spin components

$$\langle \dot{\sigma}_i^x \rangle = -\frac{\Gamma}{2}\langle \sigma_i^x \rangle, \tag{7.35}$$

$$\langle \dot{\sigma}_i^y \rangle = -\frac{\Gamma}{2}\langle \sigma_i^y \rangle, \tag{7.36}$$

$$\langle \dot{\sigma}_i^z \rangle = -\Gamma(\langle \sigma_i^z \rangle + 1). \tag{7.37}$$

Second, the additional noise terms in Eqs. (7.32)-(7.34) reintroduce spin fluctuations to preserve the length of each spin, $|\vec{s}_i|$, on average. By using the Ito-calculus [97] we obtain

$$\langle d(s_i^x)^2 \rangle = -\Gamma\langle (s_i^x)^2 \rangle dt + \Gamma\langle (s_i^y)^2 \rangle dt \tag{7.38}$$

$$\langle d(s_i^y)^2 \rangle = -\Gamma\langle (s_i^y)^2 \rangle dt + \Gamma\langle (s_i^x)^2 \rangle dt \tag{7.39}$$

$$\langle d(s_i^z)^2 \rangle = -2\Gamma\langle (s_i^z)^2 + s_i^z \rangle dt + \Gamma\langle (s_i^z + 1)^2 \rangle dt \tag{7.40}$$

where the first terms come from the deterministic part and the second terms from the stochastic part of Eqs. (7.32)-(7.34). For the length of the spin vector we therefore obtain

$$\langle d\vec{s}_i^2 \rangle = \Gamma\left(1 - \langle (s_i^z)^2 \rangle\right) dt \approx 0, \tag{7.41}$$

and in contrast to the classical noise process this requirement can only be fulfilled up to a certain level of approximation.

The reason is that for the decay process the deterministic change of the z-component, $d(s_i^z)^2 = -2\Gamma s_i^z(s_i^z + 1)dt$, is positive for $s_i^z < 0$. This cannot be compensated by a positive diffusion term. In this sense, Eqs. (7.32)-(7.34) represent a diffusion process, which reproduces the exact single-spin dynamics while conserving the length of each spin as well as possible.

In the actual numerical simulations we find that under most conditions of interest, in particular for small decay rates Γ, the condition $\langle d\vec{s}_i^2 \rangle \approx 0$ is satisfied and that the average spin length remains very close to its initial value. Specifically, in all the investigated examples reported below there was only little change of $\langle \vec{s}^2 \rangle$ and therefore no noticeable degradation of the accuracy of the predicted results has been observed, neither in the transient dynamics nor in the steady state. While, this cannot be guaranteed in general, the conservation of the spin lengths can easily be verified for a particular application. In this case, Eqs. (7.32)-(7.34) represent a faithful stochastic approximation of a spin decay process, which is fully compatible with the DTWA.

7.3 Examples and benchmarking

In this section we demonstrate the application of the DDTWA for two paradigmatic settings in quantum optics, which can also be used to benchmark the results against exact numerical simulations in certain limiting cases. The

first example is an ensemble of spin-1/2 systems with spatially varying interactions. For this system it is already known that the DTWA provides accurate results in the isolated case and we show that adding dephasing or decay does not affect the accuracy of the method. In the case of decaying spins we can also simulate the steady states of the ensemble and investigate, for example, non-equilibrium phase transitions in driven-dissipative spin systems. As a second setup we consider an ensemble of two-level atoms coupled to a common optical mode. This setting illustrates how the DDTWA can be combined with other phase space methods for continuous variable systems and shows that the relevant interplay between collective interactions and individual dephasing is accurately captured by our stochastic simulations.

7.3.1 Interacting spin ensembles

We first study the dynamics of an interacting spin ensemble under the influence of local dephasing and spontenous emission, as described by Eqs. (7.18) and (7.19). More specifically, we assume that the coherent evolution of the spins can be modeled by the transverse Ising Hamiltonian

$$H = \frac{\Omega}{2}\sum_i \sigma_i^x + \frac{1}{2}\sum_{i\neq j} J_{ij}\sigma_i^z\sigma_j^z, \tag{7.42}$$

where the spin-spin interactions,

$$J_{ij} = \frac{1}{N}\frac{J}{|\vec{r}_i - \vec{r}_j|^\alpha}, \tag{7.43}$$

decay algebraically with the (normalized) distance between the spins, $|\vec{r}_i - \vec{r}_j|$. Such a scenario appears, for example, in trapped ion systems, where $0 < \alpha < 3$ [217–219], while for an ensemble of Rydberg atoms with van-der-Waals interactions we obtain $\alpha = 6$ [224, 225, 228].

By adding the stochastic terms for local dephasing and spontaneous emission to the mean-field equations, we arrive at the following set of stochastic differential equations,

$$ds_i^x = -\sum_{j\neq i} 2J_{ij}s_i^y s_j^z dt + ds_i^x|_{\text{deph}} + ds_i^x|_{\text{decay}}, \tag{7.44}$$

$$ds_i^y = \sum_{j\neq i} 2J_{ij}s_i^x s_j^z dt - \Omega s_i^z dt + ds_i^y|_{\text{deph}} + ds_i^y|_{\text{decay}}, \tag{7.45}$$

$$ds_i^z = \Omega s_i^y dt + ds_i^z|_{\text{decay}}, \tag{7.46}$$

which we will now study in different limits of interest.

Dephasing

In Fig. 7.2 we use the DDTWA to evaluate, first of all, the dynamics of an interacting spin ensemble in the absence of the driving field, $\Omega = 0$. In

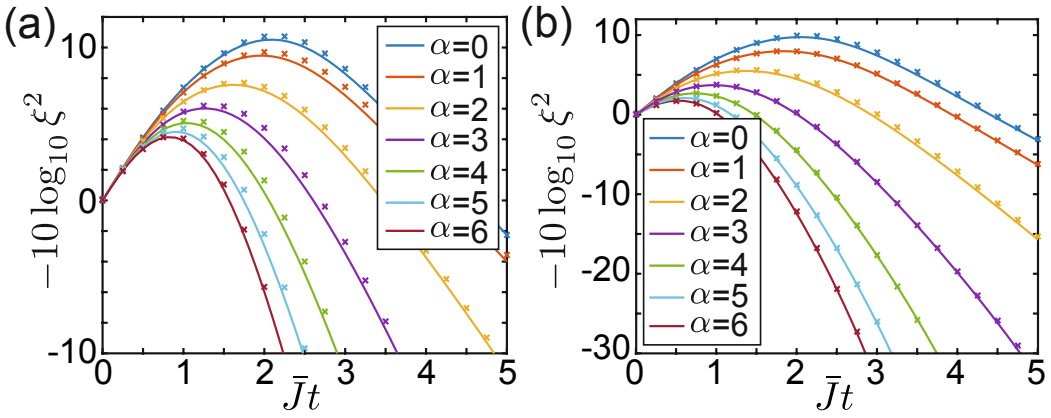

Figure 7.2: Time evolution of the squeezing parameter, ξ^2, for an ensemble of $N = 64$ spins arranged on a 3D cubic lattice with unit spacing. The spins are initially aligned along the x-direction, $|\Psi_0\rangle = \prod_i |\rightarrow\rangle_i$, where $|\rightarrow\rangle = (|\uparrow\rangle + |\downarrow\rangle)/\sqrt{2}$. For these simulations we assumed $\Omega = 0$ and an individual dephasing of each spin with a rate (a) $\Gamma_\phi/J = 0.0025$ and (b) $\Gamma_\phi/J = 0.025$. For a better comparison the curves for different α are plotted in terms of the rescaled time unit $\bar{J}^{-1}$, where $\bar{J} = \sum_{i,j} J_{ij}/N$. The solid lines show the exact results [244] for different power-law interactions. The crosses show the corresponding values obtained with the DDTWA for $n_t = 10000$ trajectories.

this example we have assumed that the $N = 64$ spins are arranged on a cubic lattice in three dimensions with unit spacing and different values of the power-law exponent α are considered. The central quantity of interest in these plots is the spin-squeezing parameter [206]

$$\xi^2 = \min_\phi (\Delta S_\phi^\perp)^2 \times \frac{N}{|\langle \vec{S} \rangle|^2}. \tag{7.47}$$

Here $\vec{S} = (S_x, S_y, S_z)$ is the collective spin operator with components $S_k = \frac{1}{2}\sum \sigma_i^k$, and $S_\phi^\perp = \vec{S} \cdot \vec{n}_\phi^\perp$ is the projection of $\vec{S}$ onto an axis $\vec{n}_\phi^\perp$ parametrized by an angle ϕ in the plane orthogonal to the mean spin vector $\langle \vec{S} \rangle$. As usual, $(\Delta O)^2 = \langle O^2 \rangle - \langle O \rangle^2$ denotes the variance of an operator O. Achieving a spin squeezing parameter of $\xi^2 < 1$ is relevant for metrological applications, but it also implies that the spins are entangled [207]. Therefore, such spin-squeezing effects cannot be described by mean-field theory.

In the absence of the driving field the z-components of all the spins are conserved and the system dynamics can still be solved efficiently for a large number of spins [244]. This allows us to directly compare the approximate stochastic simulations with the corresponding exact results. In Fig. 7.2(a) we find that for a very small dephasing rate of $\Gamma_\phi/J = 0.0025$ the squeezing parameter ξ^2 calculated with the DDTWA is accurate up to the level of a few percent, which is consistent with DTWA results for isolated systems. As shown in Fig. 7.2(b), for a slightly stronger rate of $\Gamma_\phi/J = 0.025$ the accuracy of the DDTWA improves even further. This can be attributed to the overall

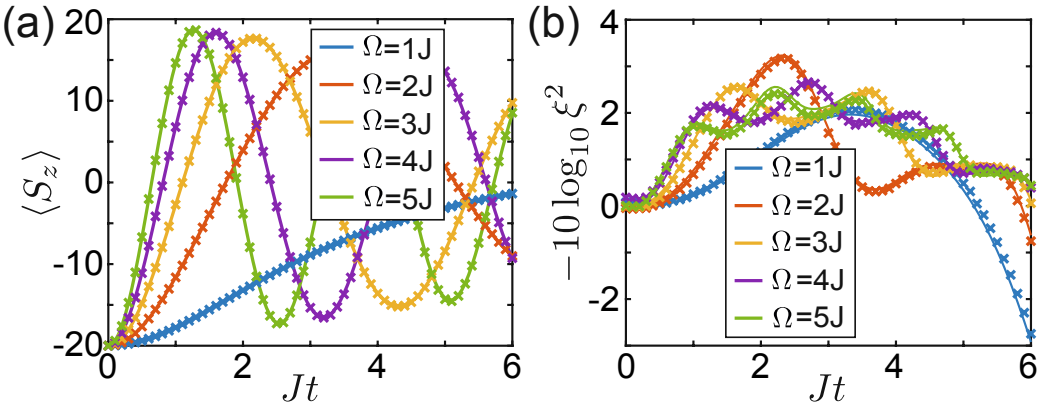

Figure 7.3: Plot of the time evolution of (a) the magnetization $\langle S_z(t)\rangle$ and (b) the squeezing parameter $\xi^2(t)$ of a driven spin ensemble with different driving strengths Ω and individual dephasing with rate $\Gamma_\phi/J = 0.2$. Initially, all the spins are polarized along the negative z-axis. In both plots, $N = 40$ and all-to-all interactions ($\alpha = 0$) are assumed. The solid lines are obtained from an exact integration of the master equation exploiting permutational invariance, while the crosses are obtained from a DDTWA simulation with $n_t = 10000$ trajectories.

reduction of quantum correlations, which are only approximately taken into account in the coherent dynamics.

As a next step we extend our analysis to finite driving strengths, $\Omega \neq 0$. In this case there are no analytic solutions available and exact numerical simulations are restricted to small spin systems, $N \lesssim 20$. However, in the limit of all-to-all interactions, i.e., $\alpha = 0$, simulations with a large number of spins, $N \sim 100$, can still be done by exploiting the permutational symmetry of the master equation. In Fig. 7.3 we use this symmetry [245, 246] to compare the DDTWA simulations of the driven Ising model with $\alpha = 0$ to the corresponding exact numerical results. Again we find that for all the considered driving strengths the DDTWA provides very accurate predictions for the mean spin components as well as for the achievable level of quantum correlations signified by the squeezing parameter.

Moreover, we consider the situation of collective dephasing. In this case both the interactions and the dephasing preserve the total spin S and the exact dynamics can be restricted to the totally-symmetric subspace with a dimension that only scales as $d_N = 2N$. In Fig. 7.4 we do so by evaluating variances and correlations of collective spin operators under the combined influence of interactions and dephasing. Again we find perfect agreement with the exact results.

Decay

Let us now continue with a similar study of the transverse Ising model for $\Gamma_\phi = 0$, but including a rate of decay, Γ. In Fig. 7.5 we plot the spin-squeezing dynamics for different power-law interactions in the absence of the driving

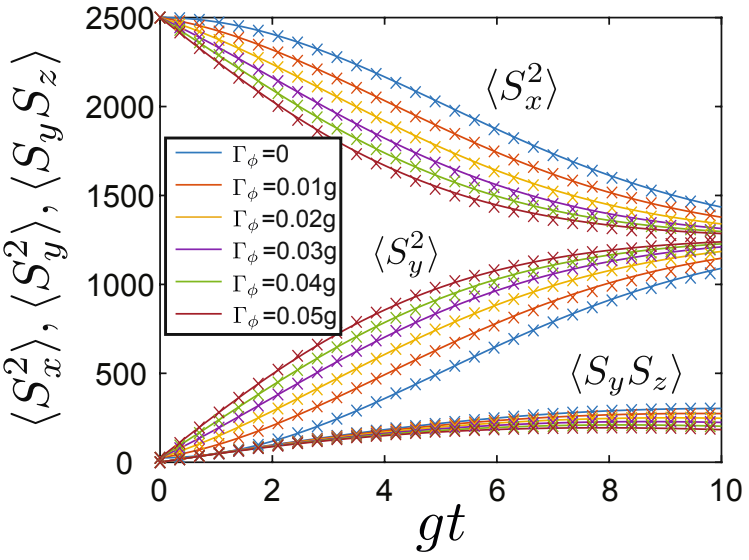

Figure 7.4: Collective quadratic operators $\langle S_x^2\rangle, \langle S_y^2\rangle$ and $\langle S_y S_z\rangle$ as a function of time t for different collective dephasing strengths $\Gamma_\phi^C = 0, 0.01g, 0.02g, 0.03g, 0.04g, 0.05g$ of the Ising model with all to all interaction $\alpha = 0$ and $N = 100$ spins. The spins are initially aligned along the x-direction, $|\Psi_0\rangle = \prod_i |\rightarrow\rangle_i$, where $|\rightarrow\rangle = (|\uparrow\rangle + |\downarrow\rangle)/\sqrt{2}$. The solid lines are from exact simulations while the crosses are obtained by the discrete truncated Wigner approximation (DTWA) method.

field, $\Omega = 0$, and two different values of Γ. Again we find excellent agreement between the DDTWA simulation and the exact solution [244], which shows that for such short-time dynamical simulations both types of decoherence processes can be accurately taken into account.

Let us now consider the case of a finite driving Ω. While under the influence of pure dephasing the spin ensemble always evolves into an infinite temperature state, this is not the case for driven spin systems in the presence of decay. As we illustrate in the following, in this case the DDTWA can also be used to simulate nontrivial steady states of the spin ensemble when $\Omega \neq 0$. In order to benchmark these simulations, we focus again on the case $\alpha = 0$, where exact numerical calculations are still possible. In Fig. 7.6 we evaluate the steady states of the dissipative transverse Ising model for varying driving strengths Ω. For all parameters we find excellent agreement between the DDTWA simulations and the exact results, both for the mean values of the collective observables $\langle S^k\rangle$ as well as for the variances $(\Delta S^k)^2$. The sharp peak in the spin fluctuations at a critical driving strength of $\Omega_c \approx J$ indicates a non-equilibrium phase transition in the steady state of the spin ensemble, which shows that the DDTWA is well suited to study such phenomena.

In summary, these examples clearly demonstrate the high level of accuracy that can be achieved with the dissipative DTWA when simulating interacting spin systems with dephasing and decay and equivalently accurate results are

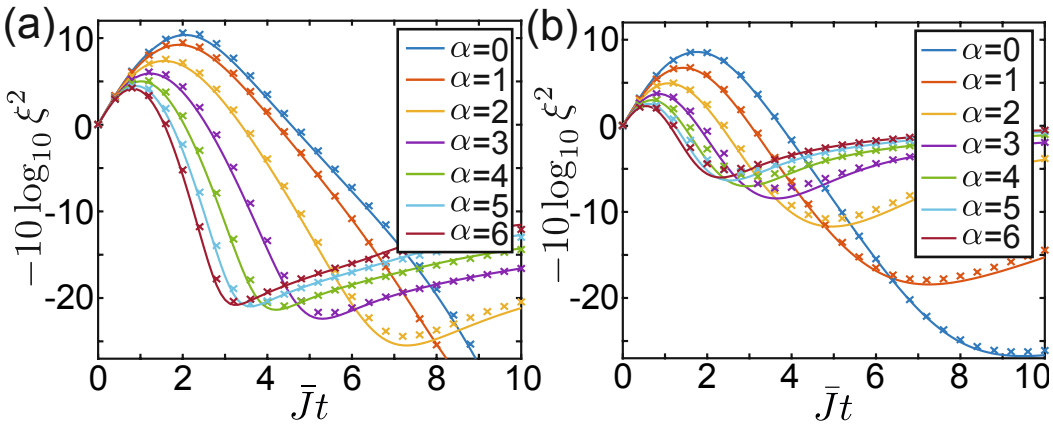

Figure 7.5: Time evolution of the squeezing parameter ξ^2 for an ensemble of $N = 64$ spins arranged on a cubic lattice with unit spacing. The spins are initially aligned along the x-direction, $|\Psi_0\rangle = \prod_i |\rightarrow\rangle_i$, where $|\rightarrow\rangle = (|\uparrow\rangle + |\downarrow\rangle)/\sqrt{2}$. For these simulations we assumed $\Omega = 0$ and individual spontaneous emission of each spin with a rate (a) $\Gamma/J = 0.0025$ and (b) $\Gamma/J = 0.025$. For a better comparison the curves for different α are plotted in terms of the rescaled time unit $\bar{J}^{-1}$, where $\bar{J} = \sum_{i,j} J_{ij}/N$. The solid lines show the exact results [244] for different power-law interactions. The crosses show the corresponding values obtained by the DDTWA method for $n_t = 10000$ trajectories.

obtained for spatially correlated dephasing. Small deviations from the exact predictions are mainly due to inaccuracies in the coherent dynamics, which takes spin-spin correlations only approximately into account. Therefore, we find that in most situations the accuracy of the DDTWA improves in the presence of decay and dephasing, where such correlations are reduced.

7.3.2 Driven Dicke model

Apart from being capable of simulating large ensembles of spins, the DDTWA can be readily combined with conventional phase space methods for continuous degrees of freedom. This is relevant for a large range of cavity QED models, where many two-level systems are coupled to a common photonic mode. As an illustrative example, we consider here the driven Dicke model with Hamiltonian

$$H = \frac{g}{\sqrt{N}}\left(S_+ a + S_- a^\dagger\right) + \Omega S_x, \tag{7.48}$$

where $S_\pm = S_x \pm iS_y$ and a ($a^\dagger$) is a bosonic annihilation (creation) operator. To model a realistic scenario, we include the dephasing of the two-level systems as well as the decay of the photonic mode with a rate 2κ. The whole system is then described by the master equation

$$\dot{\rho} = -i[H,\rho] + \mathcal{L}_{\text{deph}}(\rho) + \kappa\left(2a\rho a^\dagger - a^\dagger a\rho - \rho a^\dagger a\right). \tag{7.49}$$

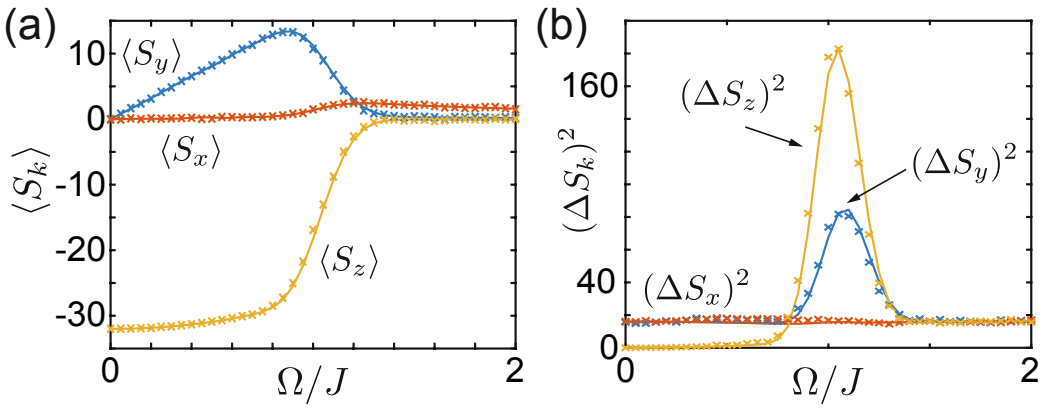

Figure 7.6: Steady state of the transverse Ising model given in Eq. (7.42) with $\alpha = 0$ and for a spin decay rate of $\Gamma/J = 0.2$. The two plots show (a) the average values of the spin components, $\langle S_{x,y,z} \rangle$, and (b) their fluctuations, $(\Delta S_k)^2 = \langle S_k^2 \rangle - \langle S_k \rangle^2$, as a function of the driving strength Ω and for $N = 64$.

To apply the DDTWA in such a mixed setting, it is natural to represent also the bosonic mode in terms of its Wigner function,

$$W(\alpha, t) = \frac{1}{\pi^2} \int d^2\beta \, e^{(\alpha\beta^* - \alpha^*\vec{\beta})} \, \mathrm{Tr} \left\{ e^{\beta a^\dagger - \beta^* a} \rho(t) \right\}. \tag{7.50}$$

In this case the moments of $W(\alpha, t)$ correspond to the symmetrically-ordered expectation values of mode operators [97, 102],

$$\langle (a^\dagger)^k a^\ell \rangle|_{\mathrm{sym}}(t) = \int d^n\alpha \, (\alpha^*)^k \alpha^\ell W(\alpha, t). \tag{7.51}$$

In the common situation where the photonic mode is initially prepared in the vacuum state or in a coherent state with amplitude α_0, the corresponding Wigner function,

$$W(\alpha, t = 0) = \frac{2}{\pi} e^{-|\alpha - \alpha_0|^2}, \tag{7.52}$$

is positive and can be interpreted as a probability distribution for the classical amplitudes α. In this case we can also sample the time evolution of $W(\alpha, t)$ by a set of stochastic trajectories $\{\alpha_n(t)\}$ and evaluate expectation values as

$$\langle (a^\dagger)^k a^\ell \rangle|_{\mathrm{sym}}(t) \simeq \frac{1}{n_t} \sum_{n=1}^{n_t} [\alpha_n^*(t)]^k \alpha_n^\ell(t). \tag{7.53}$$

In the absence of the two-level systems, these trajectories obey [97, 102]

$$d\alpha|_{\mathrm{loss}} = -\kappa\alpha dt + \sqrt{\kappa/2}(dW_1 + i dW_2), \tag{7.54}$$

and describe the loss of energy as well as the associated amount of quantum noise.

Given a stochastic description for each of the individual subsystems, we can now simulate the dynamics of the whole setup by imposing a joint TWA, i.e.,

by treating the coupling between the photonic mode and the spins on a mean-field level. As a result we obtain the following set of stochastic differential equations

$$ds_i^x = -\frac{2g}{\sqrt{N}}\mathrm{Im}(\alpha)s_i^z dt + ds_i^x|_{\mathrm{deph}}, \tag{7.55}$$

$$ds_i^y = -\frac{2g}{\sqrt{N}}\mathrm{Re}(\alpha)s_i^z dt - \Omega s_i^z dt + ds_i^y|_{\mathrm{deph}}, \tag{7.56}$$

$$ds_i^z = \frac{2g}{\sqrt{N}}\left[\mathrm{Re}(\alpha)s_i^y + \mathrm{Im}(\alpha)s_i^x\right]dt + \Omega s_i^y dt, \tag{7.57}$$

$$d\alpha = -i\frac{g}{\sqrt{4N}}\sum_i (s_i^x + is_i^y)dt + d\alpha|_{\mathrm{loss}}, \tag{7.58}$$

which are integrated for a set of $n_t \gg 1$ initial values $\vec{s}_i(0)$ and $\alpha(0)$, randomly drawn from the Wigner distributions of the individual subsystems.

In Fig. 7.7 we use this combined TWA approach to simulate the dynamics of the driven Dicke model, first of all for $N = 10$ spins, where the results can still be compared with an exact simulation of the master equation. From this comparison we find an excellent agreement between the stochastic simulations and the exact results, both for the cavity and the spin observables Although here we do not include a decay of the spins, the coupling to the lossy photonic mode still relaxes the combined system. Therefore, also this setup allows us to investigate the properties of the nontrivial steady states of this system. For example, in Fig. 7.7(c) we plot the stationary value of the two-photon correlation function

$$g^{(2)}(0) = \frac{\langle a^\dagger a^\dagger a a\rangle}{\langle a^\dagger a\rangle^2}. \tag{7.59}$$

This quantity shows a qualitative change from a coherent state, where $g^{(2)}(0) \simeq 1$, to a thermal-like state with $g^{(2)}(0) \gtrsim 2$. This crossover as a function of the driving strength depends explicitly on the spin dephasing rate Γ_ϕ. Note that in stochastic simulations, higher-order correlations typically have larger statistical errors, which can also be seen in the plot for $g^{(2)}(0)$.

As another illustrative example, we compare in Fig. 7.7(d) the time evolution of the driven Dicke model for the two limiting cases of individual dephasing and collective dephasing with the same rate Γ_ϕ. For this plot we have assumed a moderate driving and coupling strength, such that the dissipative cavity acts mainly as a collective decay channel for the spins. For collective dephasing, where the system dynamics remains constrained to the maximal angular momentum subspace, the system then quickly relaxes to a stationary state with only a small spin population. In contrast, for individual dephasing the spin population increases with a rate $\sim \Gamma_\phi$ for longer times. This can be understood from the fact that the local dephasing processes drive the spins into orthogonal subspaces with a smaller total angular momentum quantum number. Within these subspaces there exists many subradiant states, $|\psi_{\mathrm{sub}}\rangle$, which are decoupled from the cavity mode, i.e. $S_-|\psi_{\mathrm{sub}}\rangle = 0$, but still have a finite spin population that remains trapped.

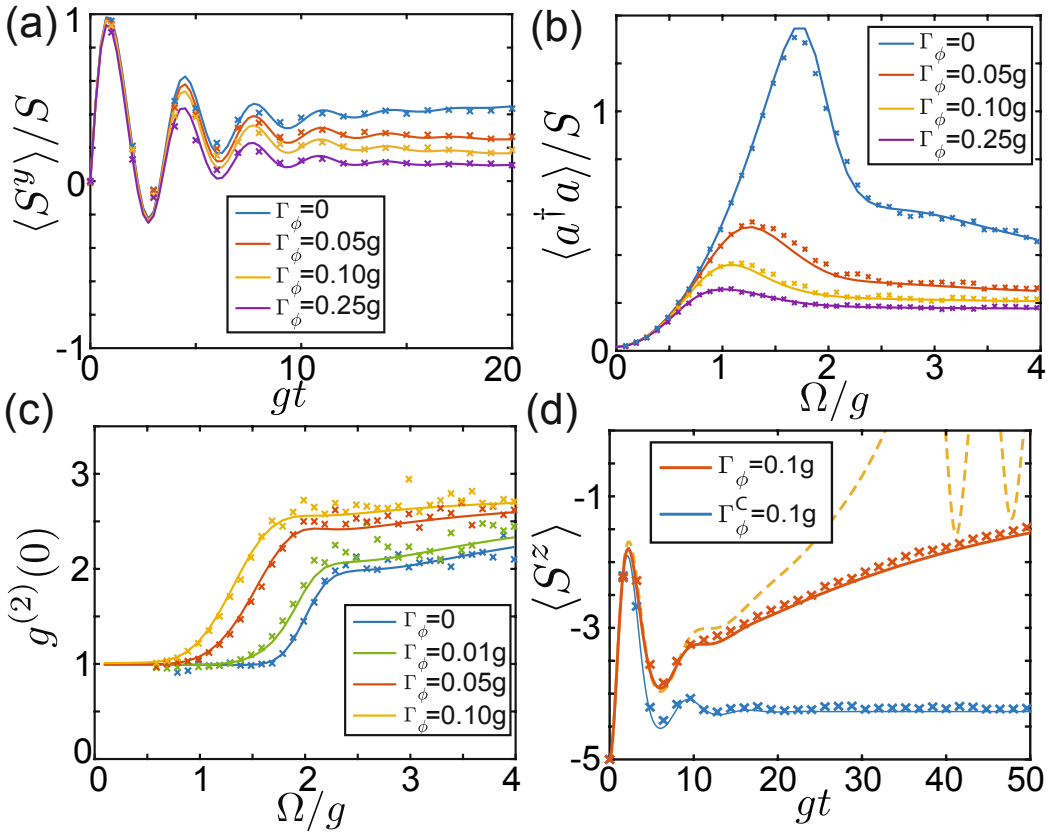

Figure 7.7: Simulation of the driven Dicke model as described in Eq. (7.49) for $N = 10$ and $\kappa = 0.5g$. (a) Time evolution of $\langle S_y(t)\rangle$ for $\Omega = 2g$ and different dephasing rates Γ_ϕ, when intially prepared in $|\Psi_0\rangle = \prod_i |\downarrow\rangle_i$. (b) Steady state cavity occupation number $\langle a^\dagger a\rangle$ and (c) steady state second order correlation function of the cavity field $g^{(2)}(0)$ as a function of the driving strength Ω and different dephasing rates Γ_ϕ. (d) Evolutions of an initial fully polarized spin in the presence of individual or collective dephasing with the same rate. For this plot $\Omega = g$. In all the plots the solid lines represent the results obtained from an exact simulations of the master equation exploiting permutational invariance while the crosses are obtained by the discrete truncated Wigner approximation (DTWA) method. The dashed line shows the prediction of mean-field theory.

In Fig. 7.7(d) we also show the prediction for $\langle S_z\rangle(t)$ obtained from mean-field theory. While mean-field theory still predicts very accurately the initial oscillations and the overall increase of the populations, the solution exhibits large, weakly-damped oscillations that are a clear artefact of this approximation. Note that the mean-field contribution to $d\vec{s}_i|_{\text{deph}}$ is the same for local and collective dephasing. Thus, a mean-field simulation cannot distinguish between spatially correlated and uncorrelated noise, a difference that is manifested only in the stochastic noise terms.

In summary, the simulation of this driven Dicke model demonstrates the applicability of the DDTWA for simulating cavity QED systems with large

ensembles of two-level systems. In particular, the example presented in Fig. 7.7(d) shows that this method captures very accurately both the collective coupling to the maximal angular momentum states as well as the physics associated with subradiant states.

7.4 Large-scale simulations

In the previous section we have focused on examples and parameter regimes, where a comparison with other exact methods was still possible. However, the main advantage of the DDTWA is that it can be easily scaled up and applied in many experimentally relevant situations where exact methods are no longer available. To illustrate this point, we consider in this section the superradiant decay of a large ensemble of interacting two-level atoms inside a lossy cavity. An old question in connection to superradiance is, how dipole-dipole interactions in dense atomic ensembles affect the decay process by inducing transitions out of the fully symmetric subspace [247]. In real experiments, similar effects can also arise from local dephasing and a relevant follow-up question is, if interaction effects can actually be distinguished from fluctuating or static frequency inhomogeneities. As we show in the following, the DDTWA can be used to answer these and related questions by direct numerical simulations.

To do so we consider the same master equation as in Section 7.3.2,

$$\dot{\rho} = -i[H,\rho] + \mathcal{L}_{\text{deph}}(\rho) + \kappa\left(2a\rho a^\dagger - a^\dagger a\rho - \rho a^\dagger a\right), \tag{7.60}$$

but with a Hamiltonian of the form

$$H = \frac{g}{\sqrt{N}}\left(S_+ a + S_- a^\dagger\right) + \sum_{i<j} J_{ij}^{xx}\sigma_i^x\sigma_j^x + \sum_i \frac{\omega_i}{2}\sigma_i^z. \tag{7.61}$$

Here the first and the second terms represent the collective atom-cavity coupling and the short-range spin-spin interactions with $J_{ij}^{xx} = J|\vec{r}_i - \vec{r}_j|^{-3}$, respectively. The last term accounts for an inhomogeneous broadening of the atomic transition frequency, where the ω_i are randomly drawn from a Gaussian distribution with variance σ^2 and zero mean.

The model defined in Eq. (7.60) and Eq. (7.61) can now be used to investigate, for example, how superradiant decay is influenced by (i) short-range interactions, (ii) Markovian dephasing and (iii) static inhomogeneous broadening. To do so we consider in Fig. 7.8 a system of $N \approx 10^5$ atoms arranged on a cubic lattice and initially prepared in the excited state. We then use the stochastic DTWA method to simulate the consecutive decay dynamics under the influence of those three processes. For these simulations we have assumed $\alpha = 3$, but all interactions with $|J_{ij}^{xx}|/J < 0.01$ have been set to zero. For the frequency distribution we have chosen a variance of $\sigma^2 = 2\Gamma_\phi^2$, such that the inhomogeneous broadening and the Markovian dephasing lead to a loss of coherence over a similar timescale. The plots in Fig. 7.8 show that while all three mechanism lead to a strong inhibition of the decay, the

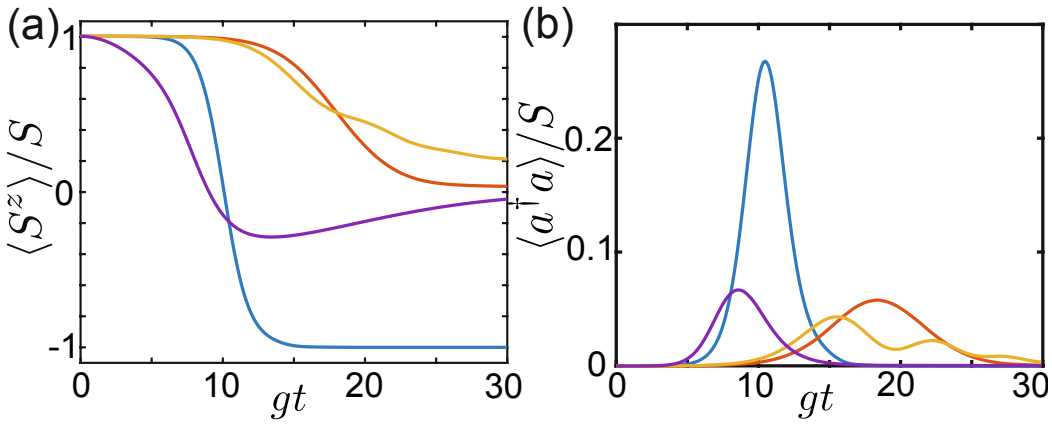

Figure 7.8: Superradiant decay of an ensemble of $N = 47^3 = 103823$ two-level systems that are initially prepared in the excited state and couple to a lossy cavity mode with $\kappa = g$, as sketched in (a). In (b) we show the decay of z-magnetization and in (c) the photon number $\langle a^\dagger a \rangle \sim I_{\mathrm{ph}}(t)$, which is proportional to the emitted field intensity. In both plots we compare the evolution of the bare non-interacting ensemble (blue line), with dynamics in the presence of additional Ising interactions $\sim \sigma_i^x \sigma_j^x$, with $J_x/g = 0.025$ and $\alpha = 3$ (purple line). The other two cases show the dynamics of a noninteracting ensemble, but in the presence of local Markovian dephasing with a rate $\Gamma_\phi/g = 0.5$ (red line) and for an inhomogeneously broadened ensemble (yellow line). In the latter case the spin frequencies ω_i have been randomly drawn from a normal distribution with zero mean and a variance of $\sigma^2 = 2\Gamma_\phi^2$. To obtain this data $n_t = 64$ trajectories were simulated.

actual decay dynamics of the atomic population and the emitted photons is both qualitatively and quantitatively very different.

While a more detailed investigation of this system is beyond the scope of this work, these basic results already show how the stochastic DTWA can be used to simulate interesting dynamical effects in large-scale spin systems under experimentally realistic conditions. Note that for the plots in Fig. 7.8 we have simulated about $N = 10^5$ atoms coupled to a cavity mode that becomes populated with many thousands of photons. We remark that the simulations shown in Fig. 7.8 have been performed on a regular PC within a day of computation time in total and with some additional programming efforts and the use of a supercomputer, the simulation of millions of spins becomes possible.

Such system sizes are far beyond the typical atom numbers of about $N \approx 150$ [245] that can be treated in exact simulations of similar models by exploiting permutation symmetry and using quantum trajectories. Moreover, both the short-range interactions as well as the inhomogeneous frequency distribution break the permutational invariance of the system such that the current type of simulations are simply not accessible with such exact numerical techniques. At the same time, since during the whole evolution $\langle \sigma_i^x \rangle = \langle \sigma_i^y \rangle = 0$, neither the initial decay nor the effect of transverse spin-spin interactions

would be captured by a simulation of the mean-field equations of motion only. Higher-order approximation schemes based on a cumulant expansion (see Chapter 2.5), which can account for such effects, already scale as N^2 or higher and are thus no longer applicable for the considered system sizes. Note that cumulant expansion techniques also often exhibit numerical instabilities, which do not occur in the DDTWA approach.

7.5 Conclusion

In this chapter, we have presented a simple and efficient numerical algorithm for simulating large spin ensembles and cavity-QED systems in the presence of realistic decoherence processes. We used a similar approach as for TWOQS (see Chapter 6) by replacing the deterministic classical equations with stochastic equations, to extend the discrete truncated Wigner approximation to open quantum system (DDTWA). By using stochastic equations it is possible to account for damping and loss of coherence while still preserving the total length of each classical spin on average. This last feature ensures that the magnitude of spin-spin interactions is not reduced and that the accuracy of the DTWA is not degraded. We benchmarked the method with exact simulations and find that the DDTWA is very well suited to simulate such systems with very high accuracy. As there are usually less correlations in a dissipative system, simulations reveal that the accuracy improves in the prescence of dissipation compared to the equilibrium case. Because of the linear scaling of stochastic equations with the number of spins, we showed that simulations of a hundred-thousand spins are possible even on a regular computer. We showed that the DDTWA can reproduce steady states very accurately and as there a no restriction on the dimensionality, it will be interesting to apply the method to 2D and 3D systems in order to investigate dissipative phase transitions. Moreover, this method is not restricted to white noise processes only, also systems in the presence of colored noise can be simulated very efficiently.

8 Summary and conclusion

"Shampoo!"

- Marko Arnautovic

In this thesis, we studied the influence of dissipation on quantum systems. We can group the main findings of this thesis into two parts. The first set of results concern the competition between coherent and incoherent processes in systems with gain and loss. We analyzed a spin chain where the coherent interactions between neighboring lattice sites compete with alternating gain and loss processes. We found that this system experiences phase transitions which are different from what we would expect from equilibrium phase transitions. We identified a discontinuous phase transition without coexistence of the two distinct phases. Moreover, when simulating large lattices of spins we identified long-range correlations at the critical point, however this phase transition was not accompanied by any symmetry breaking in the system. These unconventional phase transitions can be linked to the dynamical effect of PT-symmetry breaking in classical systems.

The effect of PT-symmetry breaking arises through the competition of coherent and incoherent processes and has been demonstrated in various classical systems in the past years. In this thesis, we introduced for the first time a symmetry relation for Liouville operators, which extends the PT-symmetry definition for classical systems to open quantum systems. This symmetry relation is not restricted to a specific kind of system such as quadratic bosonic systems, where the first order mean values coincide with the classical equations of motion. It can be used even for randomly generated systems. We proved that systems fulfilling this symmetry relation possess a symmetric phase which can be broken by increasing the dissipation strength. In the thermodynamic limit, the competition between coherent dynamics and dissipation leads to a sharp phase transition between a symmetric and a symmetry broken regime in analogy to the classical transition.

Surprisingly, the effect of symmetry breaking can be also found when studying the energy transport between two quantum machines. Depending on the injection and extraction rate of the quantum machines, the system is in a spatially symmetric or a symmetry broken steady state. This emergent symmetry crucially influences the energy transport properties and we found a noise dominated and a coherent transport regime under the influence of quantum or thermal noise. Moreover, we showed that the competition of coherent and incoherent processes and nonlinear saturation effects leads to a flow of energy which is very different from what one would intuitively expect from Ohm's law.

In order to study such extended open quantum systems, it requires new methods. In the second part of the thesis we introduced new methods to efficiently study large open quantum systems, the truncated Wigner method for open quantum Spin (TWOQS) and the discrete truncated Wigner approximation (DDTWA). Both methods are based on the truncated Wigner approximation and map a master equation to a set of stochastic equations in order to capture dissipation while still preserving the initial quantum fluctuations. As a result, both methods can accurately reproduce spin squeezing effects and even the steady states of large many-body systems. While the DDTWA can be used to study spin-1/2 systems in the presence of decay and dephasing, the TWOQS works best for large quantum spin numbers. Because the methods scale only linearly with the number of spins, large spin systems consisting of $N = 10^5$ spins can be simulated on a regular computer. Studying dissipative phase transitions of 2D and 3D spin systems is very challenging as there are no reliable numerical techniques to accurately simulate large-scale systems. As both methods are not restricted to any dimension or interaction pattern, we can finally simulate large-scale 2D and 3D systems very accurately. This will be a very important step towards a better understanding of dissipative phase transitions. Moreover, the DDTWA enables the simulation of realistic experiments by including all different forms of dephasing, decay and inhomogeneities. It would be therefore very interesting to study the effect of these imperfections on large-scale interacting spin systems. This could help experimentalist to improve their experiments as they better understand the impact of imperfections in their setups.

Acknowledgements

"Ich stehe hinter meiner Mannschaft und das bis zum letzten Tropfen."

- Marko Arnautovic

First of all, I want to thank my supervisor Peter Rabl. I really appreciate your good personal supervision and that you always took your time to discuss things. Over the past years, I really learned a lot from you and besides valuable scientific input, I am thankful for your support, calmness and kindness.

Furthermore, I want to thank Peter Kirton. I really enjoyed working with you as well as having lunch together at the Vietnamese restaurant. Moreover, I want to thank Ana Maria Rey and her group for the hospitality and interesting discussions during my three months visit at JILA.

Special thanks go to my colleges Yuri, Danielle, Giuseppe, Tuomas, Kosmas, Michael, Marc, Tom, Louis, Juan, Rocio and Inigo. I really enjoyed our endless sometimes emotional discussions not only about physics but also about politics, food and random things.

Moreover I want to thank my family, especially my parents Herta and Gottfried for giving me the opportunity to study at the university and encouraging me to learn something. I also want to thank my sister and of course little Eleonore for supporting me.

Last but not least I want to thank my girlfriend Vali for always being there for me, supporting me and cheering my life up.

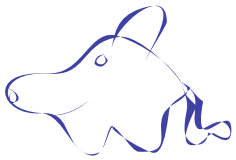

Thank you!

Appendices

A Energy transport and symmetry breaking in microscopic power grids

A.1 Fokker-Planck equation

In the following we give a detailed derivation of the mapping of the master equation Eq. (3.1) to a set of stochastic equations Eq. (3.4)-(3.6). In the regime $n_0 \gg 1$ the cutoff function $f(x)$ in Eq. (3.3) varies slowly on the scale of individual excitations and the master equation can be mapped onto a Fokker-Planck equation for the Glauber-Sudarshan P-representation [97, 99, 102]. This distribution function is defined by

$$\rho = \int \prod_\ell d^2\alpha_\ell \, P(\{\alpha_\ell\}) |\{\alpha_\ell\}\rangle\langle\{\alpha_\ell\}|, \tag{A.1}$$

where $|\{\alpha_\ell\}\rangle$ denotes a multi-component coherent state. By using the usual substitution rules [97, 102]

$$\begin{aligned} a_\ell \rho &\to \alpha_\ell P, & a_\ell^\dagger \rho &\to \left(\alpha_\ell^* - \frac{\partial}{\partial \alpha_\ell}\right) P, \\ \rho a_\ell^\dagger &\to \alpha_\ell^* P, & \rho a_\ell &\to \left(\alpha_\ell - \frac{\partial}{\partial \alpha_\ell^*}\right) P, \end{aligned} \tag{A.2}$$

we can convert Eq. (3.1) for the density operator ρ into a partial differential equation for $P(\{\alpha_\ell\})$. We obtain

$$\frac{\partial P}{\partial t} = \left.\frac{\partial P}{\partial t}\right|_{\text{lin}} + \left.\frac{\partial P}{\partial t}\right|_{\text{nl}}, \tag{A.3}$$

where the first term,

$$\begin{aligned} \left.\frac{\partial P}{\partial t}\right|_{\text{lin}} = \frac{1}{2}\Bigg[& -ig\left(\sum_{\ell=1}^{N-1} \frac{\partial}{\partial \alpha_\ell}\alpha_{\ell+1} + \sum_{\ell=2}^{N} \frac{\partial}{\partial \alpha_\ell}\alpha_{\ell-1}\right) \\ & + \gamma \sum_{\ell=1}^{N}\left(\frac{\partial}{\partial \alpha_\ell}\alpha_\ell + N_{\text{th}}\frac{\partial^2}{\partial \alpha_\ell \partial \alpha_\ell^*}\right) + c.c.\Bigg] P, \end{aligned} \tag{A.4}$$

describes the linear chain and already has the form of a Fokker-Planck equation.

The nonlinear dissipative terms in Eq. (3.1) at the ends of the chain translate into higher order derivatives for the P-distribution and additional approximations are required. To do so we first use the substitution rules from above to translate the action of $f(a^\dagger a)$ on the density operator into a differential operator acting on a coherent state,

$$f(a^\dagger a)|\alpha\rangle\langle\alpha| \;\rightarrow\; \sum_{m=0}^{\infty} \bar{f}_m \alpha^m \left(\alpha^* + \frac{\partial}{\partial\alpha}\right)^m |\alpha\rangle\langle\alpha|. \tag{A.5}$$

Here the coefficients $\bar{f}_m$ follow from an expansion of the operator $f(a^\dagger a)$ into a normally ordered series

$$f(a^\dagger a) = \sum_{m=0}^{\infty} \bar{f}_m (a^\dagger)^m a^m. \tag{A.6}$$

By using the binomial theorem

$$\begin{aligned}\left(\alpha^* + \frac{\partial}{\partial\alpha}\right)^m &= \sum_{k=0}^{m} \binom{m}{k} (\alpha^*)^{m-k} \frac{\partial^k}{\partial\alpha^k} \\ &= \sum_{k=0}^{m} \frac{1}{k!} \frac{\partial^k}{\partial\alpha^{*k}} (\alpha^{*m}) \frac{\partial^k}{\partial\alpha^k},\end{aligned} \tag{A.7}$$

and integrating by parts we obtain the following substitution (omitting the site index)

$$\begin{aligned}f(a^\dagger a)\rho \;\rightarrow\; &\sum_{m=0}^{\infty}\sum_{k=0}^{m} \bar{f}_m \alpha^m \frac{(-1)^k}{k!} \frac{\partial^k}{\partial\alpha^{*k}} (\alpha^{*m}) \frac{\partial^k}{\partial\alpha^k} P(\alpha) \\ &= \sum_{k=0}^{\infty} \frac{(-1)^k}{k!} \frac{\partial^k}{\partial\alpha^{*k}} \left[\bar{f}(\alpha,\alpha^*)\right] \frac{\partial^k}{\partial\alpha^k} P(\alpha),\end{aligned} \tag{A.8}$$

where $\bar{f}(\alpha,\alpha^*) = \langle\alpha|f(a^\dagger a)|\alpha\rangle$. Since $f(a^\dagger a)$ is a function of $a/\sqrt{n_0}$ and $a^\dagger/\sqrt{n_0}$, the derivatives of $\bar{f}(\alpha,\alpha^*)$ scale as $\frac{\partial^k}{\partial\alpha^{*k}}\bar{f}(\alpha,\alpha^*) \propto n_0^{-k/2}$. Therefore, in the limit $n_0 \rightarrow \infty$, we can neglect all derivatives and approximate

$$f(a^\dagger a)\rho \;\rightarrow\; \bar{f}(\alpha,\alpha^*)P(\alpha,\alpha^*) + \mathcal{O}\left(\frac{1}{\sqrt{n_0}}\right). \tag{A.9}$$

Note that the definition of $\bar{f}(\alpha,\alpha^*)$ is based on the normally ordered series expansion and in general $\bar{f}(\alpha,\alpha^*) \neq f(|\alpha|^2)$. Therefore, in our derivation we make a second approximation and neglect this difference, i.e.,

$$\bar{f}(\alpha,\alpha^*) = \langle\alpha|\frac{1}{(1+a^\dagger a/n_0)}|\alpha\rangle \approx \frac{1}{(1+|\alpha|^2/n_0)}. \tag{A.10}$$

To show the validity of this approximation, we first evaluate the function exactly [248]

$$\langle\alpha|\frac{1}{(1+a^\dagger a/n_0)}|\alpha\rangle = e^{-|\alpha|^2}(-|\alpha|)^{-n_0}\left[\Gamma(n_0,0) - \Gamma(n_0,-|\alpha|^2)\right] \tag{A.11}$$

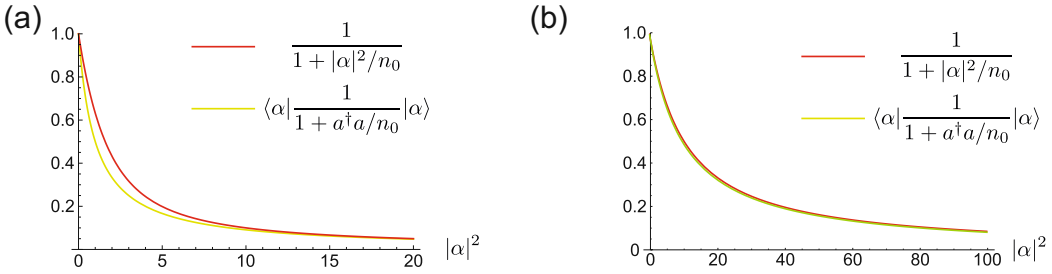

Figure A.1: Plot of the function $\bar{f}(\alpha,\alpha^*) = \langle\alpha|\frac{1}{(1+a^\dagger a/n_0)}|\alpha\rangle$ and its approximated form $\frac{1}{(1+|\alpha|^2/n_0)}$ for (a) $n_0 = 1$ and (b) $n_0 = 10$.

and compare the results with the approximate form $1/(1+|\alpha|^2/n_0)$. Here $\Gamma(n,x)$ denotes the incomplete Gamma function. Even deep in the quantum regime, $n_0 \approx 1$, these two expressions agree up to a few percent and become essentially identical for $n_0 \gtrsim 10$ as shown in Fig. A.1. Therefore, we conclude that the main approximation in the derivation of our semiclassical Fokker-Planck equation arises from neglecting higher order derivatives in Eq. (A.8). Based on these considerations we obtain the following approximate substitution rules

$$\begin{aligned} A\rho &\rightarrow \frac{\alpha}{(1+|\alpha|^2/n_0)}P(\alpha,\alpha^*), \\ A^\dagger\rho &\rightarrow \left(\alpha^* - \frac{\partial}{\partial\alpha}\right)\frac{1}{(1+|\alpha|^2/n_0)}P(\alpha,\alpha^*), \end{aligned} \tag{A.12}$$

and analogous relations for ρA and $\rho A^\dagger$. All together we then obtain

$$\left.\frac{\partial P}{\partial t}\right|_{\rm nl} = \frac{1}{2}\left[-\frac{\partial}{\partial\alpha_1}\Gamma_i(\alpha_1)\alpha_1 + \frac{\partial^2}{\partial\alpha_1\partial\alpha_1^*}\Gamma_i(\alpha_1) + \frac{\partial}{\partial\alpha_N}\Gamma_e(\alpha_N)\alpha_N + c.c.\right]P, \tag{A.13}$$

where $\Gamma_{i,e}(\alpha) = \Gamma_{i,e}f^2(|\alpha|^2)$. After this approximation, the resulting Fokker-Planck equation (A.3) can be mapped onto the set of stochastic differential as explained in Chapter 2.4.3.

$$\dot{\alpha_1} = \frac{\Gamma_i(\alpha_1)-\gamma}{2}\alpha_1 + i\frac{g}{2}\alpha_2 + \sqrt{D_{\rm th}+\Gamma_i(\alpha_1)}\xi_1(t), \tag{A.14}$$

$$\dot{\alpha_\ell} = -\frac{\gamma}{2}\alpha_\ell + i\frac{g}{2}\left(\alpha_{\ell-1}+\alpha_{\ell+1}\right) + \sqrt{D_{\rm th}}\xi_\ell(t), \tag{A.15}$$

$$\dot{\alpha_N} = -\frac{\Gamma_e(\alpha_N)+\gamma}{2}\alpha_N + i\frac{g}{2}\alpha_{N-1} + \sqrt{D_{\rm th}}\xi_N(t). \tag{A.16}$$

Here $\Gamma_{i,e}(\alpha) = \Gamma_{i,e}f^2(|\alpha|^2)$ and $D_{\rm th} = \gamma N_{\rm th}$ is the thermal diffusion rate. The $\xi_\ell(t)$ are white noise processes, which satisfy $\langle\xi_\ell^*(t)\xi_{\ell'}(t')\rangle = \delta_{\ell\ell'}\delta(t-t')$.

B Non-equilibrium magnetic phases in spin lattices with gain and loss

B.1 Holstein-Primakoff approximation

In the ordered FM and AM phases and for large S the spins are highly polarized and we can use a HPA [197] to linearize the dynamics of each spin around its mean value on the Bloch sphere. Under this approximation the collective spin operators $S^{\pm}$ and S^z are mapped onto a bosonic mode with annihilation operator c. For example, for a spin down state with $\langle S^z\rangle \approx -S$ we obtain

$$S^+ \simeq \sqrt{2S}c^\dagger, \qquad S^- \simeq \sqrt{2S}c, \qquad S^z = -S + c^\dagger c. \tag{B.1}$$

Equivalently, in the opposite limit of a spin up state, where $\langle S^z\rangle \approx S$, we find

$$S^+ \simeq \sqrt{2S}c, \qquad S^- \simeq \sqrt{2S}c^\dagger, \qquad S^z = S - c^\dagger c. \tag{B.2}$$

This approach then allows us to find a description of the system in terms of bosonic modes valid for large S in each of the ordered phases. For example, within the AM phase with all spins pointing up, which we label $|\Uparrow\Uparrow\rangle$, we obtain the linearized master equation

$$\dot{\rho} = -\frac{i}{\hbar}[H_{HPA}, \rho] + \Gamma_g \sum_{n=1}^{N} \mathcal{D}[c_{a,n}]\rho + \Gamma_l \sum_{n=1}^{N} \mathcal{D}[c_{b,n}^\dagger]\rho, \tag{B.3}$$

where

$$H_{HPA} = \hbar \sum_{n=1}^{N} g\,(c_{a,n}c_{b,n}^\dagger + c_{a,n}^\dagger c_{b,n}) + h(c_{b,n}c_{a,n+1}^\dagger + c_{b,n}^\dagger c_{a,n+1}). \tag{B.4}$$

Here we have introduced the bosonic operators $c_{a,b}$, which describe the left and right spins in each unit cell labeled by n. Similar expression are obtained for the other phases, $|\Downarrow\Downarrow\rangle$ and $|\Uparrow\Downarrow\rangle$.

B.1.1 Phase boundaries

By assuming periodic boundary conditions, the linearized master equation can be solved by changing to Fourier space,

$$c_{a/b,n} = \frac{1}{\sqrt{N}} \sum_k e^{ink} c_{a/b,k}, \tag{B.5}$$

where the Hamiltonian reads

$$H = \hbar \sum_k g_k c_{a,k} c_{b,k}^\dagger + g_k^* c_{a,k}^\dagger c_{b,k} \tag{B.6}$$

with $g_k = g + he^{ik}$. For the steady-state occupation numbers in k-space we then obtain

$$\langle c_{a,k}^\dagger c_{a,k} \rangle = \frac{\Gamma_l |g_k|^2}{(\Gamma_g - \Gamma_l)(|g_k|^2 - \Gamma_g \Gamma_l)}, \tag{B.7}$$

$$\langle c_{b,k}^\dagger c_{b,k} \rangle = \frac{\Gamma_l (|g_k|^2 + \Gamma_g(\Gamma_g - \Gamma_l))}{(\Gamma_g - \Gamma_l)(|g_k|^2 - \Gamma_g \Gamma_l)}, \tag{B.8}$$

$$\langle c_{a,k}^\dagger c_{b,k} \rangle = \frac{i g_k \Gamma_g \Gamma_l}{(\Gamma_g - \Gamma_l)(|g_k|^2 - \Gamma_g \Gamma_l)}, \tag{B.9}$$

and $\langle c_{a,k}^\dagger c_{a,k'} \rangle = 0$, etc. for $k \neq k'$. The corresponding expectation values for each lattice site are given by $\langle c_{a,n}^\dagger c_{a,n} \rangle = \frac{1}{N} \sum_k \langle c_{a,k}^\dagger c_{a,k} \rangle$ and by approximating this sum by an integral for $N \to \infty$ we obtain

$$\langle c_{b,n}^\dagger c_{b,n} \rangle = \frac{\Gamma_l}{\Gamma_g - \Gamma_l} \left(1 + \frac{\Gamma_g^2}{C} \right), \tag{B.10}$$

$$\langle c_{a,n}^\dagger c_{b,n} \rangle = \frac{i \Gamma_g \Gamma_l}{2g(\Gamma_g - \Gamma_l)} \left(1 + \frac{\Gamma_g \Gamma_l + g^2 - h^2}{C} \right), \tag{B.11}$$

where $C = \sqrt{[(g-h)^2 - \Gamma_g \Gamma_l][(g+h)^2 - \Gamma_g \Gamma_l]}$. Finally, the magnetizations of each of the inequivalent sites are $\langle S_a^z \rangle = S - \langle c_{a,n}^\dagger c_{a,n} \rangle$ and $\langle S_b^z \rangle = S - \langle c_{b,n}^\dagger c_{b,n} \rangle$.

These solutions for the occupation numbers only give real numbers when $\Gamma_g > \Gamma_l$ and $(g-h)^2 > \Gamma_g \Gamma_l$, which shows that the $|\Uparrow\Uparrow\rangle$ phase is only stable in these regions of the phase diagram. Note that the same conditions can be obtained from the linear equations of motion for the mean values $\langle c_{a/b,n} \rangle$. Equivalent calculations for the $|\Downarrow\Downarrow\rangle$ phase give

$$\langle S_a^z \rangle = -S + \frac{\Gamma_g}{\Gamma_l - \Gamma_g} \left(1 + \frac{\Gamma_l^2}{C} \right), \tag{B.12}$$

$$\langle S_b^z \rangle = -S + \frac{\Gamma_g}{\Gamma_l - \Gamma_g} \left(1 + \frac{\Gamma_g \Gamma_l}{C} \right), \tag{B.13}$$

which are only valid for $\Gamma_l > \Gamma_g$ and $(g-h)^2 > \Gamma_g \Gamma_l$, where this phase is stable. Finally, for the $|\Uparrow\Downarrow\rangle$ phase we find

$$\langle S_a^z \rangle = S - \frac{\Gamma_l}{\Gamma_l + \Gamma_g} \left(-1 + \frac{\Gamma_g \Gamma_l}{C} \right), \tag{B.14}$$

$$\langle S_b^z \rangle = -S + \frac{\Gamma_g}{\Gamma_l + \Gamma_g} \left(-1 + \frac{\Gamma_g \Gamma_l}{C} \right), \tag{B.15}$$

which sets the phase boundary for this phase as $\Gamma_g \Gamma_l > (g+h)^2$. To obtain the locations of the phase boundaries for the dimer model one may simply set $h = 0$ in these expressions.

Note that these results can be generalized in a straightforward manner to higher dimensions and other lattice geometries. For example, in a 2D square lattice we find that all the ordered phases still exist. In this case the antiferromagnetic phase is stable for $\Gamma_g\Gamma_l > 4(g+h)^2$, etc.

B.1.2 Correlation length

Close to the points where transitions between the different phases occur we see the build-up of long-range correlations in the steady-state density matrix. To quantify these correlations we calculate

$$\langle c^\dagger_{a,n} c_{a,n+s}\rangle = \frac{1}{N}\sum_k \langle c^\dagger_{a,k} c_{a,k}\rangle e^{isk}, \tag{B.16}$$

which can be evaluated in the same way as the magnetization above. For example, in the $|\Uparrow\Downarrow\rangle$ phase and for $s > 0$ this quantity takes the form

$$\langle c^\dagger_{a,n} c_{a,n+s}\rangle = \frac{\Gamma_l}{\Gamma_l+\Gamma_g}\left(\frac{\Gamma_g\Gamma_l}{C}\right)\lambda^{s-1}, \tag{B.17}$$

where

$$\lambda = \frac{\Gamma_g\Gamma_l - g^2 - h^2 - C}{2gh}. \tag{B.18}$$

This then lets us express the asymptotic form of the spin-spin correlation function as

$$|\langle S^-_{a,n} S^+_{a,n+s}\rangle| \propto e^{-|s|/\xi}, \tag{B.19}$$

with the correlation length $\xi = -1/\log(-\lambda)$.

Close to the phase boundary $\lambda \to 1$ and the correlation length diverges. We can expand around the transition point, $\Gamma_g\Gamma_l = (g+h)^2$, and find

$$\xi = \left(\frac{\Gamma_g\Gamma_l - (g+h)^2}{gh}\right)^{-1/2}. \tag{B.20}$$

Similar calculations for the other ordered phases show that the critical exponent for the correlation length in this large-spin limit is always $\nu = 1/2$.

B.1.3 Purity and entanglement

For Gaussian states we can calculate the purity and entanglement negativity from the covariance matrix [249]. Since within the HPA the steady-state is Gaussian we may examine these quantities to understand more about the nature of the phases. This calculation is only analytically tractable in the case of a single dimer, where $h = 0$, and so we focus on this case below. For the lattice, the same procedure can be carried out numerically.

The covariance matrix for the dimer is defined as

$$V_{ij} = \langle (X_i X_j + X_j X_i)\rangle/2 - \langle X_i\rangle\langle X_j\rangle, \tag{B.21}$$

where $X_1 = (c_a + c_a^\dagger)$, $X_2 = i(c_a - c_a^\dagger)$, $X_3 = (c_b + c_b^\dagger)$, $X_4 = i(c_b - c_b^\dagger)$. The covariance matrix has the following structure

$$V = \begin{pmatrix} V_A & V_C \\ V_C^T & V_B \end{pmatrix}, \tag{B.22}$$

where V_A contains correlations within the first site, V_B those in the second site and V_C the cross-correlations. The covariance matrix of the steady-state can be derived from the linearized master equation in the respective phases. The resulting analytic expression for V is already quite involved and not explicitly shown here.

Purity

For a given Gaussian state ρ with co-variance matrix V the purity can be calculated as

$$\mathrm{Tr}\{\rho^2\} = \frac{1}{\sqrt{\det V}}. \tag{B.23}$$

In the case of the $|\Uparrow\Downarrow\rangle$ phase the resulting expression for the purity of the steady-state is given by

$$\mathrm{Tr}\{\rho_0^2\} = \frac{(\Gamma_g + \Gamma_l)^2(\Gamma_g\Gamma_l - g^2)}{g^2(\Gamma_g - \Gamma_l)^2 + \Gamma_g\Gamma_l(\Gamma_g + \Gamma_l)^2}, \tag{B.24}$$

while in the other two phases $|\Uparrow\Uparrow\rangle$ and $|\Downarrow\Downarrow\rangle$ we obtain

$$\mathrm{Tr}\{\rho_0^2\} = \frac{(\Gamma_g - \Gamma_l)^2(g^2 - \Gamma_g\Gamma_l)}{\Gamma_g\Gamma_l(\Gamma_g - \Gamma_l)^2 + g^2(\Gamma_g + \Gamma_l)^2}. \tag{B.25}$$

We see that the purity vanishes at and below the phase boundary and the same behavior is found numerically for larger chains with $h \neq 0$.

Entanglement

We can calculate the entanglement negativity from the covariance matrix as

$$\mathcal{N} = \frac{1}{2}\left(\frac{1}{\eta} - 1\right), \tag{B.26}$$

where

$$\eta = \frac{\sqrt{\Sigma - \sqrt{\Sigma^2 - 4\det V}}}{\sqrt{2}} \tag{B.27}$$

and

$$\Sigma = \det V_A + \det V_B - 2\det V_C. \tag{B.28}$$

By evaluating this expression for both the $|\Uparrow\Uparrow\rangle$ and $|\Downarrow\Downarrow\rangle$ phases, we obtain a vanishing entanglement, $\mathcal{N} = 0$, while the negativity is finite in the $|\Uparrow\Downarrow\rangle$ phase. This can be understood from the fact that in the former two phases the linearized Hamiltonian contains only excitation-conserving interactions, $H \sim$

$c_a^\dagger c_b + c_a c_b^\dagger$, [see Eq. (B.6)], while in the $|\Uparrow\Downarrow\rangle$ phase the Hamiltonian creates correlated pairs of excitations, $H \sim c_a^\dagger c_b^\dagger + c_a c_b$. The resulting expression for the negativity in this phase simplifies along the PT-symmetric line, $\Gamma_g = \Gamma_l = \bar{\Gamma}$ to

$$\mathcal{N} = \frac{g}{2\bar{\Gamma}}. \tag{B.29}$$

Therefore, the maximal amount of entanglement is reached at the transition point $\bar{\Gamma} = g$. The same behavior is also found for larger chains when $h \neq 0$. Note that within the Holstein-Primakoff approximation a finite amount of entanglement is only found between neighbouring spins.

B.2 Mean-field theory

From the master equation Eq. (4.2) we can derive a set of equations of motion for the expectation values of the spin operators, $\langle S_{a,b}^{x,y,z}\rangle$. Under the mean-field approximation, we factorize all expectation values between two spin operators as $\langle AB\rangle \to \langle A\rangle\langle B\rangle$ as explained in Chapter 2.5 and make the replacement $\langle (S^x)^2 + (S^y)^2\rangle = S(S+1) - \langle (S^z)^2\rangle$. We then arrive at the closed but non-linear set of equations,

$$\begin{aligned}
\langle \dot{S}_a^x\rangle &= -\frac{\Gamma_g}{2S}\langle S_a^x\rangle(1+2\langle S_a^z\rangle) + \frac{(g+h)}{S}\langle S_a^z\rangle\langle S_b^y\rangle,\\
\langle \dot{S}_a^y\rangle &= -\frac{\Gamma_g}{2S}\langle S_a^y\rangle(1+2\langle S_a^z\rangle) - \frac{(g+h)}{S}\langle S_a^z\rangle\langle S_b^x\rangle,\\
\langle \dot{S}_a^z\rangle &= \frac{\Gamma_g}{S}\left[S(S+1) - \langle S_a^z\rangle\left(\langle S_a^z\rangle + 1\right)\right] + \frac{(g+h)}{S}(\langle S_a^y\rangle\langle S_b^x\rangle - \langle S_a^x\rangle\langle S_b^y\rangle),\\
\langle \dot{S}_b^x\rangle &= -\frac{\Gamma_l}{2S}\langle S_b^x\rangle(1-2\langle S_b^z\rangle) + \frac{(g+h)}{S}\langle S_a^y\rangle\langle S_b^z\rangle,\\
\langle \dot{S}_b^y\rangle &= -\frac{\Gamma_l}{2S}\langle S_b^y\rangle(1-2\langle S_b^z\rangle) - \frac{(g+h)}{S}\langle S_a^x\rangle\langle S_b^z\rangle,\\
\langle \dot{S}_b^z\rangle &= \frac{\Gamma_l}{S}[S(S+1) - \langle S_b^z\rangle(\langle S_b^z\rangle - 1)] + \frac{(g+h)}{S}(\langle S_a^x\rangle\langle S_b^y\rangle - \langle S_a^y\rangle\langle S_b^x\rangle).
\end{aligned}$$

Here we have dropped the n subscripts in these equations since under the mean-field approximations each unit cell is identical. These equations can then be readily integrated numerically using standard ODE solvers.

C PT-symmetry breaking in open quantum systems

C.1 Mean field equations of motion of PT-symmetric systems

In this appendix, we discuss a basic example of a bipartite quantum system, which illustrates how the same structure of the Liouville operator results in very different equations of motion for the mean values of bosonic, fermionic and spin operators. To do so we consider the following master equation

$$\dot{\rho} = -ig[O_A^\dagger O_B + O_A O_B^\dagger, \rho] + \Gamma_g \mathcal{D}[O_A^\dagger]\rho + \Gamma_l \mathcal{D}[O_B]\rho = \mathcal{L}\rho, \tag{C.1}$$

which has the same structure as the one assumed in most other examples in this paper. In particular, for $\Gamma_l = \Gamma_g$ the Liouvillian $\mathcal{L}$ satisfies the symmetry relation in Eq. (5.8) for arbitrary operators O_A and O_B.

In a first step we assume that the two subsystems are represented by two bosonic modes with annihilation operators a and b. We identify $O_A = a$ and $O_B = b$ and define the vector of expectation values $\vec{\psi}_\mathrm{b} = (\langle a\rangle, \langle b\rangle)^T$. This vector obeys the equation of motion

$$\partial_t \vec{\psi}_\mathrm{b} = -iH_\mathrm{b}\vec{\psi}_\mathrm{b}, \qquad \text{where} \qquad H_\mathrm{b} = \begin{pmatrix} i\Gamma_g & g \\ g & -i\Gamma_l \end{pmatrix}. \tag{C.2}$$

We see that for $\Gamma_l = \Gamma_g$ the Liouvillian PT symmetry is directly reflected in the non-Hermitian two-by-two matrix H_b, which satisfies $(\mathcal{PT})H_\mathrm{b}(\mathcal{PT})^{-1} = H_\mathrm{b}$. We now perform the same calculations with a and b representing fermionic annihilation operators. The mean values of these operators, $\vec{\psi}_\mathrm{f} = (\langle a\rangle, \langle b\rangle)^T$, obey a very similar equation of motion

$$\partial_t \vec{\psi}_\mathrm{f} = -iH_\mathrm{f}\vec{\psi}_\mathrm{f}, \qquad \text{where} \qquad H_\mathrm{f} = \begin{pmatrix} -i\Gamma_g & g \\ g & -i\Gamma_l \end{pmatrix}, \tag{C.3}$$

but in this case $(\mathcal{PT})H_\mathrm{f}(\mathcal{PT})^{-1} \neq H_\mathrm{f}$.

Non-interacting bosons and fermions are rather special, since in both cases the equations of motion for $\langle a\rangle$ and $\langle b\rangle$ are closed. In general, this is not the case and, for example, when considering two $S = 1/2$ particles with $O_A = \sigma_A^-$ and $O_B = \sigma_B^-$ we already obtain 16 coupled equations for the expectation values of all possible combinations of spin operators. While here we do not write out the resulting matrix H_s explicitly, it is straight forward to show

that also in this case $(\mathcal{PT})H_{\rm s}(\mathcal{PT})^{-1} \neq H_{\rm s}$. Basically, this result can already understood by looking at a single spin with loss and gain, i.e.,

$$\dot{\rho} = \Gamma_g \mathcal{D}[\sigma^+]\rho + \Gamma_l \mathcal{D}[\sigma^-]\rho = \mathcal{L}\rho. \tag{C.4}$$

For this system we define the vector $\vec{\psi}_{\rm s} = (\langle\sigma^-\rangle, \langle\sigma^+\rangle, \langle\sigma^+\sigma^-\rangle, \langle\sigma^-\sigma^+\rangle)^T$, which obeys

$$\partial_t \vec{\psi}_{\rm s} = -iH_{\rm s}\vec{\psi}_{\rm s}, \text{ where } H_{\rm s} = \begin{pmatrix} -i(\Gamma_l+\Gamma_g) & 0 & 0 & 0 \\ 0 & -i(\Gamma_l+\Gamma_g) & 0 & 0 \\ 0 & 0 & -2i\Gamma_l & +2i\Gamma_g \\ 0 & 0 & +2i\Gamma_l & -2i\Gamma_g \end{pmatrix}. \tag{C.5}$$

This simple example shows that for spin systems, exchanging gain and loss is not the same as replacing $i \to -i$ in the dynamical matrix for the evolution of mean values.

We conclude that whether or not the symmetry of the Liouville operator defined in Eq. (5.8) maps onto a conventional PT symmetry condition for the equations of motion depends on the type of quantum system under consideration. For this simple example we also find that both the Liouville operator as well as the corresponding non-Hermitian effective Hamiltonian are invariant under a particle-hole transformation,

$$a \to b^\dagger, \qquad b \to \pm a^\dagger, \tag{C.6}$$

where the plus (minus) sign applies to bosons (fermions). However, this invariance is lost when additional energy terms are added, e.g., $H \to H' = H + \omega_0(a^\dagger a + b^\dagger b)$, while it does not affect the PT symmetry.

Bibliography

[1] M. A. Nielsen and I. L. Chuang, *Quantum computation and quantum information* (Cambridge University Press, 2000).

[2] T. D. Ladd, F. Jelezko, R. Laflamme, Y. Nakamura, C. Monroe, and J. L. O'Brien, Quantum computers, *Nature (London)* **464**, 45 (2010).

[3] R. P. Feynman, Simulating physics with computers, *Int. J. Theor. Phys.* **21**, 467 (1982).

[4] S. Lloyd, Universal quantum simulators, *Science* **273**, 1073 (1996).

[5] I. M. Georgescu, S. Ashhab, and F. Nori, Quantum simulation, *Rev. Mod. Phys.* **86**, 153 (2014).

[6] N. Gisin, G. Ribordy, W. Tittel, and H. Zbinden, Quantum cryptography, *Rev. Mod. Phys.* **74**, 145 (2002).

[7] H. Breuer and F. Petruccione, *The theory of open quantum systems* (Oxford University Press, Oxford, UK, 2002).

[8] G. Lindblad, On the generators of quantum dynamical semigroups, *Communications in Mathematical Physics* **48**, 119–130 (1976).

[9] S. Diehl, A. Micheli, A. Kantian, B. Kraus, H. P. Büchler, and P. Zoller, Quantum states and phases in driven open quantum systems with cold atoms, *Nature Phys.* **4**, 878–883 (2008).

[10] J. T. Barreiro, M. Müller, P. Schindler, D. Nigg, T. Monz, M. Chwalla, M. Hennrich, C. F. Roos, P. Zoller, and R. Blatt, An open-system quantum simulator with trapped ions, *Nature* **470**, 486–491 (2011).

[11] F. Verstraete, M. M. Wolf, and J. I. Cirac, Quantum computation and quantum-state engineering driven by dissipation, *Nature Phys.* **5**, 633–636 (2009).

[12] J. I. Cirac, L. J. Garay, R. Blatt, A. S. Parkins, and P. Zoller, Laser cooling of trapped ions: the influence of micromotion, *Phys. Rev. A* **49**, 421 (1994).

[13] C. Monroe, D. M. Meekhof, B. E. King, S. R. Jefferts, W. M. Itano, D. J. Wineland, and P. Gould, Resolved-sideband raman cooling of a

bound atom to the 3d zero-point energy, *Phys. Rev. Lett.* **75**, 4011 (1995).

[14] D. Leibfried, R. Blatt, C. Monroe, and D. Wineland, Quantum dynamics of single trapped ions, *Rev. Mod. Phys* **75**, 281 (2003).

[15] T. Prosen and I. Pizor, Quantum phase transition in a far-from-equilibrium steady state of an xy spin chain, *Phys. Rev. Lett.* **101**, 105701 (2008).

[16] T. E. Lee, S. Gopalakrishnan, and M. D. Lukin, Unconventional magnetism via optical pumping of interacting spin systems, *Phys. Rev. Lett.* **110**, 257204 (2013).

[17] H. Weimer, Variational principle for steady states of dissipative quantum many-body systems, *Phys. Rev. Lett.* **114**, 040402 (2015).

[18] J. Jin, A. Biella, O. Viyuela, L. Mazza, J. Keeling, R. Fazio, and D. Rossini, Cluster mean-field approach to the steady-state phase diagram of dissipative spin systems, *Phys. Rev. X* **6**, 031011 (2016).

[19] R. Rota, F. Storme, N. Bartolo, R. Fazio, and C. Ciuti, Critical behavior of dissipative two-dimensional spin lattices, *Phys. Rev. B* **95**, 134431 (2017).

[20] J. Jin, A. Biella, O. Viyuela, C. Ciuti, R. Fazio, and D. Rossini, Phase diagram of the dissipative quantum ising model on a square lattice, *Phys. Rev. B* **98**, 241108 (2018).

[21] T. O. Puel, S. Chesi, S. Kirchner, and P. Ribeiro, Mixed-order symmetry-breaking quantum phase transition far from equilibrium, *Phys. Rev. Lett.* **122**, 235701 (2019).

[22] H. Landa, M. Schiro, and G. Misguich, Multistability of driven-dissipative quantum spins, *Phys. Rev. Lett.* **124**, 043601 (2020).

[23] S. Morrison and A. S. Parkins, Dynamical quantum phase transitions in the dissipative lipkin-meshkov-glick model with proposed realization in optical cavity qed, *Phys. Rev. Lett.* **100**, 040403 (2008).

[24] E. M. Kessler, G. Giedke, A. Imamoglu, S. F. Yelin, M. D. Lukin, and J. I. Cirac, Dissipative phase transition in a central spin system, *Phys. Rev. A* **86**, 012116 (2012).

[25] J. S. Ferreira and P. Ribeiro, Lipkin-meshkov-glick model with Markovian dissipation: a description of a collective spin on a metallic surface, *Phys. Rev. B* **100**, 184422 (2019).

[26] D. Barberena, R. J. Lewis-Swan, J. K. Thompson, and A. M. Rey, Driven-dissipative quantum dynamics in ultra-long-lived dipoles in an optical cavity, *Phys. Rev. A* **99**, 053411 (2019).

[27] D. F. Walls, P. D. Drummond, S. S. Hassan, and H. J. Carmichael, Non-equilibrium phase transitions in cooperative atomic systems, *Prog. Theor. Phys.* **64** (1978).

[28] J. Hannukainen and J. Larson, Dissipation-driven quantum phase transitions and symmetry breaking, *Phys. Rev. A* **98**, 042113 (2018).

[29] P. D. Drummond and D. F. Walls, Quantum theory of optical bistability. i. nonlinear polarisability model, *J. Phys. A: Math Gen.* **13**, 725 (1980).

[30] W. Casteels, R. Fazio, and C. Ciuti, Critical dynamical properties of a first-order dissipative phase transition, *Phys. Rev. A* **95**, 012128 (2017).

[31] N. Bartolo, F. Minganti, W. Casteels, and C. Ciuti, Exact steadystate of a kerr resonator with one- and two-photon driving and dissipation: controllable wigner-function multimodality and dissipative phase transitions, *Phys. Rev. A* **94**, 033841 (2016).

[32] F. Dimer, B. Estienne, A. S. Parkins, and H. J. Carmichael, Proposed realization of the dicke-model quantum phase transition in an optical cavity qed system, *Phys. Rev. A* **75**, 013804 (2007).

[33] J. M. Fink, A. Dombi, A. Vukics, A. Wallraff, and P. Domokos, Observation of the photon-blockade breakdown phase transition, *Phys. Rev. X* **7**, 011012 (2017).

[34] P. Kirton, M. M. Roses, J. Keeling, and E. G. D. Torre, Introduction to the dicke model: from equilibrium to nonequilibrium, and vice versa, *Adv. Quantum Technol.* **2**, 1970013 (2019).

[35] S. V. Lawande, R. R. Puri, and S. S. Hassan, Non-resonant effects in the fluorescent dicke model. i. exact steady state analysis, *J. Phys. B* **14**, 4171 (1981).

[36] F. Minganti, A. Biella, N. Bartolo, and C. Ciuti, Spectral theory of liouvillians for dissipative phase transitions, *Phys. Rev. A* **98**, 042118 (2018).

[37] A. H. Werner, D. Jaschke, P. Silvi, M. Kliesch, T. Calarco, J. Eisert, and S. Montangero, Positive tensor network approach for simulating open quantum many-body systems, *Phys. Rev. Lett.* **116**, 237201 (2016).

[38] J. Cui, J. I. Cirac, and M. C. Banuls, Variational matrix product operators for the steady state of dissipative quantum systems, *Phys. Rev. Lett.* **114**, 220601 (2015).

[39] R. Orús and G. Vidal, Infinite time-evolving block decimation algorithm beyond unitary evolution, *Phys. Rev. B.* **78**, 155117 (2008).

[40] H. J. Groenewold, "On the principles of elementary quantum mechanics", in (Springer, 1946), pp. 1–56.

[41] J. Schachenmayer, A. Pikovski, and A. M. Rey, Many-body quantum spin dynamics with monte carlo trajectories on a discrete phase space, *Phys. Rev. X* **5**, 011022 (2015).

[42] C. E. Rüter, K. G. Makris, R. El-Ganainy, D. N. Christodoulides, M. Segev, and D. Kip, Observation of parity-time symmetry in optics, *Nature Phys.* **6**, 192 (2010).

[43] B. Peng, S. K. Özdemir, F. Lei, F. Monifi, M. Gianfreda, G. L. Long, S. Fan, F. Nori, C. M. Bender, and L. Yang, Parity-time-symmetric whispering-gallery microcavities, *Nature Phys.* **10**, 394 (2014).

[44] L. Chang, X. Jiang, S. Hua, C. Yang, J. Wen, L. Jiang, G. Li, G. Wang, and M. Xiao, Parity-time symmetry and variable optical isolation in active passive-coupled microresonators, *Nat. Photonics* **8**, 524 (2014).

[45] J. Schindler, A. Li, M. C. Zheng, F. M. Ellis, and T. Kottos, Experimental study of active lrc circuits with pt symmetries, *Phys. Rev. A* **84** (2011).

[46] C. M. Bender, B. K. Berntson, D. Parker, and E. Samuel, Observation of pt phase transition in a simple mechanical system, *Am. J. Phys.* **81**, 173 (2013).

[47] C. M. Bender and S. Boettcher, Real spectra in non-hermitian hamiltonians having pt symmetry, *Phys. Rev. Lett.* **80**, 5243 (1998).

[48] C. M. Bender, Making sense of non-hermitian hamiltonians, *Rep. Prog. Phys.* **70**, 947 (2007).

[49] L. Feng, R. El-Ganainy, and L. Ge, Non-hermitian photonics based on parity?time symmetry, *Nat. Photonics* **11**, 752 (2017).

[50] S. Longhi, Parity-time symmetry meets photonics: a new twist in non-hermitian optics, *EPL* **120**, 64001 (2017).

[51] R. El-Ganainy, K. G. Makris, M. Khajavikhan, Z. H. Musslimani, S. Rotter, and D. N. Christodoulides, Non-hermitian physics and pt symmetry, *Nature Phys.* **14**, 11 (2018).

[52] S. K. Özdemir, S. Rotter, F. Nori, and L. Yang, Parity-time symmetry and exceptional points in photonics, *Nat. Mater.* **18**, 783 (2019).

[53] H. Schomerus, Quantum noise and self-sustained radiation of pt-symmetric systems, *Phys. Rev. Lett.* **104**, 233601 (2010).

[54] G. S. Agarwal and K. Qu, Spontaneous generation of photons in transmission of quantum fields in pt-symmetric optical systems, *Phys. Rev. A* **85**, 031802 (2012).

[55] K. V. Kepesidis, T. J. Milburn, J. Huber, K. G. Makris, S. Rotter, and P. Rabl, Pt-symmetry breaking in the steady state of microscopic gain-loss systems, *New J. Phys.* **18**, 095003 (2016).

[56] S. Scheel and A. Szameit, Pt-symmetric photonic quantum systems with gain and loss do not exist, *EPL* **122**, 34001 (2018).

[57] T. Prosen, Pt-symmetric quantum liouvillean dynamics, *Phys. Rev. Lett.* **109**, 090404 (2012).

[58] G. S. Ohm, *Die galvanische kette* (Berlin, 1827).

[59] D. Gelbwaser-Klimovsky, W. Niedenzu, and G. Kurizki, Thermodynamics of quantum systems under dynamical control, *Adv. At. Mol. Op.* **64** (2015).

[60] S. Vinjanampathy and J. Anders, Quantum thermodynamics, *Contemp. Phys.* **57**, 1 (2016).

[61] J. Goold, M. Huber, A. Riera, L. del Rio, and P. Skrzypczyk, The role of quantum information in thermodynamics — a topical review, *J. Phys. A: Math. Theor* **49**, 143001 (2016).

[62] R. Alicki and R. Kosloff, *Introduction to quantum thermodynamics: history and prospects*, 2018, arXiv:1801.08314.

[63] J. Millen and A. Xuereb, Perspective: quantum thermodynamics, *New J. Phys.* **18**, 011002 (2016).

[64] H. E. D. Scovil and E. O. Schulz-DuBois, Three-level masers as heat engines, *Phys. Rev. Lett.* **2**, 262 (1959).

[65] E. Geva and R. Kosloff, Three-level quantum amplifier as a heat engine: a study in finite-time thermodynamics, *Phys. Rev. E* **49**, 3903 (1994).

[66] M. O. Scully, M. S. Zubairy, G. S. Agarwal, and H. Walther, Extracting work from a single heat bath via vanishing quantum coherence, *Science* **299**, 862 (2003).

[67] T. D. Kieu, The second law and maxwell's demon and work derivable from quantum heat engines, *Phys. Rev. Lett.* **93**, 140403 (2004).

[68] H. T. Quan, Y. Liu, C. P. Sun, and F. Nori, Quantum thermodynamic cycles and quantum heat engines, *Phys. Rev. E* **76**, 031105 (2007).

[69] N. Linden, S. Popescu, and P. Skrzypczyk, How small can thermal machines be? the smallest possible refrigerator, *Phys. Rev. Lett.* **105**, 130401 (2010).

[70] O. Abah, J. Ronagel, G. Jacob, S. Deffner, F. Schmidt-Kaler, K. Singer, and E. Lutz, Single-ion heat engine at maximum power, *Phys. Rev. Lett.* **109**, 203006 (2012).

[71] D. Gelbwaser-Klimovsky, R. Alicki, and G. Kurizki, Minimal universal quantum heat machine, *Phys. Rev. E* **87**, 012140 (2013).

[72] R. Gallego, A. Riera, and J. Eisert, Thermal machines beyond the weak coupling regime, *New J. Phys.* **16**, 125009 (2014).

[73] K. Zhang, F. Bariani, and P. Meystre, Quantum optomechanical heat engine, *Phys. Rev. Lett.* **112**, 150602 (2014).

[74] C. Bergenfeldt, P. Samuelsson, B. Sothmann, C. Flindt, and M. Büttiker, Hybrid microwave-cavity heat engine, *Phys. Rev. Lett.* **112**, 076803 (2014).

[75] M. Brunelli, A. Xuereb, A. Ferraro, G. D. Chiara, N. Kiesel, and M. Paternostro, Out-of-equilibrium thermodynamics of quantum optomechanical systems, *New J. Phys.* **17**, 035016 (2015).

[76] C. Elouard, M. Richard, and A. Auffeves, Reversible work extraction in a hybrid opto-mechanical system, *New J. Phys.* **17**, 055018 (2015).

[77] A. Dechant, N. Kiesel, and E. Lutz, All-optical nanomechanical heat engine, *Phys. Rev. Lett.* **114**, 183602 (2015).

[78] A. Mari, A. Farace, and V. Giovannetti, Quantum optomechanical piston engines powered by heat, *J. Phys. B* **48**, 175501 (2015).

[79] S.-W. Li, M. B. Kim, G. S. Agarwal, and M. O. Scully, Quantum statistics of a single-atom heat engine, *Phys. Rev. A* **96**, 063806 (2017).

[80] T. Hugel, N. B. Holland, A. Cattani, L. Moroder, M. Seitz, and H. E. Gaub, Single-molecule optomechanical cycle, *Science* **296**, 1103 (2002).

[81] P. G. Steeneken, K. L. Phan, M. J. Goossens, G. E. J. Koops, G. J. A. M. Brom, C. van der Avoort, and J. T. M. van Beek, Piezoresistive heat engine and refrigerator, *Nature Phys.* **7**, 354 (2011).

[82] V. Blickle and C. Bechinger, Realization of a micrometre-sized stochastic heat engine, *Nature Phys.* **8**, 143 (2012).

[83] J.-P. Brantut, C. Grenier, J. Meineke, D. Stadler, S. Krinner, C. Kollath, T. Esslinger, and A A. Georges, Thermoelectric heat engine with ultracold atoms, *Science* **342**, 713 (2013).

[84] H. Thierschmann, R. Sanchez, B. Sothmann, F. Arnold, C. Heyn, W. Hansen, H. Buhmann, and L. W. Molenkamp, Three-terminal energy harvester with coupled quantum dots, *Nat. Nanotechnol.* **10**, 854 (2015).

[85] J. R. nagel, S. T. Dawkins, K. N. Tolazzi, O. Abah, E. Lutz, F. Schmidt-Kaler, and K. Singer, A single-atom heat engine, *Science* **352**, 325 (2016).

[86] F. Schmidt, A. Magazza, A. Callegari, L. Biancofiore, F. Cichos, and G. Volpe, Microscopic engine powered by critical demixing, *Phys. Rev. Lett.* **120**, 068004 (2018).

[87] J. Klaers, S. Faelt, A. Imamoglu, and E. Togan, Squeezed thermal reservoirs as a resource for a nano-mechanical engine beyond the carnot limit, *Phys. Rev. X* **7**, 031044 (2017).

[88] J. Huber and P. Rabl, Active energy transport and the role of symmetry breaking in microscopic power grids, *Phys. Rev. A* **100**, 012129 (2019).

[89] J. Huber, P. Kirton, and P. Rabl, Non-equilibrium magnetic phases in spin lattices with gain and loss, *Phys. Rev. A* **102**, 012219 (2020).

[90] J. Huber, P. Kirton, S. Rotter, and P. Rabl, Emergence of pt-symmetry breaking in open quantum systems, *SciPost Phys.* **9**, 052 (2020).

[91] J. Huber, P. Kirton, and P. Rabl, Phase-space methods for simulating the dissipative many-body dynamics of collective spin systems, *SciPost Phys.* **10**, 045 (2021).

[92] J. Huber, A. M. Rey, and P. Rabl, *Realistic simulations of spin squeezing and cooperative coupling effects in large ensembles of interacting two-level systems*, 2021, arXiv:2103.07402.

[93] A. Levy and R. Kosloff, The local approach to quantum transport may violate the second law of thermodynamics, *EPL* **107**, 20004 (2014).

[94] J. Dalibard, Y. Castin, and K. M. lmer, Wave-function approach to dissipative processes in quantum optics, *Phys. Rev. Lett.* **68**, 580 (1992).

[95] A. J. Daley, Quantum trajectories and open many-body quantum systems, *Adv. Phys.* **63**, 77 (2014).

[96] N. Gisin and I. C. Percival, The quantum-state diffusion model applied to open systems, *Journal of Physics A: Mathematical and General* **25**, 5677 (1992).

[97] C. W. Gardiner and P. Zoller, *Quantum noise* (Springer, 2000).

[98] E. P. Wigner, "On the quantum correction for thermodynamic equilibrium", in *Part i: physical chemistry. part ii: solid state physics* (1997), pp. 110–120.

[99] E. C. G. Sudarshan, Equivalence of semiclassical and quantum mechanical descriptions of statistical light beams, *Phys. Rev. Lett.* **10**, 277 (1963).

[100] K. Husimi, Some formal properties of the density matrix, *Proceedings of the Physico-Mathematical Society of Japan. 3rd Series* **22**, 264–314 (1940).

[101] K. E. Cahill and R. J. Glauber, Density operators and quasiprobability distributions, *Phys. Rev.* **177**, 1882 (1969).

[102] D. F. Walls and G. J. Milburn, *Quantum optics* (Springer, 1994).

[103] P. D. Drummond and C. W. Gardiner, Generalised prepresentations in quantum optics, *Journal of Physics A: Mathematical and General* **13**, 2353 (1980).

[104] A. Gilchrist, C. Gardiner, and P. Drummond, Positive p representation: application and validity, *Phys. Rev. A* **55**, 3014 (1997).

[105] M. J. Steel, M. K. Olsen, L. I. Plimak, P. D. Drummond, S. M. Tan, M. J. Collett, D. F. Walls, and R. Graham, Dynamical quantum noise in trapped bose-einstein condensates, *Phys. Rev. A* **58**, 4824 (1998).

[106] P. Blakie, A. Bradley, M. Davis, R. Ballagh, and C. Gardiner, Dynamics and statistical mechanics of ultra-cold bose gases using c-field techniques, *Advances in Physics* **57**, 363 (2008).

[107] A. Polkovnikov, Phase space representation of quantum dynamics, *Ann. Phys.* **325**, 1790 (2010).

[108] C. Gardiner, *Stochastic methods* (Springer, Berlin, 2009).

[109] R. Kubo, Generalized cumulant expansion method, *Journal of the Physical Society of Japan* **17**, 1100–1120 (1962).

[110] M. Zens, D. O. Krimer, and S. Rotter, Critical phenomena and nonlinear dynamics in a spin ensemble strongly coupled to a cavity. ii. semiclassical-to-quantum boundary, *Phys. Rev. A* **100**, 013856 (2019).

[111] K. Henschel, J. Majer, J. Schmiedmayer, and H. Ritsch, Cavity qed with an ultracold ensemble on a chip: prospects for strong magnetic coupling at finite temperatures, *Phys. Rev. A* **82**, 033810 (2010).

[112] H. A. M. Leymann, A. Foerster, and J. Wiersig, Expectation value based equation-of-motion approach for open quantum systems: a general formalism, *Phys. Rev. B* **89**, 085308 (2014).

[113] A. Vardi and J. R. Anglin, Bose-einstein condensates beyond mean field theory: quantum backreaction as decoherence, *Phys. Rev. Lett.* **86**, 568–571 (2001).

[114] S. Krämer and H. Ritsch, Generalized mean-field approach to simulate the dynamics of large open spin ensembles with long range interactions, *Eur. Phys. J. D* **69**, 1–11 (2015).

[115] D. Plankensteiner, C. Hotter, and H. Ritsch, *Quantumcumulants.jl: a julia framework for generalized mean-field equations in open quantum systems*, 2021, arXiv:2103.07402.

[116] F. Verstraete, V. Murg, and J. Cirac, Matrix product states, projected entangled pair states, and variational renormalization group methods for quantum spin systems, *Adv. Phys.* **57**, 143 (2008).

[117] G. Vidal, Efficient simulation of one-dimensional quantum many-body systems, *Phys. Rev. Lett.* **93**, 040502 (2004).

[118] S. R. White and A. E. Feiguin, Real-time evolution using the density matrix renormalization group, *Phys. Rev. Lett.* **93**, 076401 (2004).

[119] A. J. Daley, C. Kollath, U. Schollwöck, and G. Vidal, Time-dependent density-matrix renormalization-group using adaptive effective hilbert spaces, *J. of Stat. Mech.: Theory and Exp.* **2004**, P04005 (2004).

[120] U. Schollwöck, The density-matrix renormalization group in the age of matrix product states, *Ann. Phys.* **326**, 96 (2011).

[121] M. B. Hastings, An area law for one-dimensional quantum systems, *Journal of Statistical Mechanics: Theory and Experiment 2007*, P08024 (2007).

[122] J. J. Garcia-Ripoll, Time evolution of matrix product states, *New J. Phys.* **8**, 305 (2006).

[123] S. Paeckel, T. Köhler, A. Swoboda, S. R. Manmana, U. Schollwöck, and C. Hubig, Timeevolution methods for matrix-product states, *Ann. Phys.* **411**, 167998 (2019).

[124] L. Bonnes and A. M. Läuchli, *Superoperators versus trajectories for matrix product state simulations of open quantum system: a case study*, 2014, arXiv:1411.4831.

[125] E. Mascarenhas, H. Flayac, and V. Savona, Matrix-product-operator approach to the nonequilibrium steady state of driven-dissipative quantum arrays, *Phys. Rev. A* **92**, 022116 (2015).

[126] G. Vidal, Classical simulation of infinite-size quantum lattice systems in one spatial dimension, *Phys. Rev. Lett.* **98**, 070201 (2007).

[127] F. Verstraete, M. M. Wolf, D. Perez-Garcia, and J. I. Cirac, Criticality, the area law, and the computational power of projected entangled pair states, *Phys. Rev. Lett.* **96**, 220601 (2006).

[128] E. M. Stoudenmire and S. R. White, Studying two-dimensional systems with the density matrix renormalization group, *Annu. Rev. Condens. Matter Phys.* **3**, 111 (2012).

[129] J. Jordan, R. Orus, G. Vidal, F. Verstraete, and J. I. Cirac, Classical simulation of infinite-size quantum lattice systems in two spatial dimensions, *Phys. Rev. Lett.* **101**, 250602 (2008).

[130] A. Kshetrimayum, H. Weimer, and A R. Orus, Simple tensor network algorithm for two-dimensional steady states, *Nat. Commun.* **8**, 1291 (2017).

[131] C. M. Keever and M. H. Szymańska, *Dynamics of two-dimensional open quantum lattice models with tensor networks*, 2020, arXiv:2012.12233.

[132] D. Kilda, A. Biella, M. Schiro, R. Fazio, and J. Keeling, *On the stability of the infinite projected entangled pair operator ansatz for driven-dissipative 2d lattices*, 2020, arXiv:2012.03095.

[133] J. Chen, S. Cheng, H. Xie, L. Wang, and T. Xiang, On the equivalence of restricted boltzmann machines and tensor network states, *Phys. Rev. B* **97**, 085104 (2018).

[134] X. Gao and L.-M. Duan, Efficient representation of quantum many-body states with deep neural networks, *Nat. Commun.* **8**, 662 (2017).

[135] G. Carleo and M. Troyer, Solving the quantum many-body problem with artificial neural networks, *Science* **355**, 602 (2017).

[136] N. Yoshioka and R. Hamazaki, Constructing neural stationary states for open quantum many-body systems, *Phys. Rev. B* **99**, 214306 (2019).

[137] F. Vicentini, A. Biella, N. Regnault, and C. Ciuti, Variational neural network ansatz for steady states in open quantum systems, *Phys. Rev. Lett.* **122**, 250503 (2019).

[138] A. Nagy and V. Savona, Variational quantum monte carlo with neural network ansatz for open quantum systems, *Phys. Rev. Lett.* **122**, 250501 (2019).

[139] M. J. Hartmann and G. Carleo, Neural-network approach to dissipative quantum many-body dynamics, *Phys. Rev. Lett.* **122**, 250502 (2019).

[140] K. V. Kepesidis, S. D. Bennett, S. Portolan, M. D. Lukin, and P. Rabl, Phonon cooling and lasing with nitrogen-vacancy centers in diamond, *Phys. Rev. B* **88**, 064105 (2013).

[141] M. T. Mitchison and M. Plenio, Non-additive dissipation in open quantum networks out of equilibrium, *New J. Phys.* **20**, 033005 (2018).

[142] P. P. Hofer, M. Perarnau-Llobet, L. D. M Miranda, G. Haack, R. Silva, J. B. Brask, and N. Brunner, Markovian master equations for quantum thermal machines: local versus global approach, *New J. Phys.* **19**, 123037 (2017).

[143] D. Hatanaka, I. Mahboob, K. Onomitsu, and H. Yamaguchi, Phonon waveguides for electromechanical circuits, *Nat. Nanotechnol.* **9**, 520 (2014).

[144] P. Huang, L. Zhang, J. Zhou, T. Tian, P. Yin, C. Duan, and J. Du, Nonreciprocal radio frequency transduction in a parametric mechanical artificial lattice, *Phys. Rev. Lett.* **117**, 017701 (2016).

[145] J. Cha and C. Daraio, Electrical tuning of elastic wave propagation in nanomechanical lattices at mhz frequencies, *Nat. Nanotechnol.* **13**, 1016 (2018).

[146] R. N. Patel, Z. Wang, W. Jiang, C. J. Sarabalis, J. T. Hill, and A. H. Safavi-Naeini, A single-mode phononic wire, *Phys. Rev. Lett.* **121**, 040501 (2018).

[147] G.-D. Lin and L.-M. Duan, Equilibration and temperature distribution in a driven ion chain, *New J. Phys.* **13**, 075015 (2011).

[148] A. Bermudez, M. Bruderer, and M. B. Plenio, Controlling and measuring quantum transport of heat in trapped-ion crystals, *Phys. Rev. Lett.* **111**, 040601 (2013).

[149] M. Ramm, T. Pruttivarasin, and H. Häffner, Energy transport in trapped ion chains, *New J. Phys.* **16**, 063062 (2014).

[150] D. L. Underwood, W. E. Shanks, J. Koch, and A. A. Houck, Low-disorder microwave cavity lattices for quantum simulation with photons, *Phys. Rev. A* **86**, 023837 (2012).

[151] M. Fitzpatrick, N. M. Sundaresan, A. C. Y. Li, J. Koch, and A. A. Houck, Observation of a dissipative phase transition in a one-dimensional circuit qed lattice, *Phys. Rev. X* **7**, 011016 (2017).

[152] M. Mirhosseini, E. Kim, V. S. Ferreira, M. Kalaee, A. Sipahigil, A. J. Keller, and O. Painter, Superconducting metamaterials for waveguide quantum electrodynamics, *Nat. Commun.* **9**, 3706 (2018).

[153] M. Aspelmeyer, T. J. Kippenberg, and F. Marquardt, Cavity optomechanics, *Rev. Mod. Phys.* **86**, 1391 (2014).

[154] X. Gu, A. F. Kockum, A. Miranowicz, Y.-X. Liu, and F. Nori, Microwave photonics with superconducting quantum circuits, *Phys. Rep.* **718**, 1 (2017).

[155] A. Asadian, D. Manzano, M. Tiersch, and H. J. Briegel, Heat transport through lattices of quantum harmonic oscillators in arbitrary dimensions, *Phys. Rev. E* **87**, 012109 (2013).

[156] B. Peng, S. K. Özdemir, S. Rotter, H. Yilmaz, M. Liertzer, F. Moni, C. M. Bender, F. Nori, and L. Yang, Loss-induced suppression and revival of lasing, *Science* **346**, 328 (2014).

[157] M. Brandstetter, M. Liertzer, C. Deutsch, P. Klang, J. Schöberl, H. E. Türeci, G. Strasser, K. Unterrainer, and S. Rotter, Reversing the pump dependence of a laser at an exceptional point, *Nat. Commun.* **5**, 4034 (2014).

[158] A. U. Hassan, H. Hodaei, M. A. Miri, M. Khajavikhan, and D. N. Christodoulides, Nonlinear reversal of the pt-symmetric phase transition in a system of coupled semiconductor microring resonators, *Phys. Rev. A* **92**, 063807 (2015).

[159] S. Diehl, A. Tomadin, A. Micheli, R. Fazio, and P. Zoller, Dynamical phase transitions and instabilities in open atomic many-body systems, *Phys. Rev. Lett.* **105**, 015702 (2010).

[160] D. Nagy, G. Szirmai, and P. Domokos, Critical exponent of a quantum-noise-driven phase transition: the open-system dicke model, *Phys. Rev. A* **84**, 043637 (2011).

[161] B. Öztop, M. Bordyuh, O. E. Müstecaploglu, and H. E. Türeci, Excitations of optically driven atomic condensate in a cavity: theory of photodetection measurements, *New J. Phys.* **14**, 085011 (2012).

[162] W. Casteels, F. Storme, A. LeBoite, and C. Ciuti, Power laws in the dynamic hysteresis of quantum nonlinear photonic resonators, *Phys. Rev. A* **93**, 033824 (2016).

[163] M.-J. Hwang, P. Rabl, and M. B. Plenio, Dissipative phase transition in the open quantum rabi models, *Phys. Rev. A* **97**, 013825 (2018).

[164] K. Zyczkowski, P. Horodecki, A. Sanpera, and M. Lewenstein, Volume of the set of separable states, *Phys. Rev. A* **58**, 883 (1998).

[165] G. Vidal and R. F. Werner, Computable measure of entanglement, *Phys. Rev. A* **65**, 032314 (2002).

[166] D. Roscher, S. Diehl, and M. Buchhold, Phenomenology of first-order dark-state phase transitions, *Phys. Rev. A* **98**, 062117 (2018).

[167] N. D. Mermin and H. Wagner, Absence of ferromagnetism or antiferromagnetism in one- or two-dimensional isotropic heisenberg models, *Phys. Rev. Lett.* **17**, 1133 (1966).

[168] M. K. Olsen, L. I. Plimak, S. Rebic, and A. S. Bradley, Phase-space analysis of bosonic spontaneous emission, *Optics Commun.* **254**, 271 (2005).

[169] R. Ng and E. S. Sörensen, Exact real-time dynamics of quantum spin systems using the positive-p representation, *Phys. A: Math. Theor.* **44**, 065305 (2011).

[170] R. Ng, E. S. Sörensen, and P. Deuar, Simulation of the dynamics of many-body quantum spin systems using phase-space techniques, *Phys. Rev. B* **88**, 144304 (2013).

[171] S. Sachdev, *Quantum phase transitions* (Cambridge University Press, 2001).

[172] A. Bar and D. Mukamel, Mixed-order phase transition in a one-dimensional model, *Phys. Rev. Lett.* **112**, 015701 (2014).

[173] O. Vazquez-Candanedo, J. C. Hernandez-Herrejon, F. M. Izrailev, and D. N. Christodoulides, Gain- or loss-induced localization in one-dimensional pt-symmetric tight-binding models, *Phys. Rev. A* **89**, 013832 (2014).

[174] A. J. Kollar, A. T. Papageorge, V. D. Vaidya, Y. Guo, J. Keeling, and B. L. Lev, Supermode-density-wave-polariton condensation with a bose-einstein condensate in a multimode cavity, *Nature Commun.* **8**, 14386 (2017).

[175] A. Morales, P. Zupancic, J. Leonard, T. Esslinger, and T. Donner, Coupling two order parameters in a quantum gas, *Nat. Mater.* **17**, 686 (2018).

[176] A. Morales, D. Dreon, X. Li, A. B. artner, P. Zupancic, T. Donner, and T. Esslinger, Two-mode dicke model from non-degenerate polarization modes, *Phys. Rev. A* **100**, 013816 (2019).

[177] A. D. Greentree, C. Tahan, J. H. Cole, and L. C. L. Hollenberg, Quantum phase transitions of light, *Nature Phys.* **2**, 856 (2006).

[178] M. J. Hartmann, F. G. S. L. Brandao, and M. B. Plenio, Strongly interacting polaritons in coupled arrays of cavities, *Nature Phys.* **2**, 849 (2006).

[179] J. D. Thompson, T. G. Tiecke, N. P. de Leon, J. Feist, A. V. Akimov, M. Gullans, A. S. Zibrov, V. Vuletic, and M. D. Lukin, Coupling a single trapped atom to a nanoscale optical cavity, *Science* **340**, 1202 (2013).

[180] A. Goban, C.-L. Hung, S. P. Yu, J. D. Hood, J. A. Muniz, J. H. Lee, M. J. Martin, A. C. McClung, K. S. Choi, D. E. Chang, O. Painter, and H. J. Kimble, Atom-light interactions in photonic crystals, *Nature Commun.* **5**, 3808 (2014).

[181] L. Zou, D. Marcos, S. Diehl, S. Putz, J. Schmiedmayer, J. Majer, and P. Rabl, Implementation of the dicke lattice model in hybrid quantum system arrays, *Phys. Rev. Lett.* **113**, 023603 (2014).

[182] M. Naghiloo, M. Abbasi, Y. N. Joglekar, and K. W. Murch, Quantum state tomography across the exceptional point in a single dissipative qubit, *Nature Phys.* **15**, 1232 (2019).

[183] Y. Wu, W. Liu, J. Geng, X. Song, X. Ye, C.-K. Duan, X. Rong, and J. Du, Observation of parity-time symmetry breaking in a single-spin system, *Science* **364**, 878 (2019).

[184] J. Dalibard, Y. Castin, and K. M. lmer, Wave-function approach to dissipative processes in quantum optics, *Phys. Rev. Lett.* **68**, 580 (1992).

[185] T. E. Lee and C.-K. Chan, Heralded magnetism in non-hermitian atomic systems, *Phys. Rev. X* **4**, 041001 (2014).

[186] Y. Ashida, S. Furukawa, and M. Ueda, Parity-time-symmetric quantum critical phenomena, *Nature Commun.* **8**, 15791 (2017).

[187] T. Prosen, Generic examples of pt-symmetric qubit (spin-1/2) liouvillian dynamics, *Phys. Rev. A* **86** (2012).

[188] M. van Caspel and V. Gritsev, Symmetry-protected coherent relaxation of open quantum systems, *Phys. Rev. A* **97**, 052106 (2018).

[189] D. Huybrechts, F. Minganti, F. Nori, M. Wouters, and N. Shammah, Validity of mean-field theory in a dissipative critical system: liouvillian gap, pt-symmetric antigap, and permutational symmetry in the xyz model, *Phys. Rev. B* **101**, 214302 (2020).

[190] E. J. Bergholtz, J. C. Budich, and F. K. Kunst, *Exceptional topology of non-hermitian systems*, 2019, arXiv:1912.10048.

[191] K. Kawabata, K. Shiozaki, M. Ueda, and M. Sato, Symmetry and topology in non-hermitian physics, *Phys. Rev. X* **9**, 041015 (2019).

[192] H. Zhou and J. Y. Lee, Periodic table for topological bands with non-hermitian symmetries, *Phys. Rev. B* **99**, 235112 (2019).

[193] Y. Ashida, Z. Gong, and M. Ueda, *Non-hermitian physics*, 2020, arXiv:2006.01837.

[194] S. Lieu, M. McGinley, and N. R. Cooper, Tenfold way for quadratic lindbladians, *Phys. Rev. Lett.* **124**, 040401 (2020).

[195] A. Altland, M. Fleischhauer, and S. Diehl, *Symmetry classes of open fermionic quantum matter*, 2020, arXiv:2007.10448.

[196] C.-K. Chiu, J. C. Y. Teo, A. P. Schnyder, and S. Ryu, Classification of topological quantum matter with symmetries, *Rev. Mod. Phys.* **88**, 035005 (2016).

[197] T. Holstein and H. Primakoff, Field dependence of the intrinsic domain magnetization of a ferromagnet, *Phys. Rev.* **58**, 1098 (1940).

[198] A. Serafini, F. Illuminati, M. G. Paris, and S. D. Siena, Entanglement and purity of two-mode gaussian states in noisy channels, *Phys. Rev. A* **69**, 022318 (2014).

[199] M. L. Mehta, *Random matrices* (Elsevier, 2004).

[200] A. Pick, S. Silberstein, N. Moiseyev, and N. Bar-Gill, Robust mode conversion in nv centers using exceptional points, *Phys. Rev. Research* **1**, 013015 (2019).

[201] F. Minganti, A. Miranowicz, R. W. Chhajlany, and F. Nori, Quantum exceptional points of non-hermitian hamiltonians and liouvillians: the effects of quantum jumps, *Phys. Rev. A* **100**, 062131 (2019).

[202] M. Müller, S. Diehl, G. Pupillo, and P. Zoller, Engineered open systems and quantum simulations with atoms and ions, *Adv. At. Mol. Opt. Phys.* **61** (2012).

[203] F. Vicentini, F. Minganti, R. Rota, G. Orso, and C. Ciuti, Critical slowing down in driven-dissipative bose-hubbard lattices, *Phys. Rev. A* **97**, 013853 (2018).

[204] P. Deuar, A. Ferrier, M. Matuszewski, G. Orso, and M. H. S. ska, Fully quantum scalable description of driven-dissipative lattice models, *PRX Quantum* **2**, 010319 (2021).

[205] R. R. Puri and S. V. Lawande, Exact steady-state density operator for a collective atomic system in an external field, *Phys. Lett. A* **73**, 200 (1979).

[206] D. J. Wineland, J. J. Bollinger, W. M. Itano, F. L. Moore, and D. J. Heinzen, Spin squeezing and reduced quantum noise in spectroscopy, *Phys. Rev. A* **46** (1992).

[207] A. Sorensen, L.-M. Duan, J. I. Cirac, and P. Zoller, Many-particle entanglement with bose-einstein condensates, *Nature* **409**, 63–66 (2001).

[208] J. Esteve, C. Gross, A. Weller, S. Giovanazzi, and M. K. Oberthaler, Squeezing and entanglement in a bose einstein condensate, *Nature (London)* **455**, 1216 (2008).

[209] J. Appel, P. J. Windpassinger, D. Oblak, U. B. Hoff, N. K. rgaard, and E. S. Polzik, Mesoscopic atomic entanglement for precision measurements beyond the standard quantum limit, *PNAS* **106**, 10960 (2009).

[210] M. F. Riedel, P. Böhi, Y. Li, T. W. Hänsch, A. Sinatra, and P. Treutlein, Atom-chip-based generation of entanglement for quantum metrology, *Nature (London)* **464**, 1170 (2010).

[211] M. H. Schleier-Smith, I. D. Leroux, and V. Vuletic, States of an ensemble of two-level atoms with reduced quantum uncertainty, *Phys. Rev. Lett.* **104**, 073604 (2010).

[212] O. Hosten, N. J. Engelsen, R. Krishnakumar, and M. A. Kasevich, Measurement noise 100 times lower than the quantum projection limit using entangled atoms, *Nature (London)* **529**, 505 (2016).

[213] K. C. Cox, G. P. Greve, J. M. Weiner, and J. K. Thompson, Deterministic squeezed states with collective measurements and feedback, *Phys. Rev. Lett.* **116**, 093602 (2016).

[214] L. Pezze, A. Smerzi, M. K. Oberthaler, R. Schmied, and P. Treutlein, Quantum metrology with nonclassical states of atomic ensembles, *Rev. Mod. Phys.* **90**, 035005 (2018).

[215] E. Pedrozo-Penafiel, S. Colombo, C. Shu, A. F. Adiyatullin, Z. Li, E. Mendez, B. Braverman, A. Kawasaki, D. Akamatsu, Y. Xiao, and V. Vuletic, Entanglement-enhanced optical atomic clock, *Nature (London)* **588**, 414 (2020).

[216] S. S. Szigeti, O. Hosten, and S. A. Haine, *Improving cold-atom sensors with quantum entanglement: prospects and challenges*, 2020, arXiv:2010.09168.

[217] J. W. Britton, B. C. Sawyer, A. C. Keith, C.-C. J. Wang, J. K. Freericks, H. Uys, M. J. Biercuk, and J. J. Bollinger, Engineered two-dimensional ising interactions in a trapped-ion quantum simulator with hundreds of spins, *Nature (London)* **484**, 489 (2012).

[218] R. Islam, C. Senko, W. C. Campbell, S. Korenblit, J. Smith, A. Lee, E. E. Edwards, C.-C. J. Wang, J. K. Freericks, and C. Monroe, Emergence and frustration of magnetism with variable-range interactions in a quantum simulator, *Science* **340**, 583 (2013).

[219] P. Richerme, Z.-X. Gong, A. Lee, C. Senko, J. Smith, M. Foss-Feig, S. Michalakis, A. V. Gorshkov, and C. R. Monroe, Non-local propagation of correlations in quantum systems with long-range interactions, *Nature (London)* **511**, 198 (2014).

[220] J. G. Bohnet, B. C. Sawyer, J. W. Britton, M. L. Wall, A. M. Rey, M. Foss-Feig, and J. J. Bollinger, Quantum spin dynamics and entanglement generation with hundreds of trapped ions, *Science* **352**, 1297 (2016).

[221] J. Zhang, G. Pagano, P. W. Hess, A. Kyprianidis, P. Becker, H. Kaplan, A. V. Gorshkov, Z. X. Gong, and C. R. Monroe, Observation of a many-body dynamical phase transition with a 53-qubit quantum simulator, *Nature (London)* **551**, 601 (2017).

[222] N. Friis, O. Marty, C. Maier, C. Hempel, M. Holzäpfel, P. Jurcevic, M. B. Plenio, M. Huber, C. Roos, R. Blatt, and B. Lanyon, Observation of entangled states of a fully controlled 20-qubit system, *Phys. Rev. X* **8**, 021012 (2018).

[223] C. D. Bruzewicz, J. Chiaverini, R. McConnell, and J. M. Sage, Trapped-ion quantum computing: progress and challenges, *Appl. Phys. Rev.* **6**, 021314 (2019).

[224] H. Labuhn, D. Barredo, S. Ravets, S. de Lësëleuc, T. Macri, T. Lahaye, and A. Browaeys, Tunable two-dimensional arrays of single rydberg atoms for realizing quantum ising models, *Nature (London)* **534**, 667 (2016).

[225] H. Bernien, S. Schwartz, A. Keesling, H. Levine, A. Omran, H. Pichler, S. Choi, A. S. Zibrov, M. Endres, M. Greiner, V. Vuletic, and M. D. Lukin, Probing many-body dynamics on a 51-atom quantum simulator, *Nature (London)* **551**, 579 (2017).

[226] E. Guardado-Sanchez, P. T. Brown, D. Mitra, T. Devakul, D. A. Huse, P. Schauß, and W. S. Bakr, Probing the quench dynamics of antiferromagnetic correlations in a 2d quantum ising spin system, *Phys. Rev. X* **8**, 021069 (2018).

[227] I. S. Madjarov, J. P. Covey, A. L. Shaw, J. Choi, A. C. A. Kale, H. Pichler, V. Schkolnik, J. R. Williams, and M. Endres, High-fidelity entanglement and detection of alkaline-earth rydberg atoms, *Nat. Phys.* **16**, 857 (2020).

[228] A. Browaeys and T. Lahaye, Many-body physics with individually controlled rydberg atoms, *Nat. Phys.* **16**, 132 (2020).

[229] P. Scholl, M. Schuler, H. J. Williams, A. A. Eberharter, D. Barredo, K.-N. Schymik, V. Lienhard, L.-P. Henry, T. C. Lang, T. Lahaye, A. M. Läuchli, and A. Browaeys, *Programmable quantum simulation of 2d antiferromagnets with hundreds of rydberg atoms*, 2020, arXiv:2012.12268.

[230] S. Ebadi, T. T. Wang, H. Levine, A. Keesling, G. Semeghini, A. Omran, D. Bluvstein, R. Samajdar, H. Pichler, W. W. Ho, S. Choi, S. Sachdev, M. Greiner, V. Vuletic, and M. D. Lukin, *Quantum phases of matter on a 256-atom programmable quantum simulator*, 2020, arXiv:2012.12281.

[231] D. I. Schuster, A. P. Sears, E. Ginossar, L. DiCarlo, L. Frunzio, J. J. L. Morton, H. Wu, G. A. D. Briggs, B. B. Buckley, D. D. Awschalom, and R. J. Schoelkopf, High-cooperativity coupling of electron-spin ensembles to superconducting cavities, *Phys. Rev. Lett.* **105**, 140501 (2010).

[232] Y. Kubo, F. R. Ong, P. Bertet, D. Vion, V. Jacques, D. Zheng, A. Dreau, J.-F. Roch, A. Auffeves, F. Jelezko, J. Wrachtrup, M. F. Barthe, P. Bergonzo, and D. Esteve, Strong coupling of a spin ensemble to a superconducting resonator, *Phys. Rev. Lett.* **105**, 140502 (2010).

[233] R. Amsüss, C. Koller, T. Nöbauer, S. Putz, S. Rotter, K. Sandner, S. Schneider, M. Schramböck, G. Steinhauser, H. Ritsch, J. Schmiedmayer, and J. Majer, Cavity qed with magnetically coupled collective spin states, *Phys. Rev. Lett.* **107**, 060502 (2011).

[234] S. Probst, H. Rotzinger, S. Wünsch, P. Jung, M. Jerger, M. Siegel, A. V. Ustinov, and P. A. Bushev, Anisotropic rare-earth spin ensemble strongly coupled to a superconducting resonator, *Phys. Rev. Lett.* **110**, 157001 (2013).

[235] Z.-L. Xiang, S. Ashhab, J. Q. You, and F. Nori, Hybrid quantum circuits: superconducting circuits interacting with other quantum systems, *Rev. Mod. Phys.* **85**, 623 (2013).

[236] G. Kurizki, P. Bertet, Y. Kubo, K. M. lmer, D. Petrosyan, P. Rabl, and J. Schmiedmayer, Quantum technologies with hybrid systems, *PNAS* **112**, 3866 (2015).

[237] A. Angerer, K. Streltsov, T. Astner, S. Putz, H. Sumiya, S. Onoda, J. Isoya, W. J Munro, K. Nemoto, J. Schmiedmayer, and J. Majer, Superradiant hybrid quantum devices, *Nature Phys.* **14**, 1168 (2018).

[238] W. K. Wootters and A. Wigner-function, Formulation of finite-state quantum mechanics, *Ann. Phys.* **176**, 1 (1987).

[239] R. Khasseh, A. Russomanno, M. Schmitt, M. Heyl, and R. Fazio, Discrete truncated wigner approach to dynamical phase transitions in ising models after a quantum quench, *Phys. Rev. B* **102**, 014303 (2020).

[240] S. Czischek, M. Gärttner, M. Oberthaler, M. Kastner, and T. Gasenzer, Quenches near criticality of the quantum ising chain: power and

limitations of the discrete truncated wigner approximation, *Quantum Sci. Technol.* **4**, 014006 (2018).

[241] B. Zhu, A. M. Rey, and J. Schachenmayer, A generalized phase space approach for solving quantum spin dynamics, *New J. Phys.* **21**, 082001 (2019).

[242] M. A. Perlin, C. Qu, and A. M. Rey, Spin squeezing with short-range spin-exchange interactions, *Phys. Rev. Lett.* **125**, 223401 (2020).

[243] G. E. Uhlenbeck and L. S. Ornstein, On the theory of brownian motion, *Phys. Rev.* **36**, 823 (1930).

[244] M. Foss-Feig, K. R. A. Hazzard, J. J. Bollinger, and A. M. Rey, Nonequilibrium dynamics of arbitrary-range ising models with decoherence: an exact analytic solution, *Phys. Rev. A* **87**, 042101 (2013).

[245] P. Kirton and J. Keeling, Suppressing and restoring the dicke superradiance transition by dephasing and decay, *Phys. Rev. Lett.* **118**, 123602 (2017).

[246] N. Shammah, S. Ahmed, N. Lambert, S. De Liberato, and F. Nori, Open quantum systems with local and collective incoherent processes: efficient numerical simulations using permutational invariance, *Phys. Rev. A* **98**, 063815 (2018).

[247] M. Gross and S. Haroche, Superradiance: an essay on the theory of collective spontaneous emission, *Phys. Rep.* **93**, 301 (1982).

[248] J. M. Vargas-Martínez, H. Moya-Cessa, and M. F. Guasti, Normal and anti-normal ordered expressions for annihilation and creation operators, *Revista mexicana de fisica E* **52**, 13 (2006).

[249] A. Serafini, F. Illuminati, M. G. Paris, and S. D. Siena, Entanglement and purity of two-mode Gaussian states in noisy channels, *Phys. Rev. A* **69**, 022318 (2004).